Study of vertical flow treatment wetlands by X-ray tomography

German Dario Martinez Carvajal

N°d'ordre NNT : 2020LYSE1018

THÈSE de DOCTORAT DE L'UNIVERSITÉ DE LYON
opérée au sein de
l'Université Claude Bernard Lyon 1

École Doctorale N° 206
École Doctorale de Chimie

Spécialité de doctorat :
Discipline : Génie des Procédés

Soutenue publiquement le 04/02/2020, par :
MARTINEZ CARVAJAL Germán Darío

Étude des Filtres Plantés de Roseaux par Tomographie à Rayons X

Devant le jury composé de :

DOTRO Gabriela	Chercheure	University of Cranfield	Examinatrice
FONGARLAND Pascal	Professeur	Université Claude Bernard Lyon 1	Président du jury
FORQUET Nicolas	Ingénieur de Recherche	Irstea	Examinateur
GALVAO Ana	Professeure Associée	Université de Lisbonne	Rapporteuse
MOLLE Pascal	Directeur de Recherche	Irstea	Directeur de thèse
OXARANGO Laurent	Professeur	Université Grenoble Alpes	Co-Directeur de thèse
ROLLAND DU ROSCOAT Sabine	Maître de Conférences	Université Grenoble Alpes	Examinatrice
SCHMITZ Philippe	Professeur	Toulouse Biotechnology Institute	Rapporteur de thèse

STUDY OF VERTICAL FLOW TREATMENT WETLANDS BY X-RAY TOMOGRAPHY

By: Germán Darío Martínez Carvajal

April 19, 2020

DÉPARTEMENT TRANSFORM, UR REVERSAAL

INRAE

Abstract

FOULING and clogging are major concerns regarding Treatment Wetland (TW) operation and performances. Several techniques are currently used to assess these phenomena indirectly based on their relation with physical, chemical and biological parameters of TW (e.g. hydraulic conductivity, fouling material composition, and enzymatic activity respectively). Few of them focus on the geometrical structure of porous media, which is essential to understand the mechanisms governing solid filtration. This work presents the use of X-ray Computed Tomography (CT) as an imaging methodology to study French Vertical Flow Treatment Wetlands (VFTW). It is a non-destructive technique that produces 3D images of an object showing its inner structure at high resolution. Images from samples of French VFTW show the presence of three phases: voids, fouling material, and granular media (gravel). A methodology to extract, and scan the samples and segment the phases in the images is developed in this work. The use of state-of-the-art image processing algorithms to measure pore scale properties is demonstrated. The spatial representativity of pore scale measurements is assessed: (i) a 2D-Representative Elementary Volume (REV) of the volume fraction of the phases was determined. The assessment suggests that the sample diameter should be larger than 1.5 cm. To avoid significant shear stress during the sample extraction, the minimum recommended diameter is however 5 cm, (ii) pore scale properties were compared between samples extracted from different locations of a large region of a mature French VFTW, which was found to have homogeneous electrical conductivity by using a Frequency Domain Electromagnetic Method. Several similarities among the samples at the pore scale are highlighted. Finally X-ray CT was used to study the structural changes of porous media in French VFTW during the rest period and their influence on the fouling and clogging processes. Despite a limited evaporation rate (2 mm/d), a significant reduction of the deposit layer thickness that is formed above the filter has been observed (with values dropping by 12% to 34% of the initial values). Changes within the gravel filter were also noticed and account for the importance of the rest period to maintain a connected macropore network and to allow air to enter the microporosity of the fouling material in French VFTW.

Keywords
Clogging, fouling, constructed wetland, pore scale, spatial representativity, rest period, drying, porosity

Résumé

L'ENCRASSEMENT et le colmatage font partie des principales difficultés rencontrées dans l'exploitation des Filtres Plantés de Roseaux (FPR) et sont même susceptibles d'en affecter les performances. Différentes techniques ont été mises au point pour en mesurer indirectement l'effet que ce soit au travers de grandeurs physiques (e.g. la réduction de la conductivité hydraulique), chimiques (e.g. la composition des matières encrassantes) ou biologiques (e.g. activité enzymatique) dans les filtres plantés de roseaux. Cependant, peu d'approches s'intéressent à la structure géométrique de l'espace poreux qui, de fait, contrôle les mécanismes de filtration des matières en suspension. Cette thèse introduit l'usage de la tomographie à rayons X comme technique d'imagerie pour l'étude des FPR. Cette technique est non-destructive et produit des images de la structure interne des filtres en 3 dimensions à une très grande résolution. Des images obtenues à partir d'échantillons prélevés sur des FPR ont permis de mettre en évidence la présence de trois phases: les vides, la matière encrassante et les graviers. Une méthodologie permettant d'extraire et de scanner les échantillons et de segmenter l'image afin d'en identifier les phases constituantes a été mis en place. Des méthodes de pointe en traitement d'image ont été utilisées pour estimer des propriétés à l'échelle du pore. La représentativité spatiale des images a été étudiée : (i) une étude du volume élémentaire représentatif pour la fraction volumique des phases préconise un diamètre minimal d'échantillon de 1.5 cm. Pour éviter la déformation des échantillons pendant leur extraction un diamètre minimal de 5 cm reste nécessaire, (ii) les propriétés à l'échelle du pore ont été comparées entre des échantillons extraits à différents emplacements dans une zone d'un FPR dans laquelle la distribution spatiale de la conductivité électrique a été trouvée homogène grâce à l'emploi d'un conductimètre électromagnétique. Les mesures à l'échelle du pore ont montré de fortes similarités. Enfin, la tomographie à rayons X a été utilisée pour suivre temporellement les modifications de la structure de la matrice poreuse d'échantillons issus d'un FPR au cours d'une expérience de séchage représentative d'une période de repos afin d'évaluer l'impact de cette dernière sur les phénomènes de colmatage et d'encrassement. Bien que le gradient d'évaporation mesuré ait été faible (2 mm/j), une réduction importante de l'épaisseur de la couche de dépôt a été observée (avec des chutes allant de 12 à 34% de la hauteur initiale). Des effets au sein du gravier ont également été remarqués et soulignent le rôle essentiel de la période de repos dans le maintien d'une macroporosité et la possibilité pour l'air de pénétrer dans la microporosité de la matière encrassante dans les FPR.

Mots clés
Colmatage, encrassement, marais artificiel, échelle du pore, représentativité spatiale, période de repos, séchage, porosité

Résumé étendu

Montromant (France)

LES eaux usées domestiques se composent : des eaux vannes (issues des toilettes) et des eaux grises (eaux du lavabo, douche, lave-linge, cuisine ...). Ces eaux doivent être traitées avant d'être rejetées dans le milieu naturel pour le protéger en évitant des phénomènes tels que : l'accumulation de sédiments, l'augmentation de la turbidité (et par conséquent diminution de la pénétration de la lumière), la diminution de la concentration en oxygène dissout, susceptible d'entraîner la mort des espèces d'animaux qui en dépendent, l'eutrophisation, le transport de pathogènes, et l'augmentation de la toxicité. Ces phénomènes ont tous d'importantes répercussions dans la chaîne trophique et affectent par ailleurs le développement d'activités de récréation comme la baignade et la navigation.

L'assainissement des eaux usées peut prendre deux formes : l'assainissement collectif, quand les habitations sont connectés à un réseau collecteur conduisant les eaux usées à une station de traitement des eaux usées et l'Assainissement Non Collectif (ANC), où les eaux sont traités sur la parcelle et qui est préféré quand le rattachement de l'habitation à un réseau collecteur existant est plus onéreux que la construction d'un système d'épuration sur site.

Les marais artificiels de traitement (en anglais : Treatment Wetlands) et particulièrement ceux à écoulement vertical (en anglais : Vertical Flow Treatment Wetlands) sont l'une des technologies les plus répandues en France pour l'assainissement collectif en zone rurale et l'ANC. En France, cette technologie est connue sous le nom de Filtres Plantés de Roseaux (FPR) que l'écoulement soit vertical ou horizontal. Le nombre de installations construites a augmenté considérablement lors des deux derniers décennies et atteint plus de 3500 en territoire Français [82]. Nombre de stations consiste en un système de filtres arrangés en deux étages, remplis d'un matériau granulaire (du gravier pour le 1er étage et du sable pour le deuxième), plantés de roseaux (*Phragmites Australis*) et alimentés en eaux usées brutes par des bâchées suivant un cycle d'alimentation et repos à durée déterminée. Ce système est reconnu à l'international sous l'appellation « French System » dont la spécificité est le 1er étage alimenté en eaux usées brutes.

Les FPR ont démontré des performances de traitement élevées pour des polluants tels que les Matières En Suspension (MES), la Demande Chimique en Oxygène (DCO), et l'Azote Kjeldahl (NK) [79]. Dans des stations dites jeunes, les MES sont retenues dans le massif filtrant en période d'alimentation. Après quelques années de fonctionnement (suivant la charge organique reçue) les filtres du 1er étage développent une couche de dépôt surfacique composée principalement de matières organiques. À ce stade, dit mature, les MES sont pour la plus part retenues dans la

couche de dépôt; une autre fraction est toujours retenue dans le massif filtrant. Cette couche de dépôt réduit la vitesse d'infiltration mais promeut une répartition homogène de l'eau à la surface des filtres. Du fait de sa forte activité microbienne, elle participe également au traitement de l'eau. Les bactéries, et d'autres organismes microscopiques s'alimentent des polluants présents dans les eaux usées est se reproduisent autour des surfaces des matériaux granulaires en constituant un biofilm qui ralentit également l'écoulement de l'eau [27]. L'alimentation des filtres par alternance et donc le respect d'une période de repos sont essentiels pour promouvoir la déshydratation, l'oxygénation et la minéralisation du biofilm et des MES retenues, particulièrement celles dans la couche de dépôt. L'accumulation nette de solides au cours d'un cycle alimentation/repos encrasse progressivement le filtre et finira par le conduire à un état colmaté. Étant alimentés en eaux usées brutes, les filtres du 1er étage sont susceptibles de colmater plus rapidement [78].

L'encrassement (en anglais : fouling) désigne l'accumulation de solides dans le massif filtrant des FPR entraînant une réduction des vitesses d'infiltration sans pour autant compromettre les performances épuratoires. Le colmatage (en anglais : clogging) est le résultat d'une accumulation importante de matières encrassantes (encrassement excessif) et/ou d'une accumulation accélérée des solides en surface du filtre (colmatage précoce). Dans un état colmaté, la réduction de la vitesse d'infiltration est telle que le volume d'eau reçu lors d'une bâchée ne peut plus être infiltré complètement avant la bâchée consécutive. À court terme, le colmatage fait décroître la concentration d'oxygène dans les filtres et les performances épuratoire. S'il persiste, il peut notamment conduire à des dysfonctionnements graves tels que le déversement d'eaux non traitées dans le milieu naturel.

La durée de vie des FPR est déterminée par la vitesse d'accumulation nette de solides les amenant à un état colmaté [85]. Plusieurs techniques sont actuellement utilisées pour évaluer l'encrassement et le colmatage. Leur principe repose sur le lien entre ces phénomènes et des propriétés physiques (y compris hydrauliques), chimiques et biologiques des FPR et leur massif filtrants (poreux). Cependant, peu d'entre elles analysent la structure géométrique des milieux poreux dont dépendent directement les mécanismes de filtration, e.g. la sédimentation et l'interception dans des gorges. Avant le démarrage de cette thèse, seulement deux techniques d'imagerie ont été utilisées pour l'étude de la structure des milieux poreux dans les FPR : la géo-endoscopie [33] et les lames minces [50].

Le programme WetClog à Irstea (Figure 1.1) cherche à améliorer la compréhension des phénomènes de colmatage et encrassement des FPR. Il est structuré en deux axes : le premier est dédié au suivi des installations en opération (WetClog monitor) et le deuxième à l'étude des mécanismes (WetClog particulate). Le projet WetClog_Image a pour objectif de mettre en place des méthodes d'imagerie adaptées à l'étude des milieux poreux dans les FPR et le projet WetClog_Modeling de développer un modèle mécaniste de la filtration et le valider par les résultats du projet WetClog_Image.

Cette thèse porte sur l'étude de la tomographie à rayons X (TRX) pour l'étude des FPR à l'échelle du pore. La TRX est une technique non destructive qui permet l'obtention d'images de la structure interne d'un objet en 3D à haute résolution. Les images sont des matrices de voxels (un pixel en 3D) contenant des nombres représentant une nuance de gris. L'intensité de la nuance est liée à la densité des phases présentes. Le traitement d'image consiste en l'exécution d'algorithmes pour obtenir des paramètres décrivant quantitativement et qualitativement la morphologie de l'objet. L'élément central du traitement des images de tomographie est la segmentation de phases, qui consiste en l'attribution univoque de chaque voxel à l'une des phases présentes.

Méthodologie

Ce travail est organisé en trois phases: les deux premières ont eu pour but d'établir un socle solide pour l'utilisation de la TRX dans l'étude de différents phénomènes dans les FPR tels que la filtration, le séchage, ou le transport d'oxygène. La dernière phase est l'application de la TRX pour l'étude de l'importance de la période de repos dans l'atténuation des phénomènes d'encrassement et de colmatage.

La première phase a eu pour but de développer une méthodologie pour extraire et scanner des échantillons du 1er étage d'un FPR mature (c'est-à-dire ayant développé une couche de dépôt sur toute sa surface), d'ajuster un algorithme de segmentation et de démontrer l'application d'autres méthodes de traitement d'image pour quantifier des propriétés à l'échelle du pore telles que : la fraction volumique, la distribution granulométrique du gravier, la distribution de taille des vides, la surface spécifique et les chemins de percolation.

Dans la deuxième phase la représentativité spatiale des propriétés à l'échelle du pore a été évaluée. Cette analyse est souvent faite pour des études à l'échelle du pore ou en laboratoire. Elle consiste essentiellement en la détermination d'un volume minimal d'échantillon pour lequel l'étude d'un phénomène à petite échelle donnera un résultat global comparable à celui obtenu dans un étude à plus grande échelle. Deux approches ont été suivies pour étudier l'hétérogénéité des FPR chacune à deux échelles différentes. À l'échelle du filtre, la répartition de matières encrassantes à été étudiée grâce à la mesure de la conductivité électrique par des méthodes électromagnétiques. À l'échelle du pore, la TRX a été utilisée. Les résultats ont permis de mettre en évidence le lien existant entre les deux échelles spatiales.

Dans la troisième phase la TRX a été appliquée pour étudier les changements dans la structure poreuse des filtres du 1er étage des FPR pendant la période de repos à l'aide d'une expérience ex-situ. Plusieurs propriétés à l'échelle du pore ont été suivies (fraction volumiques, taille des vides, connectivité des vides) ainsi que des pertes de masse dues au séchage. La combinaison des mesures de perte de masse et de la TRX a permis d'obtenir des estimations du changement de la fraction de la micro-porosité des matières encrassantes et de sa désaturation progressive.

Résultats

L'application de la TRX pour des échantillons de FPR produit des images 3D à haute résolution en peu de temps (1 à 3 heures en dépendant de la taille de l'échantillon) et montrent un niveau de contraste suffisant pour repérer 3 phases : vides, graviers et Matières Encrassantes (MEN). Dans ces images, les MEN sont une phase homogène représentant le mélange de matières organiques, de particules minérales de taille réduite, d'eau et de tissus végétaux.

Un algorithme de segmentation a été écrit (en python) se basant sur le concept de 'croissance de régions' (en anglais, 'region growing') et d'autres méthodes de pointe en traitement d'image. L'algorithme est performant pour les spécificités des scans des FPR. Dès l'obtention des premières images et segmentations, il a été démontré que la technique peut s'appliquer pour observer la morphologie d'échantillons sans prétraitement tel que le séchage. En effet, des vides entourés par de grands quantités de MEN ont pu être segmentés malgré la teneur en eau élevée de l'échantillon. Cette observation est la base de l'étude des changements structurels des FPR par TRX du au séchage des MEN pendant la période de repos.

L'extraction des échantillons (du 1er étage) FPR nécessite une manipulation délicate pour éviter au maximum leur déstructuration, spécialement quand plusieurs rhizomes sont présents. La résolution des images dépend du diamètre de l'échantillon, de la distance entre la source à rayons X et le capteur de rayons atténués et du nombre de cellules photosensibles de ce dernier. Le diamètre de l'échantillon (cylindrique) a initialement été fixé à 5 cm. Cette taille limite sa déstructuration par des contraintes de cisaillement lors de l'extraction. Pour ce diamètre, la

résolution optimale est de 35µm/voxel. La représentativité spatiale des échantillons a été étudiée par une analyse du Volume Élémentaire Représentative (VER) en 2D pour la fraction volumique des chaque phase (vides, graviers et MEN). Un diamètre de 5 cm est suffisamment grand pour capturer l'hétérogénéité de cette propriété : les valeurs moyennes de fraction volumique sont stables pour des diamètres plus grands que 1.5 cm en l'absence de rhizomes. La hauteur maximale des échantillons scannés est de 16 cm. Elle a permis de contenir la totalité de la couche de dépôt et une partie de la couche de gravier d'un FPR en âge mature. Des échantillons plus hauts peuvent aussi être scannées tout en préservant la même résolution. Ceci est possible par l'utilisation d'un scanner à acquisition hélicoïdale ou par la concaténation de plusieurs images produites par un scanner à acquisition horizontale. La limitation en hauteur est principalement le déplacement maximale du porte-échantillon du scanner en direction verticale.

Différentes propriétés à l'échelle du pore ont été mesurées en utilisant des méthodes de traitement d'image. Quelques algorithmes ont aussi été adaptés aux particularités des échantillons pour calculer des profils de fraction volumique, des surfaces spécifiques entre les MEN et les vides, des tailles caractéristiques des graviers et des vides et la connectivité de ces derniers. La description morphologique par TRX est limitée à des tailles plus grandes que la résolution des images. Cependant, il a été démontré que des estimations de changement la micro-porosité (ici, porosité plus petite que la résolution de la tomographie) peuvent être faites en combinant des mesures volumétriques par TRX et des mesures de perte de masse.

Les expériences réalisées ont permis de faire des avancements notables dans la compréhension du fonctionnement des FPR :

- Il a été démontré que la fraction volumique des vides atteint des valeurs en dessous de 0.10 voire 0.05 dans la couche de gravier des FPR en âge mature. Cependant, ces valeurs proviennent d'un filtre performant (il n'a pas atteint un état colmaté). Cette observation doit être prise en compte dans la simulation de l'écoulement de l'eau à plus grande échelle. Elle supporte particulièrement le choix d'un modèle à double porosité qui considère le massif filtrant comme un milieu ayant une porosité 'ouverte', qui se draine facilement, et une micro-porosité où l'écoulement d'eau est gouverné par des forces capillaires [83].
- Les grains de gravier ne sont pas une phase immobile. La TRX a démontré que quelques grains sont repoussés vers le haut (dans la couche de dépôt) ce qui indique que le massif filtrant subi une expansion légère au fur et à mesure qu'il retient des MEN. Ce phénomène se rapproche du phénomène de ségrégation dans les milieux granulaires connu sous le le nom de l'effet de la noix du Brésil et qui a tendance à faire migrer les particules fines sous les plus grossières. Ce phénomène est actuellement négligé dans la modélisation de l'encrassement et le colmatage des FPR [97].
- Un critère a été établi pour délimiter le début de la couche de dépôt et de la couche de gravier dans des images de TRX. Il a été utilisé pour mesurer l'épaisseur de la couche de dépôt des FPR. Des différences de maximum 3 cm d'épaisseur ont été repérées pour des échantillons d'un FPR en âge mature, extraits à différents emplacements d'une région homogène en conductivité électrique. Ces différences peuvent être expliquées par l'impact des opérations de maintenance, l'irrégularité de la surface de la couche de dépôt et l'accumulation aléatoire de tissus aériens des roseaux. Elles produisent une micro-topographie bien différente de l'hétérogénéité induite par un répartition non homogène d'effluent à la surface des filtres. D'un côté, elles ne semblent pas avoir de répercussion significative dans la distribution de l'eau lors d'une bâchée car la surface des filtres est complètement inondée. En revanche, à l'échelle locale, ces différences peuvent représenter entre 30 et 60 % de la hauteur de la colonne d'eau lors d'une bâchée et peuvent donc influencer des processus locaux tels que des écoulements préférentiels, une augmentation ou une diminution des capacités de ré-oxygénation et, par conséquent, le développement

de zones anaérobies.

- La structure poreuse des échantillons (issus de la zone homogène en conductivité électrique) est très similaire. Elle est indépendante de leur emplacement et de l'épaisseur de la couche de dépôt. La taille des vides, les surfaces spécifiques et les profils de fraction volumique montrent des valeurs similaires qui varient seulement en fonction de la profondeur (couche de dépôt ou de gravier). Ces observations et les résultats de l'analyse du VER établissent une base solide en terme de représentativité spatiale pour l'application de la TRX dans l'étude d'autre phénomènes.
- Le séchage pendant la période de repos génère des changements structurels importants dans les FPR. Une réduction du volume des MEN jusqu'à 60 % de leur valeur initiale a été observée pendant l'expérience de séchage ex-situ. Ce volume correspond en premier lieu à une augmentation du volume des pores de diamètre compris entre 0 et 3 mm dans la couche de gravier et au centre de la couche de dépôt et en deuxième lieu à une formation de fissures de plus de 4 mm par rétrécissement et rupture mécanique des agrégats de MEN dans la partie supérieure de la couche de dépôt.
- L'expérience de séchage a démontré l'importance de la période de repos dans la restitution de la connexion des vides à l'atmosphère. En 10 jours, la connectivité des pores est rétablie sur toute la hauteur de l'échantillon, ce qui engendre une meilleur diffusion de l'oxygène. Il a été observé aussi, que les cracks par rétrécissement ne pénétraient pas toute l'épaisseur de la couche de dépôt. Si le même phénomène a lieu in-situ, l'eau s'écoulerait par des chemins préférentiels seulement pour les premiers 3cm de la couche de dépôt et non pas pour tout la hauteur de la couche contrairement à ce qui est pensé actuellement. Ces résultats ont été obtenus pour une vitesse moyenne d'évaporation de 2 mm/jour. Si cette méthodologie est appropriée pour suivre des changements structurels, une déstructuration plus marquée est attendue dans des FPR à plus grande échelle, particulièrement en été, quand les vitesses d'évapotranspiration sont maximales.
- Une augmentation de la micro-porosité des MEN remplie d'air a été estimé de 0.07 à 0.014 (v/v) par la combinaison de mesures de perte de masse et de perte de volume des MEN par TRX. La saturation en eau de cette micro-porosité a d'importantes répercussions sur la vitesse du transport d'oxygène à l'intérieur et, par conséquent, de la dégradation de la matière organique et la minéralisation des MEN.

Les mesures volumétriques ici présentées sont limitées à une description tri-phasique du massif filtrant des FPR : ni les vides à l'intérieur de MEN (micro-porosité) ni les vides correspondant aux organes creux des roseaux sont différenciés. Les différents composantes des MEN (eau, tissus végétaux) ne sont pas différenciés non plus. La mesure de la surface spécifique est limitée à la résolution des scans et son interprétation doit être faite avec du recul. Les surfaces spécifiques vides/MEN sont sous-estimées dans la mesure où des micro-pores dans les MEN sont non saturés en eau. Le traitement des images a besoin de ressources informatiques importantes suivant l'algorithme exécuté. Pour obtenir des résultats en des temps raisonnables, des serveurs ayant 128GB de RAM et 12 CPUs ont été utilisés pour le traitement d'images brutes de 8 à 16 GB. Des serveurs moins puissants peuvent être utilisées mais ils traiteront des images forcement plus petites.

Nomenclature

AD Anisotropic Diffusion

ANC Assainissement Non Collectif

BOD Biological Oxygen Demand

COD Chemical Oxygen Demand

DCO Demande chimique en oxygène

ET EvapoTranspiration

FDEM Frequency Domain Electromagnetic Method

FM Fouling Material

FPR Filtres Plantés de Roseaux

FWS Free Water Surface

IP Image Processing

IR Infiltration Rate

IR Infiltration Rate

KN Kjehdal Nitrogen

MEN Matières ENcrassantes

MES Matières en suspension

NK Azote Kjedahl

OM Organic Matter

p.e. Person equivalent

PSD Pore Size Distribution

PVE Partial Volume Effect

REV Representative Elementary Volume

RH Relative Humidity

ROI Region of Interest

RT Residence Time

RTD Residence Time Distribution

SS Suspended Solids

SSA Specific Surface Area

T Temperature

TKN Total Kjeldahl Nitrogen

TRX Tomographie à rayons X

TW Treatment Wetland

UC Uniformity Coefficient

VER Volume élémentaire représentatif

VF Volume Fraction

VFP Volume Fraction Profile

VFTW Vertical Flow Treatment Wetland

VSS Volatile Suspended Solids

X-ray CT X-ray Computed Tomography

table of CONTENTS

Contents

[2]Martinez-Carvajal, G. D., Laurent Oxarango, Jérôme Adrien, Pascal Molle, and Nicolas Forquet. *Assessment of X-Ray Computed Tomography to Characterize Filtering Media from Vertical Flow Treatment Wetlands at the Pore Scale*. **Science of the Total Environment** 658 (2019): 178–188.

[4]Martinez-Carvajal, G. D., Laurent Oxarango, Rémi Clément, Pascal Molle, and Nicolas Forquet. *Assessment of X-Ray Computed Tomography to Characterize Filtering Media from Vertical Flow Treatment Wetlands at the Pore Scale Assessment of spatial representativity of X-ray tomography to study Vertical Flow Treatment Wetlands*. **Science of the Total Environment** 713 (2020).

[6] Article to be submitted for publication to Water

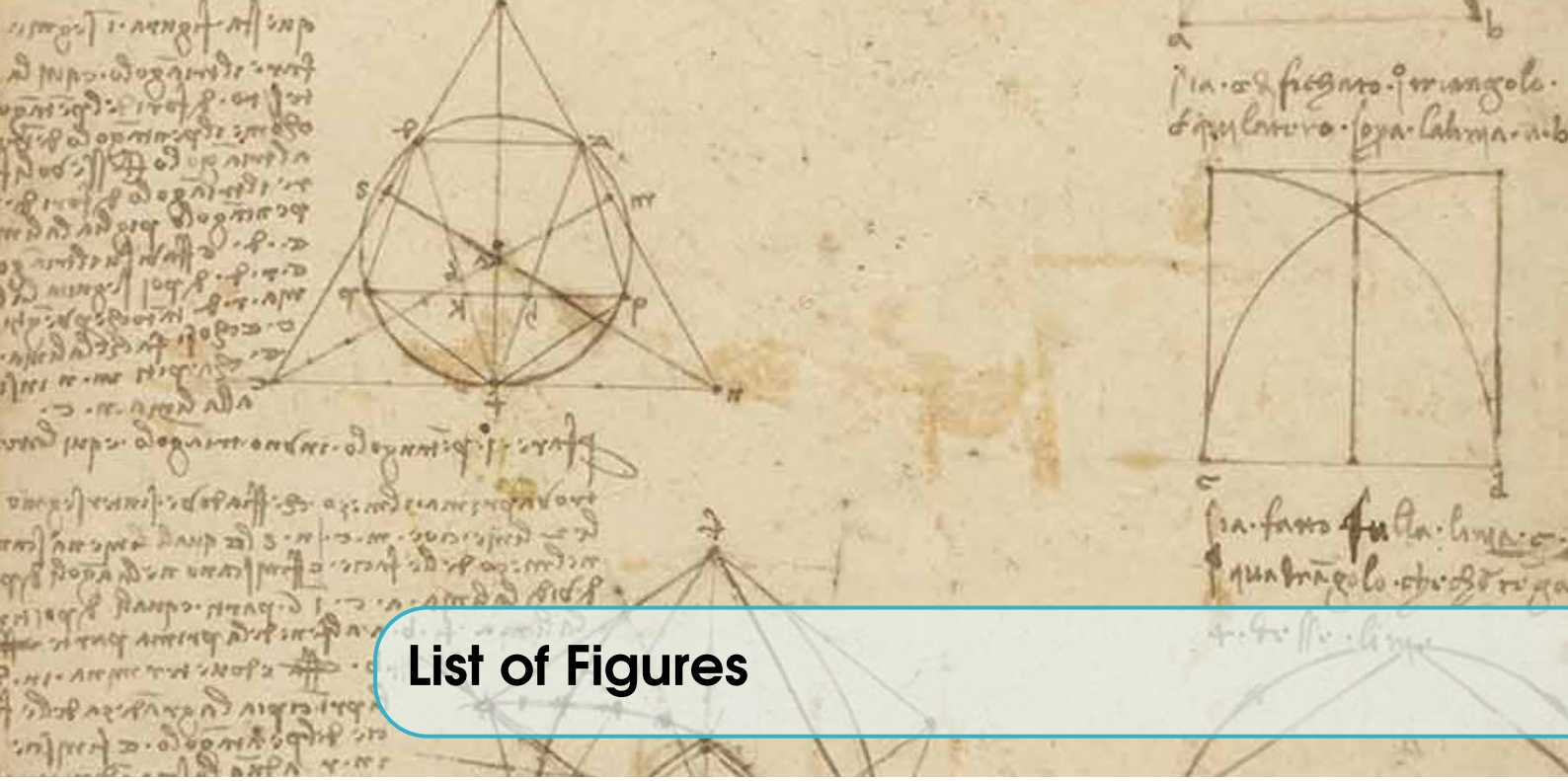

List of Figures

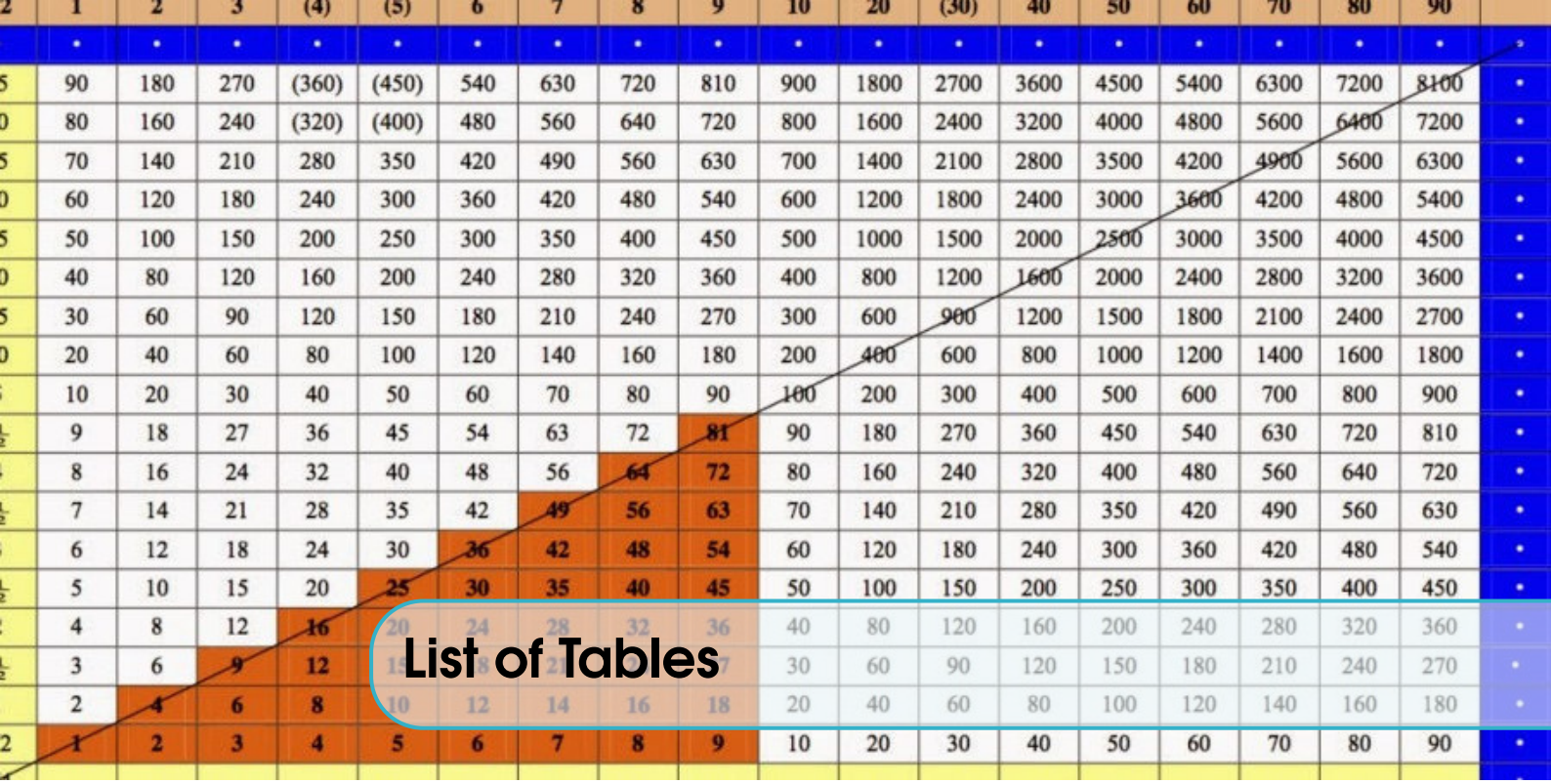

List of Tables

1. Introduction

French Vertical Flow Constructed Wetland (Copponex, France)

DOMESTIC wastewater derives from human activities in households such as baths, toilets, laundry and dish washing. In order to protect the quality of the aquatic environment, it has to be treated before being discharged, thus avoiding impacts like: accumulation of sediments, increase of turbidity (and consequently a decrease of light penetration), decrease in oxygen concentration (deadly for the aquatic life), eutrophication, pathogen spreading, and increase of toxicity. All these have strong repercussions on the trophic chain but also on human recreation activities like bathing and sailing.

Water treatment can be organized in two forms: public sanitation, when households are close enough to collect water and direct it to a wastewater treatment plant, and on-site sanitation, when the cost of constructing a small treatment plant is less than that of connecting an individual household to an existing network.

Treatment Wetlands (TW) and, particularly, Vertical Flow Flow Treatment Wetlands (VFTW) are one of the most popular technologies for public sanitation in small communities and on-site sanitation. Their number has quickly increased over the last decades. Currently, approximately 3500 TW are in operation all over the French Territory [82]. Number of them consist in a set of filters organized in two stages, containing a granular layer of gravel and sand respectively, planted with reeds (*Phragmites Australis*) and fed with raw wastewater by batches following a specific feeding/rest period cycle. This configuration is known as the French system.

French VFTW have proven to yield high performances in removal of pollutants in wastewater: Suspended Solids (SS), Chemical Oxygen Demand (COD) and Kjeldahl Nitrogen (KN) [79]. During the feeding period, SS are retained within the granular media. Mature French VFTW have developed a surface deposit layer (after 2 years approximately) made mostly of organic solids. It retains most of the SS (the rest are retained within the granular media). It also decreases the infiltration speed and therefore contributes to uniform infiltration. Finally, it participates actively to pollutant removal. Bacteria and other microorganisms living in the TW are fed by pollutants present in wastewater and grow forming a biofilm surrounding gravels which reduces also the infiltration speed [27]. The rest period is essential to promote drying, oxygenation and mineralization of the biofilm and retained solids, specially those present in the deposit layer. The net accumulation of solids over feeding/rest cycles leads to the fouling and, eventually, clogging of the filters, specially in the first stage as it is fed with raw wastewater [78].

Fouling is the phenomenon by which solids are accumulated within the granular media and

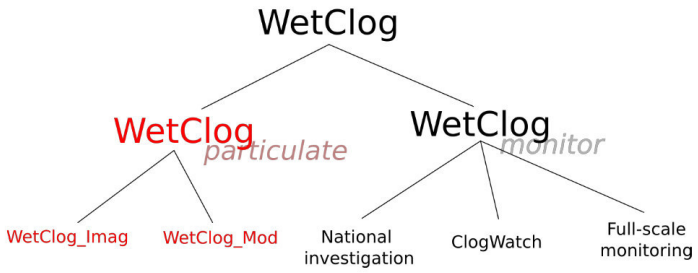

Figure 1.1: The WetClog program

reduce the infiltration speed without compromising pollutant removal performances. Clogging is the result of a high accumulation of solids within the granular media (clogging by excessive fouling) and/or a rapid accumulation of solids at the surface of the filters (premature clogging), which reduces the infiltration speed to a level at which the volume of water received during a batch does not infiltrate completely before the subsequent batch. In the short term it leads to the depletion of oxygen within the filter and then to a decrease in pollutant removal performances. If the clogging persists, it may cause the failure of the treatment plant with large volume of wastewater being discharged without treatment.

The lifespan of a TW is determined by the rate of net accumulation of solids within it, which lead them to clog [41, 40]. Several techniques are currently used to assess the fouling and clogging in TW. Many of them are based on the relation of these phenomena to physical (including hydraulic), chemical and biological properties of the TW and the porous media [85]. Nevertheless, few of them focus on the geometrical structure of the porous media, which is essential to understand the mechanisms governing solids filtration, e.g. sedimentation and geometrical interception. Before the beginning of this thesis only two imagery techniques have been used to study the geometry of porous media in TW: geo-endoscopy and thin sections [50, 33].

Study of clogging of TW has been endeavored in the WetClog program at INRAE (formerly Irstea), France (Figure 1.1). It is organized in two axes: one focused on monitoring (WetClog *Monitor*) and the other on the study of mechanisms (WetClog *Particulate*). The WetClog *Image* project aims at developing imaging methodologies suitable to study the porous structure of a TW. The WetClog *Modeling* project aims at developing a mechanistic model of filtration and will be supported on the results of WetClog *Image* to validate the model.

This thesis focuses on the use of X-ray Computed Tomography (X-ray CT) as an imaging methodology. It is a non-destructive technique that produces 3D images of an object at high resolution, which shows its inner structure. The resulting images are 3D pictures, where each voxel (a 3D-pixel) stores a gray value. The intensity of the gray value is related to the elemental composition of the phases in presence. The images are treated afterwards using image processing algorithms to obtain mathematical descriptions of the object morphology. The central step in image processing is the segmentation of the image, which consists in the attribution of each voxel to one phase.

During this PhD, my work has been organized in 3 major phases. The first two phases intend to set a solid basis for the use of X-ray CT to study different processes, such as water flow, filtration, drying or oxygen transport in gas phase, and the last is a particular application of X-ray CT to study the importance of the rest period to delay clogging.

The first phase consisted in the development of a methodology to extract and scan samples, the adjustment of a segmentation algorithm to process images, and the application of different post-processing algorithms to measure pore scale properties. This introduction to the use of

X-ray CT is presented in Chapter 4.

The second phase consisted in the assessment of the spatial representativity of pore scale measurements by X-ray CT in mature French VFTW. It is presented in Chapter 5. Evaluating the spatial representativity is a common practice in studies performed at the pore scale and/or at the laboratory scale. The major concern is defining the minimum volume of the sample for which the study of a phenomenon at a small scale will yield an average result similar to that obtained at a larger scale. In this chapter we present a study of heterogeneity in French VFTW at two scales: at the filter scale, using Frequency Domain Electromagnetic Methods (FDEM) and, at the pore scale, using X-ray CT. The links between the results at the two scales are highlighted.

In Chapter 6, the application of X-ray CT to study the structural changes of porous media in French VFTW during a rest period is presented. Several pore scale properties and mass changes were monitored during an ex-situ drying period. Properties include volume fractions, void sizes, void connectivity and estimations of the volume of microporosity. The results include several breakthroughs in the understanding of phenomena occurring at the pore scale.

Chapters 2 and 3 provide an introduction to French VFTW and X-ray CT/image processing. In Chapter 2 the physical and biological processes occurring within a French VFTW are presented with a particular emphasis on fouling and clogging. In Chapter 3 imaging and image processing methodologies used in this work are presented in detail. Chapters 4 to 6 are presented in the form of scientific papers, and thus, the reader is free to skip the introduction and methodology corresponding to image processing if he/she decides to read Chapters 2 and 3 completely.

The results of the this PhD set a solid basis for future modeling and experimental works on solid transport in VFTW. In Chapter 7 we present a list of the perspectives of this work including: (1) developing new experiments using X-ray CT, (2) using other imaging methodologies, (3) refining post-processing algorithms, (4) modeling and simulating phenomena at the pore scale, (5) determining parameters of models at larger scale and validating them experimentally. A special focus is put on the modeling of oxygen transport and consumption in French VFTW, which includes simulating the TW as a gas/liquid reactor and or as a solid/gas catalytic reactor.

Bonne lecture !

2. French Vertical Flow Treatment Wetlands

French Vertical Flow Treatment Wetland (Montromant, France)

2.1 One of many types of Treatment Wetlands in the world

WETLANDS are land areas that are wet or flooded during part or all of the year. Constructed Wetlands (CW) are wetlands designed with different specific purposes. A large group of them was conceived as a solution to treat wastewater, storm water or sludge produced by different human activities. This group constitutes the Treatment Wetlands (TW). In fact, natural wetlands have been used as discharged sites for wastewater in some locations for more than a hundred years because of their faculty to remove pollutants. TW intend to imitate and optimize the treatment provided by natural wetlands, stop indiscriminate discharges therein and preserve their quality and ecological services [45].

During the last century, many types of TW have emerged all over the world as innovative solutions for specific purposes; French Vertical Flow Treatment Wetlands (VFTW) are just an example. All TW have at least three elements in common: (1) an impermeable or semipermeable basin, which stocks water temporarily or permanently (2) a continuous or almost continuous water inflow and outflow through the basin (3) the presence of at least one plant species. Depending on specific objectives and/or restrictions their design may vary considerably. The number of types and their nomenclature are numerous. This makes sometimes difficult to classify a technology a-priori as a TW and determine whether a "new-type" is innovative or not. In particular, the term "French VFTW" may not sound familiar to a “non-scientific” member of the French wetlands community as the technology is better known under the name of “Filters Planted with Reeds”, in France: Filtres Plantés des Roseaux (FPR). Nevertheless, the French nomenclature FPR refers “Filters” to all subsurface flow TW (horizontal or vertical).

A detailed classification has been suggested by Fonder and Headley [30], which considers several hydraulics and vegetation elements. 7 subcategories are proposed in Figure 2.1.

French VFTW are located in the fifth type of the polychotomous classification proposed by [30] (VDF):

- Their main purpose is the treatment of domestic wastewater.
- Water flows through a filtering media (gravel or sand).
- Water flows (essentially) downwards (vertical). It is fed from the top (gravity driven flow).
- The filtering media is not saturated in water for most of the time.
- Water is fed intermittently by batches.
- Reeds (*Phragmites Australis*) emerge from the filtering media.

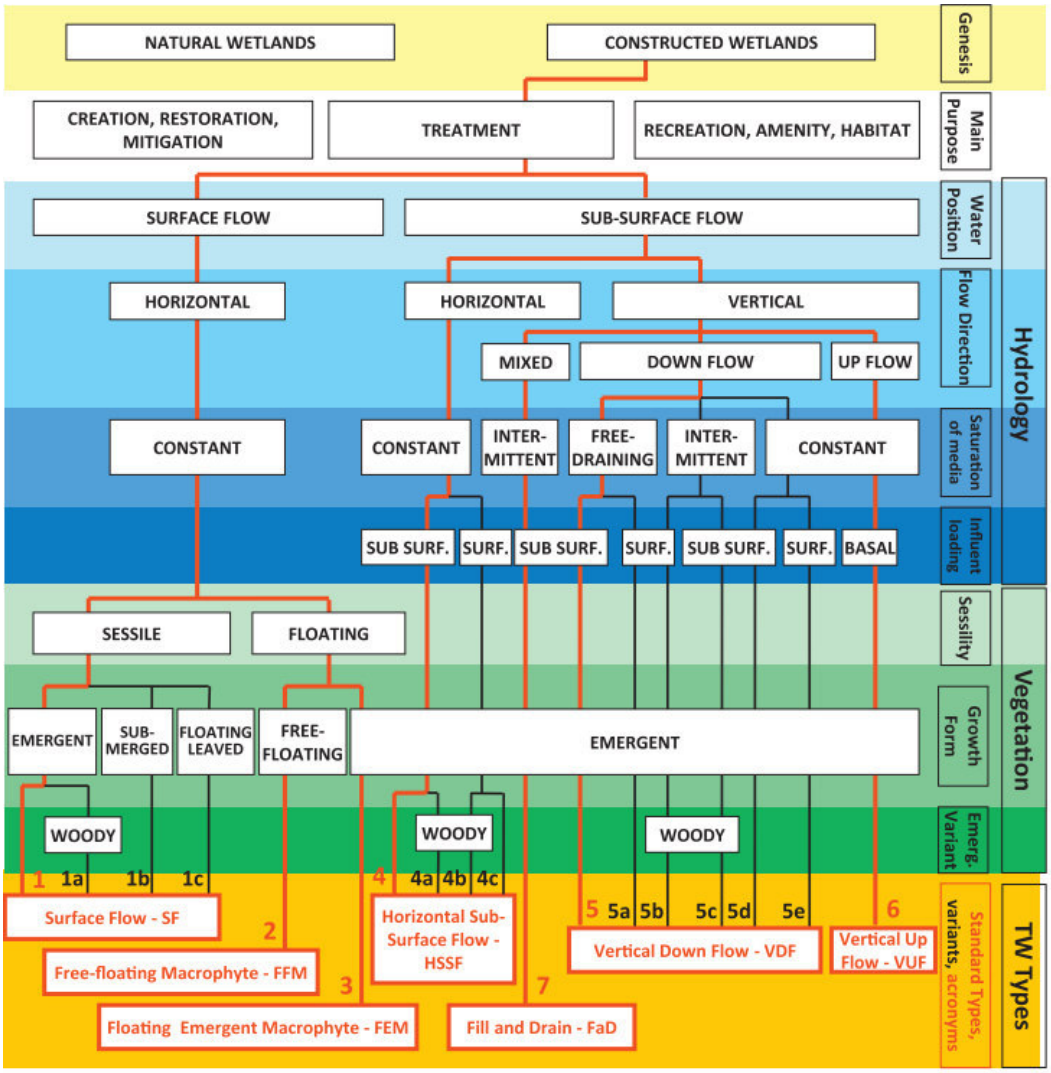

Figure 2.1: Treatment Wetlands polychotomous classification tree.
From [30]

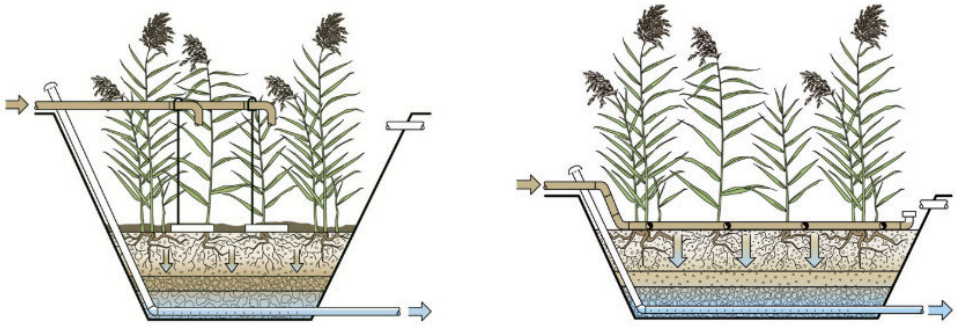

Figure 2.2: Vertical profiles of the two stages in French VFTW.
The first stage has a coarse granular material (gravel), and the second a finer one (sand). Filters have an aeration drain to avoid accumulation of water at the bottom of the wetland. From [25].

French VFTW differ from other VFTW mainly due to the presence of a first stage (Figure 2.2) filled with a coarse granular material (gravel) and receiving raw wastewater. The second stage is a "classical" VF filter filled with a finer granular material (sand). Both stages are planted with reeds. Filters follow a specific feeding/rest period cycle of 3.5 days (feeding) and 7 days (rest) for the first stage and 3.5 days (feeding) and 3.5 (rest) days for the second stage. These features imply the use of 3 and 2 filters in parallel for each stage respectively to assure a continuous treatment as is depicted in Figure 2.3.

Fouling and clogging have great impact on pollutants removal and are the major concerns in TW, specially in French VFTW because they are fed with raw wastewater.

In the remainder of this chapter, some concepts of wastewater treatment and French VFTW are explained focused on the fouling and clogging phenomena. This starts by a description of pollutants in wastewater, followed by a space scale and time scale based description of French VFTW. An intermediate section is dedicated to explain physical and biological processes related to fouling and clogging.

2.2 Pollutants in wastewater

2.2.1 Characterization and regulation

All technologies for wastewater treatment are based (or partially based) on complex physical and biological processes such as pollutant retention and degradation. A characterization of wastewater pollutants is necessary to understand these processes and predict treatment performances but it is also a difficult task because of the variety of compounds and their different physical and chemical properties.

A classical characterization divides pollutants in 5 groups: Suspended Solids (SS), Organic Matter (OM), Nitrogen (N), Phosphorous (P) and pathogens [25].

The content of OM in wastewater is often estimated either as the Chemical Oxygen Demand (COD) or Biological Oxygen Demand (BOD). These do not represent equal measurements. COD is an equivalent amount of any pollutant expressed as the mass of oxygen consumed to transform them to their more oxidized form. BOD_x is an equivalent amount of pollutants expressed as the mass of oxygen consumed by a biologically active matrix to degrade them at specific environmental conditions during a period of "x" days. Global Nitrogen (N_G) is often divided depending on its oxidation state in a molecule. Reduced forms are organic-N and NH_4^+ and their total amount is measured by the Kjeldahl method (TKN). The rest of the N (oxidized forms) is found as nitrites (NO_2^-) and nitrates (NO_3^-) ions. Global P (P_G) can also be found as

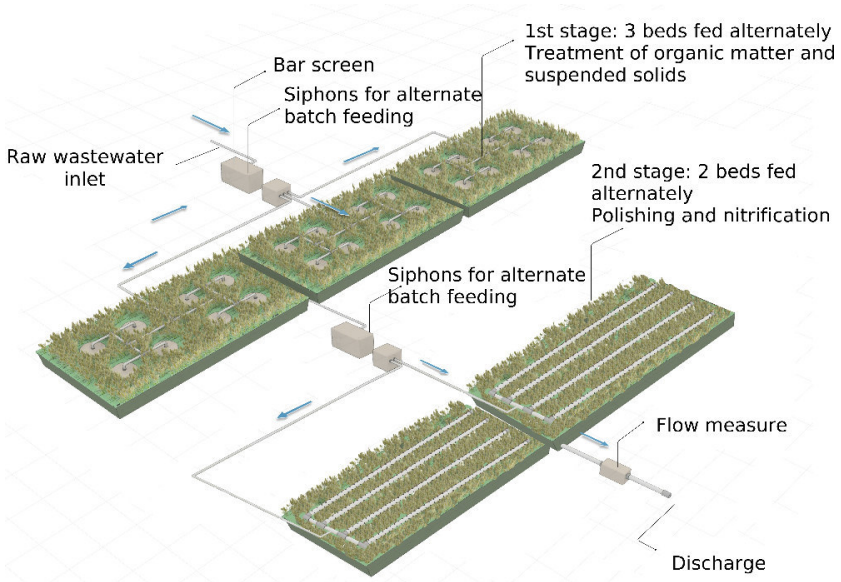

Figure 2.3: The French 2-stage VFTW (courtesy of Syntea).
Wastewater is screened before entering into the first stage. The 1st stage is composed of three filters and the 2nd stage of two filters working intermittently to assure continuous treatment.

phosphates ions (PO_4^{3-}) associated to organic matter or as free ions.

The characterization of pollutants presented above is used to evaluate the efficiency of classical treatment stages in wastewater treatment (primary, secondary, tertiary). Each stage targets a specific impact on the aquatic environment and its efficiency is assessed by at least of one of the parameters described above as it is depicted in Table 2.1.

French VFTW, should not be described following the classical treatment stages, for a single filter provides all "types" of treatment. It provides primary treatment, as SS are retained in granular media. It provides secondary treatment, as during the rest period and between intermittent batches oxygen penetrates the wetland and OM is oxidized by biological processes. Finally, it provides tertiary treatment as (1) a portion of NO_3^- in wastewater, even if it is small, is denitrified [84] and, (2) part of the P is retained in the filters by different mechanisms including precipitation and reproduction of living organisms.

The design of a treatment technology depends on the concentration of pollutants in the inflow. This depends on the habits of the communities which are especially different between rural and urban areas. A statistical study of the composition of wastewater in rural areas (< 2,000 PE) in French Territory was done by Mercoiret et al.,[74]. Tables 2.2 and 2.3 present mean and ranges for values of pollutant concentrations and specific ratios from this study.

The ratios present in Table 2.3 are used to define the mean composition of wastewater produced by a p.e. (Table 2.4). The p.e. is a regulatory definition used to estimate the size of a treatment plant of a community. It is currently defined as a rate of production of 60g-DBO_5/day and a volume of $150l \cdot d^{-1}$ [74].

Limits in TSS, DBO_5, DCO, N_G and P_G are defined by European regulation and transposed in French regulation to minimal treatment performances as presented in Tables 2.5 and 2.6. More stringent requirements can be requested according to waterbody sensitivity.

Table 2.1: Classification of treatment stages.

Classical treatment stage	Pollution targeted	Main removal mechanisms	Impact on the aquatic environment	Parameter that assesses treatment efficiency
Primary	Suspended Solids	Sedimentation, interception	Decrease of turbidity	TSS
Secondary	Soluble oxidizable matter (esp. OM and NH_4^+)	Oxidation	Decrease in oxygen consumption and toxicity	$COD_{soluble}$, $TKN_{soluble}$
Tertiary	Soluble non oxidizable mater, (esp. NO_3^- and PO_4^{3-})	Various (anaerobic reduction, precipitation, adsorption...)	Avoids eutrophication	N_G, P_G

Table 2.2: Mean values and ranges for pollutant concentration in wastewater in rural areas in France.

From [74].

		BOD5	COD	TSS	NK	N-NH_4^+	N_G	P_G
Unit		mg/l	mg/l	mg/l	mg/l	mg/l	mg/l	mg/l
Mean		265.0	645.7	288.1	67.3	54.9	72	9.4
Range	Upper Limit	570.0	1341.3	696.0	123.1	98.3	122.6	18.4
	Lower Limit	39.0	122.0	53.0	14.1	12.0	20.2	2.0
Number of observations		10275	10275	10256	9416	4266	1861	9185

Table 2.3: Mean values and ranges for specific ratios computed from table 2.2.

From [74].

		COD/BOD_5	NK/COD	P_G/COD	TSS/COD	BOD_5/NK	BOD_5/P_G	N-NH_4^+/NK
Mean		2.60	0.12	0.016	0.46	3.88	28.5	0.74
Range	Upper Limit	3.9	0.18	0.026	0.79	6.50	47.0	0.97
	Lower Limit	1.8	0.063	0.0089	0.23	1.90	12.6	0.50
Number of observations		10275	9416	9184	10256	9416	9184	4244

Table 2.4: Use of ratios from Table 2.3 to define the p.e. in rural areas.

From [74].

	BOD_5	COD	NK	NH_4^+	P_G	TSS
p.e.	60	157.2	15.5	11.5	2.1	72.0
unit	g-O_2/day	g-O_2/day	g-N/day	g-N/day	g-P/day	g-TSS/day

Table 2.5: Minimal treatment performances for three pollutants (BOD_5, COD and TSS).
Either the maximal concentration or the minimum removal rate must be respected. From [3].

Pollutant	Organic load received by the station in kg/day pf BOD_5	Maximal concentration to be respected (daily basis)	Minimum removal rate to be respected (daily basis)	Prohibitive concentration (daily basis)
BOD_5	< 120 >= 120	35 mg O_2/l 25 mg O_2/l	60% 80%	70 mg O_2/l 50 mg O_2/l
COD	< 120 >= 120	200 mg O_2/l 125 mg O_2/l	60% 75%	400 mg O_2/l 250 mg O_2/l
TSS*	< 120 >= 120	/ 35 mg O_2/l	50% 90%	85 mg O_2/l 85 mg O_2/l
Respect for the TSS pollution is facultative depending on current specific regulations (*) The values from this table refer to standardized methods for a homogeneous sample, non filtrated nor settled. Nevertheless, the measurements made at the exit of stabilization ponds are performed on filtrated samples except for TSS. The prohibitive TSS concentration in non filtrated samples is then 150 mg/l on a daily basis for any organic load.				

Table 2.6: Minimal treatment performances for parameters N and P in the case of stations discharging treated water in zones sensitive to eutrophication.
Either the maximal concentration or the minimum removal rate must be respected. From [3].

Discharge in zone sensitive to eutrophication	Parameter	Organic load received by the station in kg/J pf BOD_5	Maximal concentration to be respected (annual basis)	Minimum removal rate to be respected (annual basis)
Nitrogen	N_G(1)	> 600 et <= 6000 > 6000	15 mg/l 10 mg/l	70% 70%
Phosphorus	P_G		2 mg/l 1 mg/l	80% 80%
(1) samples used for computation of yearly averages are sampled when the temperature of the discharge in the biological reactor is higher than 12°C				

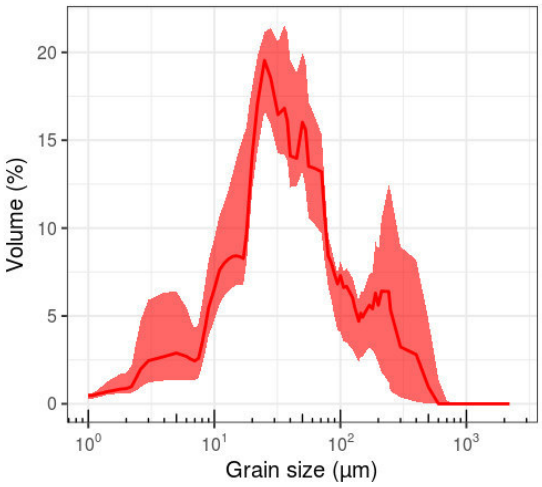

Figure 2.4: Volume size distribution of wastewater particles from 5 different wastewater treatment plants (800 < p.e. < 2000).
Data from Irstea, France by laser granulometry.

2.2.2 Focus on clogging and fouling

Although the characterization of wastewater presented above contemplates several elements, it lacks of many others which are important to understand fouling and clogging in VFTW. These elements are discussed progressively in this section.

Particle Sizes

TSS are measured by weighting the dry mass retained by a filter of 0.45 µm. Nevertheless, the size of particles present in wastewater vary significantly. More importantly, the predominant mechanisms by which they are filtrated depend on their size and their surface/volume ratio.

Solid/water mixtures can be classified as homogeneous or heterogeneous. In homogeneous mixtures the state of subdivision of solids is ionic or molecular (i.e. solutions). Heterogeneous mixtures can be (1) colloidal dispersions or (2) suspensions. In colloidal dispersions the size of the particles is small enough and repulsive electrical forces at their surface are strong enough to avoid their precipitation. In suspensions, the size of the particles is large enough for gravity forces to promote sedimentation if the mixture is at rest, or is not too much agitated. The size of dissolved solutes is roughly considered to be smaller than 1 µm, and the size of colloidal particles comprised between 1 nm and 1 µm. Larger particles correspond to suspensions.

Figure 2.4 shows the distribution of particle sizes of 5 wastewater treatment plants treating effluent from 800 to 2000 p.e. The maximum size in this figure is 2 mm and is limited by the maximum size accepted by the scanner in laser granulometry. The mean size is approximately 20 µm.

Chemical and biochemical properties

Ions and molecules present in wastewater are largely numerous. Measurements like COD are suitable to simplify the quantification of a large variety of pollutants based on its tendency to oxidize them but hide a large variety of chemical and biochemical properties. [1] However, chemical properties of pollutants in wastewater and those of intermediate degradation products are strongly related to fouling and clogging.

[1] The quantification of OM by means of the COD is a rough approximation as not only OM but ions have also a DCO equivalent, e.g. NH_4^+ and S^{2-}.

Pollutants in wetlands are either organic or inorganic. Inorganic mater is in the form of ions or their salts. They can be divided into non metallic ions (CO_3^{2-}, NH_4^+, NO_2^-, NO_3^-, PO_4^{3-}, S^{2-}, SO_4^{2-}) and metallic ions (Na^+, K^+, Mg^{2+}, Ca^{2+}, Hg^{2+}, Pb^{2+}, Fe^{2+}, Fe^{+3}, Al^{3+} ...). Organic compounds are more diverse and difficult to classify. The most simple way to study them is by there chemical functions: alcohols, aldehydes, ketones, carboxylic acids, amines, amino-acids, amides, esters, aromatic cycles (benzene and derivatives like phenols, catecholes, quinones...), non aromatic cycles, homo or heterocycles, all of them having or not saturated (alkanes) or unsaturated (alkenes) radicals...

In biochemistry, most of the organic compounds are regrouped in three classes: carbohydrates, proteins and lipids, which contain many of the organic functions listed before.

The majority of the organic compounds in wastewater are degraded by living organisms. In this process large molecules are decomposed into smaller ones by breaking chemical bonds catalyzed by enzymes. This process is called catabolism. Nevertheless, small molecules can also reform larger molecules following the inverse process, this process is called anabolism.

The energy to break a chemical bond in a organic molecule depends on the organic function. The stronger a chemical bond is, the less degradable the molecule is. Labile and non-labile organic compounds, as well as mineral compounds, have different impact on clogging and fouling

Impact of non-easily degradable organic compounds Solid particles made of molecules hardly degradable by bacteria will contribute to fouling and clogging. Humic substances are a group of the most stable compounds. They are large molecules containing several phenol and carboxylic substitutes in aromatic cycles. They may be intermediate products of the catabolism of large polymers and/or the anabolism of small monomers. As they take longer time to decompose they accumulate preferentially in TW. Knowles et al.[51] state that their colloidal nature and capacity to retain water make them suitable to induce clogging in TW. Kania et al. [46] have found larger amounts of humic substances and lower indexes of aerobic biodegradation in mature French VFTW (> 3 years of operation).

Impact of easily degradable organic compounds Easily degradable compounds like some carbohydrates, proteins and lipids are the main source of many structural components of organisms. Cells produce enzymes capable of hydrolyzing these molecules into smaller ones to either use them as a source of energy or produce new living cells and tissues. A high amount of easily degradable compounds is perhaps the main cause of rapid biofilm development. Hua et al. [27], for instance, acknowledge the role of humic and fulvic substances in fouling and clogging but state that the main factor contributing to clogging is the concentration of labile compounds.

Impact of mineral compounds Some mineral ions, can precipitate as insoluble salts depending on pH conditions. Although their contribution is minimal compared to organic matter, it will increase with time. Ferric, calcium and aluminum phosphates are some of the salts that contribute to mineral fouling in TW. $FeCl_3$ and $AlCl_3$ are, for instance, mixed with the inflow in order to precipitate PO_4^{3-} ions, retain them inside the TW and avoid their discharge, especially in environments sensitive to eutrophication.

2.3 Understanding the context

2.3.1 3.1 Global performances

French VFTW provide treatment for most of the pollutants present in domestic wastewater. A recent study of the treatment performances of French VFTW using a database collected over

Table 2.7: Effluent pollutant concentrations and removal efficiencies from the two-stage VFCW system.

From [82]

	COD		TSS		TKN	
	Outlet concentration (mg L^{-1})	Removal efficiency (%)	Outlet concentration (mg L^{-1})	Removal efficiency (%)	Outlet concentration (mg L^{-1})	Removal efficiency (%)
Mean ± X (*N*) SD	74 ± 16 (417) 168	87 ± 2 (409) 14	17 ± 6 (418) 64	93 ± 1 (411) 9	11 ± 2 (357) 13	84 ± 2 (329) 17
Molle *et al.* (2005)	66 ± 13 (49) 46	91 ± 3 (49) 46	14 ± 5 (49) 18	95 ± 2 (49) 18	13 ± 5 (49) 18	85 ± 5 (49) 17

SD: standard deviation; *N*: the number of values; $\pm X = 1.96*(SD/\sqrt{N})$: 95% confidence interval.

the last 30 years [82] presents their performance in the reduction of three of the most important pollutant groups: COD, TSS and TKN (Table 2.7). Limits on maximal concentration and minimal removal rates from Table 2.5 are respected. The efficiency of removal of TKN is also very high. Nevertheless the French VFTW do not proportion efficient treatment for N_G nor P_G. In the case of an eutrophication sensitive environment other solutions have to be considered. Some of them rely on the construction of filters with materials promoting precipitation of PO_4^{3-} and others adding a saturated layer to promote denitrification (references in[78]).

2.3.2 3.2 Use in French territory

VFTW is a land-extensive wastewater treatment technology with low operating and power requirements. Land-extensive treatment technologies are perfectly suited for small communities (less than 5000 p.e.). VFTW have been introduced when other land-extensive technologies could not provide anymore solution to more stringent regulations for discharge limits in TSS, COD, BOD and N_G. The examples of stabilization ponds, sand filters (also known as infiltration basins), Imhoff tanks, and trickling filters are mentioned in [61]. Moreover, other VFTW features made of them a very attractive solution.

Their comparison with settlers is specially interesting. Settlers are intended to remove most of SS by sedimentation and prevent clogging in downstream operations. However, settlers need to be emptied frequently and the quality of the primary settled sludge (low siccity and high fermentability) limits the options for their disposal. Furthermore, settlers are highly sensitive to hydraulic shocks (storm events). Although French VFTW were thought to clog rapidly at the beginning, they have proven to have high performances to treat raw wastewater directly. Moreover, due to OM mineralization in VFTW, they minimize the amount of solids to be managed, the frequency at which they have to be removed (in "average" once every 10-15 years [78]), and more interestingly, the sludge quality allows direct land application in agriculture as well as composting [79].

French VFTW are part of the ecological engineering solutions for wastewater treatment [18]. They mimic natural systems like swamps and optimize some of the processes that occur inside them without using energy resources intensively. This is an essential feature that helped TW to integrate the natural landscape of rural areas and to be accepted by the communities. If the landscape presents a sufficient slope, not even pumping is necessary: the systems are constructed at the lowest part of the villages and the water flow is driven only by gravity. Furthermore, their operation does not require specific electro-technical knowledge and can be performed by communities technical staff.

To summarize, all these features have made of French VFTW a very popular technology for communities with less than 5000 p.e. (Figure 2.5). The number of plants built in France has increased to a value of about 3000.

In 2017, 20% of all wastewater treatment plants in France are TW. The cumulative treatment

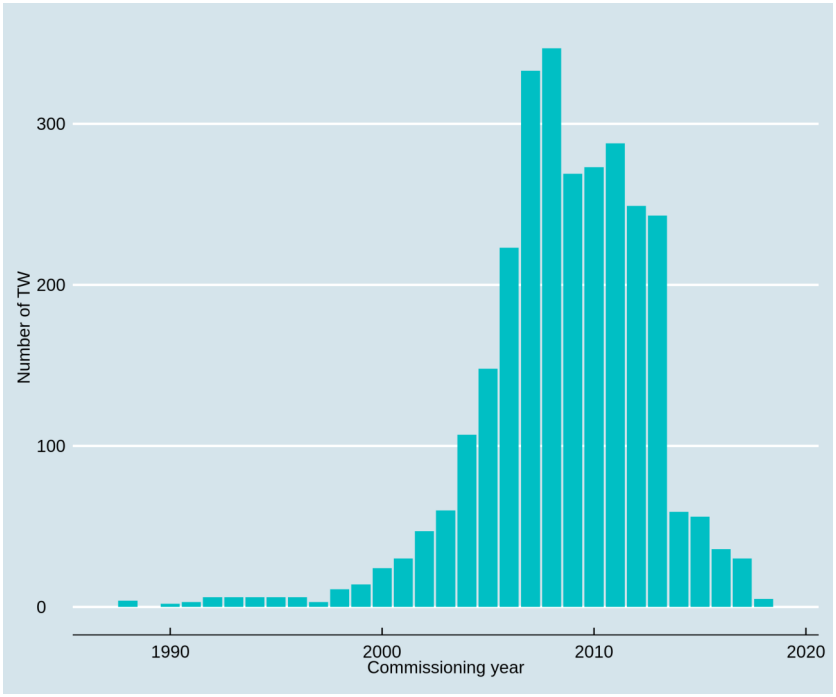

(a) number distribution

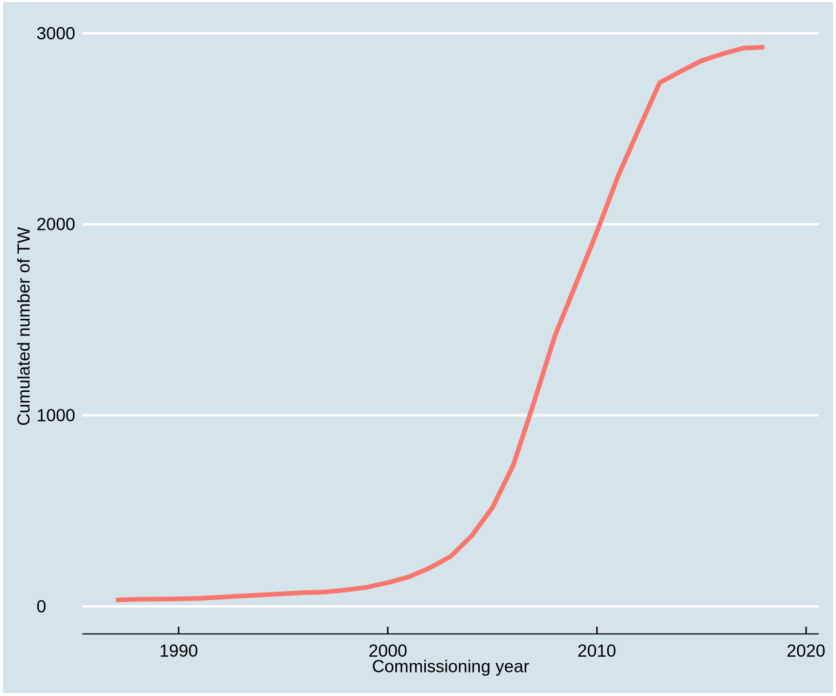

(b) cumulative distribution

Figure 2.5: Evolution of the use TW built in France.
Data from Ministère de l'Environemment, 2019.

capacity of all TW represents less than 2% of the cumulative treatment capacity of all wastewater treatment plants. The technology choice as well as the wastewater treatment strategy (centralized vs decentralized) is already a research topic as it must include economical aspects (the cost of land, treatment plant and sewer investment cost, operational cost, ...), potential for circular economy (reuse, local economical activities), environmental aspects (life cycle assessment [100]), social aspects (stakeholder and public acceptance) and an integrated water resource management.

Perhaps one of the most innovating research topics in the scientific community working on wastewater treatment, is the change of the paradigm from the centralized treatment to decentralized treatment. This change of paradigm may broaden the field of application of TW in the future, even in large cities [69].

2.3.3 Historical evolution

It is agreed that the pioneer work of Kate Seidel in the 50"s made possible the development of VFTW. INRAE (formerly Irstea and Cemagref) has played a key role in the adaptation of the original design by Kate Seidel to the French-type VFTW thanks to the efforts of Alain Liénard and Catherine Boutin. Their first three attempts to use VFTW in the historical sites of Saint-Bohaire, Pont Rémy and Gensac la Pallue set a robust basis for the establishment of the state-of-the-art rules for design and operation [61]. These rules were later refined by several scientific works in partnership with SINT, a TW design company. All over this period of development, features like: the number of stages in series, the number of filters in parallel for each stage, the duration of the feeding and rest periods, the number and type of layers of granular material, the plant species, the hydraulic load and organic loads were empirically defined, some of them by assessing hydraulic limits and performances in pollutants removal. Finally, these works gave birth to state-of-the-art rules resumed in [79], which are presented in section 2.4.1. Figures 2.6 and 2.7 present the evolution of the French TW. A significant simplification in the design of TW was done including: (1) reduction of treatment stages (2) reduction of parallel filters in the first stage (3) use of only one plant species (4) reduction of the number of layers with different grain sizes. These features helped popularizing the French system by making them easier to build using market available granular materials .

Clogging and fouling are perhaps the phenomena that preoccupies users of French VFTW the most. With a few exceptions, it can be said that French VFTW built according to the state-of-the art rules have not still reached a drastic fouling that leads to them to clog. A recent Irstea's survey showed that less than 1 % of the existing TW are suffering from clogging issues. Consequently, the clogging issue has to be studied seriously to anticipate possible problems. Scientific developments leading to a better comprehension of the underpinnings of these phenomena are highly appreciated in order to estimate the lifespan of filters [51], or to explain why few treatment plants clog at premature ages (an example is pictured in Figure 2.8). In this context, a study of clogging and fouling at the pore scale, cf. chapter 4, seems promising to provide new insights.

2.4 Spatial scale description of French VFTW

This section describes all the elements present in a classical French VFTW starting from the largest components at the filter scale and ending at the microorganism scale.

2.4.1 General structure

French VFTW have four important large scale elements: screens, water collectors, water distribution systems, and the filters, which are pictured in Figure 2.3.

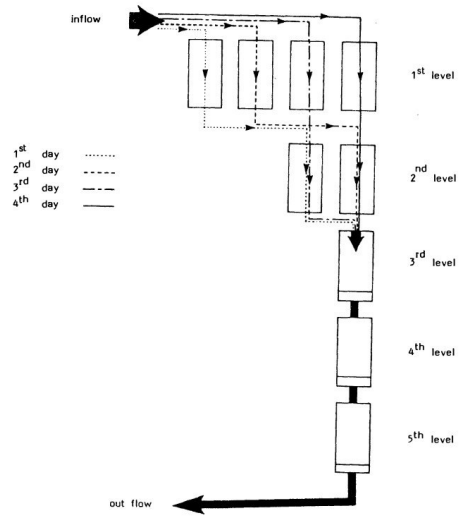

(a) 5-stages system.

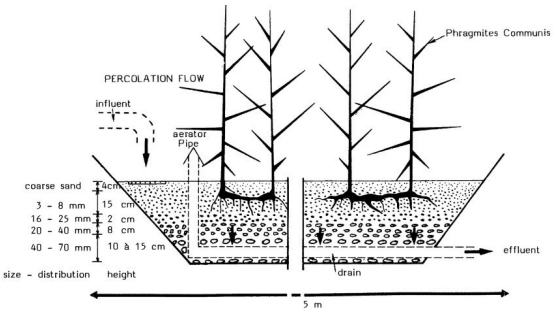

(b) 1st and 2nd level planted with Phragmites communis.

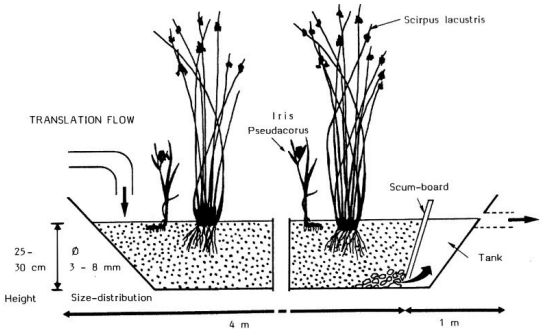

(c) 3rd and 4th level planted with Sirpus Lacustris. 5th level planted with Iris Pseudacorus.

Figure 2.6: Saint Bohaire's System.

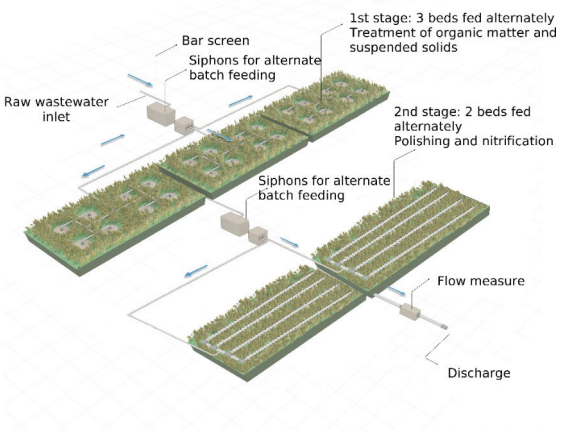

(a) 2-stages system.

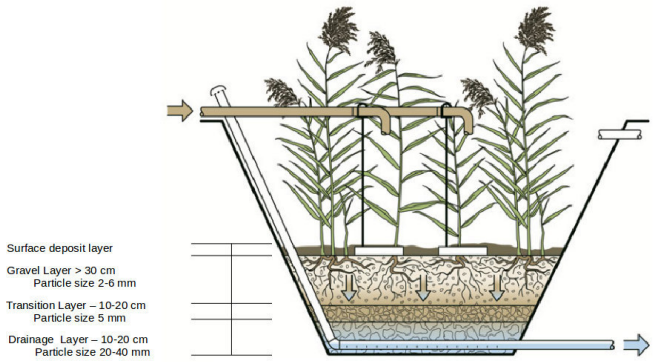

(b) 1st stage planted with Phragmites Australis.

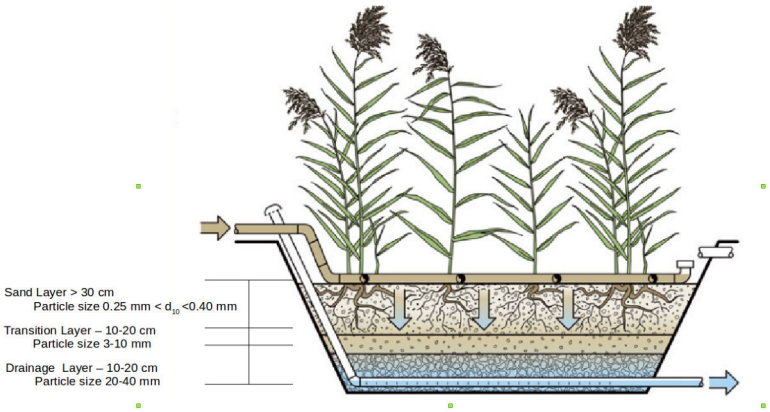

(c) 2nd stage planted with Phragmites Australis.

Figure 2.7: “French” System.

Figure 2.8: Clogged 1st stage in Copponex TW (Haute-Savoie, France, 2016).

Table 2.8: Maximum design loads for classical French VFTW under dry weather conditions. .
Values given are per square meter of bed in operation. From [25].

Treatment Stage	HLR ($m^3/m^2 \cdot d$)	COD ($g/m^2 \cdot d$)	BOD_5 ($g/m^2 \cdot d$)	TSS ($g/m^2 \cdot d$)	TKN ($g/m^2 \cdot d$)
First stage	0.37	350	150	150	30
Removal [a]		$0.80 \times M_i$	$0.90 \times M_i$	$0.90 \times M_i$	$1.1128 \times M_i^{0.8126}$
Second stage	0.37	70	20	30	15
Removal [b]		$0.75 \times M_i$	$0.80 \times M_i$	$0.80 \times M_i$	$1.194 \times M_i^{0.8622}$

[a] All correlations from Molle et al (2005), except TKN from Molle et al (2008), M_i stands for mass load in $g/m^2 \cdot d$
[b] All correlations from Molle et al (2005)

Coarse screens retain solids from the wastewater network with size larger than 20 millimeters (20 – 40 mm is recommended as screen size) thus preventing them to enter the TW as they may damage mechanical elements or plug pipes. These screens usually require maintenance twice per week.

The water collectors store sufficient amount of water before releasing it onto the surface of the filters in order to creating a ponding of 2.5 - 5 cm in depth [25]. The mechanisms to release water can be purely mechanical (siphons) or electrical (pumps). The first are suitable in locations with enough slope, are completely autonomous and do not represent any operational cost. In newly built filters, water tends to infiltrate rapidly at the vicinity of feeding points. Some months/years (according to the organic load) after the beginning of the operation, a deposit layer is formed on the surface of the filters and helps to distribute water homogeneously over all the surface. The size of the feeding pipes and the number and distribution of feeding points (> 1 feeding point per 50 m²) may follow different designs but should always contribute to a uniform distribution of water all over the surface, ensuring equal volume flow per feeding point and, at the same time, avoiding the exit of the pipes to be clogged by solids, e.g. when little gravels are carried by the water flow and when the diameter at the outlet of the feeding pipes is small.

Filters are built by excavation/backfill. Their dimensions guidelines [25] are presented in Table 2.8.

Most feeding systems will release 10 - 15 batches per day based on the rate of wastewater production (150 $l.d^{-1}.p.e.^{-1}$), the surface of the first stage (1.2 – 1.5 $m^2.p.e^{-1}$), according to storm event acceptance, and the height of the "uniform" water column of (2.5 - 5 cm).

Pipes collecting water at the bottom of the filter must be built assuring continuous drainage and providing good aeration. For this purpose the pipes are connected to the atmosphere as shown in Figure 2.7.

2.4.2 Layers of granular material

The thickness of the layers of granular material and the rules for grain size distribution are presented in Figure 2.7. The size of the granular material in the different layers of a filter increases from top to bottom while the size of the granular material used in the filtration layer (the topmost layer) decreases from the first to the second stage.

The first stage is the innovative feature of French VFTW, which replaces a settler and avoids the clogging of the sand in the second stage. Liénard recommends to use a granular material ranging from 2 to 6 mm in filtration layer of the first stage [61].

The first layer of granular material (gravel and sand for each stage respectively) is a porous media responsible for most of the solids retention and biological activity. It is placed intentionally at the top of the filters as (1) if it clogs, solids can be more easily removed than if they were at the bottom of the filters (2) it enhances contact of solids with the atmosphere, which enhances their drying and mineralization as well. The deposit layer formed at the top of the gravel layer in the first stage is also a porous media that participates in retention of solids. This layer is presented with more detail in subsection 2.6.2.

2.4.3 Plants

The volume occupation and distribution of reeds on the TW depends on the maturity of the system (cf. section 2.6, and on the size of the plant organs. Organ size vary from a few mm (roots) to a couple of meters in plants of mature age (stems height) passing through intermediate sizes: 2 to 3 cm (leaves, rhizomes and stem diameter). Figure 2.10 shows reeds growing during spring in Montromant's station (Rhone, France). The largest portion of plant biomass is above the surface of the granular media and harvested once a year.

The role of the reeds in treatment has also been studied but their relative importance is discussed differently in many works. The rhizosphere is a very biologically active zone where bacteria and roots interact. For instance, plants release oxygen and exudates that may fuel bacterial activity while bacteria provide nutrients to the plants [108]. Others state that their contribution to pollutant removal is very limited: their release of oxygen at the roots is minimal, and their contribution to treatment is mainly due to their mechanical role: once the deposit layer is formed, they help water to infiltrate faster into the filters by piercing the deposit layer and creating cracks when stems are moved by the wind [77]. Furthermore, if the above ground portion is not harvested, their detritus contribute considerably to the clogging of the TW [25]. A common misconception is that plants remove most of the nitrogen in treatment wetlands. Emergent macrophytes do store nitrogen in their tissues and plant uptake results in relative low removal of nitrogen depending on the macrophyte species that is considered [25].

The role of reeds in the drying of retained solids is perhaps one of the most important and has been studied particularly in the application of VFTW for sludge drying [122]. The amount of water evaporated by transpiration is a non negligible component of the water budget, particularly in warm seasons in temperate climates (references in [122]). One of the approaches to model Evapotranspiration (ET) is the FAO 56 method. It relies on the determination of a cultural coefficient (K_c) which is the ratio of the maximal ET rate of a plant and a reference ET of another plant (ET_0) whose properties are well known, like grass or alfalfa. Each plant species has then a proper K_c. A stress coefficient (K_s) ranging from 0 to 1 models the changes in the ET rate at different states of growth of a plant. The whole model is resumed by equation 2.1. In Figure 2.9, a linear-constant model of the change of K_c is presented.

$$ET = K_c * ET_0 = K_s K_{c,max} * ET_0 \tag{2.1}$$

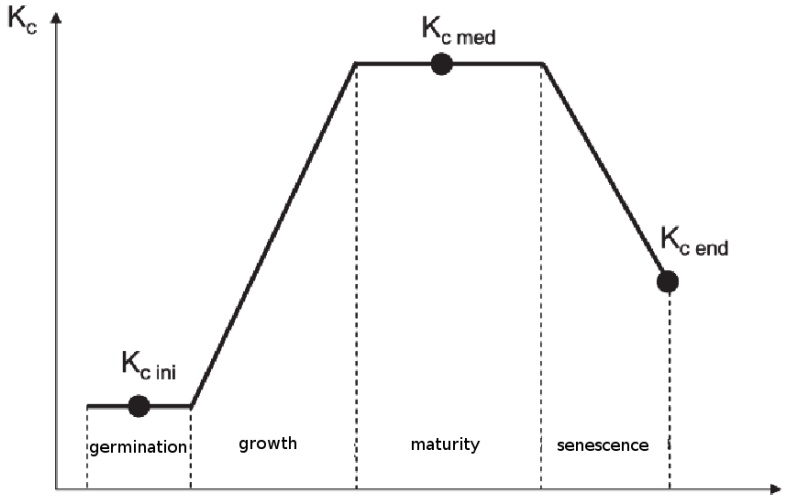

Figure 2.9: Model describing the evolution of the cultural coefficient as a function of the stage of growth of a plant.

From [122].

Figure 2.10: Reeds growing in the first stage of Montromant's VFTW

In French metropolitan territory the gravel and sand layers are planted with reeds (*Phragmites Australis*). The choice of the species, has been largely studied. Although there is no definite consensus on which is the "best" species to be "used" [12] *Phragmites Australis* is perhaps the most common as it is one of the species that adapts the better to changing environmental conditions in French VFTW (intermittent flooding).

2.4.4 Retained solids and Fouling Material (FM)

Solids particles in wastewater range from 0.1 µm to a few mm (Figure 2.4). They are retained within the pore media (deposit, gravel and sand layers). The solids in wastewater foul the porous media progressively, and thus are the most important fraction of the Fouling Material (FM) in TW. The FM is a concept that has been formally introduced in the characterization of TW by X-ray Tomography [67], cf. chapter 4, and is defined as the ensemble of material that fills the pore space in a TW: mineral solids, organic solids, water associated to solids, plant tissues and biofilm. The volume fraction of FM varies with the distance from the surface of the filter.

Large aggregates of solids can measure some centimeters in height, like those in the deposit layer. These aggregates measure from 1 to 20 cm maximum (Figure 2.13) before it is dredged out according to empirical recommendations [78], or measure a few millimeters when occupying

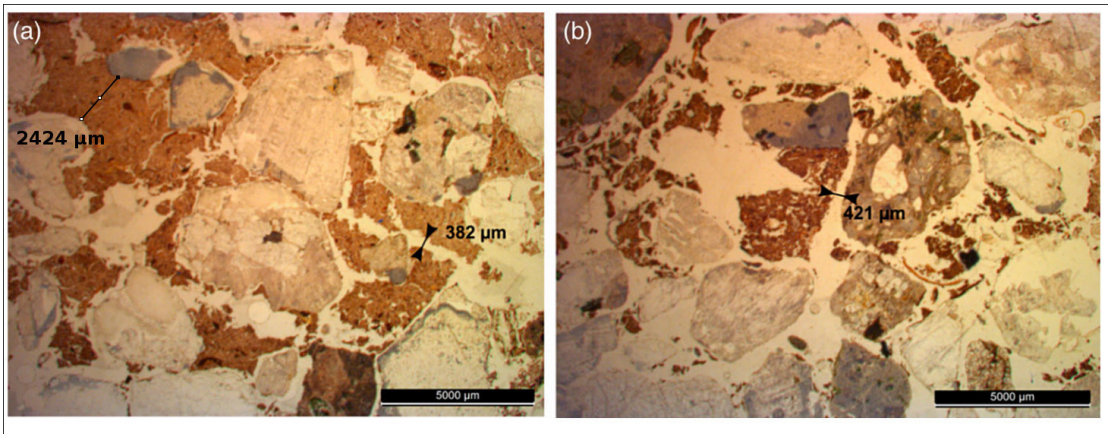

Figure 2.11: Magnified images from thin sections of VFTW filtering media.
From [50].

the pore space in the gravel layer, as it can be seen in the thin sections obtained by Kim and Forquet [50] (Figure 2.4.4).

FM in TW is mostly composed of water, followed by organic and mineral matter. FM in the deposit layer tends to have larger contents of OM than in the gravel layer. The predominance of OM or mineral matter depends on the degree of mineralization of the FM which is higher (low OM content) at deeper depths and on the age of a wetland (Figure 2.12).

2.4.5 Macrofauna

Many species of invertebrates participate actively in the structural change and biological degradation of solids in TW [87]. Just to mention: earthworms, slugs, spiders, flies, whose size vary from less than 1mm to a few centimeters can be present in TW, especially in the deposit layer [34] (Figure 2.14). Predators of these species contribute to the export of animal biomass out of the TW.

2.4.6 Porosity and voids

Porosity in TW corresponds to volume in pore media that is occupied by (1) air (voids), (2) water, when it is (full/partially) saturated and (3) FM. Void sizes range from a few millimeters to a few micrometers depending on the depth in the filters. Cracks of some millimeters in width are often observed in the topmost part of the deposit layer of French VFTW (Figure 2.15). Different classes of void sizes may be observed in the FM. Kim and Forquet measured voids ranging from 0 to 100 µm within FM aggregates (which in their study was called “deposit”) as well as voids ranging from 100 µm to 3 mm between FM aggregates and gravel grains (Figure 2.16) [50].

2.4.7 Microflora

Microscopic metazoans (puricellular eukaryots), protozoans (unicellular eukaryots) and bacteria (prokaryots, and thus unicellular) constitute microflora. An example of metazoans is shown in Figure 2.17. Their biological activity is fundamental for pollutant removal, and is described with a little more detail in section 2.5.2.

2.4.8 Molecules and ions

FM is actually composed of several molecules and ions which are the same time (1) nutrients present in extracellular/intracellular liquids and (2) solid structural components present in FM aggregates and inside all living beings in TW. Hania et al. investigated the chemical composition

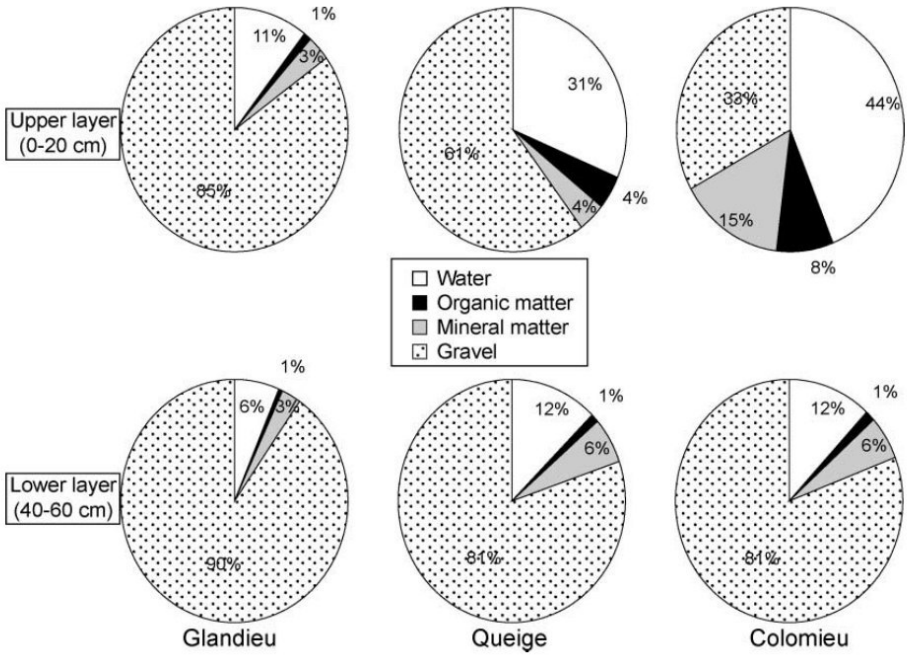

Figure 2.12: Sample composition of Fouling Material of three TW depending on the depth.
The upper layer corresponds to the deposit layer and the lower layer to the gravel layer in a first stage. From [17].

Figure 2.13: Deposit layer of Gensac la Pallue (France) 1st stage filter (dredging in 2001).

Figure 2.14: Earthworms (Macrofauna) in a fouled gravel layer of a French VFTW.

Figure 2.15: Cracks of a few mm in the topmost part of a deposit layer in Montromant VFTW.

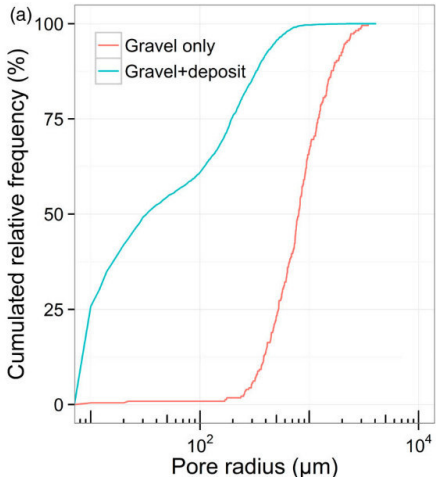

Figure 2.16: Cumulative pore-size frequency distributions between gravel and gravel + FM in thin sections.

From [50]. In their work, deposit stands for what is called Fouling Material in this thesis.

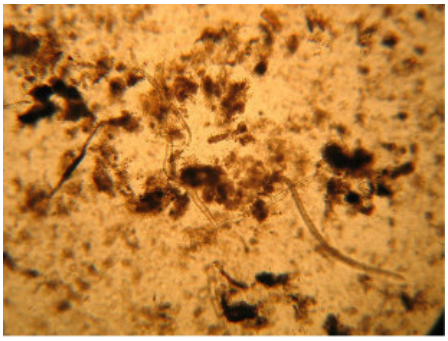

Figure 2.17: Metazoans (likely n in FM of TW.

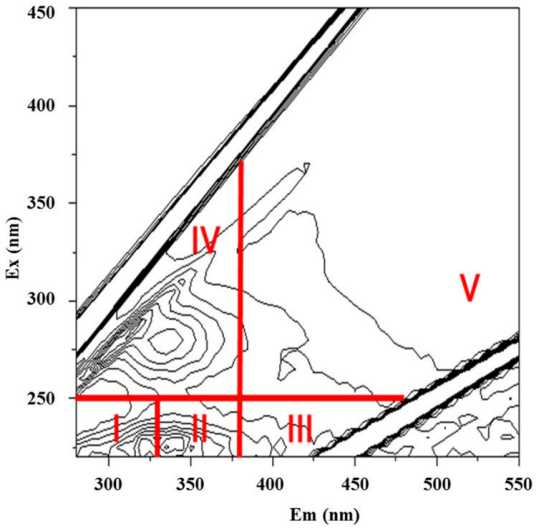

Figure 2.18: Illustration of the regions defined to exploit 3D EEM fluorescence spectra with associated types of organic constituents.
The matrices are built gathering the subsequent scanning emissions spectra (Em) by varying the excitation wavelength (Ex). From [48].

of inflow SS and FM in French VFTW using 3D fluorescence Excitation-Emission-Matrix (EEM) spectroscopy [48]. They applied this methodology on different chemical fractions (soluble, readily, slowly and hardly extractable) which indicates the presence of 5 groups of substances that are pictures in Figure 2.18. Regions I and II correspond to aromatic amino-acids, peptides and related compounds; region III to fulvic-like acids; region IV to low-molecular size compounds such as microbial metabolites, proteins and related compounds, and region V corresponds to ligno-cellulosic and humic-like acids. The spectra collected revealed that along the treatment chain, OM is hydrolyzed and partially mineralized, and the residual fraction is progressively humified.

2.5 Physical and biological processes

Pollutants from wastewater are removed in TW by several physical, chemical and biological processes, which are briefly described in this section.

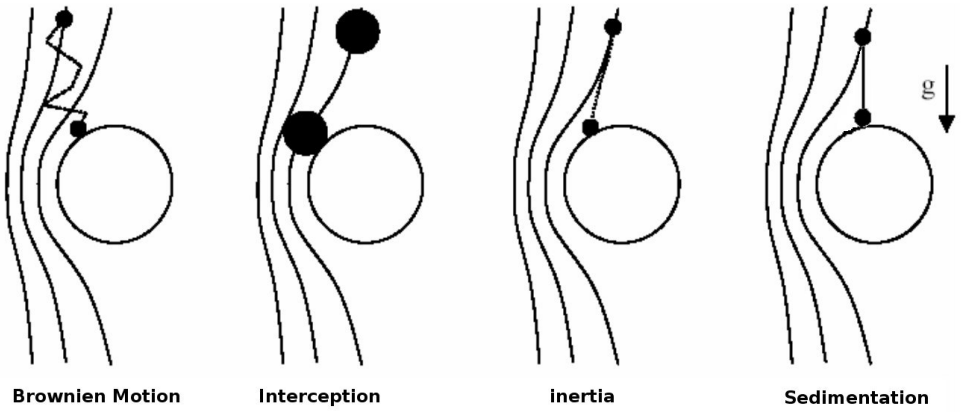

Figure 2.19: Filtration mechanisms by which particles following a current (solid lines) are filtrated by a static surface.
The static surface is represented here by a circumference. From [88].

2.5.1 Physical processes

As the conductive thread of this thesis is the fouling and clogging, here the reader will find only a focus on physical phenomena related to solid transport and drying. Other phenomena such as the water and oxygen transport are studied at the Darcy's scale during the feeding period in the work of Forquet [32].

Solid transport and filtration

Solid transport can be defined as the set of phenomena describing the movement of solid particles, dragged by a liquid or gas flow and influenced by a static surface. Static surfaces help to retain solid particles and separating them from the main flow. Solid particles are thus "filtrated". Examples of static surfaces are surfaces and pores walls in a membrane filter or the surface of gravels in a French VFTW.

The mechanisms of solid filtration are described in the work of Oxarango [88]. Besides from filtration mechanisms, it is common two describe two different regimes of accumulation of solid particles: cake layer filtration and deep bed filtration.

Filtration mechanisms Before being filtrated particles follow current lines. Current lines describe the trajectory of a particle following the direction of the velocity gradient. There are four mechanisms which are illustrated in Figure 2.19 and conceptually explained as it follows:

- Brownien movement: although the Brownien movement of particles may be negligible compared to the main flow, near a static surface, a particle can exit a line current following this pattern and touch the walls of the surface thus being retained: the flow velocity at a surface is 0, i.e. the no-slip condition.
- Inertia: As in Brownien movement, filtration by inertia is an important mechanism only near a static surface. The density of a solid particle is higher than the density of a the liquid, and locally, a particle may cut the line currents and touch a static surface. An example that helps to picture this mechanism is a kid being ejected at a certain point from the main trajectory of a carousel (circular current line) when it suddenly starts turning too fast; the kid follows a tangent line (inertia) at that certain point, and is then stopped miraculously in his father's arms (static surface).
- Interception: when a particle follows a line current, if its radius is larger than the distance from a static surface at a certain location, then it is retained. This mechanism is the same

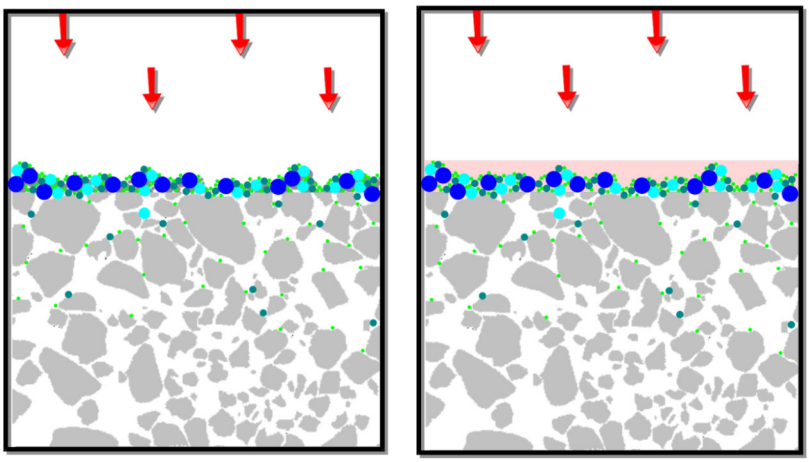

Figure 2.20: Schematic representation of cake filtration.
Big particles are retained at the surface of the granular media (left) and lead to the formation of a deposit layer (pink) in French VFTW (right)

that explains the filtration of a particle when it reaches "a throat" on its way, like fruit pulp when it is retained in the grids of a sieve.

- Sedimentation: when the difference of densities of the liquid and the solid is high enough, the contribution of gravity is enough to make a particle cut a line current and reach a static surface.

When a particle approaches to a static surface by any of the mechanism explained above, the interaction forces between the particle and the static surface may be greater than the forces induced by the flow (mechanical) and help to retain the particle. These forces are mostly electrical.

Filtration modes Different modes are defined by different preferential accumulation of particles at specific locations in a filter. There are two modes of regimes commonly cited: deep bed filtration and cake filtration:

- Cake filtration: it is commonly referred to as the process by which separation of particles from slurries is done by the use of a medium which is permeable to liquid flow but does not allow the passage of the particles. The particles retained at the surface of the granular medium form a cake [112]. This cake works essentially as a new barrier for new inflow solid particles. As a result, the cake thickness increases with time. In the case of French VFTW the SS arriving on top of the filter during the subsequent batches, are preferentially retained at the surface and form progressively a deposit layer (cake), see Figure 2.20. The structure of this cake changes with its degree of mineralization [48], and siccity. If the structure and thickness of the cake induce a drastic reduction of the infiltration velocities, it leads the VFTW to clog. Hopefully, clogging cakes are “easily” removed by dredging.
- Deep bed filtration: deep bed filtration is different from cake filtration in that (1) removal takes place through the whole depth of the granular media, (2) the particles adhere to the grain surfaces rather than forming a filtration medium themselves, (3) as a consequence of the previous point, particles can be retained within a pore even if the particle size is smaller than the pore size (Figure 2.21) [42]. Eventually, the accumulation of particles within the granular media will reduce drastically the infiltration rate leading the TW to clog. Solids entrapped within the granular material are much more difficult to manage. See section 2.7.2.

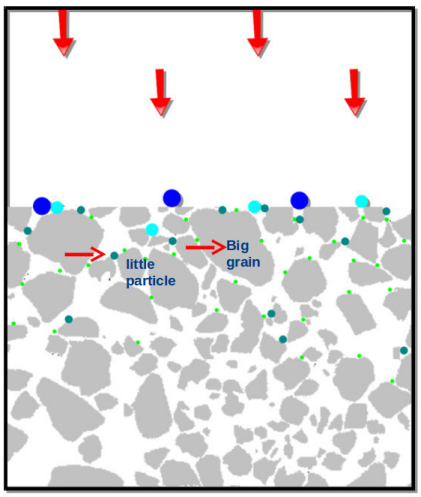

Figure 2.21: Schematic representation of deep bed filtration.
Small particles are retained within the gravel layer.

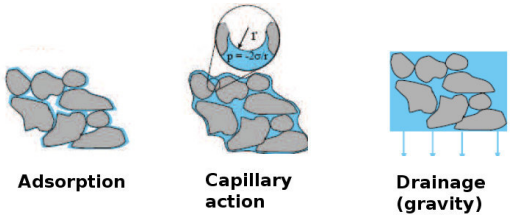

Figure 2.22: Schematic representation of different water – solid interactions in porous media.
Adapted from [122].

Solids dewatering

Importance of drying Dewatering of the FM in French VFTW, is not a process that removes pollutants in the outflow of French VFTW, but it is an important process that affects the volume occupation of FM in pore media, which to its turn, has an influence in solids, water and gas transport in pore media.

Mechanisms The dewatering of FM is achieved by two complementary mechanisms: drainage and evapotranspiration.

During drainage, the "free water" or "gravitational water" flows through the pores of the filters driven mainly by gravity. Water retained by adsorption forces and by capillary forces is still retained within the filters after drainage (Figure 2.22).

Evapotranspiration is the combined phenomenon of evaporation and plant transpiration. Evaporation is the change of water phase from the liquid phase to the atmosphere driven only by an humidity gradient. Transpiration is the movement of water inside plants from the root substrate to the leaves, where it can evaporate through stomas (leaf pores). Plants work as living "water pumps". They can suck water from their soil substrate until capillary pressure reaches a threshold named the wilting point, above which the plant is enable to pump more water. The rate of evapotranspiration depends on the potential of water to be transported, meteorological conditions and physiological characteristics of plants, including its vegetative period. Figure 2.23 resumes the different states of water in soils and its relationship with the two drying mechanisms mentioned above, where : w_h is the humidity content after evaporation, w_w is the wilting point and w_{FC} is field capacity, defined as the water content after drainage during 48h.

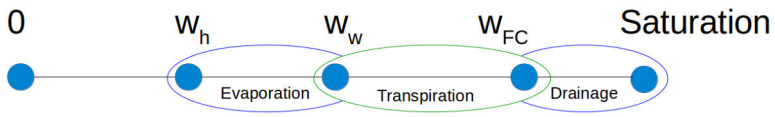

Figure 2.23: Linear representation of different characteristic water contents in porous media.
Adapted from [122].

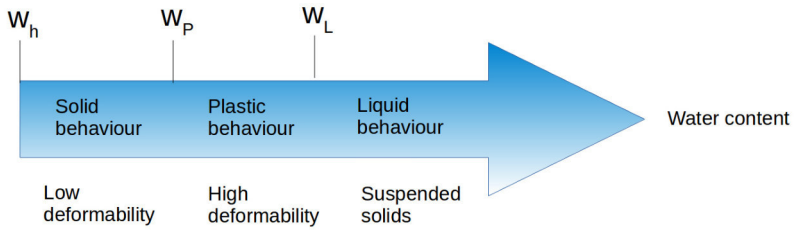

Figure 2.24: Schematic representation of consistency of solid/water mixtures.
Adapted from [122].

The mechanical and hydrotextural properties of the deposit and FM The physical properties of solid-liquid mixtures, like the surface deposit and the FM evolve during dewatering. Vincent [122] summarized several concepts that have been developed for the study of mixture and applied them for the comprehension of sludge drying reed beds. Depending on its water content, a mixture can be present in one of three states: solid, plastic and liquid. The limits between these states are called the plastic limit and the liquid limit as depicted in Figure 2.24.

Models trying to characterize mixtures have been developed recently based on this concept. The model of Ruiz et al. [103] is used to describe the hydrotextural properties of sludges in the work of Vincent [123]. This model defines a pathway for the drying of solid/water mixtures, which has two parts: a first where the mixture contains only water and solids (water saturated mixture), and a second, where drying induces the formation or air-filled porosity in the mixture. The limit is defined by a constant value of water content (w_{unsat}) and is determined as the point where the solid volume fraction as a function of the water content, separates from the curve modeling a saturated mixture.

The model relies on the assumptions that solids and water are immiscible. This implies that the volume corresponding to a gravimetric water loss during drying equals the loss of volume of the mixture. This hypothesis is exploited to predict and quantify the formation of porosity inside the FM during a drying period in chapter 6.

2.5.2 Biological processes

Biological process occurring in French VFTW are more numerous and complex than physical processes. Although filtration removes solid pollutants from wastewater, it only accounts for their accumulation. The transformation of the FM and dissolved solutes is essentially driven by biological processes. More importantly, biological processes govern also the rate at which FM is "created", by the growth of living tissues like biofilm, or "destroyed" by mineralization.

Here, biological processes are presented from two points of view: a global one, which describes mineralization and humification, and a microscopic one, which focuses on microbial metabolism.

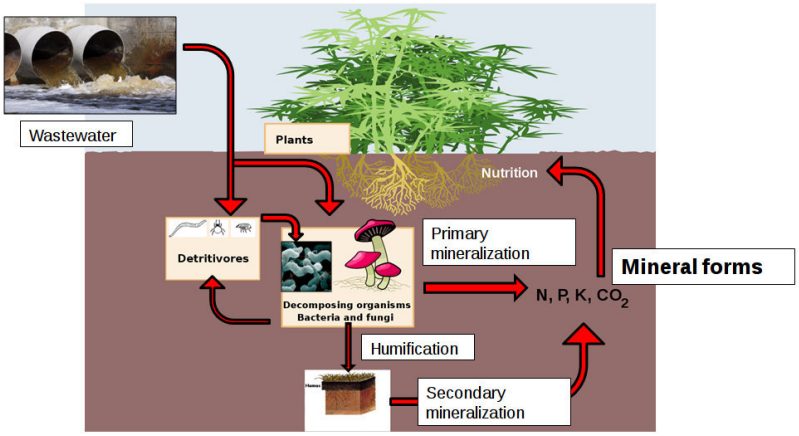

Figure 2.25: Schematic representation of mineralization and humification.

A global view: soil mineralization and humification

The FM in French VFTW has many similarities with soil. Soil can by defined as a "globally solid phase mixture" of OM and minerals, but also contains gases, liquids, and living organisms. Pedogenesis is the process by which soils are formed. In the domain of pedology two processes are often referred: mineralization and humification.

Mineralization is the transformation of the OM into water, CO_2 and mineral salts (of N, P and K for instance). Although the ultimate degradation of OM is done by microorganisms, different living organisms (macroorganisms) are involved in the mineralization as predecessors. Sometimes the products of their metabolism are already mineralized. This is described in a simple manner in Figure 2.25. Humification is the process by which some organic compounds, instead of being completely mineralized are transformed into other "large molecular size" and persistent "humic substances" [56]. A secondary mineralization process will transform humus-like substances into water CO_2 and mineral salts.

Long-standing theory suggests that soil organic matter is composed of inherently stable and chemically unique compounds (i.e. the humus-like substances). This theory is being reformulated and other conceptual models describing the fate of OM in soils have been developed. Lehmann and Kleber resume four conceptual models which are schematized in Figure 2.26 [56]. A first model, "the classical humification", describes OM transformation in soils as a process where the decomposition products of bacteria and fauna lead to the synthesis of highly stable compounds (humus). Eventually these compounds are also oxidized to form CO_2. A second model, "selective preservation", states that some compounds are degraded faster than others and classified into labile and stable compounds, which leads to a progressive accumulation of the more stable compounds. The difference with classical humification is that stable compounds are no longer only humus-like substances, but can be also other polymers or monomers. A third model, "progressive decomposition", describes the fate of OM in a similar way than "selective preservation" but without the distinction of more labile or stable compounds. Finally, the authors propose a consolidated view of the transformation of organic matter. In this model, the focus is put on the concept of a continuous soil, where there is no preponderance of the "large molecular size" and persistence "humic substances", but a threshold for assimilable (small polymers) and not assimilable (large polymers) compounds by bacteria. In all models, the transformation of large polymers into small polymers is done by the use of exoenzymes.

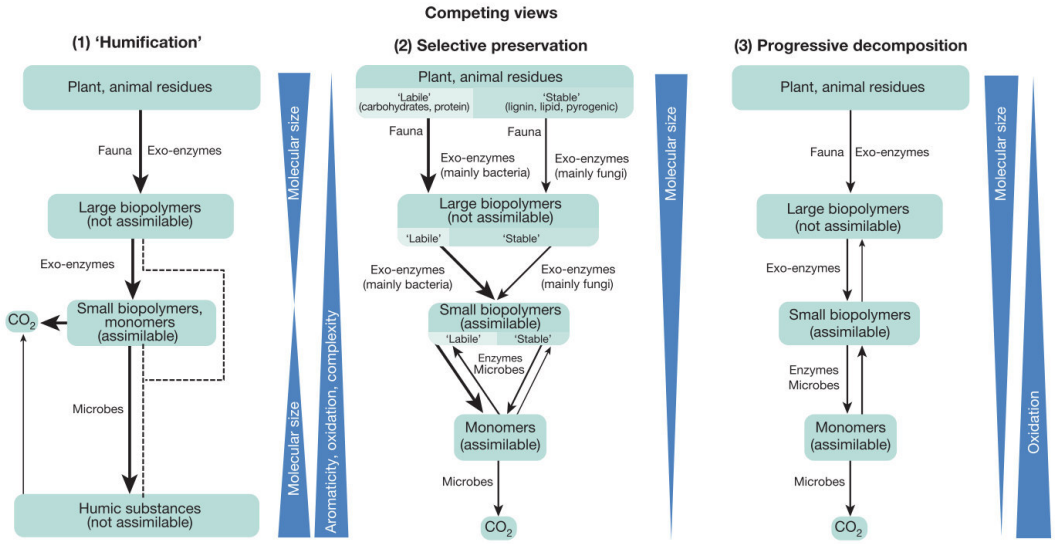

(a) conceptual models

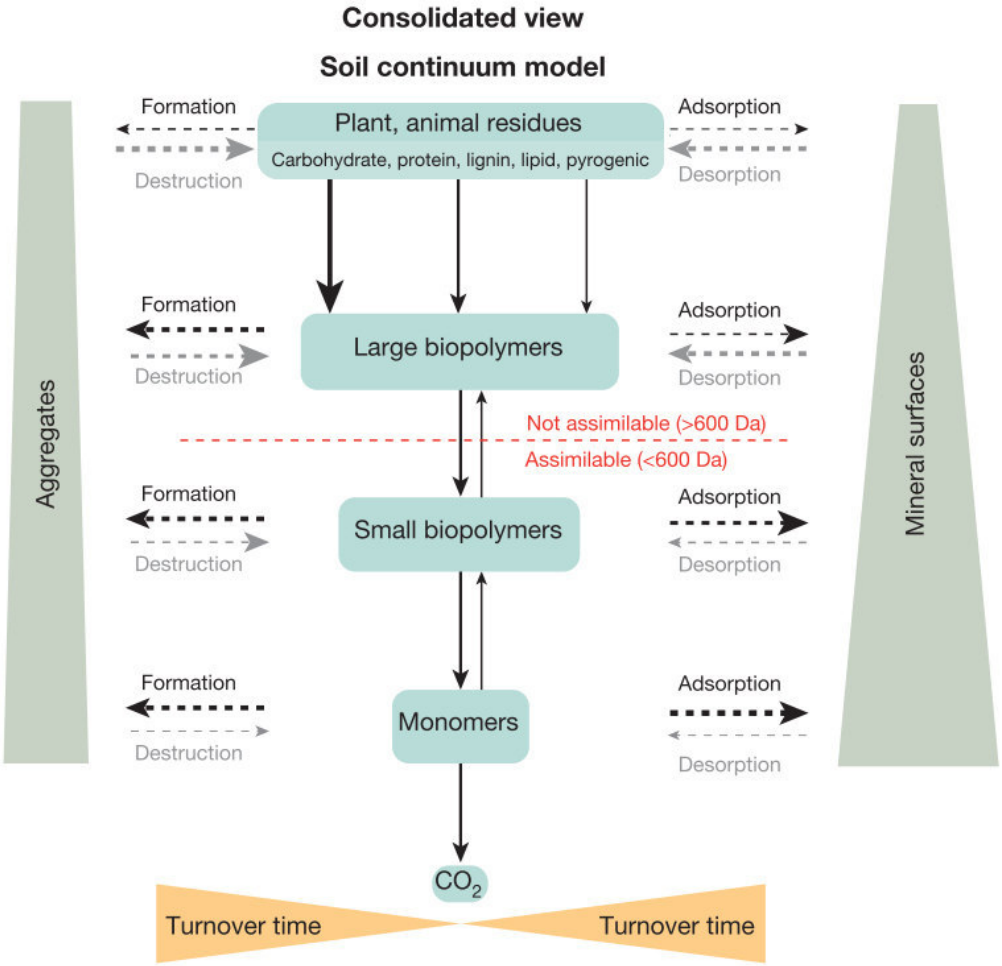

(b) recontiliation

Figure 2.26: Reconciliation of current conceptual models for the fate of organic debris into a consolidated view of a soil continuum model of OM cycles and ecosystem controls in soil.
From [56].

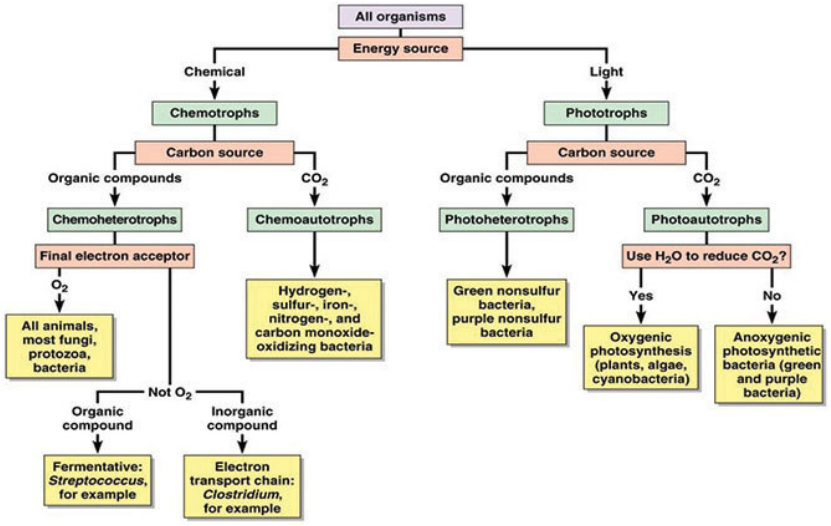

Figure 2.27: Nutritional types of organisms.

A microscopic view: focus on bacteria

Bacteria participate in mineralization and humification of OM which tend to reduce part of the volume of FM, but as they nourish they grow too and form biofilms and thus contribute to the increase of FM volume.

In this section a focus on the nutrition and metabolism at the cell-scale is presented. A simplified description of the nutritional types (or metabolic types) of organisms is resumed in Figure 2.27. This classification starts with the energy source, which may be chemical (chemical energy liberated by the decomposition of organic molecules) or luminous. The second level of classification is based on whether or not carbon atoms used to build structural components come from organic compounds or mineral compounds (CO_2, CO_3^{2-}). In all types of metabolisms there is an electron donor/acceptor molecule.

- Electron donors can be: atoms of H, C, N, S, O in reduced forms: (1) H2 (2) C from organic compounds like carbohydrates, lipids, and proteins, (3) N from NH_4^+, aminoacids and peptides, (4) S^{2-} (5) O from H_2O.
- Electron acceptors can be oxidized forms of H, C, N, S, O like: (1) C in mineral form (CO_3^{2-}), (2) C in partially oxidized organic compounds like acetates (3) NO_2^- and NO_3^-, (4) SO_4^{2-} (5) H^+ ions in acid environments and (6) O_2.

From this classification some groups of organisms are briefly described in Table 2.9. A focus is put on the electron donor/acceptor and the transformation of pollutants in wastewater. From a microscopic point of view, pollutants are retained in structural components of the cells of living organisms. As long as they remain living (thus not mineralized), they retain pollutant and increase the amount of FM in a TW in the form of a biofilm. The chemical composition of a cell is described in Figure 2.28.

Two elements should be mentioned [25]: (1) The predominant metabolic pathway of pollutants is usually defined by the presence and concentration of the electron acceptor. For instance, the DCO/SO_4^{2-} ratio may be used to predict the predominance of sulphate-reducing bacteria or methanogenic microorganisms. (2) “Each pathway has an optimal redox potential and therefore may be active in different locations within the same wetland”. Strong red-ox gradients exist in TW as a function of the level of saturation, the distance from the water surface and plant roots, and the presence of couples of electron donors and acceptors. These gradients range from strongly anaerobic (less than –100 mV) to fully aerobic (greater than +400 mV). Gradients of

Table 2.9: Metabolic description of several nutritional types of microorganisms and emphasis on some pollutant transformations

Example of organism	Chemo/Photo	Hetero/Auto	Electron acceptor	Electron Donor	Pollutant Original Form	Pollutant Final Form
Fauna, Saprophytic, Parasitic bacteria	Chemo	Hetero	O_2	C (OM)	C (OM)	CO_2
Azotobacter Plant symbiotic bacteria	Chemo	Hetero	O_2	N_2		NO_3^-
Denitrifying Bacteria	Chemo	Hetero	NO_3^-	C (OM)	C (OM) NO_3- NO_2^-	CO_2 NO_2^- N_2
Sulphate reducing prokaryotes	Chemo	Hetero	SO_4^{2-}	C (OM)	SO_4^{2-}	H_2S (odors)
Methanogenic Archaea	Chemo	Hetero	CO_2	C (OM)	C (OM)	CH_4/ CO_2
Nitrifying Bacteria	Chemo	Auto	O_2	NH_4^+ (Nitrosomonas) NO_2^- (Nitrobacter)	CO_3^{2-} NH_4^+ NO_2^-	C (OM) NO_2^- NO_3^-
Plants	Photo	Auto	C (CO_2)	O (H_2O)	C (CO_2)	C (OM)

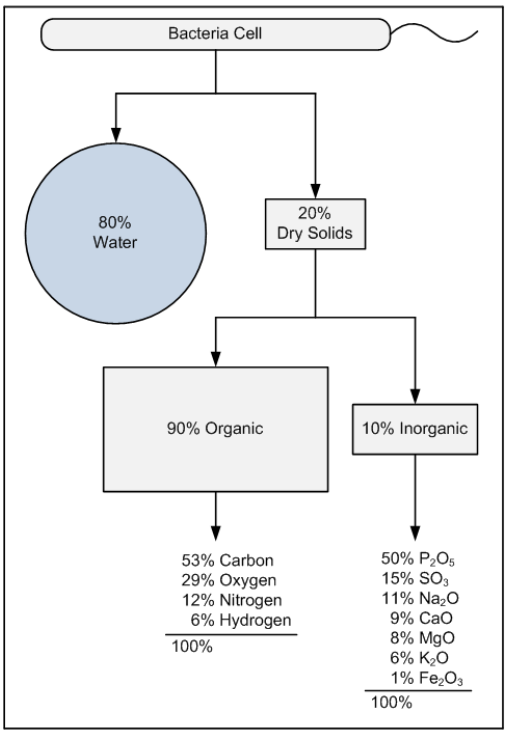

Figure 2.28: Average chemical composition of bacteria cell.

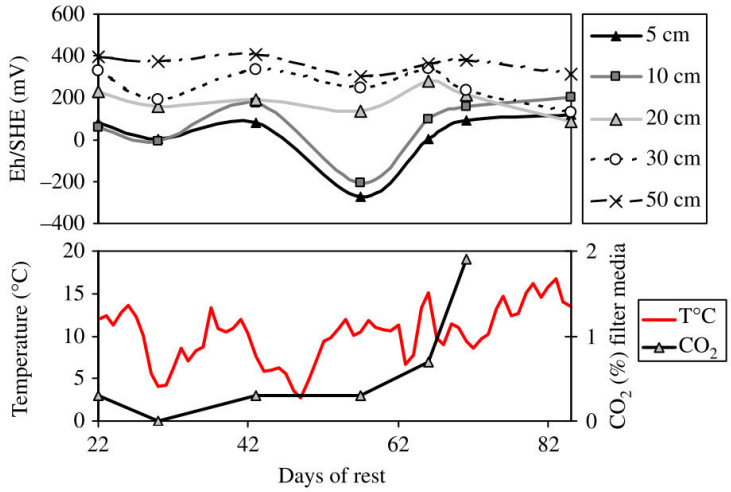

Figure 2.29: Oxidation Reduction potential in the sludge deposit at different depths under the sludge surface.

From [118].

red-ox potentials can be measured in depth of the FM of a VFTW and evolve during the rest period as depicted in Figure 2.29.

2.6 Time scale description of VFTW

Once "the majority" of the components and the physical and biological processes in French VFTW have been introduced, it shall be easier to understand their evolution over time. It is particularly interesting to describe the operation of French VFTW from a time scale perspective because it helps to understand the dynamics of the processes that lead the system to reach a mature state and how it eventually becomes clogged.

The figures presented in this section do not show the presence of reeds nor f
the retention of solid particles in the pore media, but the reader must be aware
in all the processes described in section 2.5.2. Also, unless it is specified, th
the first stage of treatment.

2.6.1 Before reaching a "mature state"

A "mature state" in French VFTW shall be understood as the moment where a deposit layer is fully developed at the surface of filters of the first stage. By experience, a VFTW built following the state-of-the-art guidelines will develop this layer from months to a couple of years [78]. The evolution of a non mature VFTW is described below.

Minutes to hours (batches)

Once the inlet water collectors before each stage are filled with water, a siphon or pump will be activated and release a batch. The collector empties the water into the filters in a couple of minutes. Depending on the granulometry of the gravel and on its degree of fouling, water will take a different amount of time to pass through the filter. The mean Residence Time (RT) of water in new filters is at its minimum value. The RT in the first stage is lower than in the second stage. Figure 2.30 shows different RT distributions for different batch frequencies in a second stage of a French VFTW. In a new filter, water infiltrates predominantly near the feeding points.

As wastewater flows through the porosity of the granular media, suspended particles are retained at the surface or in depth depending of the size of the pores and of the particles, and

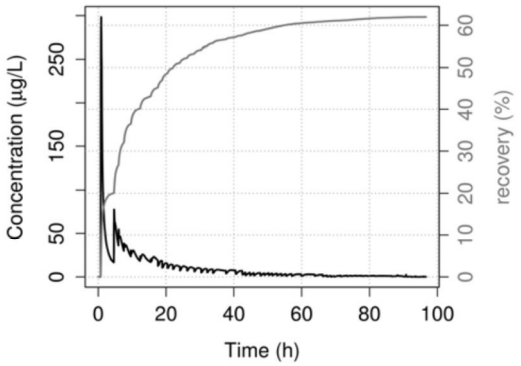

(a)

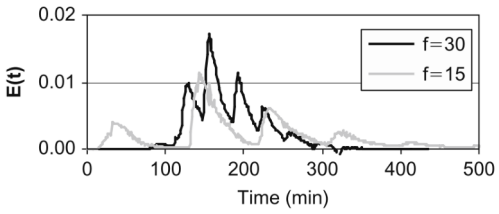

(b)

Figure 2.30: Tracer experiments.
(a) On a first stage. From [83]. (b) On a second stage of a French VFTW. From [116]. (f stands for batch frequency per day).

their interaction with the static surfaces. In a new filter, wide pores of the gravel allow small particles to enter the porous media, where some of them are retained by "deep bed" filtration (Figure 2.31a). Large particles will be directly retained at the surface mainly by interception (Figure 2.31b). 83% of the suspended solids [82] are retained in the filters of the first stage. Bacteria degrade pollutants present in wastewater, and start forming a biofilm on gravels and preferentially on roots surface, where favorable conditions exist (Figure 2.31c). During a batch the oxygen needed to sustain aerobic bacterial activity is mainly renewed by convection [32].

Days to weeks (feeding/rest period cycle)

In a young filter, water content increases significantly during the first 2 days of feeding before reaching a pseudo plateau. Higher water contents are found near the feeding points as shown in fig 2.32.

After 3.5 days of feeding, many particles have been retained and biofilms start to build up within the gravel layer. During the rest period, no nutrients enter the TW, the bacterial growth rate decreases and eventually leads to the mineralization and the reduction of the FM volume in the wetland.

At this point is seems convenient to introduce the mass balance of the fouling process in a TW over a feeding/rest period cycle (FP/RP). S stands for solid mass rate:

$$S_{accum_{TW}} = S_{inflow} - S_{outflow} + S_{production} - S_{consumption}$$
$$S_{accum_{TW}} = S_{inlet_{wastewater}} + S_{biomass_{(plants,animals,microorganisms)}} - S_{outlet} - S_{mineralization} - S_{export_{predators,harvesting}}$$

The successive sequence of feeding and rest periods induces an evolution of water content (increase during feeding and decrease during rest period) as well as biomass growth and decay and the accumulation and mineralization of FM. Consequently the filtration efficiency of the filter varies over days. This is more relevant during feeding days, when the fresh and not very

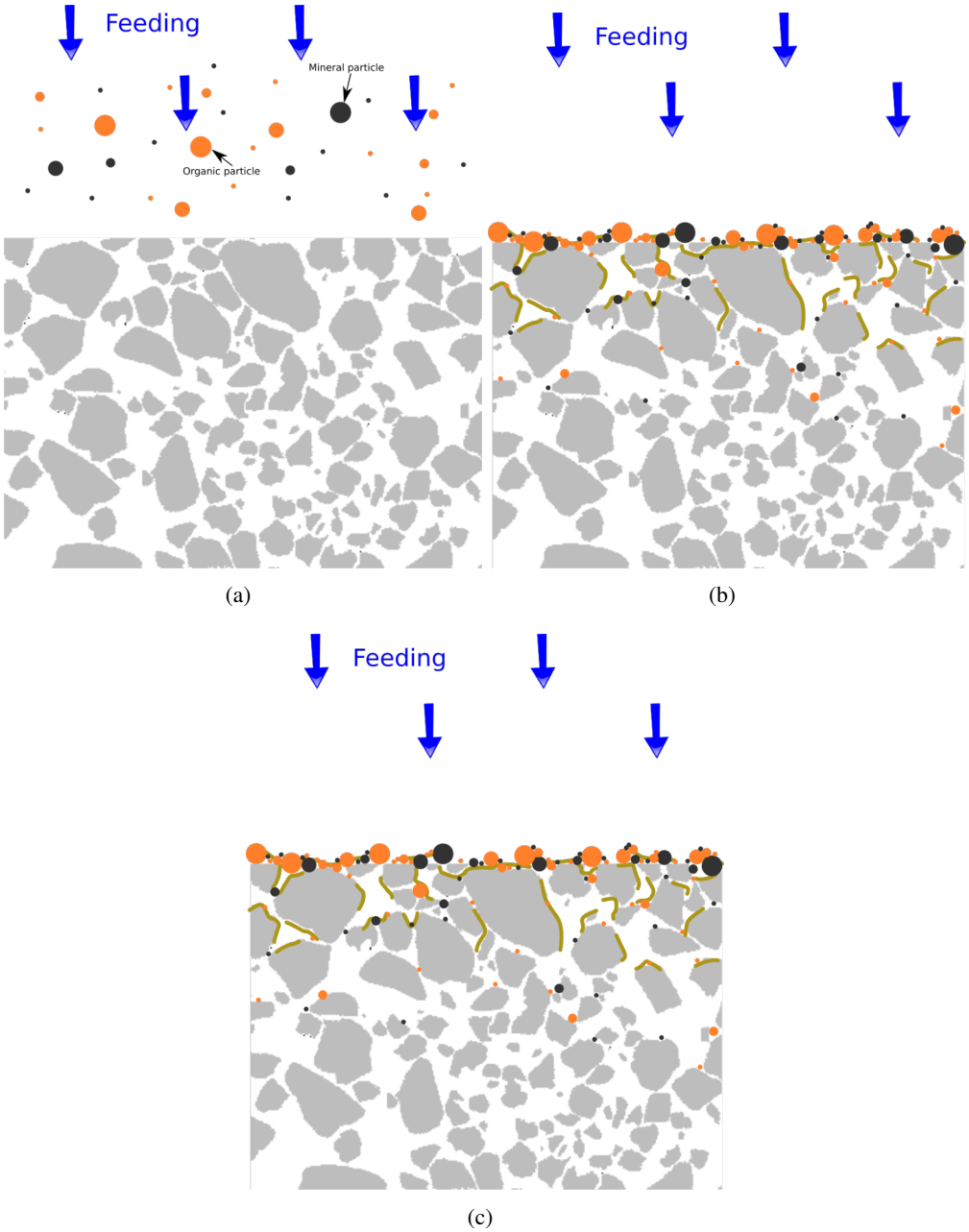

Figure 2.31: Development of FM during a feeding period in young filters.
(a) depth filtration in new filters (b) progressive cake filtration and (c) biofilm growth.

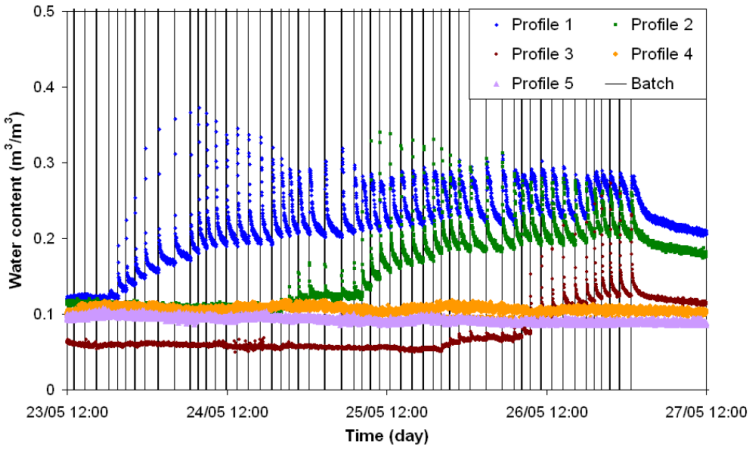

Figure 2.32: Evolution of global water content during a feeding period of a young filter at different distances from a feeding point.
Distance increase with the profile number. Measurements were done using TDR Probes. From [65].

thick OM deposit on the top of the filter, not mineralized, increase significantly the filtration efficiency of the filter.

Months and seasons

As months pass by, gradual accumulation of solids in the filter becomes more evident. Although reeds may have been seeded or planted at the construction of the TW, they may have not spread all over the surface of the filters. During the spring and summer season the reeds biomass production is maximized. A part of this mass is located above the surface of the granular material (stems and leaves) and another part is located under it (roots and rhizomes). In new filters it is highly probable to find a preferential distribution of plants near the feeding points, where water is more accessible (Figure 2.33). During autumn and winter, the accumulation of plant detritus at the surface of the filters is also maximized. To limit the contribution of biomass to fouling, plants are harvested during the winter.

Reeds influence on filter dewatering strongly depends on the age of the TW and on the season. The influence of the reed age on the evapotranspiration rate has been studied experimentally and modeled in the work of Vincent [122]. Figure 2.34 shows measurements and a model for the prediction of the cultural coefficient and the ET of a plant as a function of its vegetative period in the study of Sludge Drying Beds (SDB).

The metabolic rate of bacteria is also influenced by the temperature changes. It finds a minimum value during the winter season. Figure 2.35 shows the decrease in the removal rate of adsorbed NH_4^+ as temperature decreases.

Years

On the one hand, reed density becomes stable after some years and the amount of plant biomass above the surface reaches a pseudo-stationary state (growing and harvesting, Figure 2.36). On the other hand, the surface of the filters will have accumulated enough solids to form a uniform deposit layer. The rate of accumulation is roughly estimated at 2 cm/year. From this moment, the filtration of SS mostly occurs by cake filtration. Solid accumulation is not constant over seasons. Mineralization occurs faster during spring, summer and autumn season. Consequently a faster accumulation rate is observed in winter while a decrease of the deposit depth is observed in summer.

Figure 2.33: Reeds distribution in a young French VFTW.

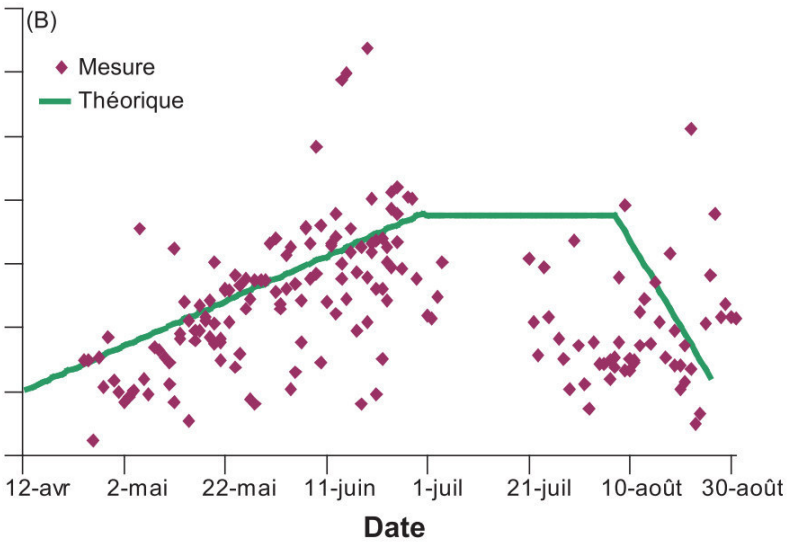

Figure 2.34: Evolution of the cultural coefficient over a year in *Phragmites Australis* from a SDB TW.

From [122].

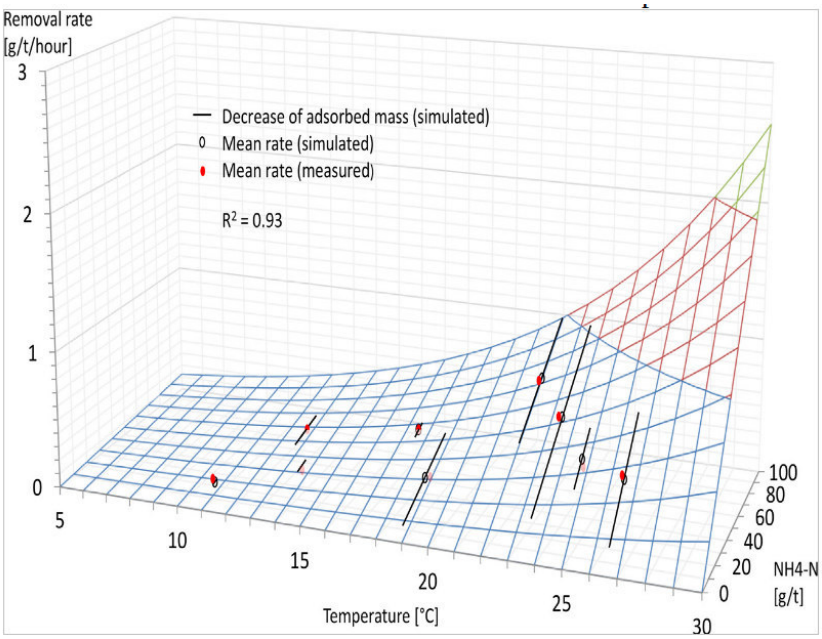

Figure 2.35: Simulation of removal of NH_4^+ in VFTW for treatment of combined sewer overflow.

From [89].

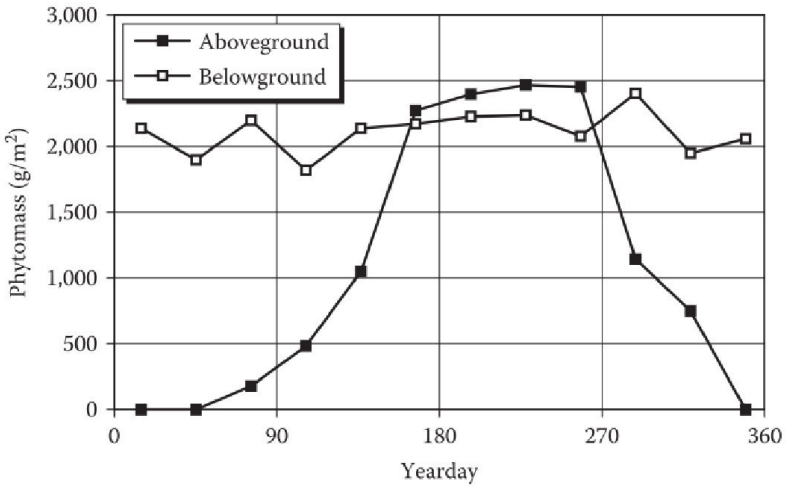

Figure 2.36: Example of seasonal patterns of above and below ground phytomass.
From [45].

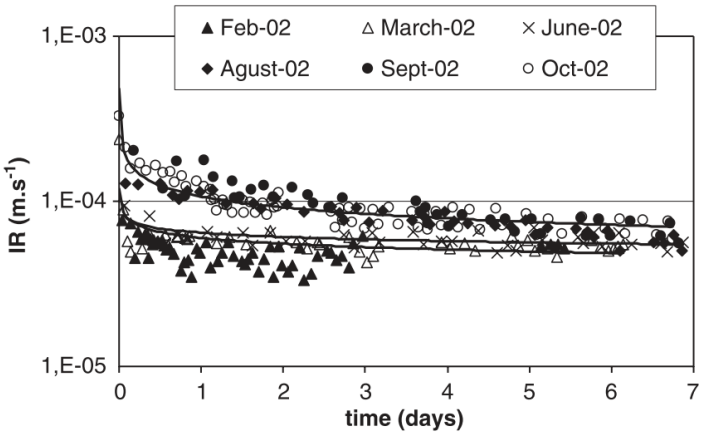

Figure 2.37: IR changes in a first stage filter for the Colomieu plant during the year 2002. From [77].

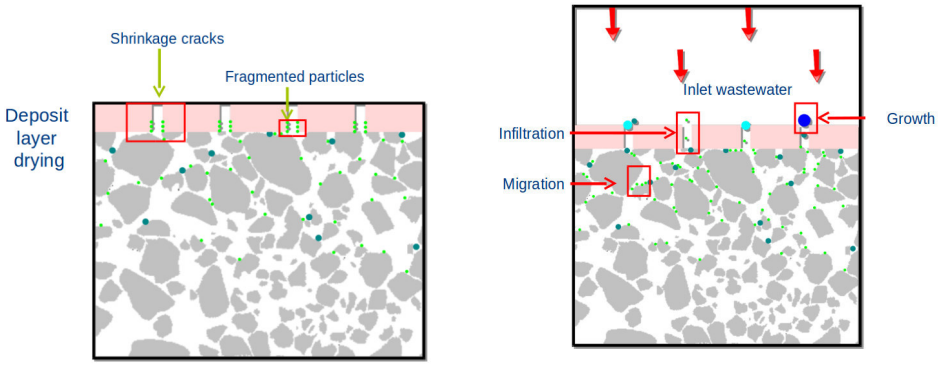

(a) disaggregation (b) remobilisation

Figure 2.38: Schematic representation of migration of fragmented particles of the deposit layer into the gravel layer.

2.6.2 After reaching a "mature state"

Minutes to hours (batches)

In a mature filter wastewater ponds uniformly over the filter surface during a batch and infiltrates more slowly than in young filters. The infiltration rate has been measured by Molle et al. in mature filters [77]. The mechanical effect of reeds is thought to be of major importance at this age as it helps to maintain relatively high infiltration rates (Figure 2.37).

Most of the suspended solids are retained at the surface deposit layer (cake filtration regime), but some may also enter the gravel layer thanks to cracks that have formed in the deposit layer during the precedent rest period (Figure 2.38). Deep bed filtration is not the predominant regime but still remains important for SS removal.

Days to weeks (feeding/rest period cycle)

In a mature filter, water will be absorbed and retained temporarily by the FM during the feeding period. It is to be noted that, thanks to this mechanism, a mature filter retains more water (Figure 2.39) and achieve better treatment performances than a young one as long as enough oxygen can enter into the filter. In a mature filter the water content changes during the feeding period are uniform except at locations near the feeding points (Fig 2.40).

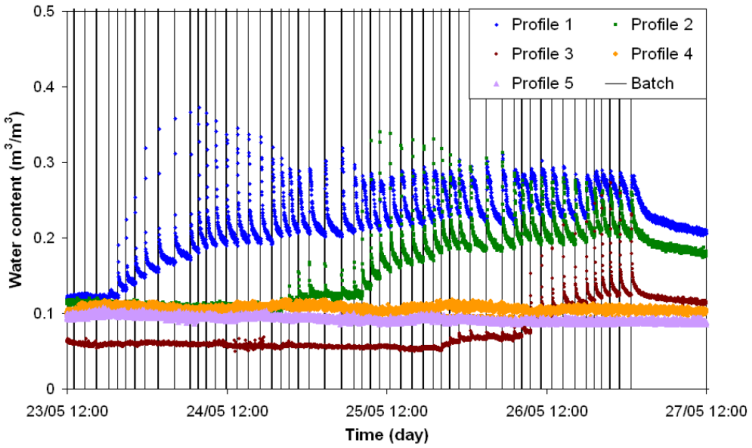

(a) young filter

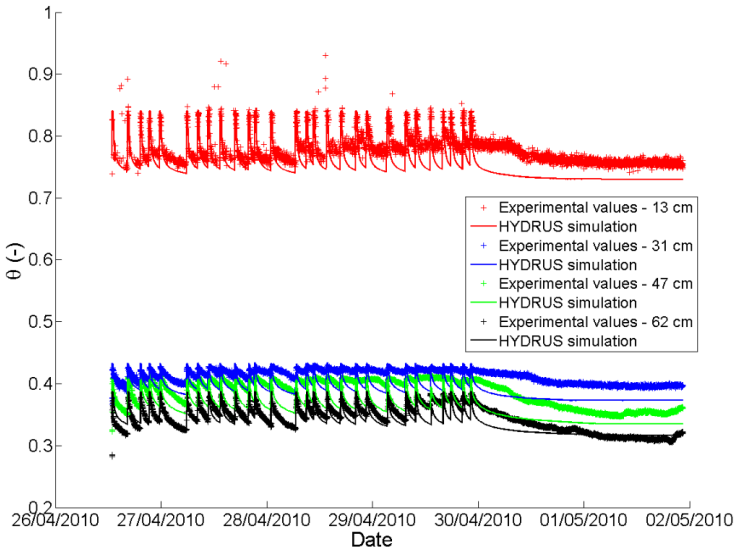

(b) mature filter

Figure 2.39: Comparison of water retention in young and mature filters.
Young filter (left). From [65]. Mature filter (right). From [81].

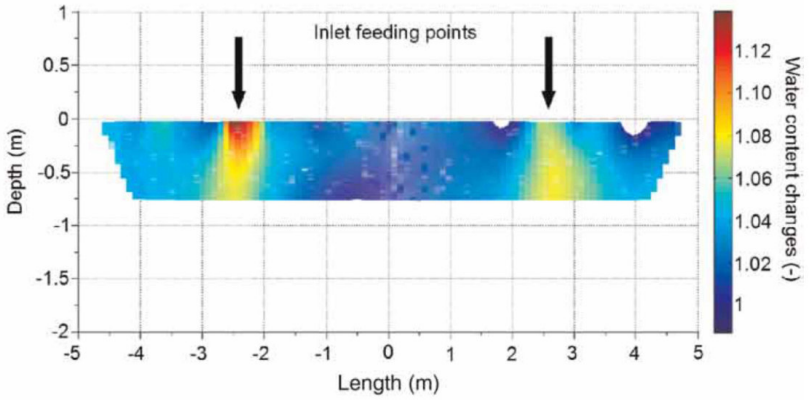

Figure 2.40: Relative variation of water content in a feeding period of a mature French VFTW.
From [78].

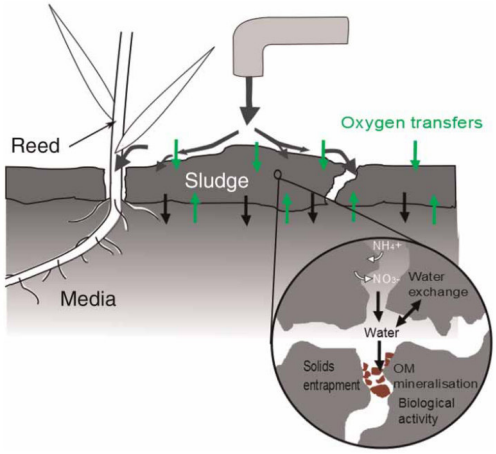

Figure 2.41: Schematic representation of processes in the deposit layer.
From [78].

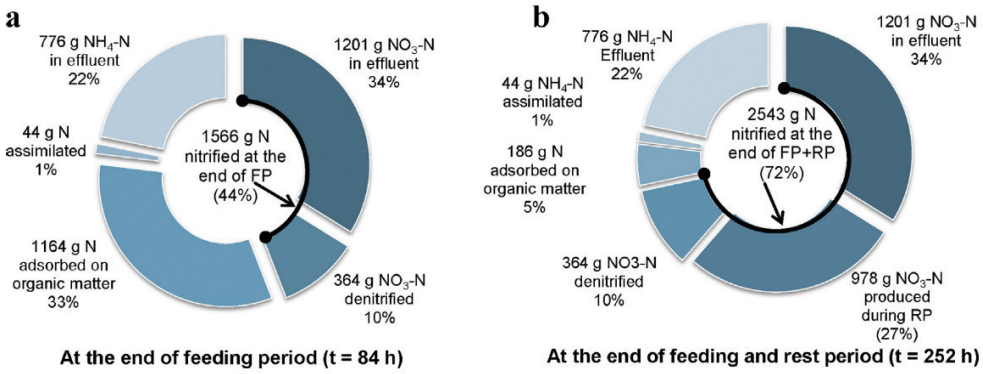

Figure 2.42: Nitrogen mass balance calculated for (a) the feeding period (FP) and for (b) the feeding + rest periods (FP + RP).
From [84].

Water transport mechanisms change depending on the maturity of the system. In a young system the flow will be mainly driven by gravity as the voids in the pore media are large enough for gravity forces to be predominant on capillary forces. In a mature system water can flow through macropores, where the water flow is mainly driven by gravity, or through the micropores inside the FM, where capillary forces play an important role. As a result, the Residence Time distribution (RTD) spreads out in mature systems. Morvannou et al. have suggested a dual porosity model to simulate water flow in French VFTW [83].

In a mature system, the rest period becomes more important. It is essential to promote drying of the FM, reduce its volume occupation and maintain aerobic conditions, which in turn ensure the proper mineralization of the FM in the deposit layer and the gravel layer.

Accumulation of the FM also promotes nitrification. An important part of NH_4^+ ions are adsorbed in the FM during the feeding period, especially in the deposit layer, and are nitrified during the rest period. This is illustrated in Figure 2.41. The rest period is essential for nitrifying bacteria, whose metabolic rate is much lower than that of chemoheterotrophs. Morvannou et al. present results of the simulation of N treatment in French VFTW [84]. A mass balance in the first stage of treatment over a feeding and rest period is shown in Figure 2.42.

Also, the activity of microfauna is more evident during the rest period of mature filters. If

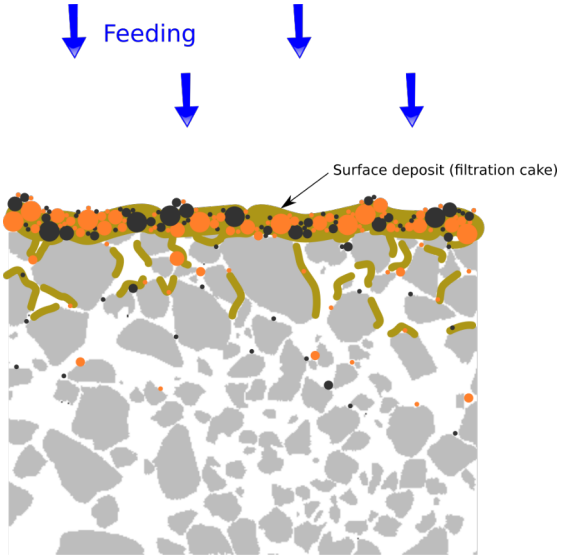

(a) Feeding period

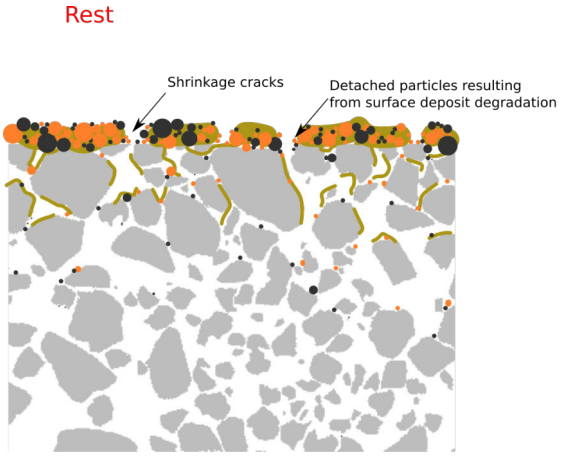

(b) Rest period

Figure 2.43: Schematic representation of changes in FM structure structure in a feeding/rest period in a mature TW.

the deposit layer is well aerated, these organisms will colonize it and promote even more the oxygenation by participating actively to structural changes (digging).

As the water content decreases in the rest period, biofilms start also to be mineralized. Under this stress, bacteria produce exopolymers that reduce the rate of evaporation and increase the volume and viscosity of the biofilm (Figure 2.43).

Months and seasons

During rest periods in summer, drying promotes the formation of cracks in the surface layer. During winter the water infiltration rate decreases (Figure 2.37) as well as the time of exposure of the deposit layer to the atmosphere during intervals between batches. Evaporation reduces and therefore deposit layer tends to build up quicker.

The extra accumulation of solids during winter tends to be counterbalanced with a higher degradation rate during spring and summer. The systems can then reach a pseudo-stationary state at the year scale. However, a net accumulation of solids is observed over years, especially in the deposit layer. The increase of FM at different depths on a mature TW can be observed by

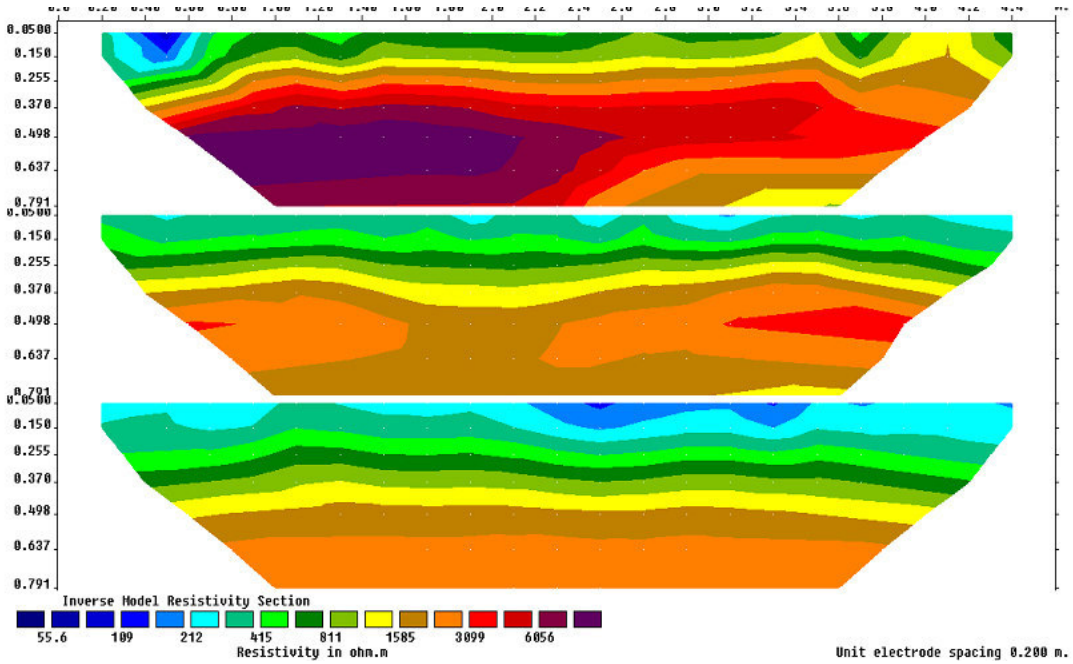

Figure 2.44: Evolution of electric resistivity profiles in a sand filter at three different years.
Spacing in meters. Years: 2006 (up), 2008 (middle), 2009 (down). From [101].

(a) (b)

Figure 2.45: Dredging of the deposit layer in French VFTW

a decrease in the electrical resistivity. Figure 2.44 presents an evolution of electric resistivity profiles due to fouling in filters of the second stage of a French system. A decrease of this property is noticeable in the topmost centimeters of the filter.

Years

After several years, the thickness of the deposit layer will have augmented considerably. The mean rate of growth of this layer is estimated to be approximately 2cm/year. It is recommended to dredge it out once it has reached 20 cm in height (Figure 2.45). The FM material in the deposit layer reaches a high degree of mineralization and can be used for agricultural purposes as long as no industries are connected on the sewerage network [79].

After dredging

After the first dredging operation the evolution of the filters will follow the same trend described above. The process could repeat in cycles marked by a dredging frequency of "approximately" once every 10 years. However, yearly mean rates of accumulation of solids from one cycle

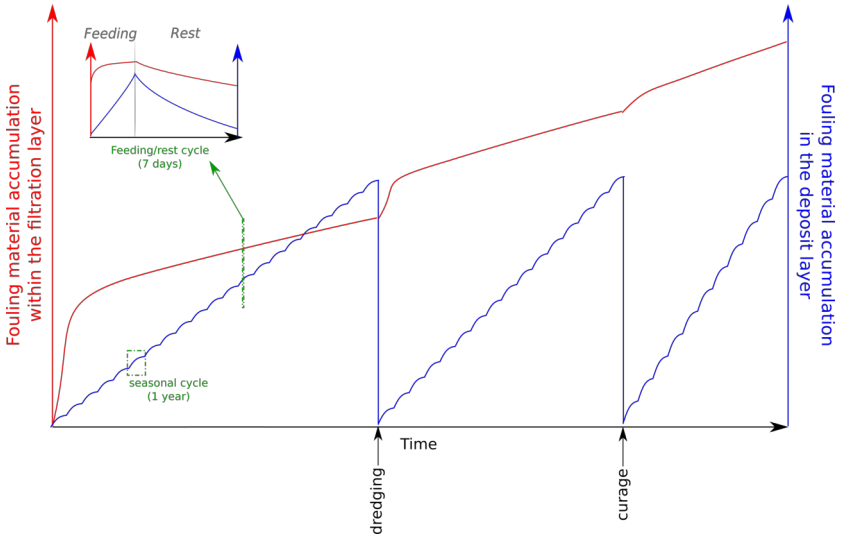

Figure 2.46: Conceptual model for fouling and clogging in French VFTW.

Figure 2.47: Clogging layer (light brown) over a surface deposit layer (dark brown) in a mature French VFTW.

to another are expected to increase as the the FM content within the gravel layer increases progressively (Figure 2.46).

FM within the gravel layer is never exported and will eventually reach a level that will not permit a sufficient infiltration rate or oxygen transfer and ensure nitrification. Low infiltration within the granular media (the gravel layer) will then be the bottleneck hydraulic process and dredging of the deposit layer will become inefficient. Eventually, this will lead to a degradation of treatment performances. At that moment, the gravel layer will reach formally a clogged state, and curative measurements must be taken.

The evolution of French VFTW described until this point follows an "ideal" conception of the fouling/clogging process. Nevertheless few cases of premature clogging have been observed in some TW despite they have been built following the state-of-the-art guidelines. Premature clogging must be interpreted as a rapid fouling of the TW that imposes dredging of the deposit layer at frequencies greater than once every 10 years. To the date, there exist no model explaining why such TW clog faster than the others.

The impact of clogging on the physical properties of the surface deposit layer is well illustrated in Figure 2.47. In this figure, a light brown layer of solids at the top of the deposit layer has formed. The chemical composition of the deposit layer is still a subject of study.

Knowles et al. state that clogging layers of FM are basically formed of humic substances [51], but their influence on the clogging process has been questioned by Kania et al. [48] who found also considerable amount of humic susbtances in the FM of non-clogged filters. Hua et al. [27] state that although "stable humic" subtances are present in clogging layers, the main factor leading to clogging is the presence of "labile" organic compounds, which promotes biofilm growth.

Irstea tries to keep up-to-date a census of French VFTW in the French territory through the platform Plantdefi (web host - Irstea). To the date, the second oldest French VFTW in regular operation in Montromant (Rhône), which was commissioned 25 years ago has only been dredged once. It does not present signs of clogging nor reduced treatment performances in TSS, DCO and DBO according to current regulations. This treatment plant was chosen as experimental site for the studies presented in chapters 4, 5 and 6 because of its age and maturity. The TW in Copponex (Haute Savoie) has been in operation for 15 years. There are two types of filtering material at the first treatment stage as some filters were added in 2011 to increase treatment capacity. The two types of filter material respect the state-of-the-art granulometry range (2 - 8 mm). However, the oldest filters were filled using an alluvial pea gravels. Due to the increasing scarcity of this type of material, the most recent filters were filled with crushed gravels. The later have clogged after only 6 years of operation. Copponex is one of the few premature clogging cases that have been identified in France. This treatment plant is subject to large hydraulic overloads during spring due to snow melt and large volume of clear water intrusion within the sewer network.

2.7 Clogging: detection and alleviation

2.7.1 Detection

By definition, clogging in TW may be predicted by measuring the evolution of infiltration rates and determining the moment where there is no "rest period" between batches of a feeding period. Nevertheless, as clogging is strongly linked to hydraulics and biological processes, monitoring other parameters may also inform about clogging. A classification of methodologies is proposed in Table 2.10 based on the parameter that is measured.

Altough there are several links between clogging and other processes in TW, clogging and fouling remain phenomena governed by the occupation of solids in the porosity of a granular material, where both, their amount and geometrical distribution, are important. Table 2.10 only cites 3 techniques that allow to obtain a spatialized description of pore media and solids distribution: geopedoscopy, thin sections and X-ray tomography.

2.7.2 Alleviation

Several measurements to address the problem of clogging have been considered and listed below. The majority of them are onerous, but most importantly, their long term efficiency is not well assessed yet.

- Replacing fouled gravel by "new" clean gravel.
- Gravel dredging and in-place cleaning.
- Chemical treatment with H_2O_2.
- Chemical treatment with NaClO.
- Biological treatment with earthworms.
- Use of solutions with specific ratios of nutrients concentration (to promote the metabolism of bacteria with high consumption of organic matter).
- Use of surfactants to solubilize large bio-polymers.

Table 2.10: Parameters and methodologies to assess clogging in TW.

Parameter	Unit	Type of the variable	Methodology
Solids humid/ dry density	kg/m^3	Physical (Thermodynamic)	Gravimetry + Volumetry Gas Picnometry
Saturated Hydraulic Conductivity	m/s	Hydraulic	In/ex-situ measurement Estimated from pore morphology / pore networks
Unsaturated Hydraulic conductivity	m/s	Hydraulic	Ex-situ measurements Estimated from pore morphology / pore networks
Infiltration Rates	m/s	Hydraulic	In/ex-situ measurements with water level probes
Residence Time Distribution	s	Hydraulic	Dye tracing
Porosity (voids volume)	m^3 or m^3/m^3	Physical (Structure)	Spatialized measurements • Geo-endoscopy • Thin sections • X-ray Tomography
Drainable Porositym^3 or m^3/m^3	m^3 or m^3/m^3	Physical (Structure)	Global measurement • Gravimetric
Solids Volume	m^3		Global measurements • Combination of solids density + mass measurements Spatialized measurements • Geo-endoscopy • Thin sections • X-ray Tomography

Table 2.11: Continuation...

Gas dispersion coefficient	m^2/s	Physical (Gas transport)	From simulations at Darcy Scale
Tortuosity	m/m	Physical (Structure)	Estimated from a pore model at Darcy Scale Measured at the pore scale • Thin Sections • X-ray Tomography
Specific Surface (total, volumetric or gravimetric)	m^2 or m^2/m^3 m^2/kg	Physical (Structure)	Global estimations from • gravimetric methods • Gas/solution adsorption Measured at the pore scale • Thin Sections • X-ray Tomography
Water / water content	Gravimetric (kg/kg) Volumetric (m3/m3)	Physico-chemical	Measured by • Gravimetry (drying 105 °C) • Gravimetry/Volumetry Spatialized estimation by • Capacitive electrodes • Nuclear Magnetic Resonance • Electrical Resistivity Tomography
Oxygen (concentration)	mol/m_3 m^3/m^3	Physico-chemical	Environmental measurements • Luminescent probes

Table 2.12: Continuation...

	mol/mol		
Solid Particle Size (& distribution)	Size (m) and distribution (volume/mass vs size)	Physical	Tangential Filtration Laser Granulometry
Mechanical resistance	LA coefficient (kg/kg)	Physical	Angeles Test
Topology			Scanning Electron Microscopy
Volatile Solids	kg kg/kg	Chemical	Calcination (550°C)
Organic Molecules (Polysaccharides, proteins, humic acids, etc)	kg/kg, kg/m3 mol/mol		Chemical Fractioning
Mineral composition	kg/kg ??		X-ray diffraction
Red-ox potential	eV	Physico-chemical	Voltammetry
Oxygen Consumption	kg/s	Biological	Respirometry
DNA composition		Biological	DNA sequencing • Polymerase Chain Reaction (PCR) • Denaturing Gradient Gel Electrophoresis (DGGE)

2.7.3 Highlighting the potential of X-ray tomography

The application of geo-endoscopy and thin sections for the study of clogging in TW was already studied in the work of Breul and Gourves[11] and Kim and Forquet [50] and focused on the volume occupation of FM. This thesis presents, for the first time, several works on the application of X-ray CT to understand fouling and clogging in French VFTW. The following chapters set a solid basis for its use by explaining in detail how to process images from X-ray CT (cf. 4 and 6) and by studying the spatial representativity of the measurements (Chapter 5). As a methodology with a high potential to describe porous media, not only the volume occupation is relevant, but the structure of the voids and even the distribution of size of gravel.

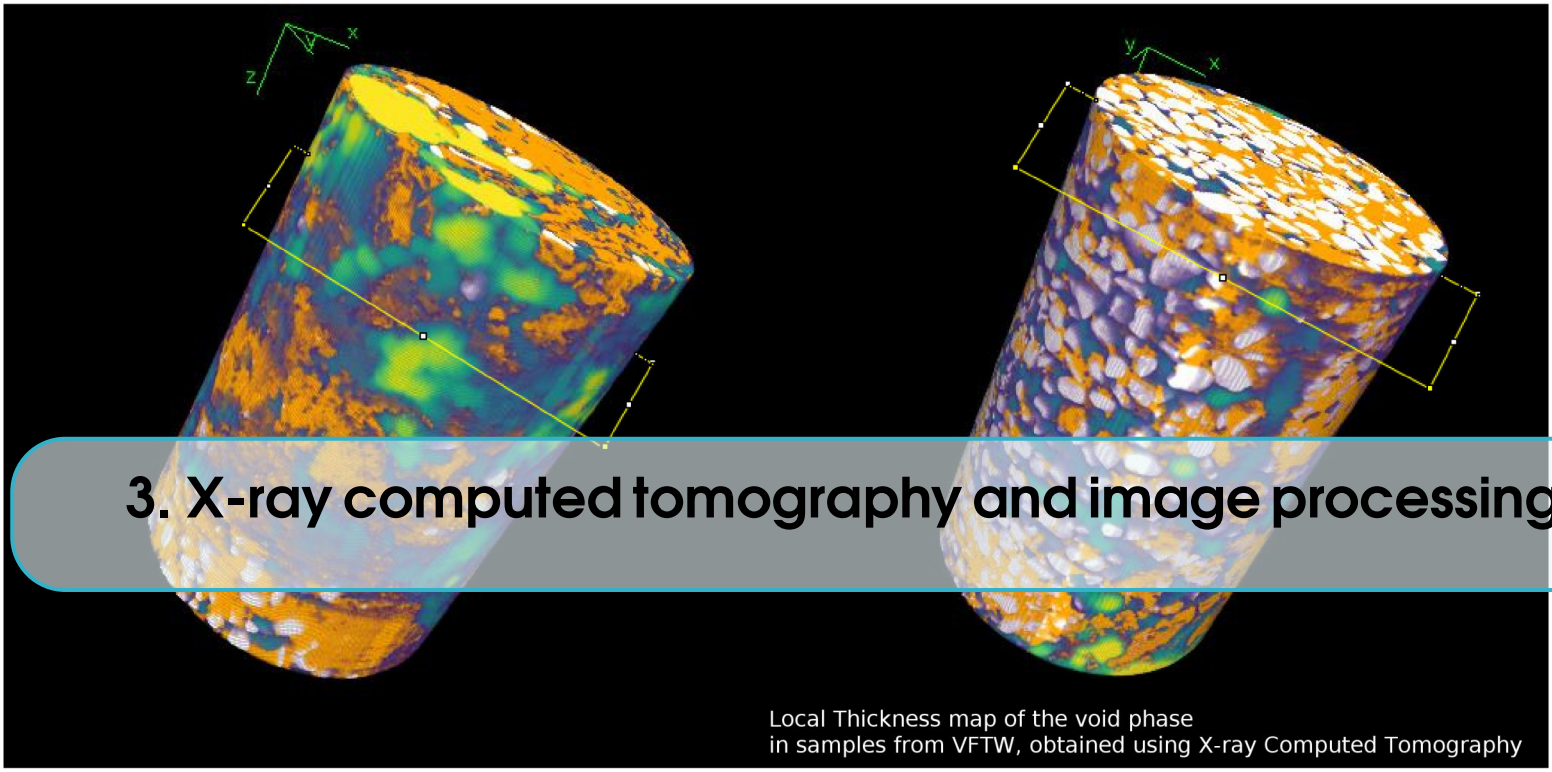

Local Thickness map of the void phase
in samples from VFTW, obtained using X-ray Computed Tomography

3. X-ray computed tomography and image processing

3.1 Introduction

X-ray Computed Tomography (CT) has been used to study the inner morphology of 3D objects for the first time thanks to the work of Godfrey Hounsfield and Allan McCormack in 1960 [125]. The use of X-ray CT was then restrained due to the low number and high cost of X-ray facilities. From the 60's to the beginning of the XXI century this methodology has greatly evolved and many types of scanners can now be found on the market. Currently X-ray CT is used in various fields including geology, archeology, biology, biomedical, electronics, materials and food science.

Image treatment refers to all algorithms necessary to perform a segmentation of a X-ray CT scan. Segmentation is the most important procedure in quantitative image analysis. It consists in delimiting zones, objects or phases in a digital image. Post-treatment refers to algorithms used to study the geometrical structure of segmented images. In this chapter, some principles of X-ray CT, image acquisition and image treatment are presented. After this presentation, image post-treatment algorithms are introduced in more detail.

The aim of this chapter is to guide a X-ray CT neophyte into Image Processing (IP) so he/she could apply the same methodology to treat samples from TW. Nevertheless, more complete reviews on X-ray imaging and image processing are readily found in the literature. The reviews presented in [110, 125, 115] are recommended if the reader wants to explore thoroughly or optimize the methodologies presented in this chapter.

As a major contribution of this thesis to the community of TW and image processing, an algorithm for the segmentation of multiphase images has been written in python based on the work of Hashemi et al. [35], as well as some post-treatment algorithms, for the characterization of TW samples. These are available in the repository below:

`https://gitlab.irstea.fr/german.martinez-carvajal/Wetlands_Xray_Tomopgraphy.git`

Great part of the algorithms used in this work are already available in Fiji (a distribution of ImageJ free software) and in the Scipy library (python).

More complete descriptions of a variety of image processing algorithms can be found in the Fiji user guide available in the link below:

`https://imagej.net/docs/guide/`

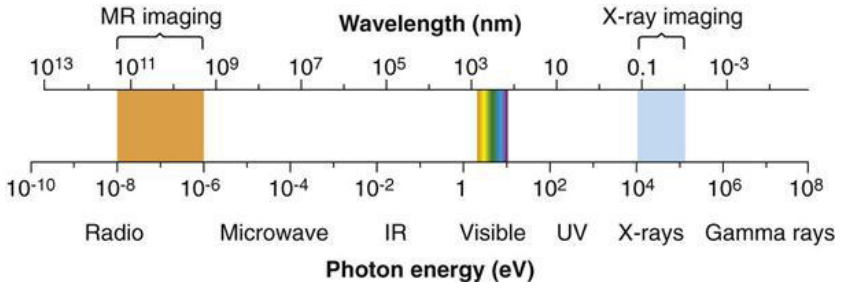

Figure 3.1: The electromagnetic spectrum.

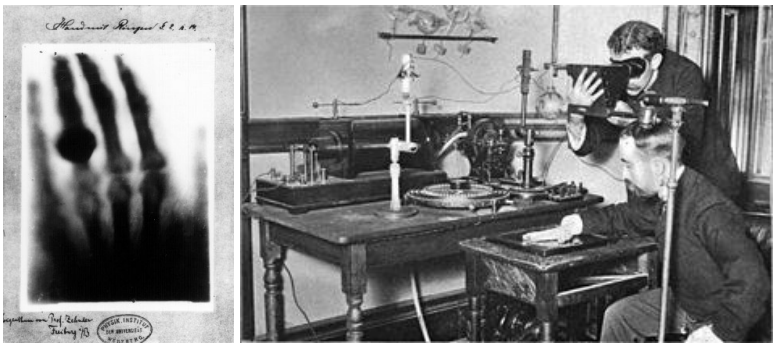

(a) Print of Wilhelm Röntgen's first "medical" X-ray image of his wife's hand.

(b) Taking an X-ray image with early Crookes tube apparatus, late 1800's.

Figure 3.2: Beginnings of X-ray imaging.
Photos from https://en.wikipedia.org/wiki/X-ray

3.2 X-rays

X-rays are a form of high energy electromagnetic radiation. They are produced when charged particles (electrons or ions) interact with other atoms at specific conditions. At the lab scale, X-ray are produced in cathode-ray tubes, where a high voltage is used to accelerate electrons released by the cathode. The electrons collide with the anode (or anti-cathode) and, when they have enough energy, they may eject a low energy electron from the anode, i.e. inner shell electrons of atoms of the anode material. Afterwards, an electron at higher energy level fills in the vacancy left by the ejected electron. The displacement of this electron to a lower energy level is accompanied by an emission an X-ray of a characteristic energy.

X-rays can not be described entirely as a wave, they behave sometimes as particles. This conundrum is referred in quantum mechanics as the wave-particle duality. On the one hand, X-rays form part of the electromagnetic spectrum which goes from radio waves to gamma rays (Figure 3.1). Therefore X-rays are characterized by specific energy levels and wavelength ranges. On the other hand, following the quantum theory, the energy of the X-ray is composed of photons. A photon is defined as a particle with no mass containing the minimum quantity of electromagnetic wave energy.

3.2.1 A little history

The first images recording the interaction of X-rays with objects were obtained by William Röntgen (Germany) in 1895 when he was experimenting with cathode-ray tubes. He wrapped a tube with a black cardboard to avoid visible light to interfere with one of his experiments. He

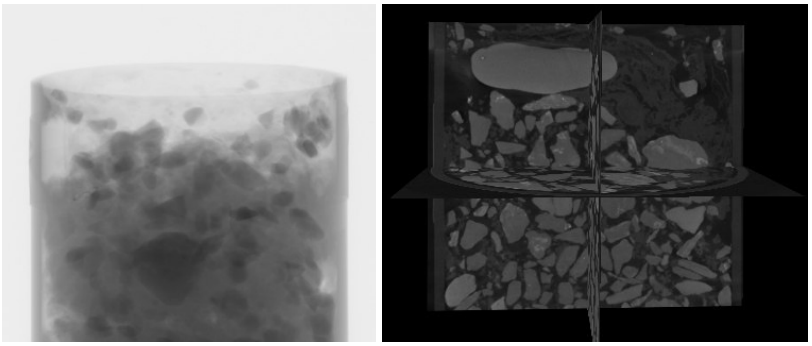

(a) A single projection.

(b) 3D reconstruction after treating several 2D projections.

Figure 3.3: 2D X-ray projection and 3D reconstruction in computed tomography.

also used fluorescent screens painted with barium platinocyanide for other experiments. Despite he covered the tube, he noticed that the screens glowed when producing the cathode ray. He deduced that a different and unknown type of rays (that he decided to call X-rays) were produced in the tube, passed trough the cardboard and reached the screens, making them glow. He also observed that the rays were capable of passing through other objects in his laboratory (books, laboratory equipment...) and let a dark trace on the screen. Röntgen was the first person to produce an image of a body part using X-rays when he made a picture of his wife's hand (Figure 3.2(a)) which makes him the pioneer of X-ray use for medical purposes (Figure 3.2(b)).

3.3 Computed Tomography

The term Computed Tomography (CT), or computerized axial tomography, means that several 2D projections of an object are obtained by irradiating the object from different angles while its being rotated around a single axis. The 2D projections are treated by computational algorithms to generate a 3D representation of the internal structure of the object. The 3D representation is made of a set of cross sectional 2D-images: xy, xz and yz planes (Figure 3.3b). Several types of computed tomographies exist. Their principle is based on different interactions between photons and matter. Transmission X-ray CT is the most frequently used type of X-ray CT but the use of phase contrast and fluorescence tomography is increasing specially for the the study of samples from the environment (geological and biological) [125] .

3.3.1 Transmission X-ray CT

X-ray photons interact with matter in different ways, they can be either absorbed, scattered (elastic or inelastic), refracted, or diffracted [125]. Rays which pass through the object in the same direction than the incident ray are "transmitted" (Figure 3.4).

As the rays pass through the object, their intensity decreases. It is measured in W/m^{2}of the orthogonal surface to the ray direction. For a monochromatic ray, i.e. with unique wavelength and energy, the intensity of the X-ray decreases unidirectionally following Beer's law (Equation 3.1). When a detector senses the decrease of the X-ray energy intensity the technique is called transmission X-ray CT. This is the type of technique used to study the structure of porous media of VFTW in the remainder of this thesis.

$$I = I_0 \exp(\mu x) \tag{3.1}$$

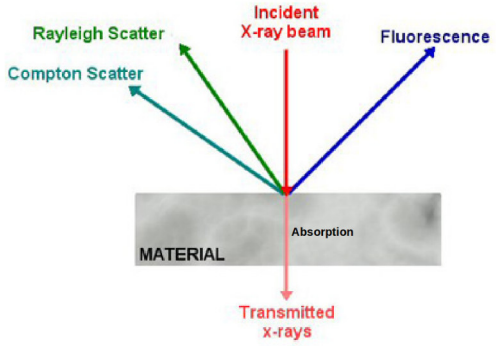

Figure 3.4: Different interactions of X-rays with matter.

Table 3.1: Mass attenuation coefficients (μ/ρ) in 10^{-1}cm^2/g for different materials. From [115].

Material	Z	Density (g/cm^3)	Photon energy (keV)							
			50	100	150	200	300	400	500	1000
Air		1.2 *10^{-3}	1.96	1.51	1.34	1.23	1.06	0.953	0.870	0.636
Water		1.0	2.14	1.68	1.49	1.36	1.18	1.060	0.967	0.707
Muscle		>1.0	2.14	1.66	1.48	1.35	1.17	1.050	0.959	0.700
Bones		1.7-2	3.27	1.74	1.47	1.32	1.14	1.010	0.925	0.675
Concrete		2.3	3.61	1.70	1.40	1.25	1.07	0.958	0.873	0.637
Aluminium	13	2.7	3.34	1.62	1.34	1.20	1.03	0.922	0.841	0.624
Iron	26	7.86	18.4	3.42	1.84	1.39	1.07	0.921	0.829	0.596
Copper	29	8.93	25.0	4.27	2.08	1.48	1.08	0.919	0.822	0.589
Tungsten	74	19.3	54.00	42.90	15.00	7.38	3.02	1.800	1.290	0.639
Lead	82	11.34	72.20	52.30	18.90	9.45	3.83	2.200	1.540	0.690

The attenuation of the ray is modeled by the attenuation coefficient (μ) in equation 3.1and depends mainly on two factors: (1) the atomic electron density of the material, which is often (but not always) proportional to the material bulk density and (2) the energy of the incident ray. Dense materials attenuate more X-rays than light materials. High energy rays pass more easily trough an object than low energy rays. Table 3.1 presents the variation of the attenuation coefficient for different materials.

Intensity attenuation by photon absorption is strongly dependent on the atomic number. For low X-ray energies (50 – 100 keV), photon absorption dominates followed by coherent scattering. For higher energies, up to 5 MeV, attenuation is caused by other phenomena like incoherent diffusion (Compton effect) [115].

3.3.2 Fluorescence X-ray CT

When X-rays photons are absorbed not only the the intensity of the incident beam is attenuated but it also leads to the ejection of inner electrons from the irradiated object atoms. When these ionized atoms return to a neutral state a new emission of energy occurs in the form of another X-ray (fluoresced X-ray) whose direction is different from that of the incident ray. In X-ray fluorescence tomography a second detector (fluorescence detector) senses the presence fluoresced rays (Figure 3.5). The intensity of the fluoresced rays depend highly on the elements present in the sample which makes this technique suitable for obtaining accurate information on the elemental composition of a variety of materials.

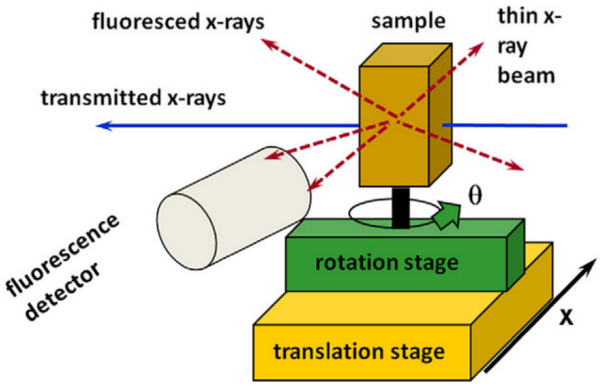

Figure 3.5: Set up for Fluoresced X-ray CT.
From [125].

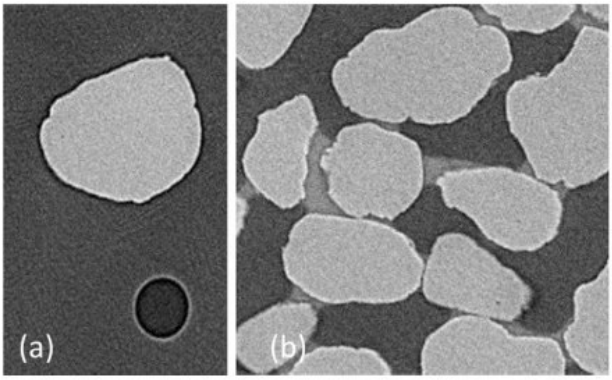

Figure 3.6: Examples of X-ray phase contrast images.
(a) Image of single quartz grain embedded in epoxy with adjacent air bubble
(b) Sandstone sample with residual wetting phase between the grains. From [125].

3.3.3 Phase contrast X-ray CT

When X-rays are refracted, e.g. when they pass trough an object made of different density materials (composite samples), their speed, wavelength and direction change causing also a change in the "phase" of the wave. When the refracted rays reach the detector, the intensity will be higher at cells where the rays are converging and lower where they are diverging. If this intensity variation is captured by the detector, the technique is called phase contrast.

Phase contrast X-ray CT is more complex than transmission CT as it requires using an algorithm to retrieve the phase based only on the measurements of intensity attenuation. This technique works at best to identify interfaces between materials (Figure 3.6).

3.4 From the object to the reconstructed image

3.4.1 Sample extraction and preparation

For the studies presented in chapters 4, 5, and 6, cylindrical samples were obtained from the topmost part of a TW (Figure 3.7). The extraction method consists in inserting a cylinder slowly to avoid the compaction of the deposit layer while progressively removing the media surrounding the cylinder to decrease the shear stress and avoid alteration of the sample structure. Samples must be drained out before scanning them. The reason is that it takes 30 to 60 minutes for regular scanners to produce one image of the object. If the structure of the sample (including its water

Figure 3.7: Samples.
Plastic cylinders for X-ray CT and Kubiena tins to produce thin sections.

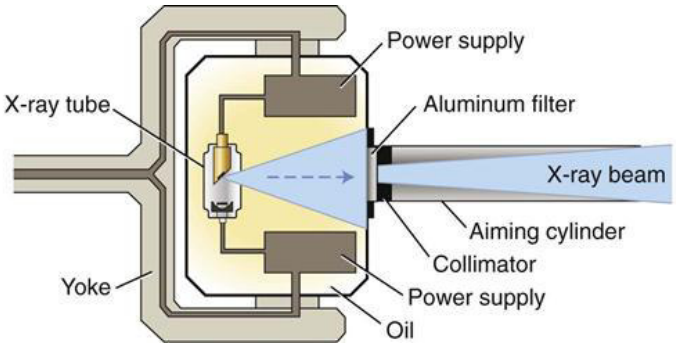

Figure 3.8: Schematic representation of an X-ray source.

distribution) changes significantly during the scanning, the results may not be exploitable.

3.4.2 Scanning

Source of light

Figure 3.8 shows the structure of an X-ray source. The X-ray tube is a cathode-ray tube containing often a tungsten anode. The radiation produced by the tube correspond to a spectrum of frequencies rather than a single frequency. This means that the ray is composed of different wavelengths and is thus called polychromatic (by analogy with visible light).

Filters and hardening

The X-rays are projected outside the X-ray tube and pass through a filter (an aluminum foil in Figure 3.8), which will absorb part of the X-ray photons letting pass only rays with higher energies. This process is known as hardening (rays with higher energy values are “harder”). A filter tends to reduce the total ray energy and the wavelength range making it less polychromatic.

Adding a filter to harden a ray may enhance the quality of a projection. A non uniform transmission of low energy rays (from a non filtered source) may be responsible of uneven bright spots (saturation) in materials of homogeneous composition (Figure 3.9(a)). The image produced with a hardened ray is less brilliant but more homogeneous (Figure 3.9(b)).

Hardening a ray has also an influence on the deconvolution step as it is easier to treat signals produced by monochromatic rays than polychromatic rays. The total energy intensity of a polychromatic ray will not decrease exponentially. Nevertheless, if a filter absorbs to many X-ray photons, the filtered ray may not have enough energy to pass through the object. Therefore the filter material and its thickness should be chosen wisely. Some filters are presented in Figure 3.10. In studies presented in chapters 5 and 6, the X-ray source was filtered with a 0.1 mm

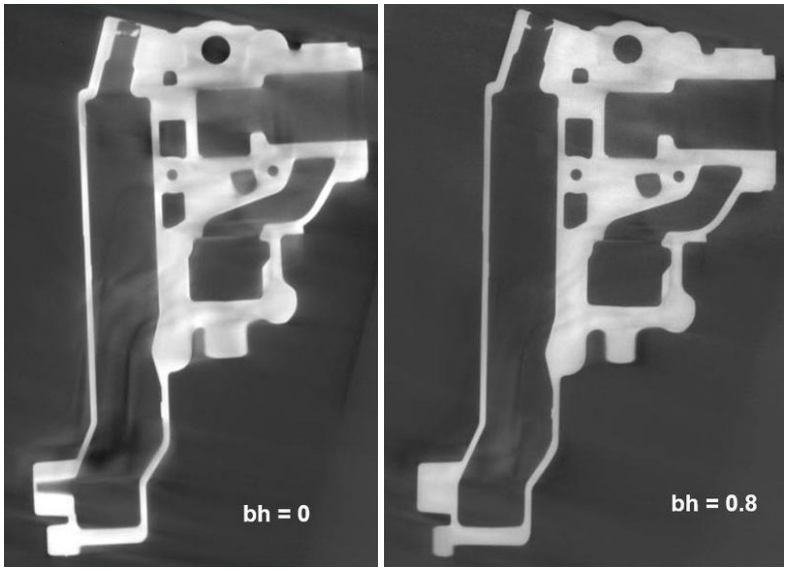

(a) Without X-ray hardening. (b) With X-ray hardening.

Figure 3.9: Comparison of images produced with or without hardening filters
From https://4nsi.com/blog/2016/02/12/beam-hardening/

Figure 3.10: Beam Filtering materials.
From https://4nsi.com/blog/2016/02/12/beam-hardening/

copper foil.

Collimators and beam shape

Collimation means orienting something (an apparatus or a ray) to a precise point. In X-ray tomography, a collimator serves to cause the direction of rays to become more parallel and/or to narrow the cross sectional area of a beam (Figure 3.8). Collimation changes the shape of a beam. A cone shape beam is produced naturally by the source but could also be narrowed by a circular slit. The size of the slit depends on the aimed cross sectional area. A fan beam has been collimated by a narrow rectangular slit as shown in Figure 3.11(b). A cone-shaped beam is advantageous as it allows efficient large area detectors to be used, but the mathematical treatment of the object projections is more simple for images produced with fan beams than with cone beams.

Detector and resolution

Depending on the distance of the object to the X-ray source and the detector, the size of its projection on the detector surface varies. These distances are optimized to have the largest projection possible and thus the best resolution.

For a cone shape beam, the 3D resolution of the image in the three dimensions is a function of 3 parameters. The resolution in vertical direction is determined by the number of cells in the detector in the vertical direction. The resolution $(m \cdot n)$ of slices orthogonal to the vertical

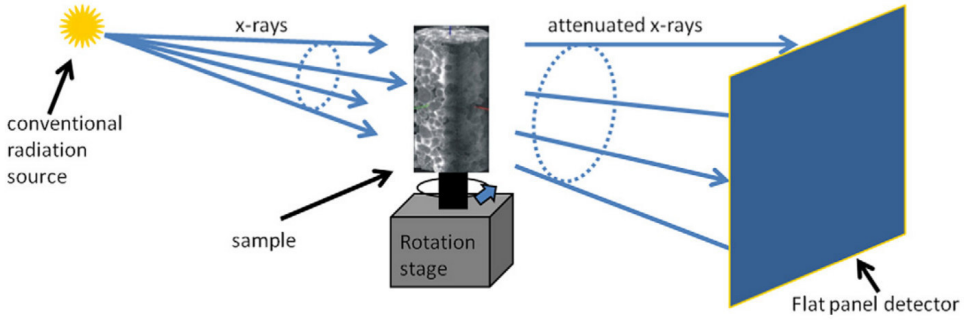

(a) Cone beam.

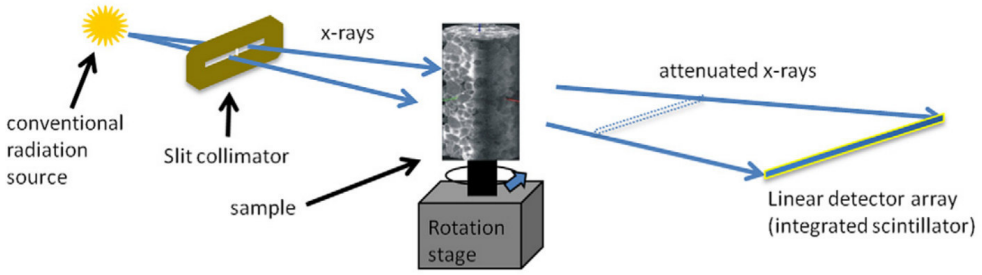

(b) Fan (collimated) beam.

Figure 3.11: Beam configurations.
From [125].

direction depends on the the number -m- of cells in the detector in the horizontal direction and of the number of scans -n- at different angles, where the angle step is 180°/n [115].

Helical and horizontal acquisition

When the projected height of the irradiated object surpasses the detector height, an image of the whole object can be obtained preserving the resolution by either of these procedures:

- Setting different constant vertical positions and performing a scan for each one, i.e. the vertical position of the sample does not vary while it is being rotated. These 2 or more images have to be concatenated afterwards. In this thesis this is referred as horizontal acquisition[1]
- Obtaining projections of the objects while both rotational and vertical translation occur. This is called a helical acquisition[2]

The size sample size is limited by the maximal vertical displacement of the sample supporting platform. While in horizontal acquisition it is recommended to perform different scans with small overlay, in helical acquisition it is mandatory to start the scan at a higher position and finish it at a lower position to have enough data for a good quality reconstruction of the extremities of the sample. (See video 2).

Scan duration

For each projection, the object is irradiated during a period of time of a fraction of a second. The duration can be adjusted if more photons have to be irradiated to pass through a dense sample, but it must avoid saturating the detector cells. The scan time depends thus on the duration of each

[1] A video of 2D projections from an horizontal acquisition can be seen here: `https://www.youtube.com/watch?v=djrNLsdOTro&feature=youtu.be`

[2] A video of 2D projections from an helical acquisition can be seen here: `https://www.youtube.com/watch?v=xRav6wkuZBg&feature=youtu.be`

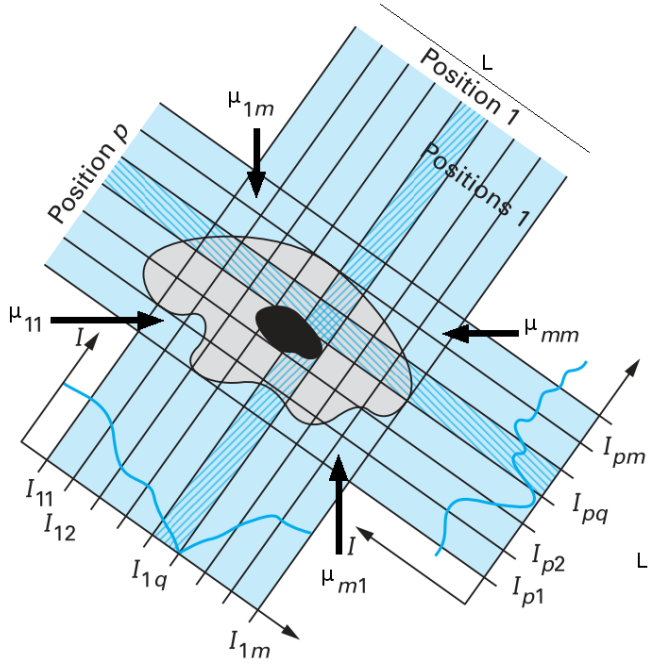

Figure 3.12: Mathematical principle of the reconstruction.
Adapted from [115].

projection and the number of of angular steps. It is a common practice to irradiate the sample 2 or 3 times for each angle then keeping only the an average projection.

3.4.3 3D reconstruction

The reconstruction is a key process in CT in which 2D projections are used to reconstruct the 3D volume of an object. There exist many methods to achieve this objective. Here, only the basic concepts of this process are explained for a simple geometry.

In Figure 3.12 an object is being irradiated by parallel rays. The source is being rotated instead of the object.

In this figure:

- Each stripe represents transmitted and detected rays by a single cell. The detector has a total of -m- cells.
- -p- represents the position of the source light which goes up to the integer -n-. The system is thus able to produce a projection for -n- different angles.
- The image of the object will be divided in $m \cdot n$ pixels.
- -q- represents the q-th detector (varying from 1 to m)
- A single attenuation coefficient $\mu_{i,j}$ is attributed to each pixel. Both -i- and -j- vary from 1 to m.

Assuming Beer's law, the attenuation measured by the q-th cell at the position p = 1 is modeled by one of the following equations:

$$\ln \frac{I_0}{I_{p=1,q=1}} = (\mu_{1,1} + \mu_{1,2} + \ldots + \mu_{1,m}) * \frac{L}{m}$$

$$\ln \frac{I_0}{I_{p=1,q=2}} = (\mu_{2,1} + \mu_{2,2} + \ldots + \mu_{2,m}) * \frac{L}{m} \text{ etc...}$$

For position p, attenuation is modeled as follows:

$$\ln \frac{I_0}{I_{p=p,q=1}} = (\mu_{1,1} + \mu_{2,1} + \ldots + \mu_{m,1}) * \frac{L}{m}$$

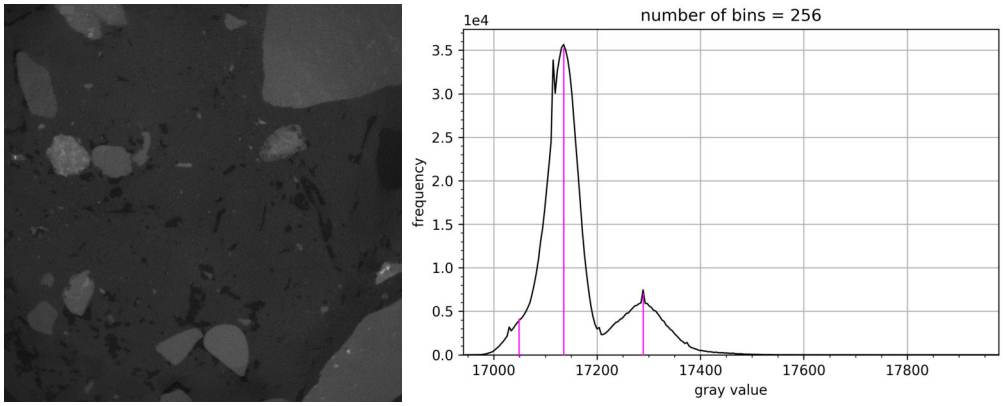

(a) (b)

Figure 3.13: Reconstructed image and histogram of gray value intensities.
The histogram can be described as a superposition of three peaks with three different mean values around 17050, 17150 and 17300 (16-bit).

$$\ln \frac{I_0}{I_{p=p,q=1}} = (\mu_{1,2} + \mu_{2,2} + ... + \mu_{m,2}) * \frac{L}{m} \text{etc...}$$

All $\mu_{i,j}$ values are unknown and have to be found. The decrease in the intensity $\frac{I_0}{I_{p,q}}$ is measured by the q-th detector at the position -p-. The length -L- of the object and the number of -m- of cells are known.

By increasing the number of positions to m (one projection for each angle, where the angle step is 180/m) the number of equations equals the number of unknowns. In an "ideal" case the system of equations is linear represented by a vector of intensity values, a vector of μ unknowns and a matrix of coefficients. The system should be solved by finding the inverse of the coefficients matrix. For the two positions depicted in Figure 3.12 the coefficients of all the unknowns $\mu_{i,j}$ is L/m, but for the other positions the equations are not a linear combination of $\mu_{i,j}$values.

Hopefully Godfrey Hounsfield and Allan McCormack rediscovered the Radon transform. It can be used to write a set of linear equations representing intensity attenuation. Additionally, the problem induced by the rotation is solved by using the theorem of the central section and the Fourier's Transform (details can be found in [115]). In this way it is theoretically possible to reconstruct an image of the inner structure, where each voxel stores a $\mu_{i,j}$value. Nevertheless solving the Radon's transform and its inverse demands high computational resources. Other methods have been developed to solve this problem. They are often divided into two subgroups: the filtered back projection and the iterative methods.

The form of the beam (parallel, fanned or coned) changes also the complexity of the mathematical problem. The Feldkamp algorithm (referenced in [125]) provided the first filtered back projection reconstruction method for cone beam geometries.

3.4.4 The reconstructed image

The reconstructed image consists in a 3D-image where each voxel (a 3-D pixel) contains a gray value representative (but not equal) to the attenuation coefficient of the material of that voxel. The gray values are thus correlated to the material density: the higher the gray value is, the denser the material is. The frequency distribution often shows that different elements or phases in the image are associated to different gray value ranges which are likely to superpose (Figure 3.13).

3.4.5 The treatment workflow

Although the reconstruction process is the first step in data manipulation, it is not a common practice for people debuting in image acquisition to modify reconstruction algorithms with the aim of enhancing the image quality. Instead, the reconstructed image is treated (image processing) for further quantitative analysis.

Image processing can be simply resumed in three major groups of operations: pretreatment, segmentation and post-treatment. Segmentation is the most important step, which consists in the attribution of each voxel to a single phase (solid or air for instance) based on its gray value and those of its neighbors. Before the segmentation, pretreatment operations are often performed to reduce noise or eliminate artifacts. After the segmentation, several morphological properties of the object can be measured. The algorithms used to obtain different geometrical descriptions constitute the post-treatment steps. All these steps are described in the remainder of this chapter focusing on specific characteristics found in scans from VFTW.

3.5 Important features of tomographic images

3.5.1 Dealing with image format and types

Formats: non compressed, lossy and lossless compression

The 3D reconstructed image is often a ".vol" or ".tif" file, which can be roughly described as a 3D matrix containing numbers representing a different gray value.

There exist other common image formats such as .png, and .jpg. These are compressed formats. They allow to store the same or "almost" the same image using a smaller amount of memory. The .jpg format is very efficient for storage but uses lossy compression which alters the original data. The .png format uses lossless compression and is the best for presentation purposes. For quantitative analysis the use of non compressed formats .vol or .tif is mandatory.

Types: 8bit, 16-bit and 32-bit

The common display convention assigns white to the largest stored gray value and black to the lowest. Intermediate values correspond to different shades of gray. The gray value can be an integer or a float depending on the image type. Common types are 8-bit integers, 16-bit integers (both of which can either be unsigned or signed) and 32-bit which is the type for float numbers. The difference among these consists in the total number of values that can be stored as well as the memory consumption.

- 8–bit images can store one of 256 (2^8) different gray values per voxel. In unsigned type the values go from 0 (black) up to 255 (white), in signed type from -128 to 128.
- 16–bit images can store one of 65 536 (2^{16}) different gray values per voxel.
- 32–bit images can store one of (2^{32}) different gray values per voxel. Voxels are described by floating point values and can have any intensity value including NaN (Not a Number).
- RGB Color images can display 256 values in the Red (255,0,0), Green (0,255,0) and Blue (0,0,255) channels. These are 24–bit (3*8-bit) images.

Gray values from a reconstructed image are often 16-bit type. Nevertheless the stored values may not cover the whole range of this type. Images studied in this thesis contain for instance only 2000 to 3000 of the 65 536 possible discrete values.

Memory consumption

A larger number of possible discrete values means a more sensitive measurement of intensity attenuation (by the detector cells), but also means a higher memory consumption per image. This is analog to measuring the length of the same object with two rules, firstly with a 1 mm subdivision and secondly with a 1 cm subdivision. The first measurement is more precise but needs writing more significant digits (more memory consumption).

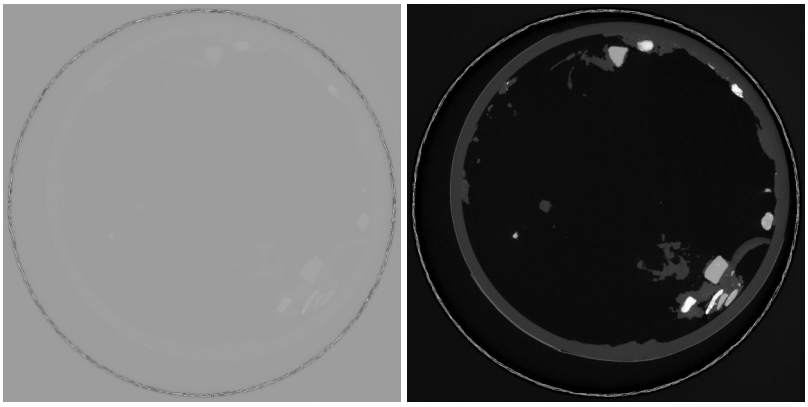

(a) Non optimum look up. (b) Optimum look up.

Figure 3.14: Ring artifact with two displayed with two different look up tables.
Both images store the same information in 16-bit format but a wrong look up in figure (a) would give the impression the file is corrupted.

An image of 1024*1024 pixels in 8-bit consumes 1 MB for instance. The same image in 16-bit consumes 2 MB and in 32-bit 4-MB.

A 3D image of a VFTW sample of 5 cm in diameter and 10 cm in height at a resolution of 0.05 µm/vox occupies thus nearly 2 GB and 4 GB in 8-bit and 16-bit respectively, which already surpasses the RAM of regular laptops. Image treatment will demand additional RAM availability which obligates disposing of more powerful computational resources.

The problem of screen display

A regular computer screen displays colors as in a RGB image: (255, 255, 255) represents white, (0,0,0) black and (128, 128, 128) medium gray. All grays are represented by a 3 size vector containing the same values. The maximum number of different gray values displayed in a screen is then 128.

To display a 16-bit image computers use a look up table which attributes one of the 256 possible gray values to one of 256 classes built from the 16-bit image total range. Therefore, two different look up tables differ then on the way the class has been built; for instance, two different classes are those linear evenly distributed or logarithmic evenly distributed, with different max and minimum values.

When a 16-bit image is opened in Fiji (ImageJ), the look up table is computed automatically but it may be not optimal to visualize image details. This is specially annoying if there exist saturated pixels in the image: one may have the impression the file was corrupted. The look up table can be changed using the brightness and contrast tool without changing the original values stored in the image (Figure 3.14).

NOTE: In image processing guided by a user interface it is mandatory to check both the image and its the gray values distribution to observe if real data changed during a manipulation.

Trying to reduce memory consumption

As a general rule it is preferable not to change the type of the image from 16-bit to 8-bit. Nevertheless, since some image processing algorithms are based mainly on histogram computations, changing the image format may be a solution to reduce memory consumption to the half. This means that the histograms the image before and after type conversion must be similar. If this approach is considered, it is very important to change the format of the image after it has been normalized (See section 3.6.1). This is important in Fiji as the algorithm changing the type of data from 16-bit to 8-bit is based on the current look up table, which may not be optimized for

the specific features of an image. Optimal type change is exemplified in Figures 3.15 and 3.16.

3.5.2 Artifacts and noises

The reconstructed image may show artifacts, which are a set of voxels that do not represent a real feature of the sample. Saturated spots in Figure 3.9(a) are a kind of artifact as the object density is not higher at those spots. Artifacts can appear either by the nature of the imaging setup or created during the reconstruction.

Ring artifacts

The whiter pixels in Figure 3.17 form ring artifact in an image of a sample from VFTW. Ring artifacts are produced during the reconstruction. Hopefully this type of artifact never reached the center of the samples of this thesis and is readily removed by setting a value = 0 for pixels outside the cylinder. Nevertheless it is possible to find them in images from porous media (Figure 3.18). Image filtering (Section 3.6.4) provides a solution of this problem if encountered.

Hardening artifacts

Hardening artifacts were already presented in Figure 3.9. On the one hand, they can be partially avoided by X-ray filtration at the source. On the other hand, the filtered incident X-rays are still polychromatic (in a lower degree) and as they pass through the sample they will be hardened: lower energy rays are absorbed predominantly at the sample borders. During the reconstruction, higher attenuation coefficients (higher bulk density) are attributed to voxels at the edges. This is called also a hardening artifact. An example is present in Figure 3.19. This artifact can be treated using specific filters [110] but was not encountered in this study.

Propagating glow

For multiple horizontal acquisition a special type of artifact was systematically found in the form of an almost concentric glow. It is located at the extremity scan slices. The glow propagates from the center to the borders of the image until it covers it uniformly. During this transition, the concerned slices show significant changes in gray value distribution, sometimes represented by double mode peak for one phase (Figure 3.20). For slices at the middle of a scan the glow is uniformly distributed [3].

This artifact is removed during the concatenation of the scans (Section 3.6.2)[4]

Changes of gray value distribution over depth

3D-raw (i.e. non treated) reconstructed images from VFTW display 3 main ranges of gray values corresponding to three phases: (1) voids, (2) gravel and (3) a mixture of water, plant tissues, organic solids and mineral solids that foul the space between gravels (i.e. the fouling material). The volume fraction of these phases vary significantly over the sample depth. Apparently, this vertically heterogeneous phase distribution affects the relative position of peaks of the gray value distribution. This phenomena is illustrated in Figure 3.21[5]. One way of dealing with this type of artifact is to normalize the image (Section 3.6.1) so the mean value for each peak is the same for every horizontal slice.

[3] A video presenting a scan with propagating glow can be found in `https://www.youtube.com/watch?v=wj47-oGpptQ&feature=youtu.be`

[4] It may exist references on this kind of artifact and how to remove it. The key words “Propagating glow” are certainly not correct. A more rigorous review on this artifact should be done.

[5] A video presenting a scan with propagating glow can be found in `https://www.youtube.com/watch?v=0QbrtPXHvY8&feature=youtu.be`

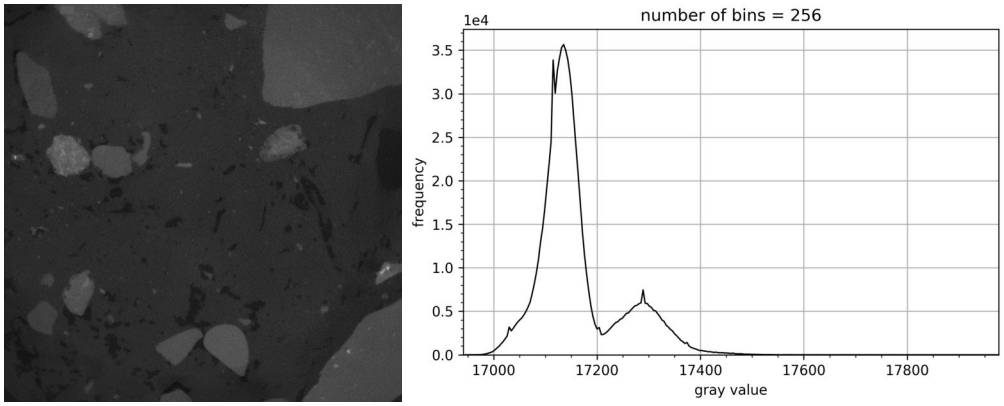

(a) (b)

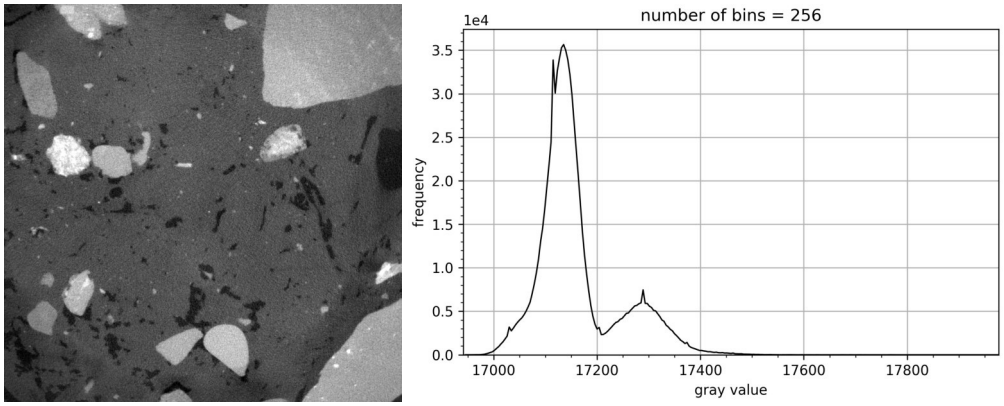

(c) (d)

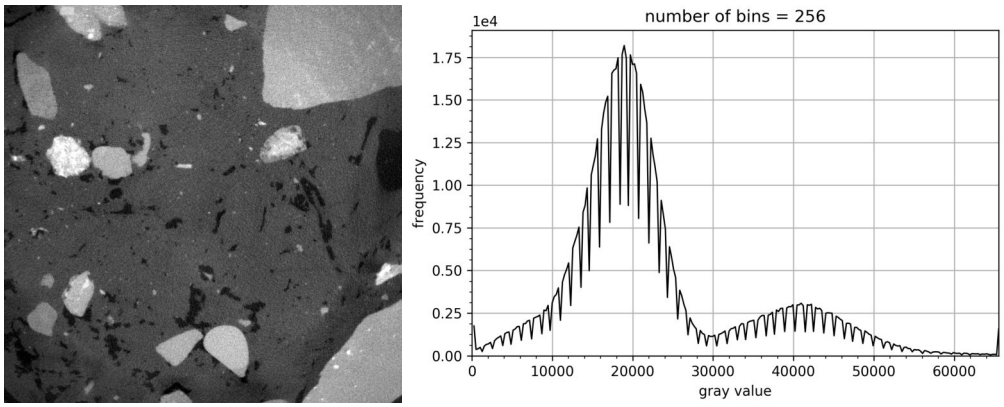

(e) (f)

Figure 3.15: Image type and screen display

(a) Image displayed with original look up. (b) Histogram of image 3.15(a).
(c) Image 3.15(a) with better original look up table. (d) Histogram of image 3.15(c) (the same of image 3.15(a)). Changes in the look up table do not alter data.
(e) Image 3.15(a) after normalization to whole 16-bit range. (f) Histogram of image 3.15(e). After normalization histograms are less smooth. All bins are not attributed smoothly.

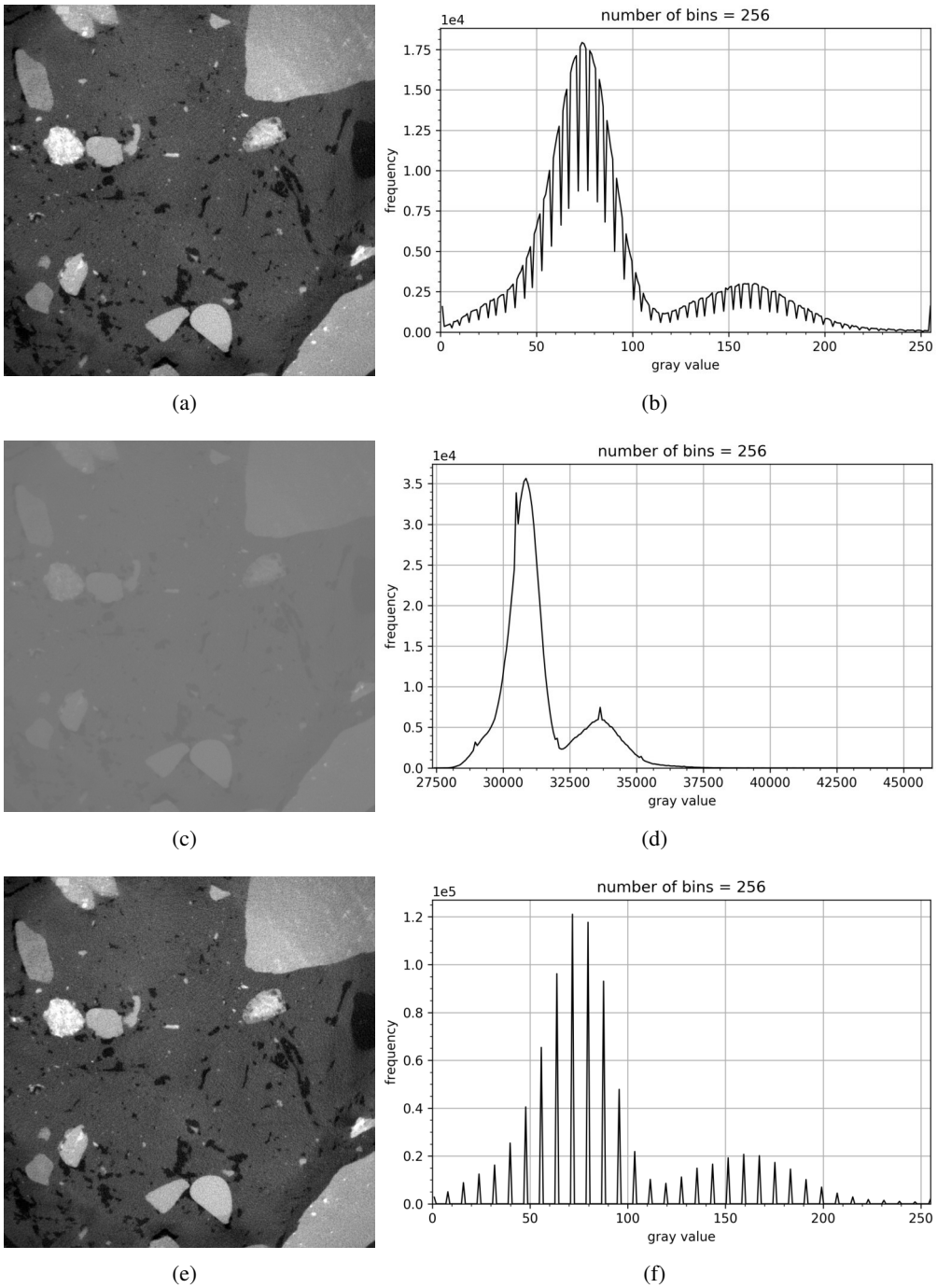

(a) (b)

(c) (d)

(e) (f)

Figure 3.16: Image type and screen display (continuation)

(a) Image 3.16(a) transformed to 8-bit format using a look up table. (b) Histogram of image 3.16(a), similar to histogram in figure 3.16(b). This is the optimum change of format.

(c) Image 3.15(a) displayed with a non optimum look up table (16-bit). (d) Histogram of image 3.16(c).

(e) Image 3.16(c) transformed to 8-bit then normalized to the whole 8-bit range. (f) Histogram of image 3.16(e), although the image contrast seems not to have changed, data quality decreased considerably: a lot of bins are no longer attributed compared to histogram in Figure 3.16(b).

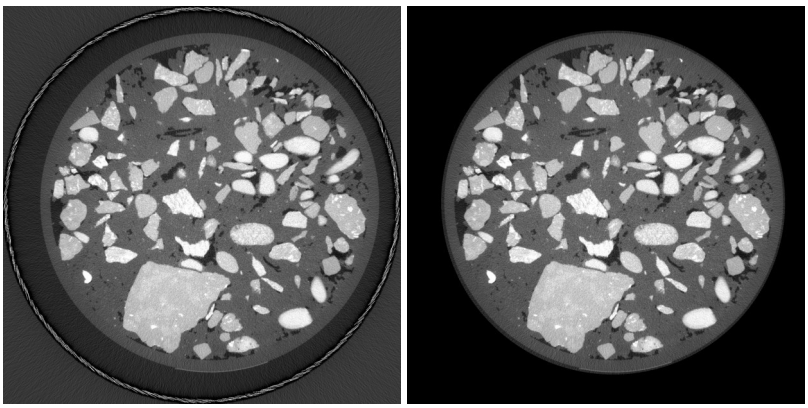

(a) Ring artifact. (b) Ring removal.

Figure 3.17: Ring artifact and easy removal.

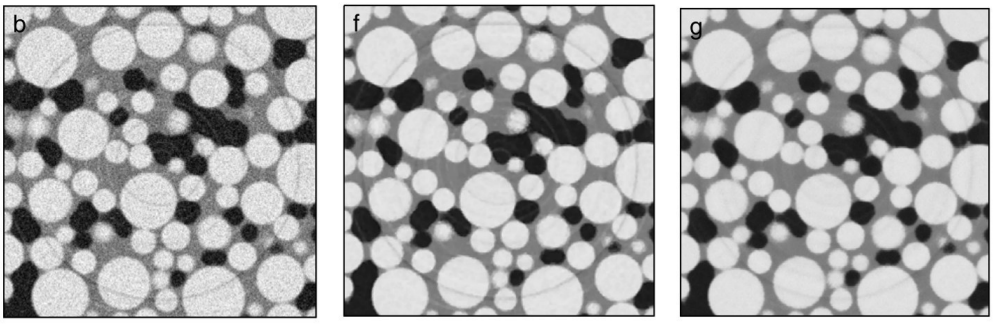

(a) Raw image (I) exhibiting ring artifacts (curve b below)

(b) Image I after using a total variation filter and unsharped mask filter (curve f below)

(c) Image I after using a non local filter and unsharped mask (curve g below)

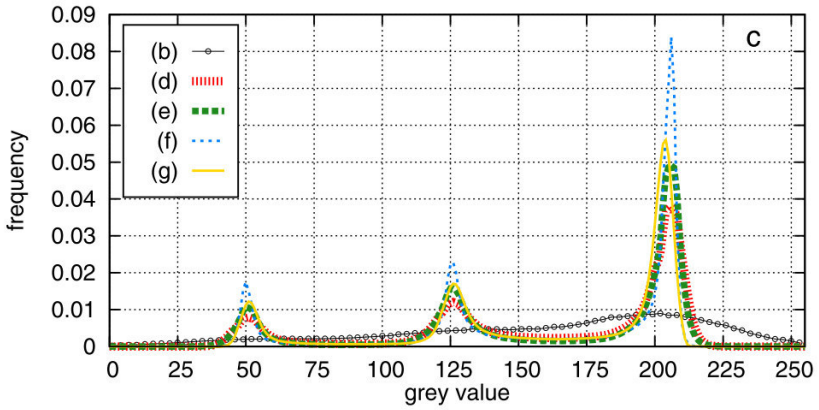

(d) gray value distibution after diferent treatments

Local features matter! Note that ring removal was better for image (g) even if the peaks in gray value distribution for image (f) are higher and better separated

Figure 3.18: Ring artifacts removal by filters.
From [110].

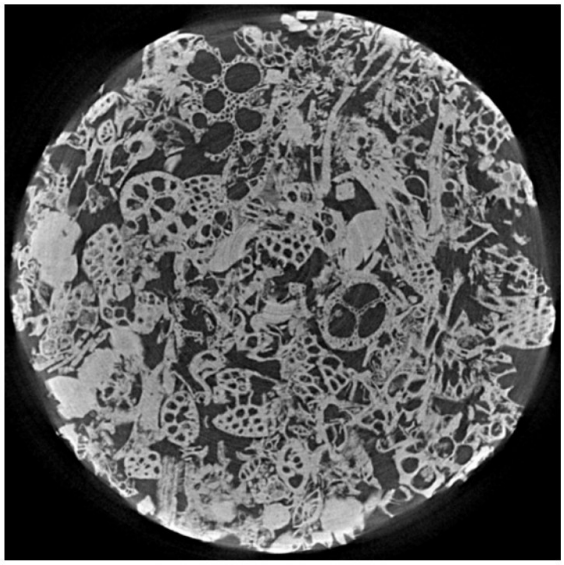

Figure 3.19: Hardening at the border of a limestone sample.
From [125].

Salt and pepper noise

This is a common type of noise present in raw images which is represented by high or low scattered gray values (Figure 3.22). Salt and pepper noise is one of the causes accounting for peaks superposition (Figure 3.23).

3.5.3 Partial Volume Effect (PVE)

Partial Volume Effect (PVE) appears when two phases are taken into account into a single voxel, thus making harder its attribution to a unique phase. Figure 3.24(a) presents a focus on this common feature of tomographic images. Far from interfaces, gravel and FM phases are represented by two separated peaks in the green histogram in Figure 3.24. Near the interface, where the PVE is most likely to appear, the gray value distribution (red histogram) shows no clear distinction of two different classes of voxels. PVE represents a challenge for segmentation. In this work, PVE voxels are identified using an edge filter and attributed (during the segmentation) by region growing.

3.6 Pretreatment

Pretreatment steps help removing noise and artifacts from raw images, the two most important steps are contrast enhancement and filtering. Other steps such as concatenation (for horizontal acquisition) and straightening (redressing cylinder tilting) are also commented. At the end of this section a task workflow resumes all operations to be done.

3.6.1 Contrast enhancement and normalization

Contrast enhancement is done by histogram stretching (normalization) or equalization (See Fiji user guide). Here the focus is put only on normalization. A function in python scipy library (contrast stretching) as well as in Fiji (slice or stack normalization) performs this computation.

Normalization is an arithmetic operation that allows increasing the gray value range of the image. Contrast enhancement by normalization differs from using a look up table as it actually modifies the gray values.

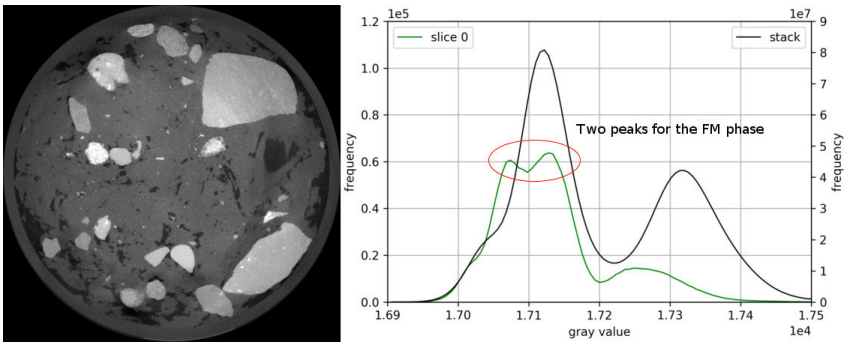

(a)

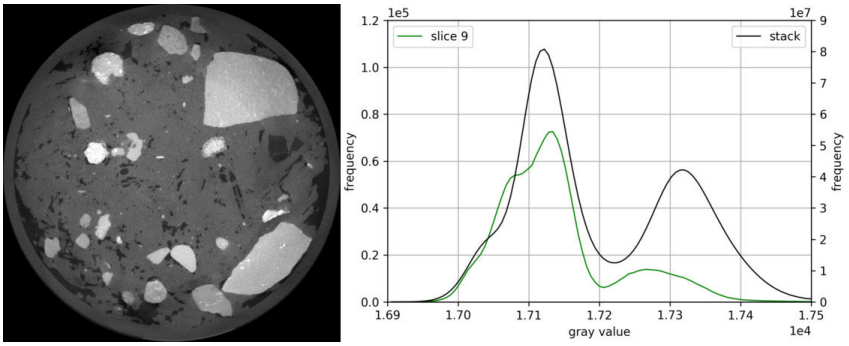

(b)

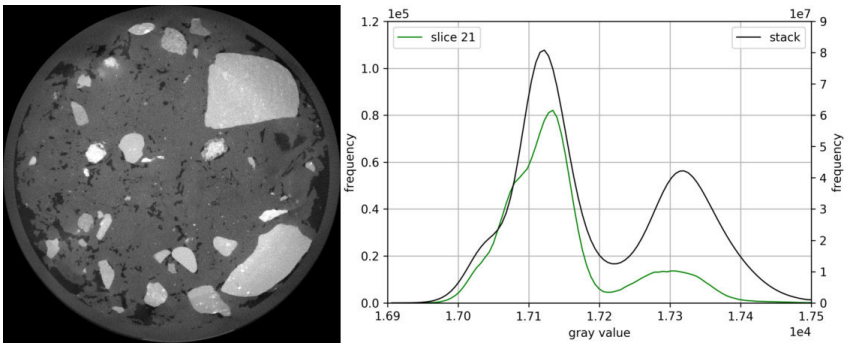

(c)

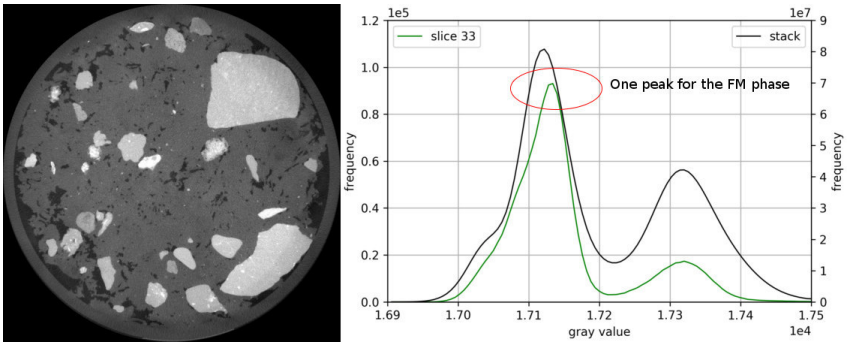

(d)

Figure 3.20: Propagating glow.
The propagating glow is readily perceived on the big gravel at the top right part if the image.

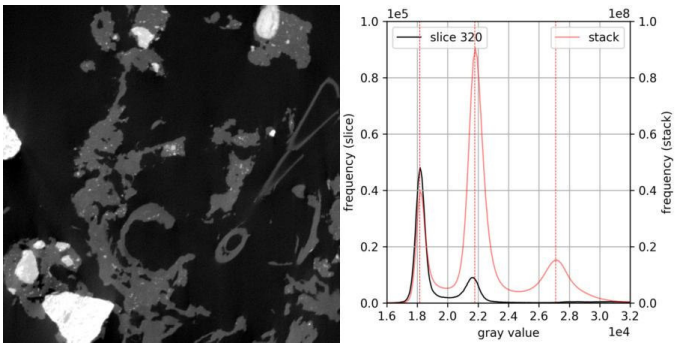

(a)

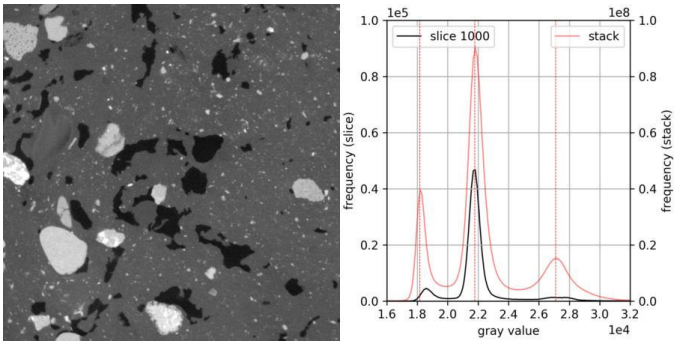

(b)

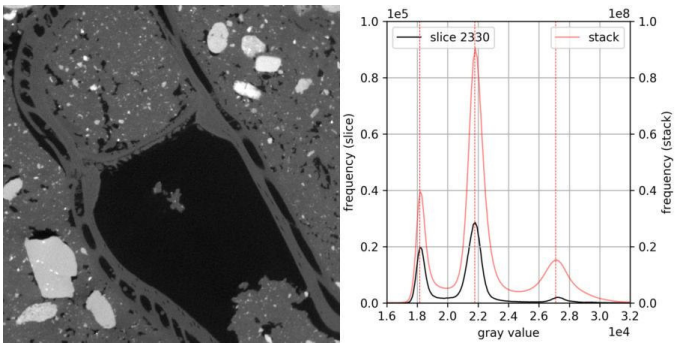

(c)

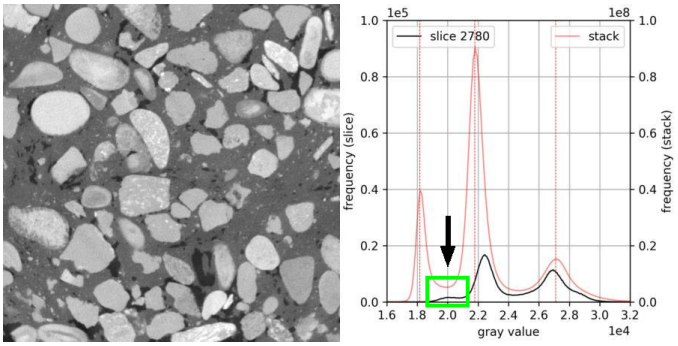

(d)

Figure 3.21: Gray intensity changes over depth.
Note that the mean value for each peak differs from that of the stack (all the slices) histogram. In figure (d), due to variations in depth, the void peak is aligned with the superposed zone of the FM and void peaks for the stack histogram.

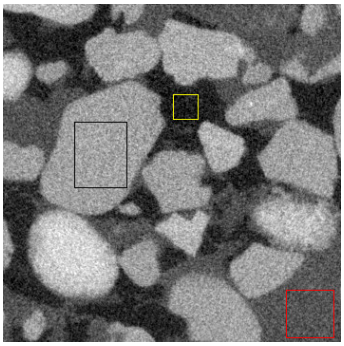

Figure 3.22: Salt and pepper noise.
Three Regions of Interest (ROI), one for each phase (gravel, FM, and voids), are selected to draw the histogram in Figure 3.23.

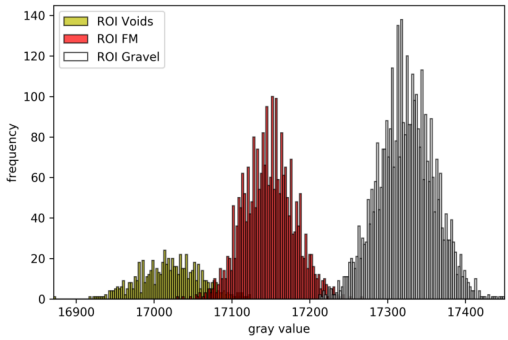

Figure 3.23: Histogram for different ROI in Figure 3.22.

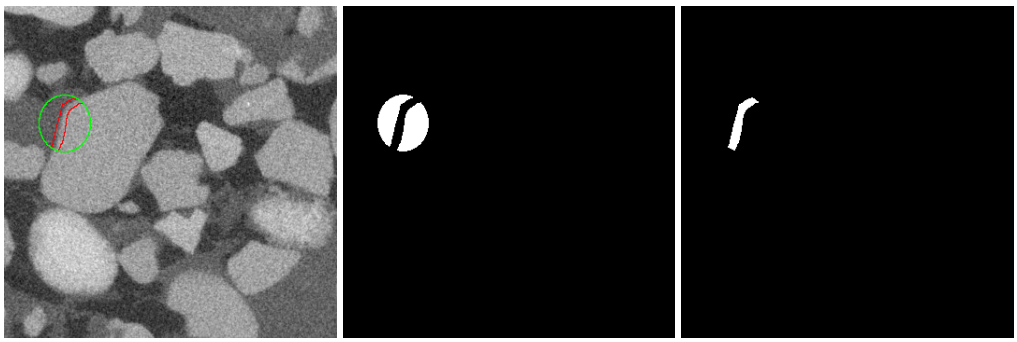

(a) Focusing on PVE voxels. (b) Mask for voxels far from an edge. (c) Mask for voxels near an edge.

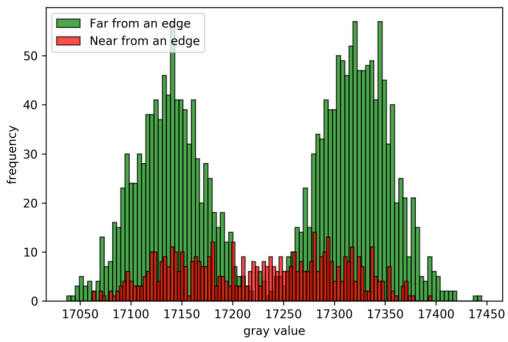

(d) Histogram of ROI in figure (a).

Figure 3.24: Partial Volume Effect (PVE).

Equation 3.2 resumes a general case of normalization with or without saturation. -I- represents the voxel gray value or intensity at the voxel x, y, z. The type of the image does not change during normalization. The maximum output value c, is set to the highest value of the image type (255 in 8-bit for instance) and the minimum output value is 0 (in unsigned format). -b- and -a- are the pivot values for the stretching. They can be set to the minimum and maximum gray values of the input image. In that case (non saturating normalization) the fraction multiplying c is comprised between [0,1] and the output maximum and minimum values are equal to the maximum and minimum of the image type. On the other hand, -b- can be a lower value than the maximum of the input image and- a- a larger value than the minimum. In that case (saturating normalization) output values out of the image type range are automatically set to its upper and lower limits (0 or 255 in 8-bit). -a- and -b- are often computed as a q-th percentile so the number of saturated pixels is constant.

Stretching by normalization does not mean that every value will be attributed, but that they will be evenly distributed. This is depicted in Figure 3.15(f).

$$I_{output}(x,y,z) = \frac{(I_{input}(x,y,z) - a)}{b-a} * c \tag{3.2}$$

-b- and -a- can be computed for each slice (slice normalization) or for the whole stack (stack normalization). As a general recommendation, it is preferable to perform stack operations in samples from VFTW. Figure 3.25 shows two different successful normalizations on a single slice with different saturation levels. [6].

Figure 3.26 illustrates how uneven contrast may be obtained in a non optimal normalization slice per slice [7]. Note that for slices with very low presence of gravels (Figure 3.26(b)), saturation may induce to a excessive displacement of the peaks to the right. If present, this issue can be overcome during the segmentation by performing a seeding in different sections.

3.6.2 Concatenation

If a sample was scanned in several parts (horizontal acquisition) it must be concatenated. It is recommended that the raw scans contain an overlay region. The choice of the concatenation slice is done depending on the quality of the slices, privileging the removal of propagating glow. If a stack normalization is successful, i.e. the contrast is even for all depths of the sample, concatenation can be done automatically by a choosing a slice in the upper scan and finding the most similar slice in the lower scan by image subtraction. Figure 3.27 illustrates the concatenation procedure. Hopefully, the overlay regions (100 - 200 voxels) are larger than regions with propagating glow. Nevertheless, until solutions for both propagating glow and optimal normalization are found, it is better to chose these slices manually.

3.6.3 Straightening

Micro-scale tomographies detect clearly if a cylindrical sample is tilted (this is pretty clear in video 1). Straightening is not mandatory, but for a more accurate sample comparison (e.g. when the same sample is scanned at different times, cf. chapter 6) the image can be treated by two consecutive rotations around the y and x axis. When rotating an image in Fiji, the process may be accompanied by pixel averaging or not. Sometimes, the rotation produces a special artifact, like it is presented from slices 1140 to 1170 in video 7. The cause of this noise could not be well

[6] It is probable that the user will have to choose a slice operation because of bugs in Fiji's stack normalization routine or because of high RAM consumption in used in the scipy function for contrast stretching.

[7] A video of normalization slice per slice can be seen at `https://www.youtube.com/watch?v=U3R-1FjD2AU&feature=youtu.be`

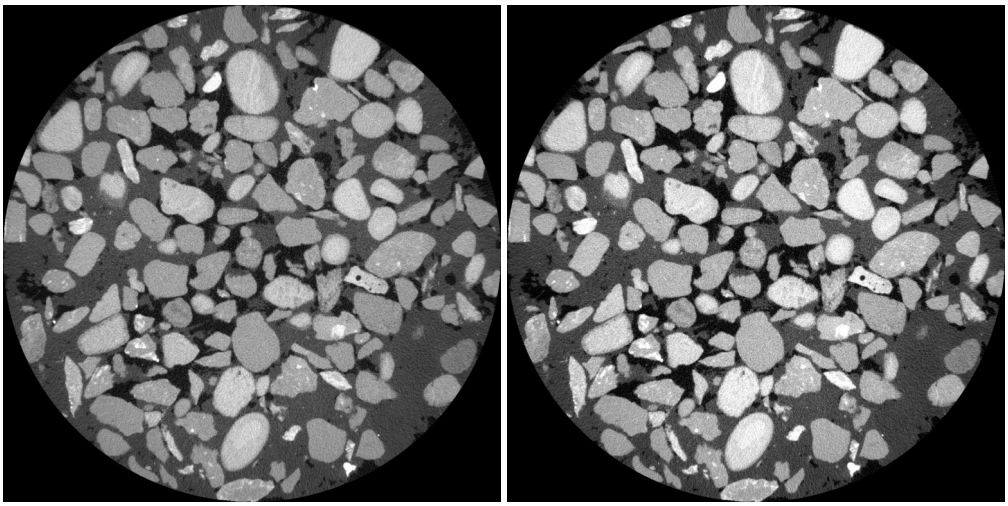

(a) (b)

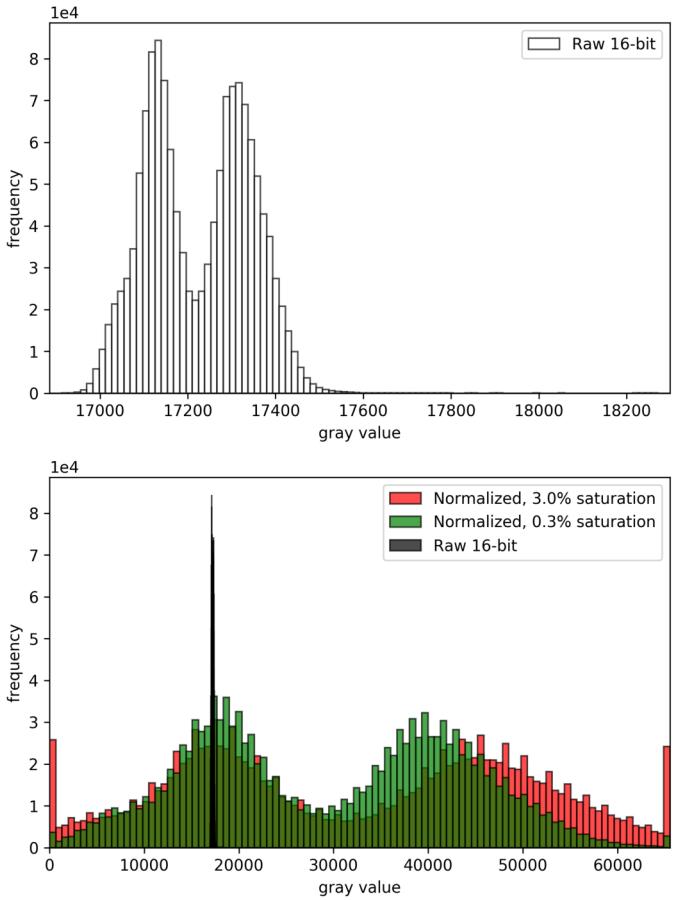

(c) Histogram

Figure 3.25: Successful normalizations for two different saturation levels.
(a) 0.3% of voxels were saturated in this image (16-bit). (b) 3.0 % of voxels were saturated in this image (16-bit).

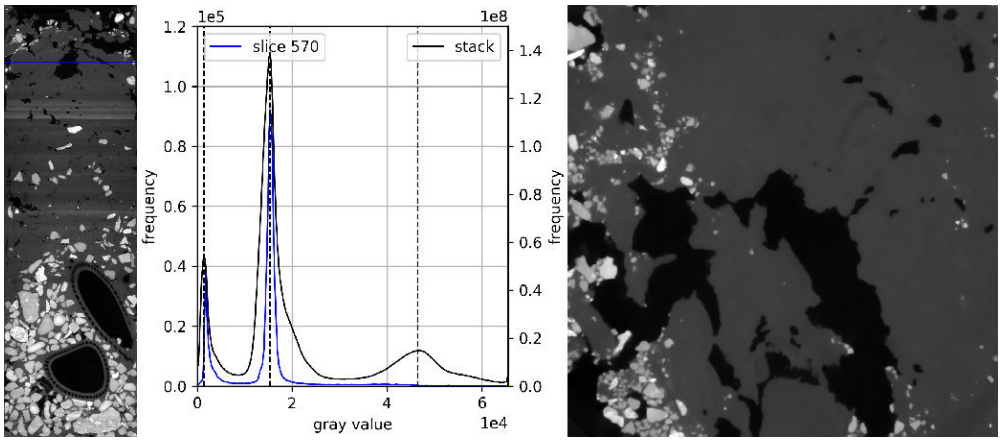

(a)

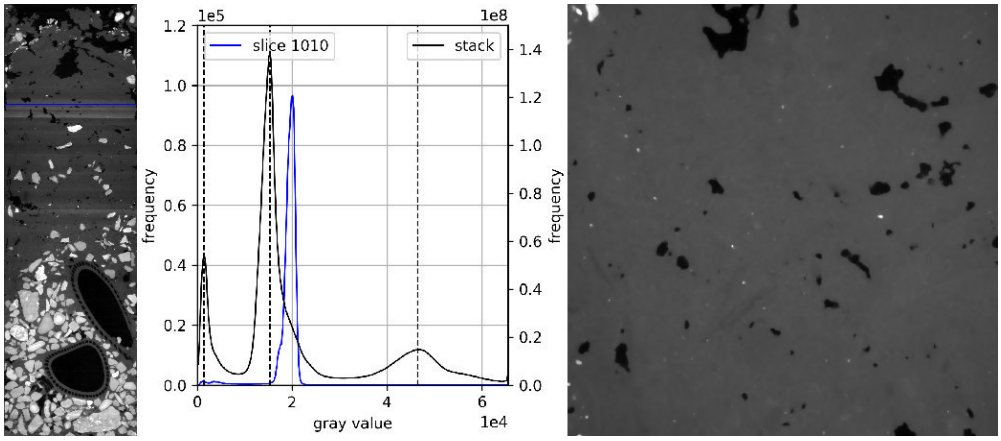

(b)

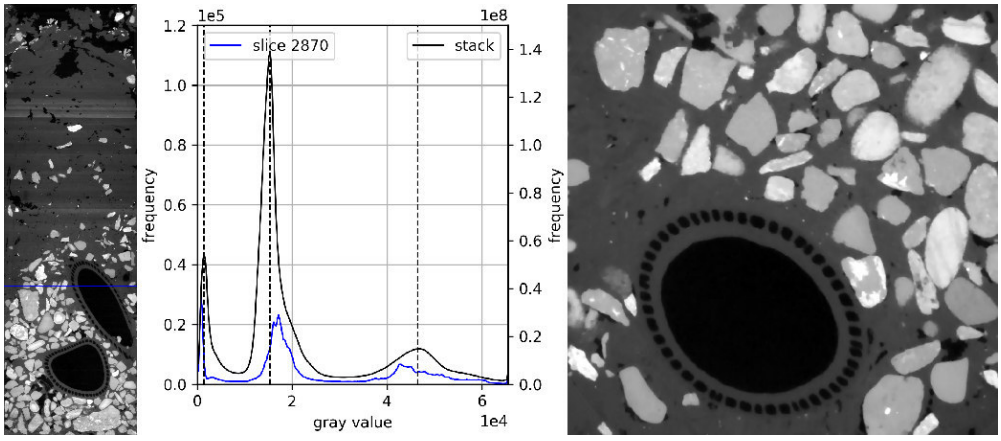

(c)

Figure 3.26: Not optimal slice per slice normalization.

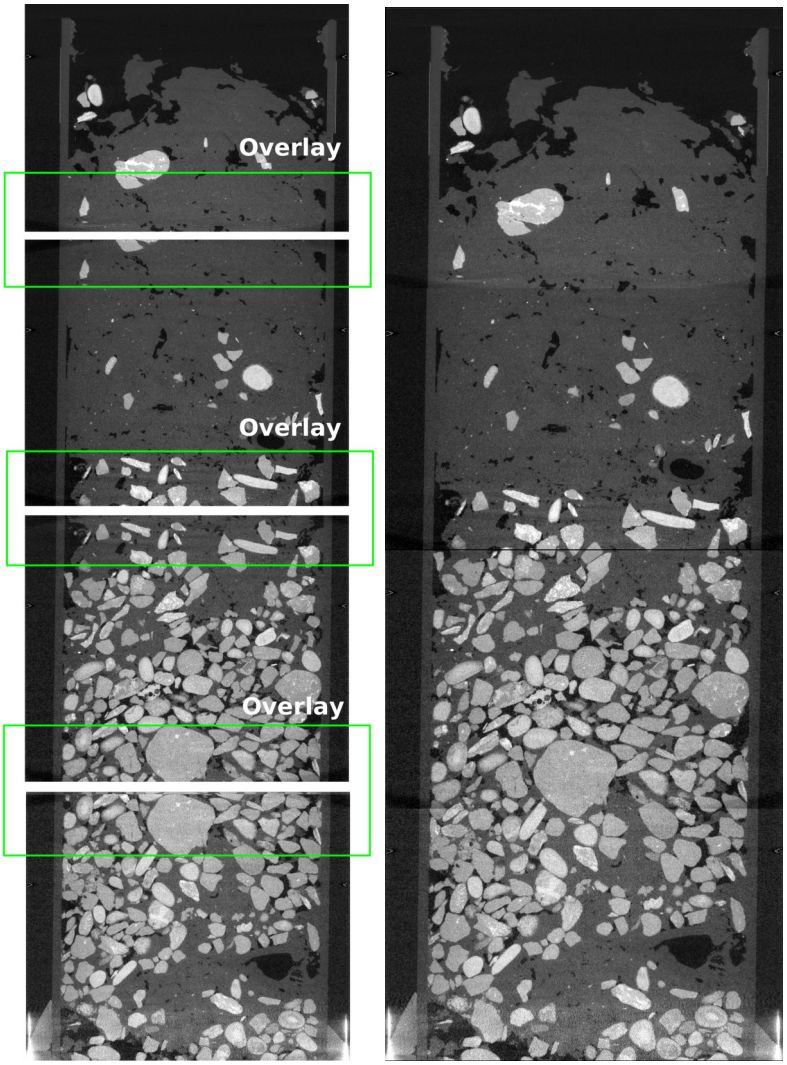

(a) Before concatenation (b) After concatenation

Figure 3.27: Concatenation: elimination of overlay in multiple horizontal acquisitions.

$$\left(\begin{bmatrix} a & b & c \\ d & e & f \\ g & h & i \end{bmatrix} * \begin{bmatrix} 1 & 2 & 3 \\ 4 & 5 & 6 \\ 7 & 8 & 9 \end{bmatrix}\right)[2,2] = (i \cdot 1) + (h \cdot 2) + (g \cdot 3) + (f \cdot 4) + (e \cdot 5) + (d \cdot 6) + (c \cdot 7) + (b \cdot 8) + (a \cdot 9)$$

Figure 3.28: Filtering by kernel convolution.
Convolution of two three-by-three matrices. The left one is a kernel, and the right one an image piece. Convolution is the process of flipping both the rows and columns of the kernel, multiplying locally similar entries and summing. The element at coordinates [2, 2] (the central element) of the resulting image is a weighted combination of all the entries of the image matrix, with weights given by the kernel. Other entries are similarly weighted.

identified in this thesis but it is thought to be the combination of averaging when a propagating glow or when uneven normalization are present in concatenated images.

3.6.4 Filtering and kernels

Filtering is the name for number of mathematical operations aiming to enhance the perception of a specific feature of an image, like the area or the perimeter of an object. Different filters "let pass" different relevant information depending on their purpose. Many types of filters were conceived to remove noise or artifacts.

Filtering is often accomplished by doing a convolution between a kernel and the image. A kernel is a (convolution) matrix storing different coefficients. Different coefficients arrangements produce different results. Convolution is the process of adding each element of the image to its local neighbors, weighted by the kernel (Figure 3.28).

Blurring filters

Some filters are intended to homogenize gray values. This is visually perceived as a blurring operation. They enhance the perception of homogeneous areas while decreasing the perception of edges or perimeters. They are suitable to deal with salt and pepper noise and, depending on the type of filter, they may be more or less suitable for PVE voxel identification.

Commonly used filters are median and mean filters. Median filters cannot be computed using kernels. Many other blurring filters work based on convolution. A mean filter can be programmed as image convolution by a m^2 kernel where coefficients are equal to $1/m^2$(in 2D). For mean and median filters, each voxel gray value is computed for a cubic region with specific "diameter" (square length) centered at the voxel.

Anisotropic Diffusion (AD) is another common kernel based filter used in image processing. It applies a smoothing in edge tangential directions based on a gradient computation but not in the normal direction, thus preserving the location of interfaces [7].

Figure 3.29(f) compares the performance of different filters. All the filters succeed in reducing salt and pepper noise and also enhance significantly the gray value distribution.

- The voids peak on the left is more clearly noticed compared to the normalized image before filtering (orange square). Also, the presence of two different classes of gravel voxels is revealed (light gray and near white gravels), which may be explained by an heterogeneous mineral distribution.
- The median filter does not smooth gray values (previous normalization is accompanied by non smooth bin attribution). The mean and AD filters deal well with this issue.
- AD decreases peak superposition slightly better but it consumes far more computational resources (time and RAM memory)
- Filter combination (Mean + AD filter) does not perform better than separate filters regarding peak superposition, nevertheless it offers a possibility to enhancing edge detection (cf. section 3.6.4).[8]

[8]Combining filters was not studied in image treatment in chapters 4, 5 and 6 and should be considered for further

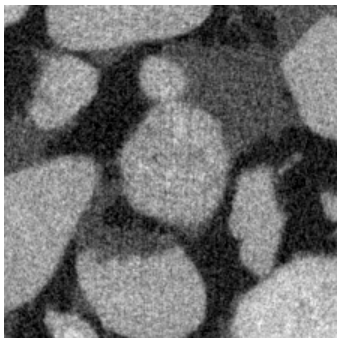

(a) Normalized image (I) (before filtering)

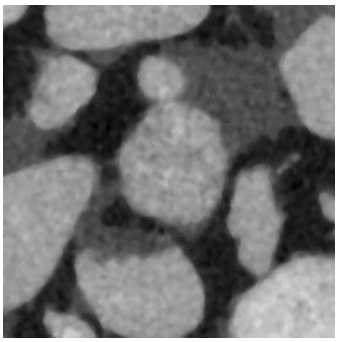

(b) (I) after median filter

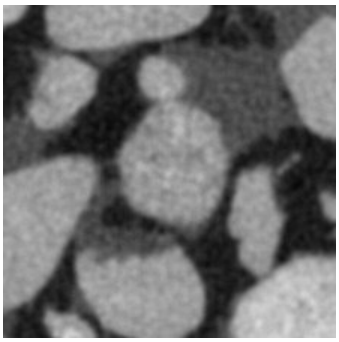

(c) (I) after mean filter

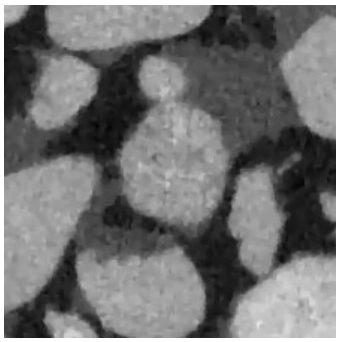

(d) (I) after anisotropic diffusion (AD) filter

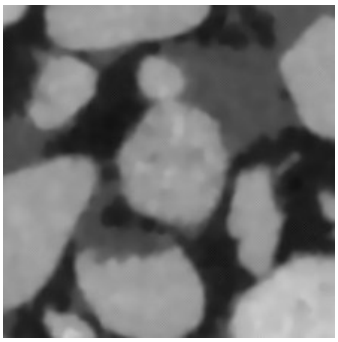

(e) (I) mean and AD filters

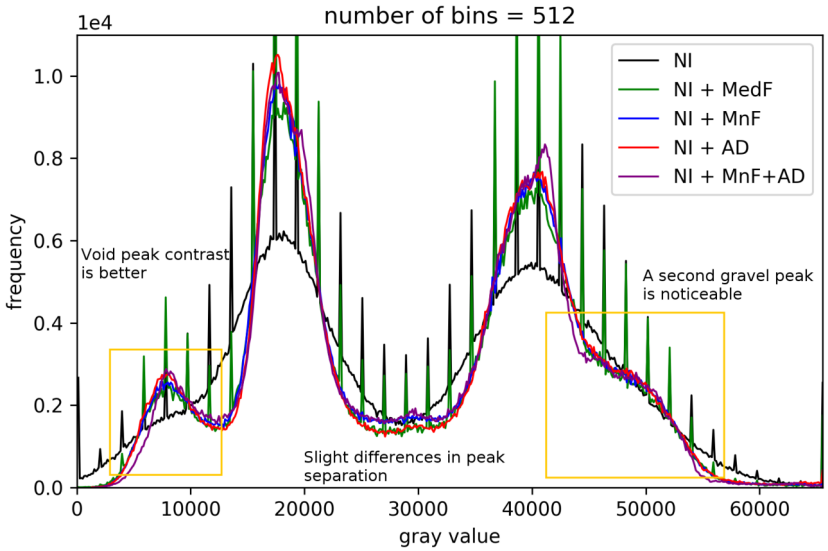

(f) Comparison

Figure 3.29: Blurring filters comparison.
NI: Normalized image, MedF: Median filter, MnF: Mean filter, AD: Anisotropic Diffusion

$$\begin{matrix} 1 & 2 & 1 \\ 0 & 0 & 0 \\ -1 & -2 & -1 \end{matrix} \qquad \begin{matrix} 1 & 0 & -1 \\ 2 & 0 & -2 \\ 1 & 0 & -1 \end{matrix}$$

Figure 3.30: Kernels for Fiji 2D find edges plug-in.

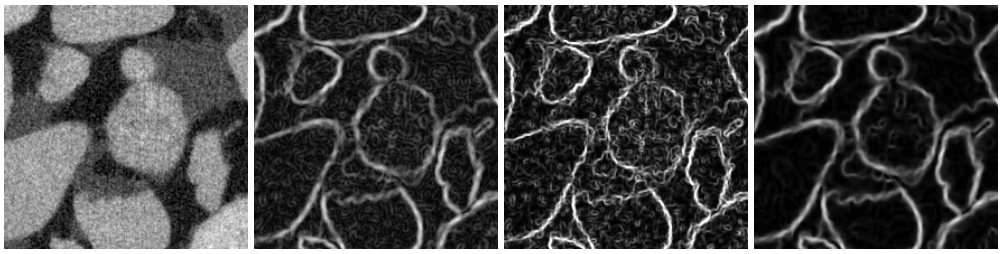

(a) (b) (c) (d)

Figure 3.31: Find edges plug-in applied to different images
(a): Before filtering
(b): (a) after mean filter + find edges
(c): (a) after AD filter + find edges
(d): (a) after mean and AD filters + find edges

Edge detection filters

Edge detectors are used to highlight sharp changes of gray values like at interfaces between different phases (voids, FM or gravel). This type of filter is used in this thesis to detect PVE voxels, which is an important prerequisite for segmentation (Section 3.7).

The Fiji 2D find edges plug-in uses two 3×3 convolution kernels (Figure 3.30) to generate vertical and horizontal derivatives. The filtered image is produced by combining the two derivatives using the square root of the sum of the squares. The intensity values are higher (whiter) at the edges/interfaces, where the derivatives are higher. [9]

Figure 3.31 shows the result of the edge filter applied to the same image blurred by three different methods. In all cases, the main edges are readily observed. In particular, when AD is applied, non relevant edges (like local features within gravel) have better contrast.

The gray level distribution of edge images differs significantly depending on the filter that has been used (Figure 3.32). The combination of the mean and AD filters is particularly interesting. A higher number of voxels with low intensity values (peak on the left) is a sign of better smoothing as long as high gray value voxels (tail on the right) are preserved. This is explained by the fact that the number of voxels located at the interfaces is much lower than those far from interfaces.

In this thesis, the determination of PVE voxels is done by thresholding: voxels whose gray value is superior to a threshold (75th percentile for instance) are defined as PVE. The lower the threshold is, the more PVE voxels are attributed (Figure 3.33).

When PVE voxels are not taken into account, the histogram of gray levels of filtered image changes significantly. Figure 3.34 shows that most of the PVE voxels correspond to the zone where peaks for each phase are mixing. Similar results are obtained for all filter types, nevertheless, the location of the PVE voxels changes significantly with the type of filter.

(i) Figures 3.35 focus on voxels between the 90-th and 100-th percentiles of gray values in the edge image. The best edge identification is done by the AD filtered image (only), where

development of the pretreatment methodology.

[9] If edge detection is performed in Fiji, the image type must be changed to 32-bit (float type) prior to edge filtering to avoid loss of relevant information.

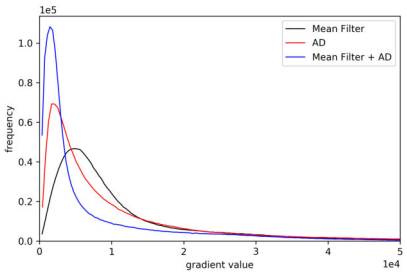

Figure 3.32: Gray value distribution of edge filtered images in Figure 3.31.

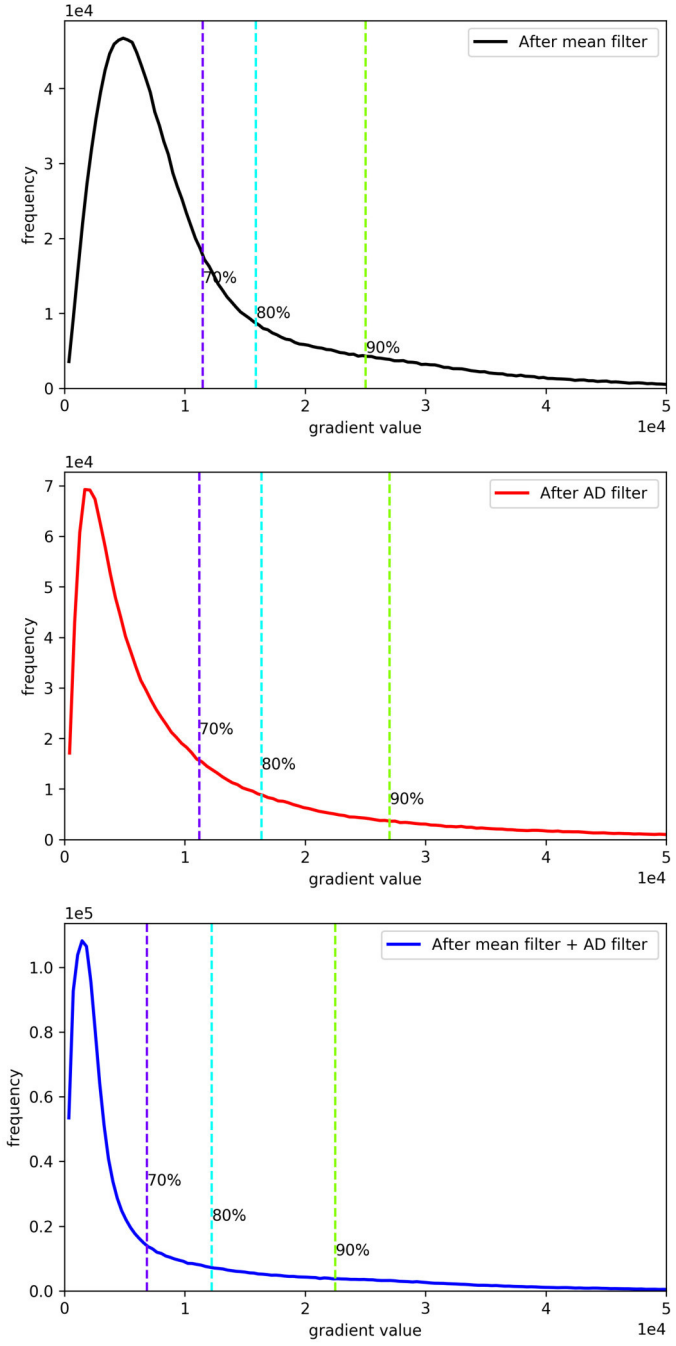

Figure 3.33: Percentiles for different edge filtered images in Figure 3.31.

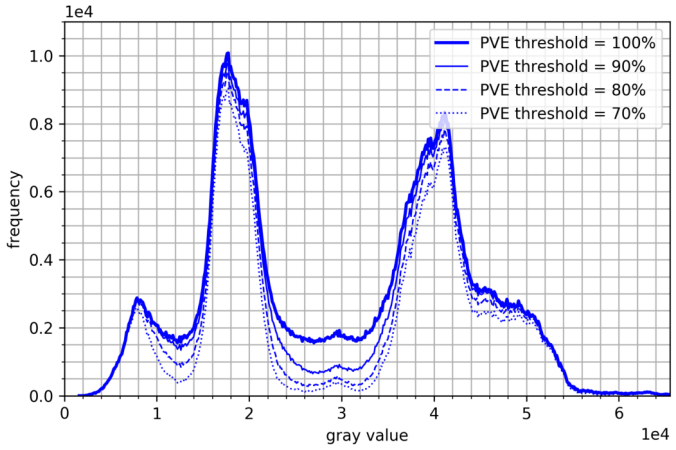

Figure 3.34: Influence of PVE removal on gray value distribution
Filter = mean + AD.

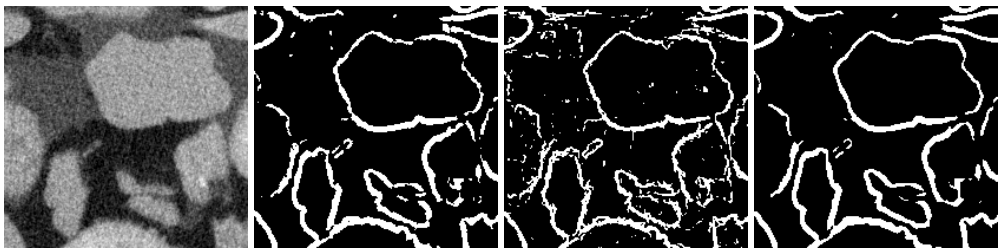

(a) (b) (c) (d)

Figure 3.35: PVE voxel removal : focus on 90-th to 100-th percentile range
(a): Before filtering
(b): (a) after mean filter + find edges
(c): (a) after AD filter + find edges
(d): (a) after mean and AD filters + find edges

not only the gravel-FM interface is well noticed but a larger part of the voids-FM interface is identified.

(ii) If the focus is put on voxels between the 80-th and 90-th percentiles (Figure 3.36), the borders identified in the AD filtered image are not relevant and the mean filter seems then more suitable to track voxels at the voids-FM interface. This could be explained by the fact that salt and pepper noise induces the detection of irrelevant borders when using AD filtering. The combination of mean and AD filters is useful to eliminate salt and pepper noise and enhance edge perception respectively (See foot note 8).

(iii) Figure 3.37 shows that the gravel-FM or gravel-voids interface corresponds to higher edge intensities (90-th to 100-th percentile) and the FM-voids interface corresponds to a little lower edge intensity (80-th to 90-th percentile). This range of voxels corresponds also to neighbors of interface voxels previously identified within the 90-th to 100-th percentiles.

3.6.5 Pretreatment task workflow

Treating several images require to set a common pretreatment workflow. The workflow presented in Figure 3.38 is recommended. Except for the concatenation step (necessary only in horizontal acquisitions) and the type of filter, it was the methodology used to pretreat 3D images in the studies presented in chapters 4, 5 and 6. As a general rule, all codes should be performed using 3D implementations. This is the case of blurring filters and edge finding filters. Currently, there

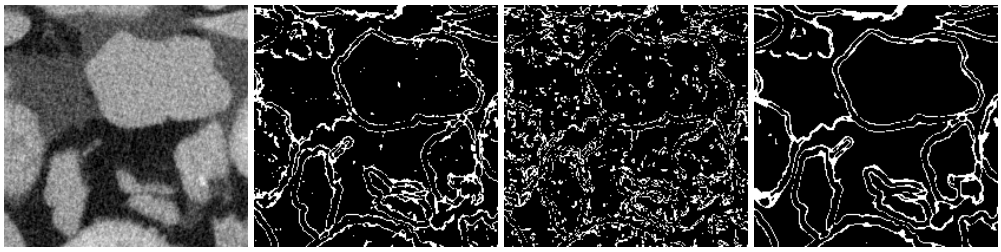

(a) (b) (c) (d)

Figure 3.36: PVE voxel removal : focus on 80th to 90th percentile range
(a): Before filtering
(b): (a) after mean filter + find edges
(c): (a) after AD filter + find edges
(d): (a) after mean and AD filters + find edges

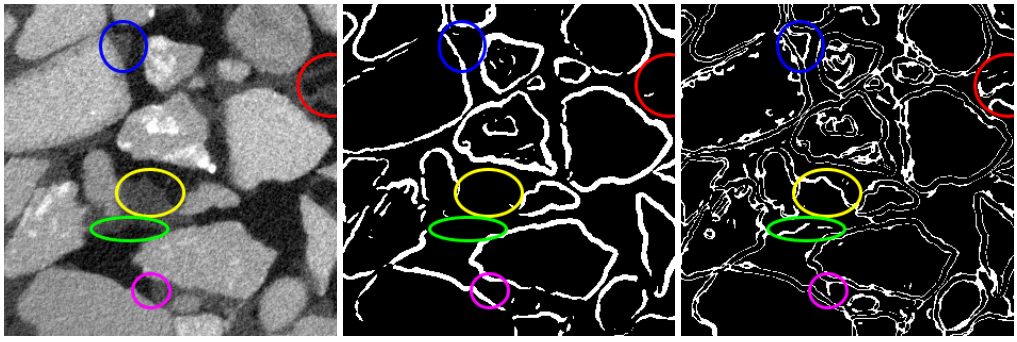

(a) (b) (c)

Figure 3.37: PVE voxels, thresholds and interfaces.
Filter: mean + AD. (a) Filtered image (b) PVE 90 to 100 th percentiles. (c) PVE 80 to 90 th percentiles. Colored circles highlight interfaces detected at lower PVE thresholds.

	Parameter
Normalization	0. Use Fiji or python.1: Stack normalization.2: Saturation = 0.3%.
Straightening	0. Use the Fiji macro available in the code repository. 1: Two pivot coordinates. 2: Avoid averaging when rotating.
Mean Filter	0: Use 3D filter in Fiji. 1: Radius = 2 voxel.
Anisotropic Diffusion	0: Use 2D filter in Fiji. 1: See Figure 3.39 for parameters.
Find edges	0: Use 3D plug in Fiji. 1: Use default alpha Canny = 0.5. 2: If 2D plug in used, kernels are presented in Figure 3.30.

Table 3.2: Parameters for the pretreatment workflow in Figure 3.38.

	Input parameter
Gaussian fitting	User initial values. One value representing the mean value of each peak representing a single phase (gravel, OM or voids).
PVE removal	Default = 75% (when 2D find edges plug in is used).
Seed tolerance	75%

Table 3.3: Input parameters of the segmentation function.
You may download this function as a .py (python) file from the repository referenced at the beginning of this chapter.

is no 3D implementation of the anisotropic diffusion filter in ImageJ.

Table 3.2 resumes inputs and parameters used in each pretreatment step. Saturation was set to no more than 0.3% of the voxels during the normalization steps. In chapter 4 the median filter (3D) radius was 2 voxels. The mean filter, recommended in Figure 3.38 could also be performed with a 2 voxel radius. In chapters 5 and 6the default ImageJ parameters were used to perform the anisotropic diffusion filter (2D). These are presented in Figure 3.39. The find edge plug-in used in chapters 4, 5 and 6 is a 2D implementation, but a 3D implementation is now available in Fiji and should be considered.

3.7 Segmentation

3.7.1 Introduction

There exist several segmentation methods based on two different approaches. In global approaches, operations are based only on gray value distributions, i.e. they are histogram based. In local approaches, the specific location of a voxel in the image and the gray value of its neighbors are also taken into account [110].

The segmentation method presented in this section is based on the work of Hashemi et al. and was used to treat scans from VFTW [35]. It is a multiphase segmentation method based on consecutive dilations (region growing) of a seed image. The seed image is built by partial thresholding (a global approach) while the rest of the segmentation is done by region growing (a local approach). Figure 3.40 resumes the segmentation methodology applied in this work and Table 3.3 resumes the recommended input parameters.

3.7.2 Gaussian fitting

The gray value distribution of X-ray scans resembles to a sum of three individual Gaussian bells/peaks. The number of Gaussian peaks equals the number of phases to be segmented. The number of phases is thus defined a-priori by the user. In this work, a maximum of three peaks was assumed even if sometimes two different peaks seem to represent the gravel phase.

In a general case, the histogram of the whole stack is fitted. If there exists important

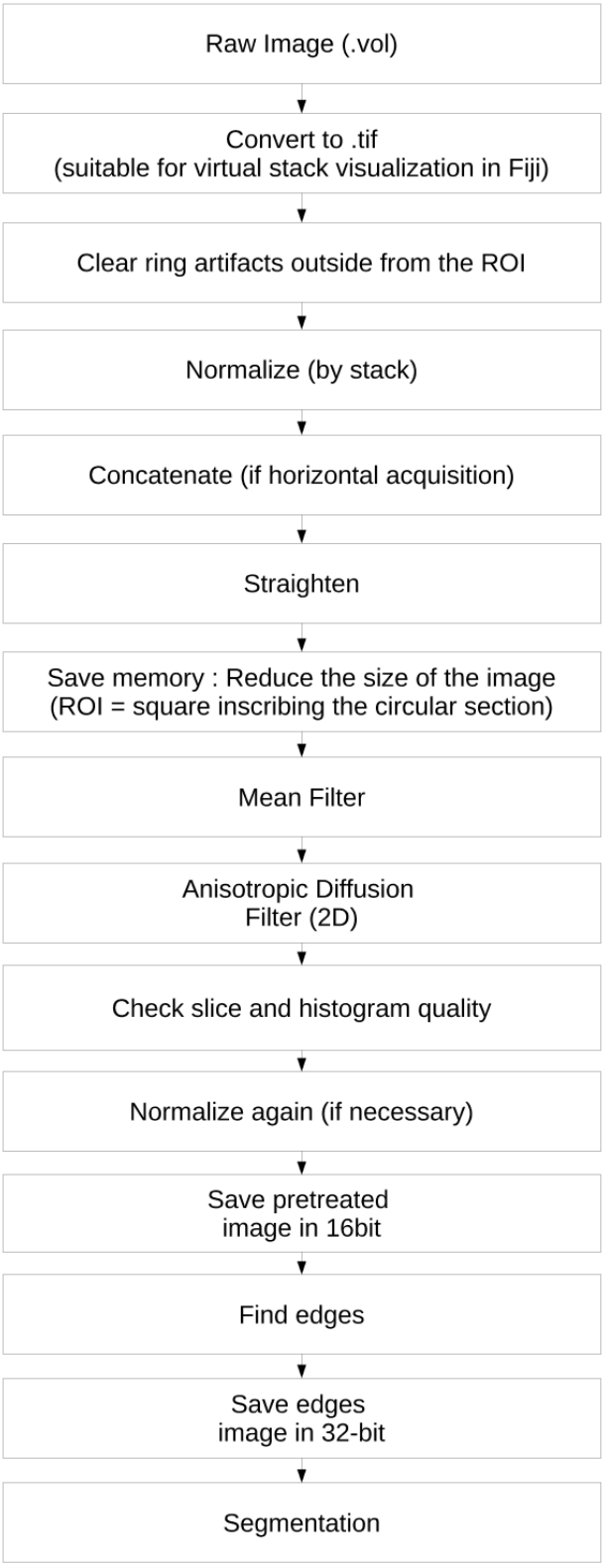

Figure 3.38: Pretreatment workflow

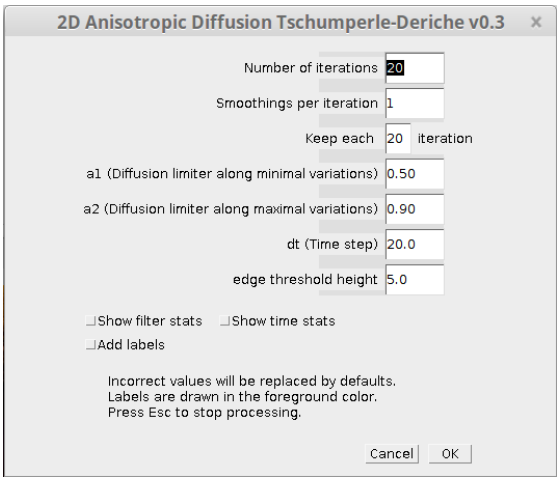

Figure 3.39: Parameters of the anisotropic diffusion filter (default ImageJ parameters).

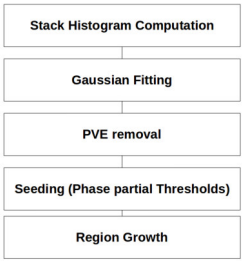

Figure 3.40: Segmentation workflow.

heterogeneities in gray value distribution over depth, the stack can be divided in subsections and the fitting and seeding can be performed separately for each of them.

In this work, the fitting was performed for the filtered image after PVE voxel removal. This helped to focus on better separated peaks.

PVE threshold and Gaussian fitting

The PVE threshold is set by default by computing the the 75-th percentile, but it can be modified depending on the quality of the image.

Figure 3.41 regroups four different cases of PVE removal and Gaussian fitting depending on (i) the presence of a significant volume of gravel phase and (ii) two different choices of PVE thresholds: 80-th and 100-th percentiles, the latter meaning there is no PVE voxel removal. These are illustrative examples that correspond to small volumes of only 10 slices in depth.

PVE voxel removal is not necessary for the sample in Figure 3.41(a). The quality of the raw image and the performance of the pretreatments were good enough produce an image with very distinct peaks for each phase.

PVE voxel removal separates well the gravel and FM peaks in Figure 3.41(g). Although a 4-peak fitting would be better, the 3-peak approximation succeeds to separate both gravel phase peaks from the FM phase peak.

3.7.3 Partial thresholding and seeding

Creating a seed consists in defining an initial set of voxels from which each phase will grow by successive dilations. This procedure allows assign a phase to PVE voxels, and voxels corresponding to peaks where an important degree of mixing may still exist (see the mixing of peaks of Figure 3.41(g) for instance).

The more reliable is the seed, the better the segmentation is. If a region lacks of a seed pixel, it will be (wrongly) attributed to any other phase during the growing phase. By analogy, a seed voxel placed in a wrong location will also induce an error in the segmentation.

Percentile thresholds

In this work, seed thresholding is based on percentile computation and is here referred as the "tolerance" (the limit of the colored regions below the curves in Figure 3.42). Nevertheless, there exist other methods for thresholding: maximum variance, maximum entropy, minimums... which were not considered in this methodology [110].

The 75-th percentile is a good choice to start but, depending on the quality of the image, another choice could be made. In any case, the seed quality must be checked both in the histograms and locally in the image.

Different seeds are presented in Figure 3.42 for the same images presented in Figure 3.41. For sample B, all thresholds are computed with a tolerance of 75%. In this sample, removing PVE voxels decreases the number of seed voxels but helps to avoid attributing a wrong phase for voxels at the gravel surface (this feature is more clear once the growing has been computed. See Figure 3.46). For sample A, the flat region between the void and FM peaks corresponds to the smallest voids in the sample. Thresholding this area by computing the percentile of a Gaussian function represents technical limitation of the methodology as it would require very high (and non realistic) tolerance to be set. Thus a manual (arbitrary) threshold shows to be more convenient to compute the seed of sample A (Figure 3.42(f)).

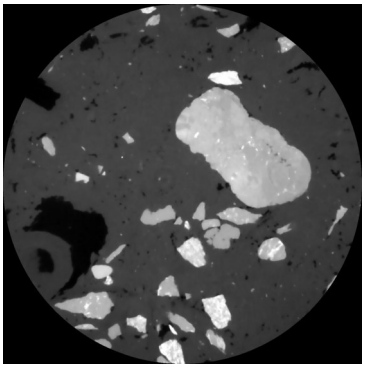

(a) (A) 3 peak image. Relative low void and gravel volume.

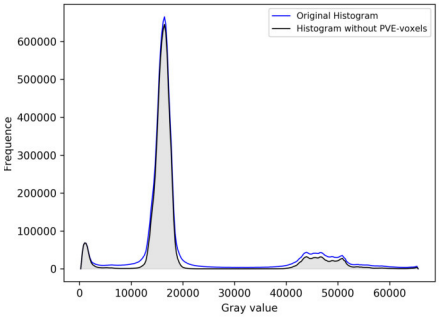

(b) Histogram of (A). PVE removal: 80-th percentile.

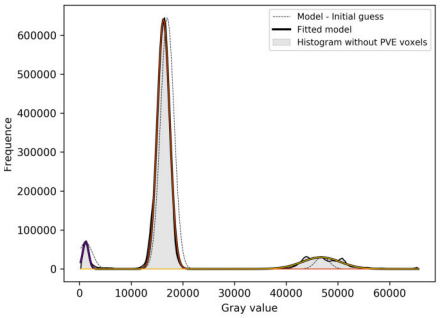

(c) Fitting of (A), PVE removal: 80-th percentile.

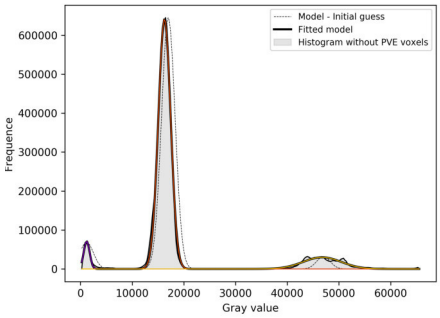

(d) Fitting of (A), no PVE removal.

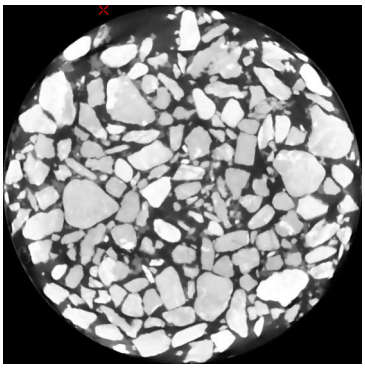

(e) (B) 4 peak image. Relative high gravel volume.

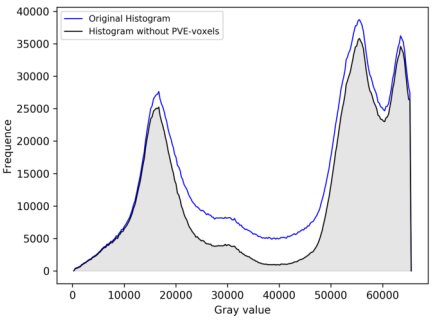

(f) Histogram of (B). PVE removal: 80-th percentile.

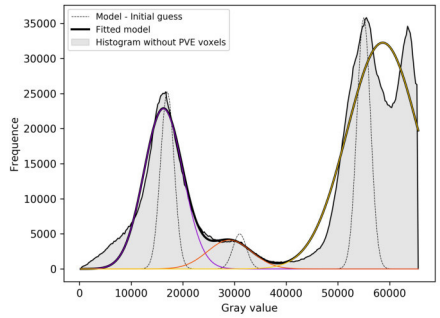

(g) Fitting of (B), PVE removal: 80-th percentile.

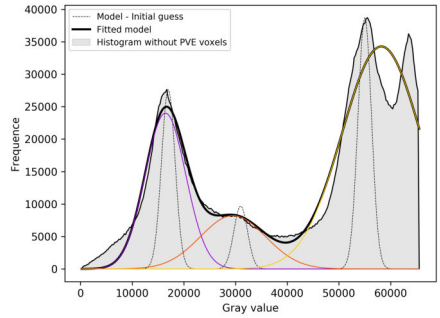

(h) Fitting of (B), no PVE removal.

Figure 3.41: PVE threshold and Gaussian fitting.
Purple peaks: void phase Gaussian bell.
Orange peaks: FM phase Gaussian bell.
Yellow peaks: gravel phase Gaussian bell.

NOTE: The choice of a threshold for both PVE voxels and for seeding represents a methodology issue. On the one hand, a robust segmentation methodology should lack of user defined parameters and is characterized by generating good quality results independently of variation of input parameters. Setting a unique set of input parameters (e.g. PVE and tolerance thresholds) allows large sets of images to be compared. On the other hand, choosing wisely a set of input parameters may result in a very accurate morphological description and may be necessary if the quality of the raw images vary significantly.

3.7.4 Region growing

Region growing procedure is performed to attribute the remaining voxels: (1) the PVE voxels and (2) those between tolerance thresholds for each phase (the non colored regions in images from Figure 3.42). It consist in performing consecutive 1-voxel dilations simultaneously for all phases on seed voxels. The Venn diagram in Figure 3.43 summarizes the growing algorithm and Figure 3.44 shows different steps of growing[10].

The set M_i in Figure 3.43 represents the set of voxels added to each phase after one dilation. An additional step is done which consists in removing some voxels from the M_i set if growing occurs in a non logical sense. This is process is detailed in Figure 3.45 and applies only for 3 or more multiphase segmentation: after the growth of the void phase, new void voxels are accepted only if they belong to the "uncertain" void-FM region and rejected if they belong to the "uncertain" gravel-FM region. The same behavior is valid for gravel voxels. FM voxels can grow into the two different uncertain regions.

Region growing stops when interface are found (white pixels in Figure 3.44). The growing loop always converges. During the first dilation steps growing is faster (Figure 3.44(h)).

3.7.5 Interface pixels attribution

According to the methodology presented in [35], interface pixels are attributed by probability. For each interface voxel, the number of neighboring voxels belonging to the other phases is counted. Finally the phase with the highest counter is attributed to that interface voxel.
[11]

Figure 3.46 presents fully segmented images after interface attribution.

3.7.6 Segmentation accuracy

The assessment of the segmentation accuracy is important to assure reliable results during the post-treatment, nevertheless it is a less common subject of study. Three methods can be mentioned: visual assessment, comparison with macroscopic measurements, and segmentation of theoretical images. The latter has been assessed in the original work of Hashemi et al. [35]. They claim the methodology yields good results for theoretical images such as glass beads packings.

Visual assessment consist in comparing individually raw and segmented images and is still the most effective way to assess the quality of images. For different applications there exist benchmark images, i.e. reference images that serve as a point of comparison. An interesting methodology is to create a manual benchmark segmentation. The procedure would consist in segmenting a whole slice manually and use this segmentation as a reference to assess if an optimization or even a new methodology yield better results.

[10] A video of the region growing algorithm can be found in `https://www.youtube.com/watch?v=aq97M-gfk_E&feature=youtu.be`

[11] To the date, the algorithm performing this operation is not time efficient and was replaced by an additional growing step for each phase (gravel, then FM, then void). The last phase to grow has thus a greater probability to fill interface voxels.

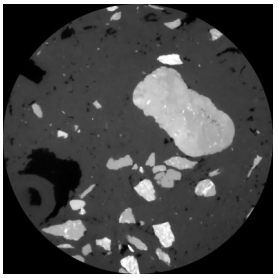

(a) (A)

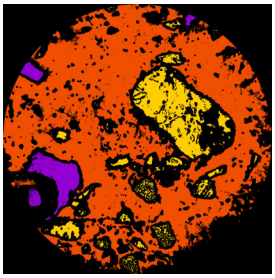

(b) (A) Seed, PVE: 80-th percentile.

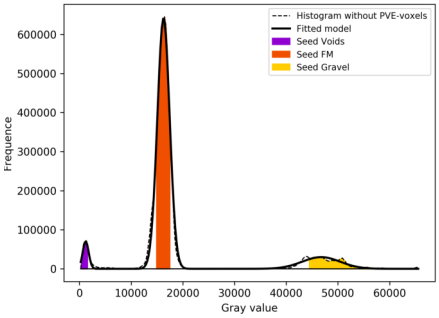

(c) Seed. Tolerance = 0.75.

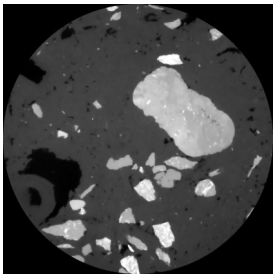

(d) (A)

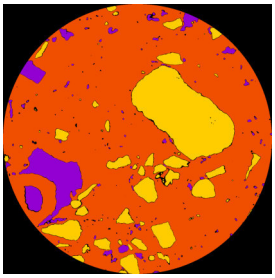

(e) (A) Seed, no PVE removal.

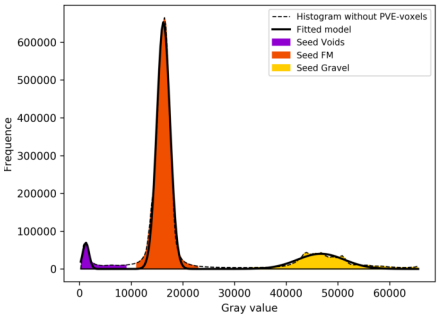

(f) Manual seed.

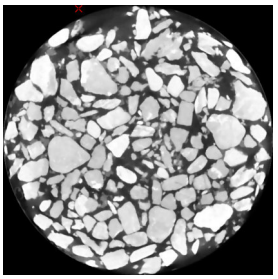

(g) (B)

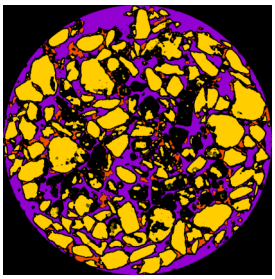

(h) (B) Seed, PVE: 80-th percentile.

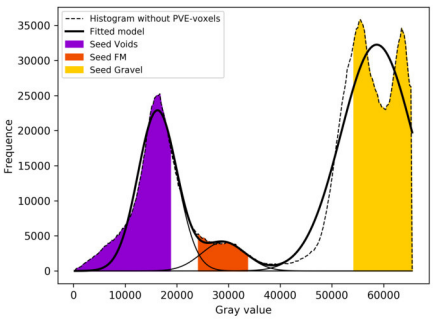

(i) Seed. Tolerance = 0.75.

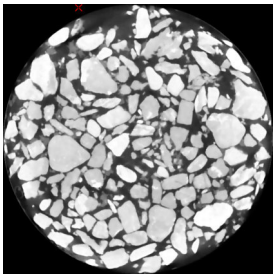

(j) (B)

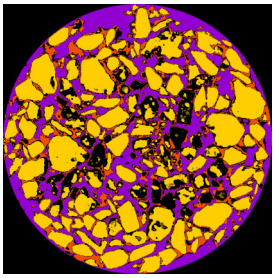

(k) (B) Seed, no PVE removal.

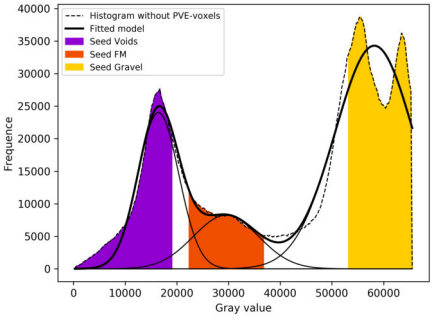

(l) Seed. Tolerance = 0.75.

Figure 3.42: Seeding.

For image d, an arbitrary threshold was done to create the seed image. For the rest of the images, a tolerance of 75% (75% of the peaks area) was selected to build the seed image. Note: These results can still be enhanced by combining filters during the pretreatment step.

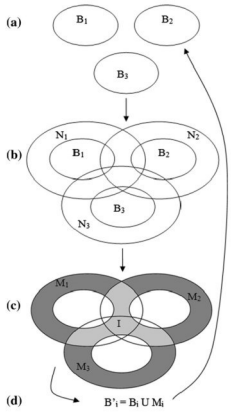

Figure 3.43: Algorithm for region growing.
Venn diagrams showing how growing is programmed:
(a) the initial set of phases B_i.
(b) the N_i set represents the neighbors of B_i.
(c) the neighbors added to the -i-th phase do not intersect neighbors of other phases (M_i), otherwise they are defined as interface voxels (I).
(d) the set M_i is added to B_i and the loop restarts.
From [35].

Macroscopic measurements consist in comparing measurements obtained by X-ray scanning with measurements of any property of the whole sample such as the total volume of a phase, the number of particles or objects, or even the number of contact points (e.g. when the sample consists of a uniformly bead packed bed column). Samples can be generated by X-ray imaging or can be build theoretically with subsequent artificial creation of noise.

3.8 Post-Treatment

3.8.1 Introduction

Advances in post-treatment algorithms are also numerous. They could be studied considering two characteristics: (1) their purpose or (2) their mathematical principle.

The main goal of this chapter is to guide readers interested in obtaining morphological descriptions of VFTW by imaging methods. For this reason a description of a post-processing algorithms is presented here based the algorithm purpose. The Fiji user guide details well several algorithms that can be used for image post-processing. The reader is also referenced to other compendiums on image treatment if he/she wants to explore more on the subject [[93, 111, 5]].

Purposes may be: determining the interface surface areas, counting objects, determining the size and shape factors of an object, computing the medial axis of a channel inside an object, etc.

Different purposes can be achieved using different mathematical principles. For example: the medial axis of an object (or a segmented phase) can be found (i) by performing consecutive erosions of the object until a 1-voxel wide line remains, i.e. by thinning algorithms [63]or (ii) by computing maximal distances to the borders of the object using derivatives [38].

Also, a single mathematical principle can be used to achieve different purposes. One of the most used mathematical principle in image processing is the “watershed”. Figure 3.47 illustrates the watershed principle. It consists in partitioning a domain into different sections (the basins) based on the gray values of the image: (i) if the image is a X-ray CT scan, watershed can be used to segment phases [125], (ii) if the image is an euclidean distance map of a phase (like in figure 3.47(b)), watershed can be used to “segment” the phase into different parts. Using watershed as a post-treatment step is useful to characterize pore size distribution and generate pore network

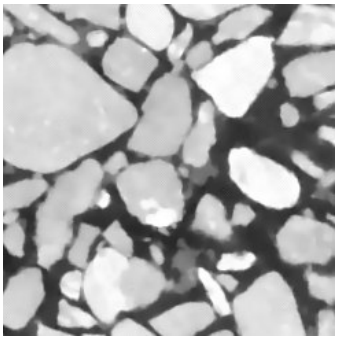

(a)

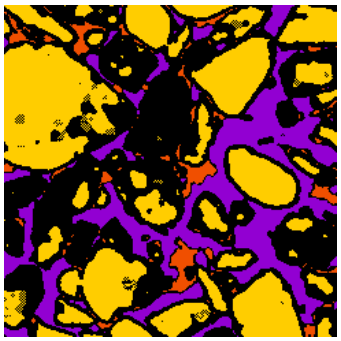

(b) Seed.

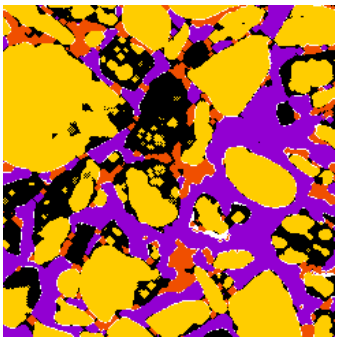

(c) Grow step 1.

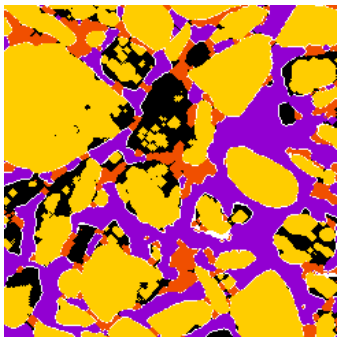

(d) Grow step 2.

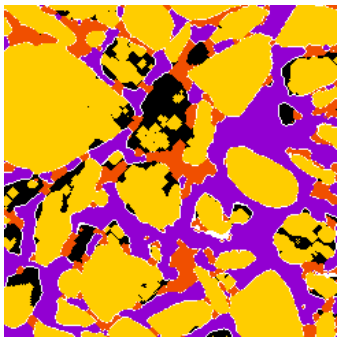

(e) Grow step 3.

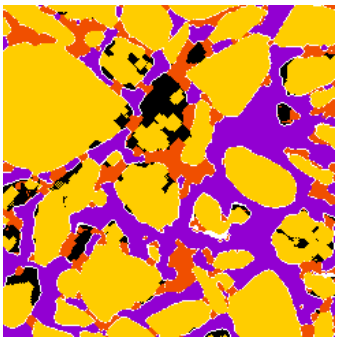

(f) Grow step 4.

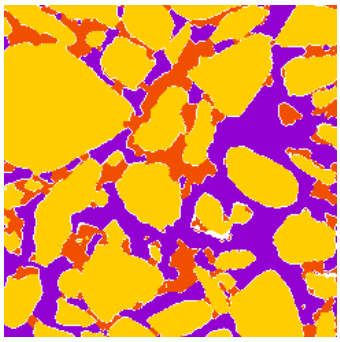

(g) Final Step.

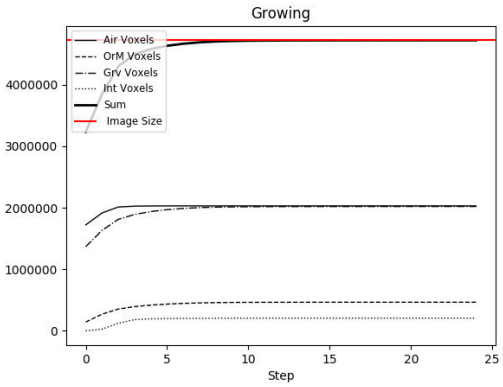

(h) Growing speed.

Figure 3.44: Growing steps.
White voxels represent interface voxels (both phases reached white voxels at the same time during growing).

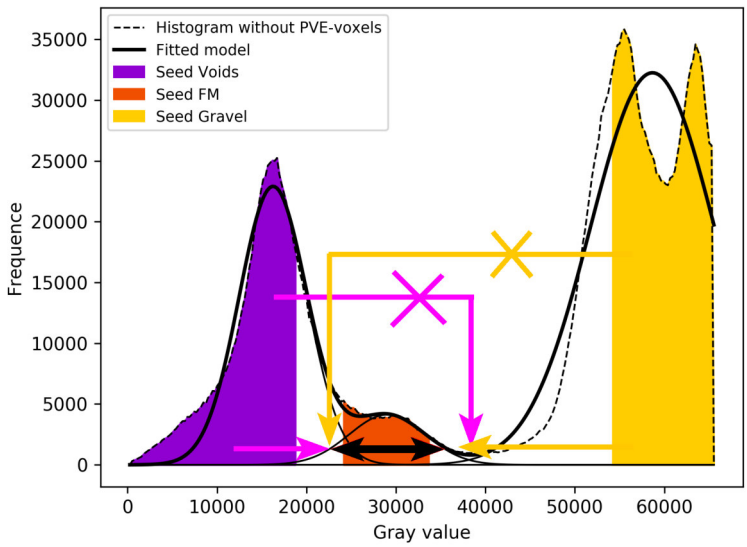

Figure 3.45: Growing sense.
The crosses stand for forbidden growing senses.

models [96]. This method was used by [50] to partition the voids phase in VFTW samples and generate pore size distributions.

3.8.2 Volume fraction profiles

VFTW are naturally heterogeneous in depth. The presence of two distinct layers (deposit and gravel) plus the preferential accumulation of solids at near the surface of the wetland constitute the major causes of this heterogeneity. Computing profiles of the volumetric fractions is a straightforward methodology to quantify this distribution.

The vertical profile in Figure 3.49(c) was obtained by computing fractions on every horizontal slice of a segmented image. Fractions are readily computed by counting the number of voxels of each phase, and dividing by the total number of voxels. Slice per slice profiles are noisy and should be smoothed using an averaging moving window (Figure 3.49(d)). The size of the moving window is arbitrary. A size of 2 mm (the smallest gravel size recommended in the state-of-the-art rules) was selected in this case.

3.8.3 Specific surfaces

Surfaces and the Specific Surface Area (SSA), especially that of the FM-void interface, are of particular interest regarding mas transfer. In this work, the SSA is obtained by dividing the void-FM surface area by the bulk volume (voids + gravel + FM). The void-FM surface area was computed using the Cauchy-Crofton cutting line method [55, 54, 107]. This method allows a numerically efficient estimate of interface areas with a better accuracy than the direct counting of interface voxels, which presents a "staircase effect". In addition, it has a much lower computational cost than methods based on surface meshes.

Equation 3.3 details the computation of the surface using the Cauchy-Crofton method. For each voxel belonging to the void phase and located at the interface with the FM phase, the method consists in counting the number of neighboring voxels in the FM phase with respect to 3 families of connection (Figure 3.50): family A: 1-connected (face-connection), family B: $\sqrt{2}$-connected (2D diagonal/edge connection) or family C: $\sqrt{3}$-connected (3D diagonal/corner

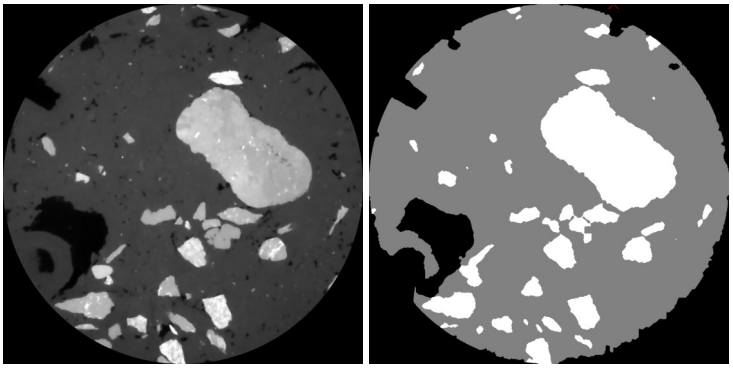

(a) (A)

(b) Segmentation of (A) PVE: 80-th percentile, tolerance 0.75.

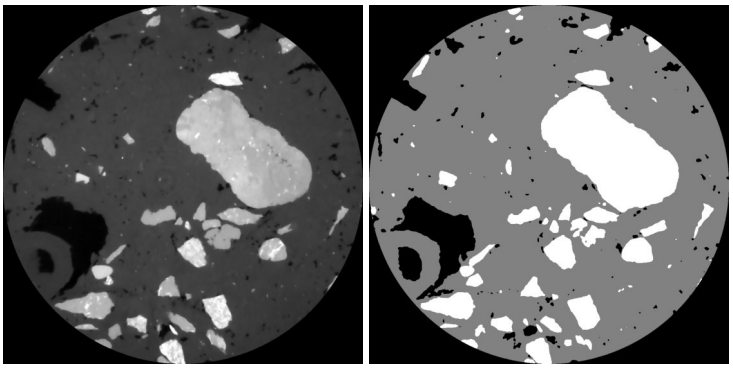

(c) (A)

(d) Segmentation of (A) No PVE removal, manual tolerances.

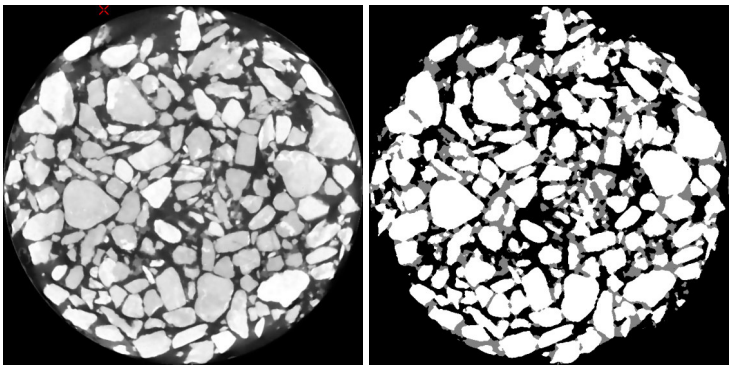

(e) (B)

(f) Segmentation of (B) PVE: 80-th percentile, tolerance 0.75.

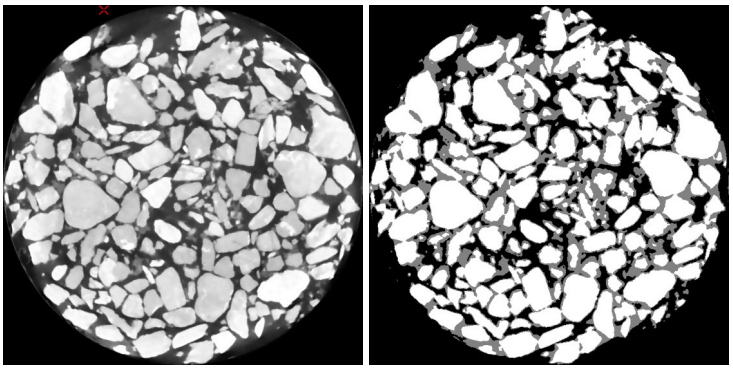

(g) (B)

(h) Segmentation of (B) No PVE removal, tolerance 0.75.

Figure 3.46: Segmentations.

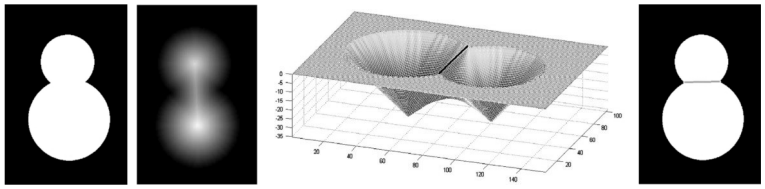

(a) Void phase (white). (b) Euclidean distance map of (A). (c) Catchment basins and watershed ridge line. (d) Voids partitioning.)

Figure 3.47: Watershed principle.
The euclidean distance map is an image that stores the lowest distance from a voxel inside an object to any voxel at its borders.

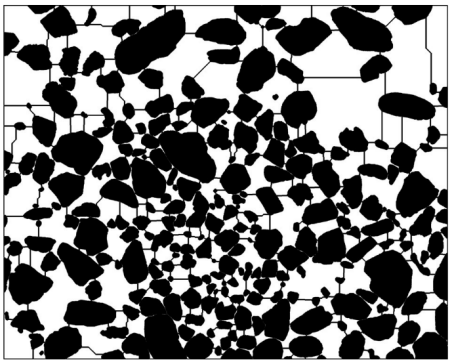

Figure 3.48: Void segmentation using watershed method in thin sections of VFTW.
From [50].

connection). The number of connections of each type is then multiplied by a characteristic coefficient (v_A, v_B or v_C) obtained from the Voronoi's tessellation of the unit sphere. r stands for the resolution (voxel side length). The sum of these contributions results in the value of the surface.

$$S = (A + B + C) \tag{3.3}$$

$A = 4\frac{v_A}{\lambda_A} \cdot a \quad B = 4\frac{v_B}{\lambda_B} \cdot b \quad C = 4\frac{v_C}{\lambda_C} \cdot c$
$\lambda_A = r^2 * \sqrt{1} \quad \lambda = r^2 * \sqrt{2} \quad \lambda_C = r^2 * \sqrt{3}$
$v_A = 0.0457 \quad v_A = 0.0369 \quad v_A = 0.0351$
$a = int$, count of A-type connections
$b = int$, count of B-type connections
$c = int$, count of C-type connections

The profile in Figure (3.51) is obtained by computing the SSA of subsections of 2 mm in height (57 voxels for a resolution of 0.035 mm/voxel) without overlay. The profiles are less smooth than volume fraction profiles but show clearly global trends. The reason not to perform computations with an overlay is that SSA profiles require more computational resources than volume fraction profiles.

3.8.4 Counting connected regions/objects

A region inside an object (or a phase) is a group of connected voxels of equal gray value. Depending on the type of connection (the same 3 groups presented in Figure 3.50) a set of

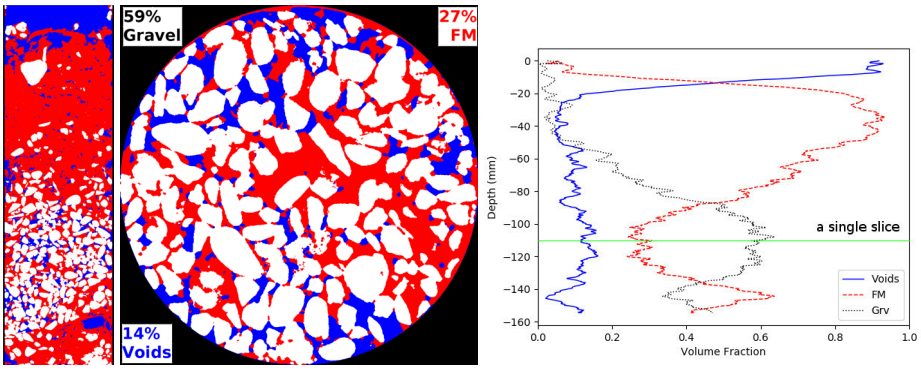

(a) Segmented image. Vertical slice.

(b) Horizontal slice.

(c) Raw volume fraction profile.

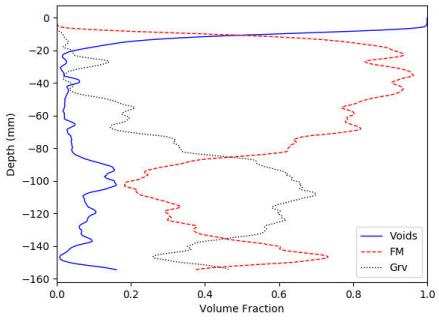

(d) Smoothed profile.

Figure 3.49: Volume fraction profiles.

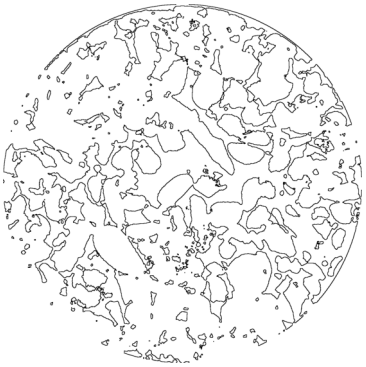

(a) Interface voxels.

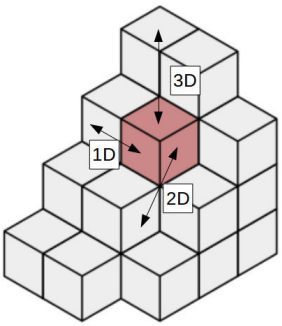

(b) Types of neighbors.

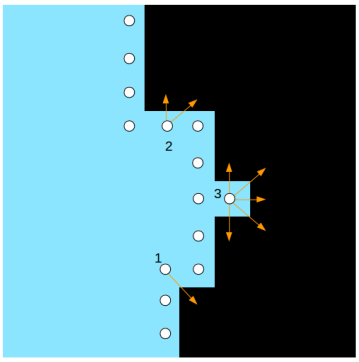

(c) Focus

Figure 3.50: Counting of neighbor voxels at the interface - (Cauchy-Crofton)
Voxel #1 has only one $\sqrt{2}$-connected neighbor. Voxel #2 has one 1-connected neighbor and one $\sqrt{2}$-connected neighbor. Voxel 3 has three 1-connected neighbors and two $\sqrt{2}$-connected neighbors.

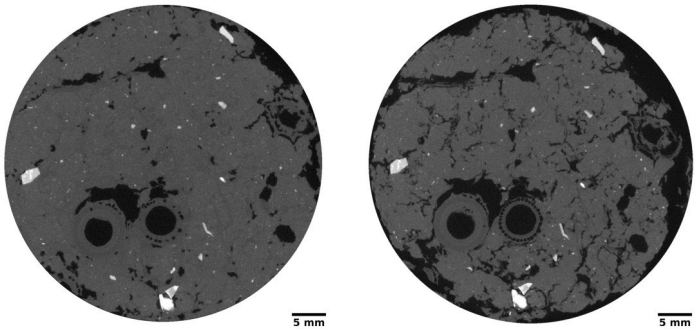

(a) A humid sample. (b) A dry sample.

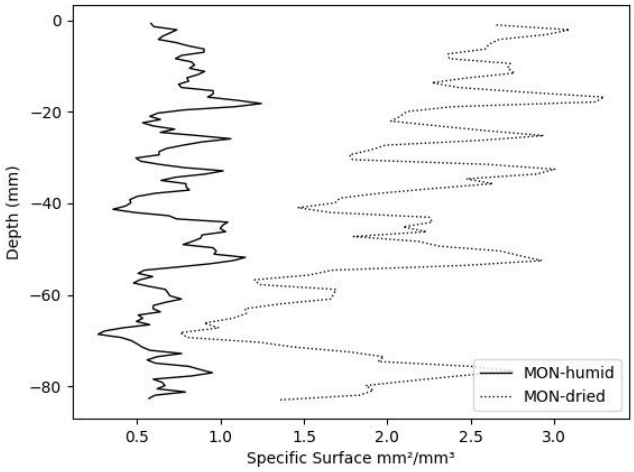

(c) SSA profiles.

Figure 3.51: SSA profiles.

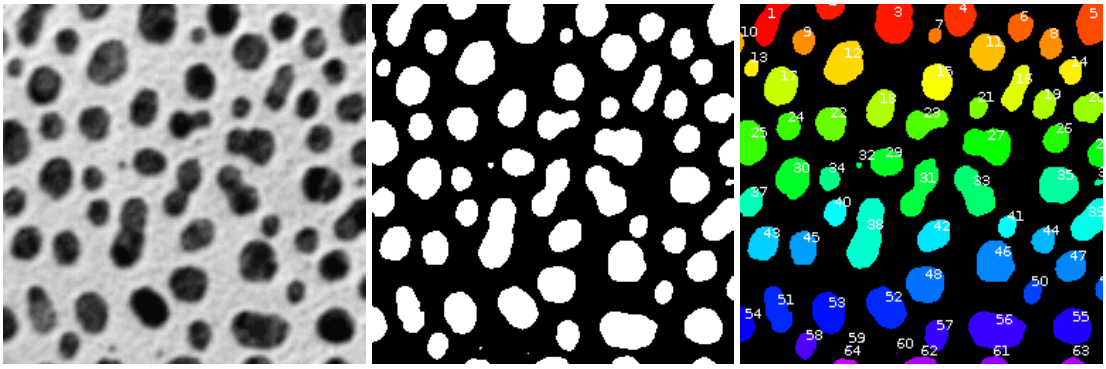

(a) Blobs. (b) Segmentation. (c) Counting.

Figure 3.52: Counting objects.

voxels may represent one or many objects. Usually, voxels connected by a 3D diagonal are not considered to form a same connected region. An example is presented in figure 3.52.

Although identifying a connected region or object relies on a simple concept, algorithms to perform such a computation are complex and time consuming. There exist two different plug-ins in Fiji that count and label connected regions or objects: (1) the 3D-object counter and (2) the find connected 3D-regions. The first was used in chapter 4 to count gravels and compute digital grain size distributions (Figure 4.9), and the second to identify connected void structures in chapter 6 and compute profiles of connectivity ratios (Figure 6.9). Although both of them do basically the same job [12] their memory management is very different. The RAM consumption of these algorithms is very high and their execution on whole VFTW samples is (almost) impossible even with servers with 128 GB of RAM. [13] [14].

To overcome this issue, the plug-in can be executed on sections of the image that will have to be wisely fused afterwards. In this work, images of about 1200*1200*4000 voxels were divided in four regions (1200*1200*1000 each) with an overlay of one slice. Afterwards, the overlay slice was used to relabel the connected regions through an iterative procedure described in Figure 3.53. The code of this function was written in python and is available in the repository referred to at the beginning of this chapter.

Gravel counting and gravel size distribution

Although apparently simple, counting gravels is a challenging task. Gravel grains may fuse during the segmentation due to successive dilations (Figure 3.44). There are different methods to separate grains: two of them are (i) eroding the gravel phase or (ii) using 3D watershed segmentation (Amira-Avizo commercial software). The 3D object counter plug-in can be used afterwards to count the gravels and compute gravel size distribution. In Figure 3.54 the size distribution was obtained by computing equivalent sphere diameters based on the volume of each gravel. The erosion radius is added to the equivalent diameter. The similarity if these results with those obtained by sieving is remarkable. These results are discussed in detail in chapter 4. Nevertheless, this computation can be enhanced by considering realistic shape parameters.

[12] The 3D object counter computes also many other parameters such as volume, surface, centroids and bounding box sizes.

[13] The find connected regions plug in can identify up to 2^{32} different regions in an image.

[14] The 3D object counter executes correctly only if the total number of voxels of the image is less than 2^{32}.

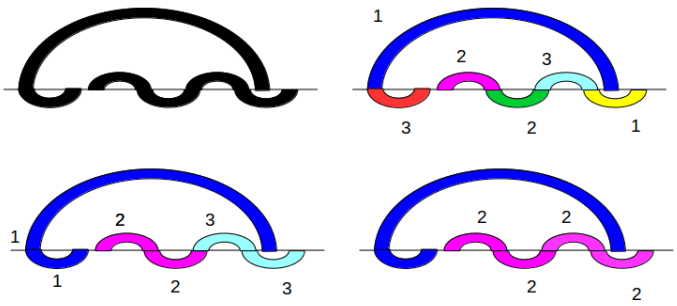

Figure 3.53: Conceptual explanation of fusion of sections containing connected voids.
The overlay slice is here represented by a horizontal line.
Upper left: Curve lines represent void regions.
Upper right: After the division, the Find Connected regions determines 3 different connected zones above and below the dividing line.
Lower left: After a first iteration some regions are fused from above the dividing line
Lower right: after a second iteration regions are fused from below the dividing line
The process is repeated until the number of labels above and below the dividing line does not decreases in an iteration.

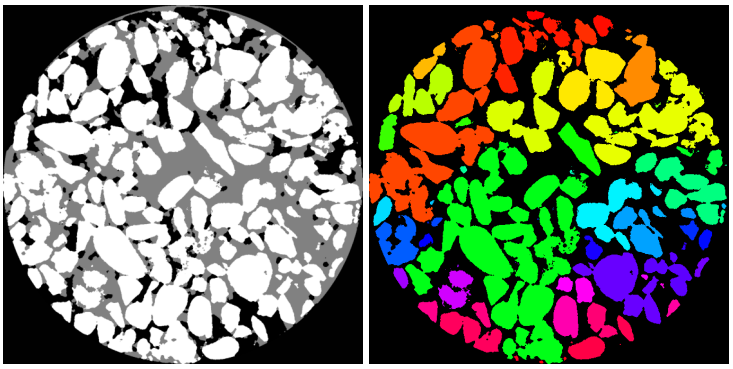

(a) Segmentation.

(b) Gravel count on raw segmentation.

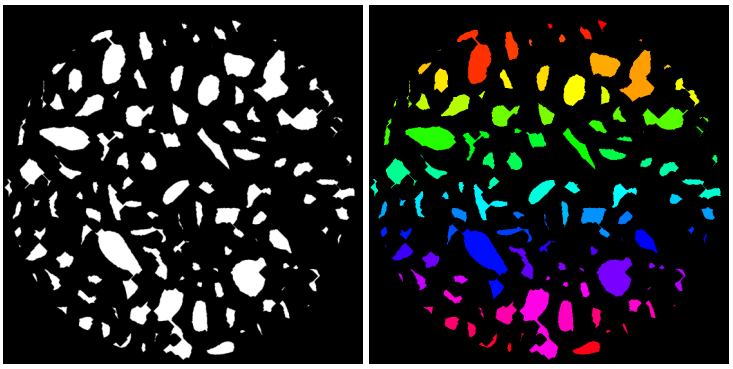

(c) Eroded gravels.

(d) Gravel count on eroded segmentation.

Figure 3.54: Counting gravels.

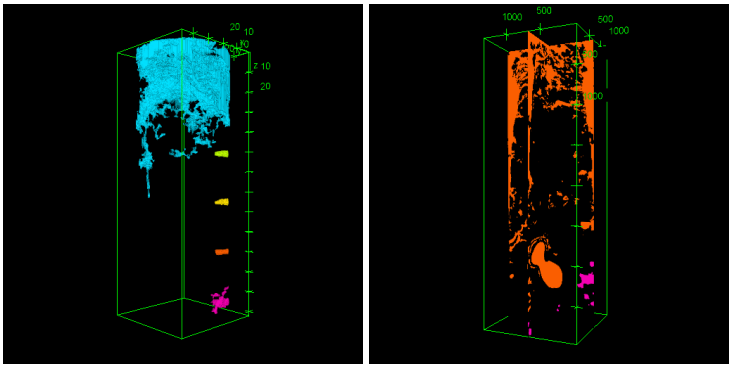

(a) Sample MONB. (b) After drying, most of the volume of the sample was connected.

Figure 3.55: Connected voids
For better visualization sample MONB is displayed as orthogonal slices in figure (b).

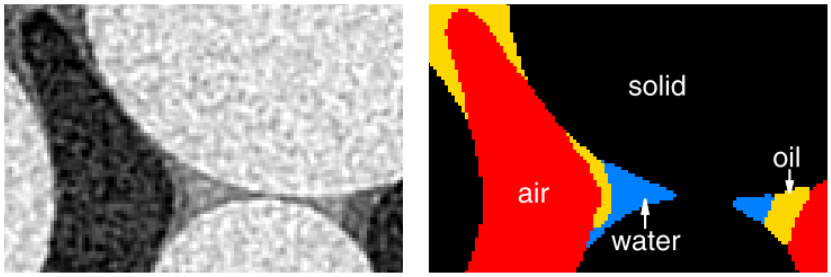

Figure 3.56: Example of air, water, and oil filled porosity.
From [125].

Connected voids

Studying void connectivity is important to understand oxygenation in VFTW. Figure 3.55 shows voids connected to the volume occupied by oxygen probes inserted into VFTW samples. The objective of determining the connectivity of this zones was to study the influence of changes in voids structure on oxygenation during a drying process.[15]. A discussion on this subject is present in chapter 7.

3.8.5 Pores and pore size distribution

The definition of a pore

Voids and pores are different concepts in image treatment, but their differentiation is not very clear in hydrogeology. The term voids stands for the volume of an object filled with air. The definition of a pore is more complex.

On the one hand, a pore could be defined initially as a volume not filled by a solid. This is the basis to define different concepts in hydrogeology such as: air filled porosity, water filled porosity, oil filled porosity (Figure 3.56) ... and respective saturations (volume fractions with reference to the total porosity).

On the other hand, a pore may be defined as section of the void phase with specific size and shape. This approach started to be followed when Haines and Child in the 30's and 40's suggested that "soil voids, (or pores), could be linked to straight capillaries of varying diameters"

[15] Videos of connected voids are available at `https://www.youtube.com/watch?v=sCz58TL2GDs&feature=youtu.be`
and `https://www.youtube.com/watch?v=UtiHIaJCALs&feature=youtu.be`

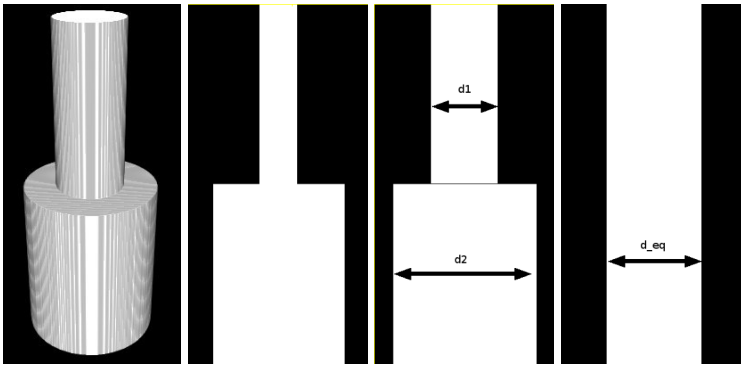

(a) A theorical void region. (b) (c) (d)

Figure 3.57: The pore concept.
(a) 3D void space consisting of two concatenated cylinders
(b) This void can be considered theoretically as a single pore (connected void)
(c) or as two different cylindrical pores of definite diameters and lengths
(d) but could be simplified as an equivalent pore of equivalent diameter $d_1 < d_{eq} < d_2$

and that their size distribution would provide the type of direct quantitative information needed to describe the functioning of soils [39]. A void space contains then as many as "pores" as capillaries. Depending on the method to generate an equivalent capillary network, the number and size and shape of capillaries will change. Figure 3.57 illustrates this issue.

Describing the pore structure of a void region is a process that often implies computing the Pore Size Distributions (PSD). In [39] several methods to compute PSD are studied, which follow different approaches: medial axis, maximum inscribed balls, morphological opening, and object separation. In this work, the concept of local thickness [37, 105] was used to study the structure of the void phase of VFTW samples.[16] It is based on then same concept that maximum inscribed balls without including the "engulfing" stage.

Local thickness maps

The local thickness at a voxel (x, y, z) inside an object or a phase (e.g. the voids phase) is the diameter of the largest sphere that fits inside the sphere and contains the point (Figure 3.58). The local thickness map of an object is an array (another image) that stores the local thickness of every voxel of the object. Figures 3.59(a),3.59(b) and 3.59(c) present the local thickness map and the local thickness distribution of the voids is illustrated in Figure 3.57. The distribution in Figure 3.59(b) is an approximation of the theoretical volume distribution that can be deduced from Figure 3.57, i.e. only two discrete diameters are attributed. Figure 3.59(c) shows better the influence of corners on the volume distribution of local thicknesses. Figure 3.59(d) presents a local thickness map and distribution in a slice from a VFTW.

3.8.6 Skeleton/medial axis

The medial axis is the line passing through the geometrical center of an object. Because of its shape, it is often called the skeleton of an object, and the procedure to compute it is referred as skeletonization. 2D and 3D skeletonization are algorithms implemented in Fiji and obtained by consecutive erosions. Figure 3.60 presents a skeleton of a 2D object.

Studying the skeleton of the void phase is of high interest as the length of the pathways account for its tortuosity. Tortuosity is a variable used often in models describing processes in

[16] The choice of the methodology to generate a PSD of the void phase was primarily guided by computational performances.

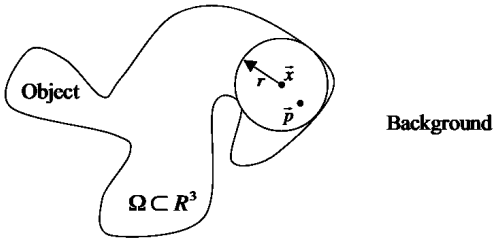

Local Thickness $\tau(\vec{p}) = 2\max\left(\left\{r \mid \vec{p} \in sph(\vec{x}, r) \subseteq \Omega, \vec{x} \in \Omega\right\}\right)$

Figure 3.58: Local thickness definition.

porous media. Figure 3.61 [17], shows a skeleton of the voids phase. Most of the image correspond to 1-voxel wide lines. The nut like artifacts are caused by segmentation errors and correspond to aggregates of FM and gravels completely surrounded by voids with no contact point with the rest of the solid matrix. Further discussion on the computation of tortuosity is presented in chapter 7.

3.9 Conclusion

Image processing is a vast subject that has achieved a high degree of development recently. Here, a small but efficient set of methodologies is explained and applied to the study of porous media of VFTW. All of the phases in image processing (pretreatment, segmentation and post-treatment) can be further optimized and developed. For pretreatment and segmentation, it is highly recommended to establish a set of benchmark segmentations to assess whether or not future developments perform better than the methodologies presented here. For post-treatment, Pore Network Extraction (the partitioning of the voids phase to generate an equivalent pore networks) is one of the promising tools that could help to obtain non realistic but simpler representation of complex porous media [8].

[17] a video of a skeleton is available in `https://studio.youtube.com/video/rHW4bAq4pK4/edit`

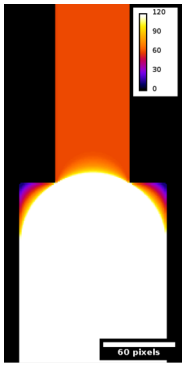

(a) LTM of a theoretical region.

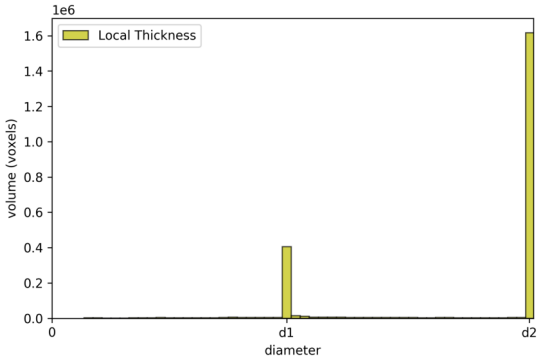

(b) Local Thickness distribution of (a) in linear scale.

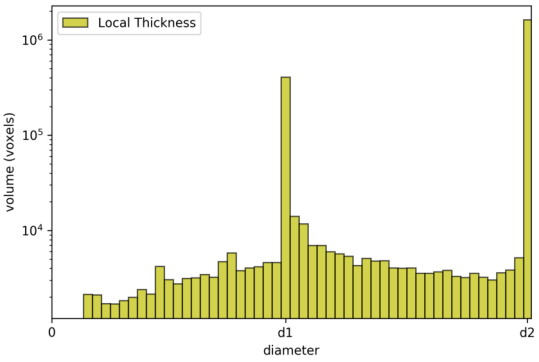

(c) In log scale.

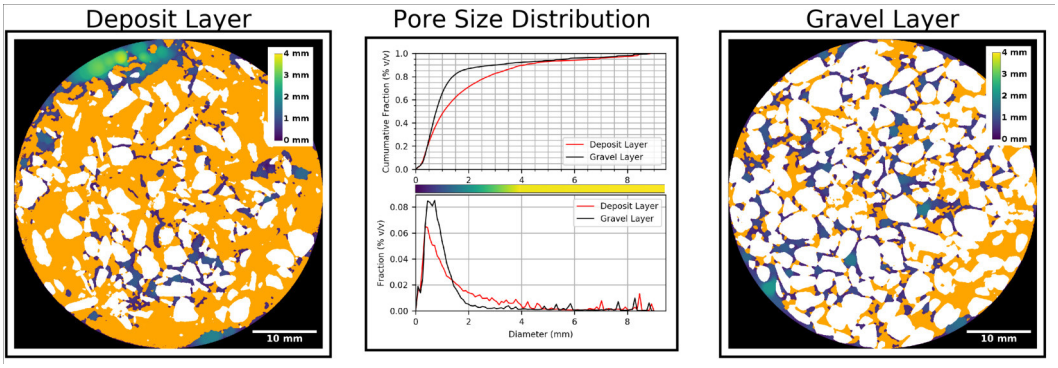

(d) LTM of VFTW samples.

Figure 3.59: Local thickness maps (LTM).

(a) Original. (b) Skeleton.

Figure 3.60: Skeletonization.

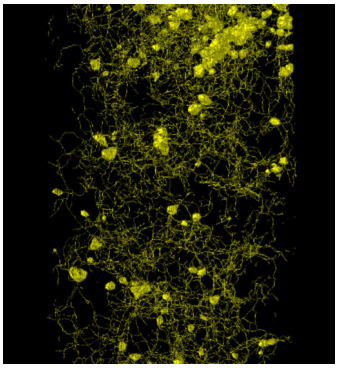

Figure 3.61: Skeletonization of the void phase in a VFTW.

4. Assessment of X-ray Computed Tomography to characterize filtering media from Vertical Flow Treatment Wetlands at the pore scale[a]

[a]Martinez-Carvajal, G. D., Laurent Oxarango, Jérôme Adrien, Pascal Molle, and Nicolas Forquet. *Assessment of X-Ray Computed Tomography to Characterize Filtering Media from Vertical Flow Treatment Wetlands at the Pore Scale*. **Science of the Total Environment** 658 (2019): 178–188.

4.1 Introduction

With more than 4000 plants built in France during the last 30 years, Treatment Wetlands (TW) have positioned themselves as one of the most reliable and efficient technologies to treat domestic wastewater for small communities (under 2000 population equivalent) [82]. The most frequent TW configuration, known as the "French System", is a 2-stage vertical flow plant. Its first stage is the specific feature of the "French System" as it consists of three gravel filters in parallel fed with raw wastewater following a specific pattern of feeding/rest periods [79] (Figure 4.1). The statistical study of more than 400 French Systems recently carried out by [82] demonstrates the suitability of their design criteria and enlightens their performance in terms of pollutant removal.

Being fed by raw wastewater, French systems filter Suspended Solids (SS). After some years of operation, this accumulation leads to the formation of a "deposit layer" over the filtration media of the 1st stage. This layer does not impair wastewater infiltration. Indeed, it could even impact positively the hydraulic behavior, biological activity, and mass transfer [78]. The rate of solids accumulation in the deposit layer is roughly between 2 and 3 cm/year. When the deposit layer reaches 20 cm, it has to be dredged out to ensure its aerobic biological degradation and avoid a too strong reduction of infiltration capacity.

Filtration in porous media is driven by two different mechanisms [104]: (i) deep bed filtration and (ii) cake filtration. Solid particles are collected within the filtering medium during deep bed filtration. Cake filtration stands for interception of particles at the surface of the filtering medium. Deep bed filtration is predominant in new filters as SS are mostly retained within the gravel porosity (Figure 4.2(a)). This takes place until the formation of the deposit layer, moment from when cake filtration becomes the predominant mechanism (Figure 4.2(b)).

By analogy to nomenclature of filtration processes like Membrane Bio Reactors (MBR) [43], solid retention by deep bed filtration leads to long term fouling while cake filtration leads to surface clogging of VFTW. Comprehension of solids retention is therefore critical in order to give a better insight into the failure and lifespan of any type of filter. It is necessary to get descriptions and develop models that explain the accumulation of solids. A geometric description of solid retention is very important to validate models that aim at predicting fouling and clogging processes. In the domain of treatment wetlands, clogging has been the focus of many researches that have been summarized in three review papers [51, 22, 85]. However, few of them provide

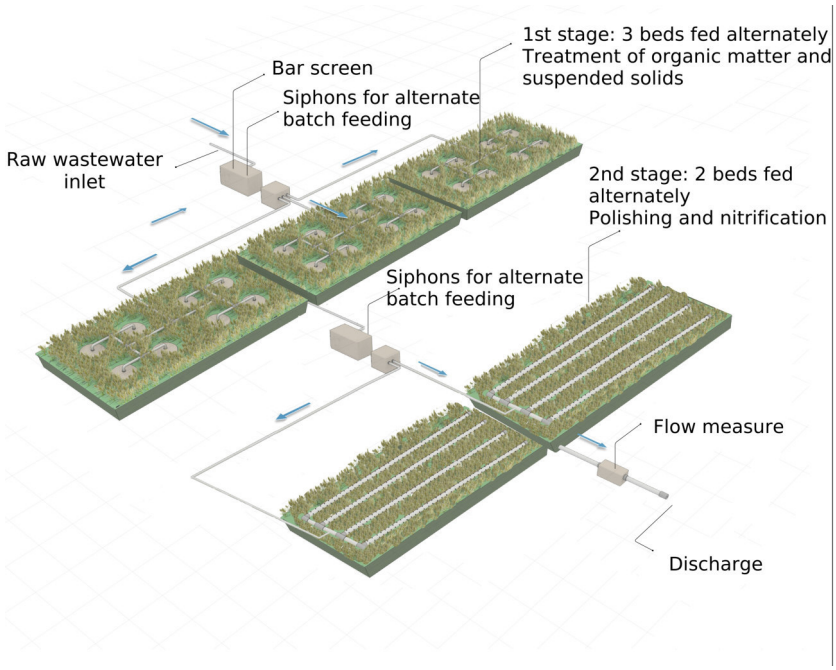

Figure 4.1: The 2-stage VF treatment wetland (courtesy of Syntea).

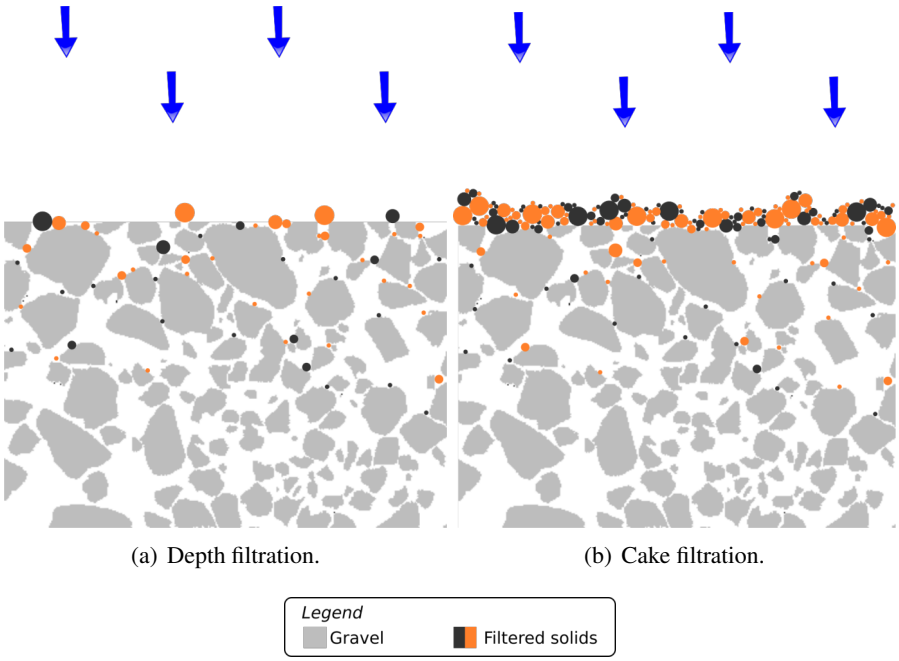

(a) Depth filtration. (b) Cake filtration.

Figure 4.2: Filtration mechanisms in VFTW.

evidence on how clogging effectively happens and to quote [85]: “the technical underpinnings are still not well understood”.

Recently, Kim and Forquet [50] have obtained 2D images (5 × 7 cm) of the filtration media using the “thin section method”, a widespread practice in soil characterization [66]. Their images show the distribution of three phases: gravel, fouling material, and voids within the filtering media of a first stage filter. They analyzed the images and estimated phase volume fractions and void size distributions.

Nevertheless, the thin section method has some shortcomings when describing void and fouling material distribution. It does not account properly for variations in three dimensions since it could consider only a small number of slices. Furthermore, it remains uncertain if water replacement by acetone, required for this technique, may alter the phase distribution in the filtering media of TW, especially that of voids and fouling material, which is mainly a mix of organic and mineral compounds and water. An imaging technique that provides 3D information and avoids changes in sample constitution when measuring should allow overcoming the limitations of the thin section method.

3D morphologic analysis of porous systems has evolved greatly for the last 30 years based on X-ray tomography. The introduction and development of X-ray imagery and associated image processing techniques are well documented in [35, 62]. X-Ray tomography is a non-destructive technique to obtain 3D gray scale images of an object. The object to be characterized rotates around a single axis while a set of 2D X-ray absorption images is recorded. Using mathematical principles of tomography, this series of images is reconstructed to produce a 3D digital image, where each voxel (volume element or 3D pixel) represents the X-ray absorption at that point. Attenuation is higher for components consisting of higher Z-elements obeying Beer’s Law. Applications range from industrial purposes, like defects detection or deformation in materials and mechanical parts, to dynamic monitoring of phenomena like liquid flow through porous media [115]. Computed Tomography has been used to investigate how size and shape of voids affect the flow of water through peat soils [99]. Other scientists use porous media Computed Tomography (CT) to generate pore networks and use them as inputs for simpler pore scale models to simulate single or multiphase flow [23].

3D imagery is now widely spread in the scientific community and used to give insight into physical phenomena at the pore scale, but there is no reference of its application to analyze filtering media in treatment wetlands yet. As 2D and 3D imagery became a common practice in different domains, the development of algorithms to treat digital images boosted as well. Phase segmentation is the process by which an object or region in a color/gray scale image is recognized and attributed to a unique phase. In phase segmentation, the scans are transformed into binary images. It is based on common image processing routines such as blurring (e.g. averaging), edge detection and threshold computation [6]. Phase segmentation opens the gate to the usage of numerous characterization tools providing quantitative information like: (i) particle counting [9] and thus computation of particle size distribution, (ii) distance, surface and volume computations [10, 54] or (iii) percolation pathway analysis based on skeletonization [53]. In this study, segmentation aims at differentiating three phases: void, gravel and fouling material (plant tissues are included in this phase). In the perspective of applying such methodologies to TW filtering media, identifying the 3D distribution of these phases should provide an original insight into the fouling and clogging processes.

In this paper the applicability of X-ray CT to produce exploitable images of filtering media in vertical flow TW is explored. Samples were extracted from two different full-scale operating plants. An investigation on whether or not a thermal pretreatment improves image quality is done. The 3D-digital images were treated using image processing algorithms for multiphase segmentation in order to identify 3 different phases: gravel, Fouling Material (FM), and voids.

Table 4.1: Sample description.

Sample	Deposit removal during sampling	Gravel description	Sampling season	Cumulated SS load ($kg \cdot m^{-2}$)	UC
MON	No	Crushed gravel	Spring	1326	1.5
COP-01	No	Crushed gravel	Spring	356	2.1
COP-02	Yes	Pea gravel	Summer	623	2.0

The images were treated to obtain gravel 3D-distribution, gravel size distribution, phase volume fraction profiles, specific surface profiles, and percolation pathways. Finally, some perspectives of the use of X-ray tomography to understand physical processes in TW are presented.

4.2 Materials and methods

4.2.1 Site description

Two different Vertical Flow TWs were chosen to test the methodology, Montromant (Rhone, France) and Copponex (Haute Savoie, France). They have been designed according to French standards defined in [79] and have been planted with *Phragmites Australis*. There are two treatment stages, with three filters in parallel in the first stage and two in the second, with successive periods of feeding (3.5 days) and rest (7 days for the first stage and 3.5 days for the second one) to maintain permeability, oxygen content and to control biomass growth [82]. First stage filters, which will be under focus in this study, have a filtration layer made of gravels with diameter ranging from 2 to 6 mm. The choice of a coarse material has been made because filters are directly fed with raw wastewater [79].

The treatment plant of Montromant is one of the oldest VFTW in France. It has been commissioned in 1994 and was designed to treat effluent from 200 people equivalent (P.E.). Based on self-monitoring measurements performed in 2013, the suspended solids (SS) and the Chemical Oxygen Demand (COD) loads applied to the operating first stage filter were 158 $g \cdot m^{-2}d^{-1}$ and 262 $g \cdot m^{-2}d^{-1}$, respectively. The hydraulic load was 20.5 $cm \cdot d^{-1}$. In 2009, the deposit cake of the first stage was dredged out and an additional parallel filter started receiving raw wastewater. The duration of the feeding period in the first stage remained 3.5 days and the rest period was augmented to 10.5 days.

The treatment plant of Copponex was built in 2003 and its capacity has been doubled in 2011 to reach 1500 P.E. The extension was carried out simply by doubling the number of filters using the same layout and surface than existing filters, differing only in the filtering material. Consequently, there are 6 first stage filters and 4 seconds stage filters. Based on self-monitoring measurements performed in 2016, the SS and COD loads applied to the operating first stage filter were 122 $g \cdot m^{-2}d^{-1}$ and 247 $g \cdot m^{-2}d^{-1}$, respectively. The hydraulic load was 28.7 $cm \cdot d^{-1}$.

Figure 4.3 shows the gravel size distribution of the first filtration layer for all filters mentioned above. The dry sieving method was used according to the European Standard NF EN 933-1/A1. In Table 4.1, an estimate of the total inlet SS charge received by these treatment plants since their construction until 2017 is presented as well as the Uniformity Coefficients (UC) of gravel size distribution ($\frac{d_{60}}{d_{10}}$).

4.2.2 Sampling

Three samples were collected on the first stage treatment filters: one at Montromant (MON) and two at Copponex (COP01 on a filter built in 2011 and COP02 on a filter built in 2003). Samples were taken on April 4th, April 11th and July 24th 2017, respectively during the rest period. An

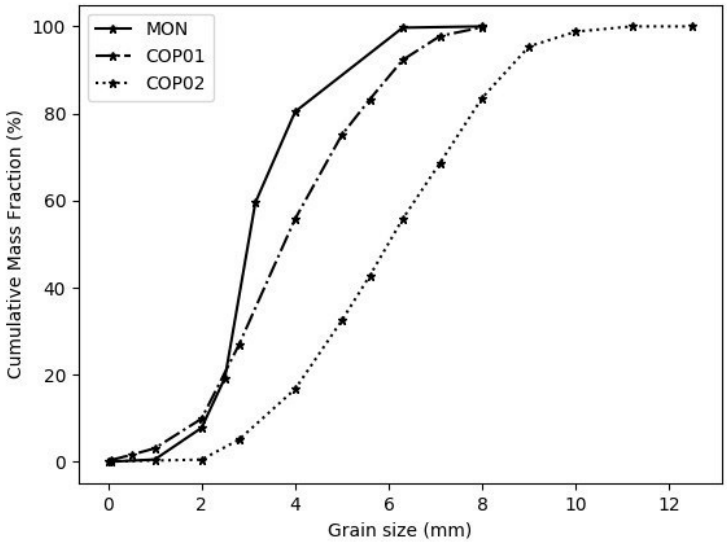

Figure 4.3: Gravel size distribution of the three types of gravels present in this study.

area was cleared of reed stems at less than 2 m from a feeding point. Then a cylinder 5 cm in diameter and 10 cm in height was manually inserted. As the cylinder was buried into the filter, gravels surrounding the cylinder were progressively dug out and any rhizome found was cut to avoid compaction and changes in sample structure.

Despite of care given during extraction, surface deposit has been slightly deformed due to its plasticity and presence of dead leaves larger than the sampling cylinder. Therefore, when deformations were too important, the deposit layer was removed. Table 4.1 specifies such cases and gives additional information on the samples.

4.2.3 Drying

A major concern regarding the application of X-ray tomography on VFTW samples is the influence of water content on image contrast, i.e. it is feared that high water content in raw samples may produce blurry images and thus it will not be possible to distinguish the void space from he FM. Therefore, two treatments were applied in order to assess the impact of the water content on image contrast. Samples COP-01 and COP-02 were dried in the oven at 45 °C for 24 h before X-ray scanning. MON sample was maintained for less than 24 h under refrigeration before performing a first X-ray scan which is called MON-humid. A second scan of the MON sample (MON-dried) was performed after drying it at the same conditions than COP-01 and COP-02. This gives a total of 4 scans out of 3 different samples.

4.2.4 X-ray tomography

Tomographies were performed at the Mateis laboratory (Insa Lyon, France) in a scanner equipped with a 160 kV X-ray tube. The scanner was operated with an accelerating voltage of 140 kV and a current of 100 μA with an exposure time of 333 ms. A 0.1 mm copper foil filter was put in front of the X-ray source to reduce beam hardening artifacts. 900 projections distributed among 360° were recorded. The sensor area is 250 × 200 mm and the 3D images consist of about $1500 \times 1500 \times 1350$ ($l \times w \times h$) voxels with a voxel size of 35 μm. Since the height of the samples is about 10 cm, each scan was performed in two parts: top and bottom. These

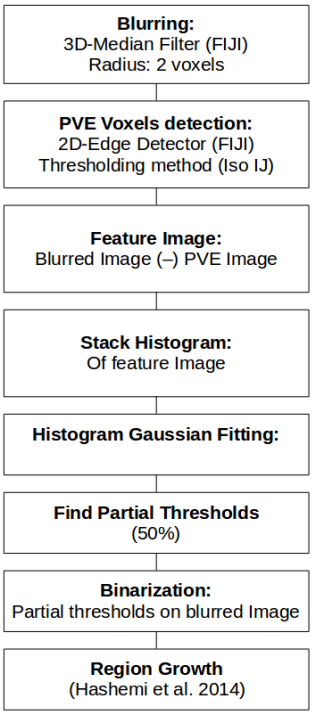

Figure 4.4: Workflow for phase segmentation.

parts have a small overlay region of about 100 voxels to help the concatenation during image processing. The data were reconstructed by a filtered back projection Feldkamp-algorithm [28]. The reconstructed data were processed and visualized with the public domain ImageJ/Fiji shareware [109].

4.2.5 Image processing - segmentation

Segmentation is a research subject in constant evolution. An algorithm based on the region growing method proposed by [35] was applied with some modifications to account for the specificities of the samples. Firstly, an edge detection filtering was performed followed by the default thresholding method available in ImageJ [109] to identify the Partial Volume Effect (PVE) voxels of the Hashemi's method. PVE voxels are a set voxels located around the interface of two phases (e.g. voids/gravel, gravel/FM...) and contain fractions of both. Secondly, a Gaussian fitting of the stack histogram of the image excluding the PVE voxels was performed. This allowed a better recognition of the peaks during the fitting and led to satisfactory partial thresholding for phase identification. This method allowed three different phases to be separated in all scans: voids, Fouling Material (FM) and gravel (Grv). Figure 4.4 describes the segmentation workflow.

4.2.6 Phase descriptions

4.2.6.1 Gravel size distributions

To compute the size distribution of gravels, grains were eroded to eliminate fusions that may have occurred during the growing-algorithm in phase segmentation. The chosen erosion diameter was set to 1.5 mm, close to the d_{10} gravel diameter (the diameter at which 10% of the sample mass is comprised of grains with a diameter less than this value), and was determined using the standardized sieving method for experimental measurement of particle size distribution (European Standard NF EN 933-1/A1). The gravels were labeled using the FIJI (ImageJ) 3D object counter developed by Cordelières [9, 20]. Size classes were obtained by computing the

diameter of the equivalent volume spheres of the gravels. All the measurements were corrected to take into account the former erosion step in gravel size by adding the erosion diameter to the diameter of the equivalent sphere.

4.2.6.2 Volume fraction profiles

Volume fraction profiles for each phase are readily computed by performing a ratio of voxels attributed to each phase for each 2D slice along the depth of the image. The profiles were smoothed with a 57-voxel average window (2 mm). This value is close to the d_{10} gravel diameter of the size distribution.

4.2.6.3 Specific Surface Area (SSA) profiles

Void-FM surface was computed using the Cauchy-Crofton cutting line method [54, 55, 107]. This method allows a numerically efficient estimate of interfacial areas with a better accuracy than the direct counting of interface voxels, which presents a "staircase effect". In addition, it has a much lower computational cost than methods based on surface meshes. Surfaces were computed within a moving average window of 0.7 mm (20 voxels). The Specific Surface Area (SSA) is then obtained by dividing the (void-FM) surface by the FM volume. SSA profiles computed using CT-scans are free from geometrical assumptions and have a high spatial resolution compared to all former methods used in the field of TW [4].

4.2.6.4 Skeletons and percolation pathways

The void phase available for water flow and particle transport should be studied with care since it probably drives the evolution of the filter. In order to investigate this particular point, the skeleton and distance map concepts could be of interest. The skeleton is a line that defines the medial axis of a 3D object. It is often obtained by burning (erosion) algorithms [63]. The distance map of an object is the calculation of the shortest distance from each voxel in the object to the closest surface. By using this information together on the void phase, a percolation pathway may be defined for a specific class of void size through the filter.

The skeletons display clearly the tortuosity of the pathway that a solid particle could follow. Disconnections in the pathways indicate that either the particle could be retained within the filter by geometric interception (e.g. throats) or trapped in a dead zone or in an isolated loop. In this article, only the computation for voids larger than 35 μm in diameter (the image resolution) was carried out to observe the tortuosity of the percolation pathways. Skeletons were obtained using the 3D skeletonize method implemented in ImageJ [53]. The skeletons were then treated using a burning algorithm coded in Python to delete disconnected branches.

4.3 Results and discussion

4.3.1 Feasibility of the X-ray CT scan

The methodology can be applied to obtain images of VFTW porous media with enough contrast to distinguish phases in the sample. Figure 4.5 shows (A) a slice of the CT scan of MON-humid and (B) an enlargement of a part of it. Based on human visual perception, the gray contrast among the elements is enough to readily distinguish gravels, voids, and FM. It may also be noticed that voids corresponding to stem channels (in green) cannot be distinguished from voids corresponding to pores (in blue) based on the gray level. However, the differentiation can be done based on their shape. The gray-value histogram of the scans is found in Figure 4.6. The middle peak cannot be split into different phases to distinguish plant tissues, suspended solids or biomass and thus they form one single phase (called FM in this study).

Figure 4.7(a) highlights that only few cavities have formed on the edge of the cylinder and radial compression has been minimized since voids are evenly distributed over the slice. This

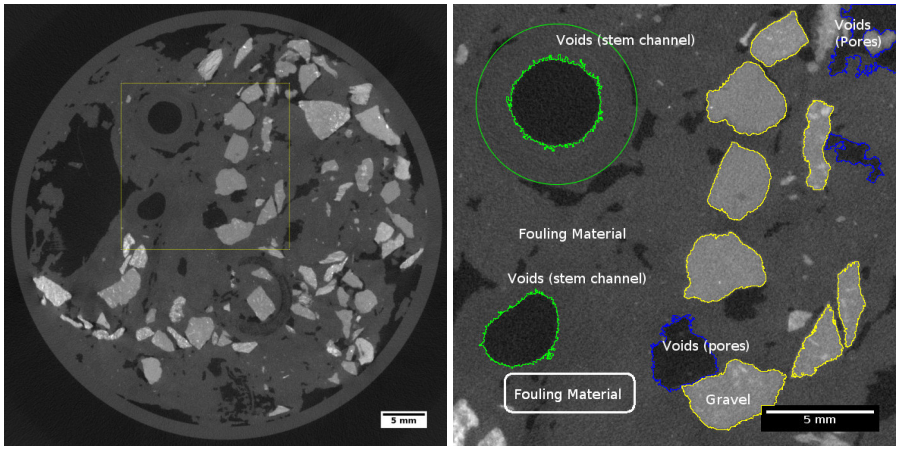

(a) Slice of MON-humid CT scan. (b) Zoom on panel (a).

Figure 4.5: A slice before segmentation and its features.

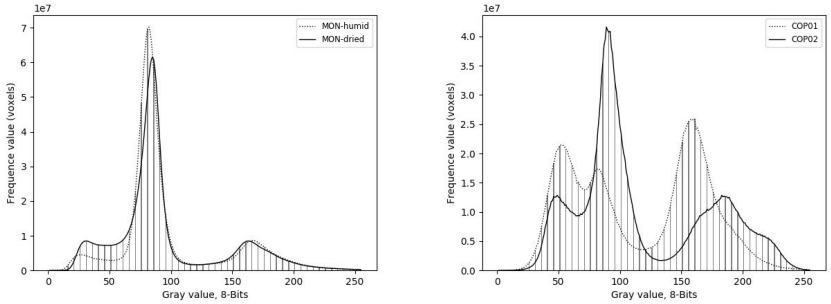

Figure 4.6: Stack histograms of CT scans.
Peak order: voids, FM, and gravel from left to right.

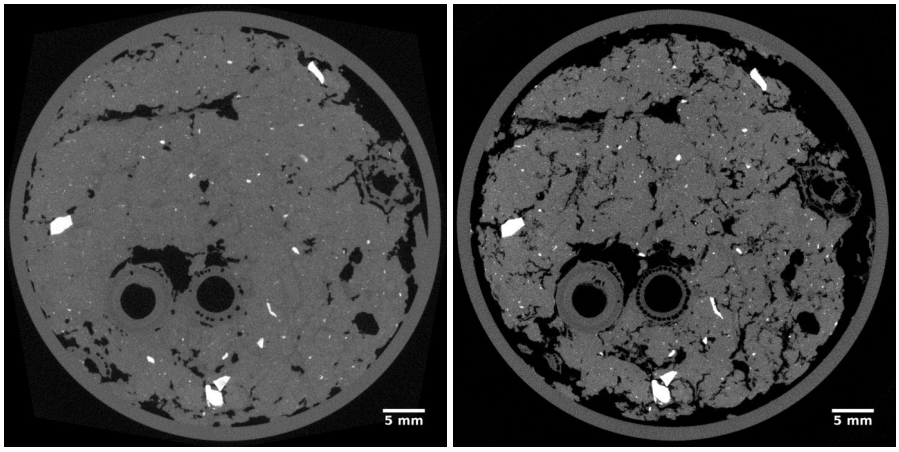

(a) MON-humid. (b) MON-dried.

Figure 4.7: Effect of drying on samples as observed by X-ray CT-scan.

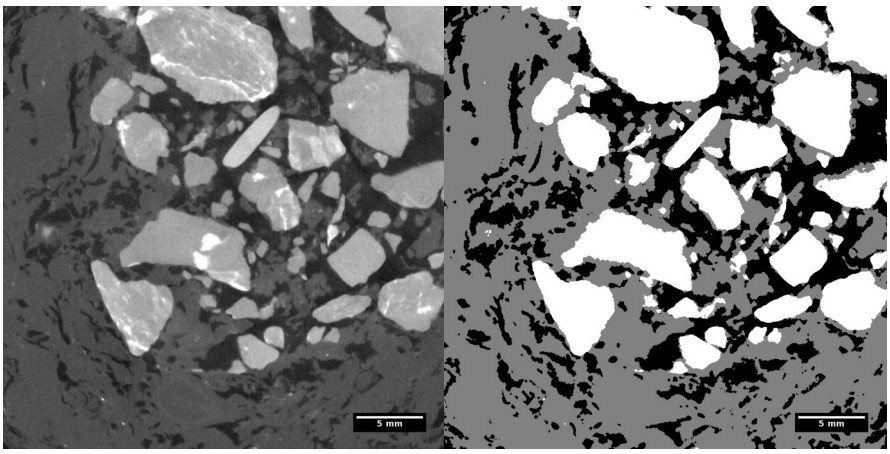

(a) Slice of COP01 scan before segmentation. (b) Slice of COP01 scan after segmentation.

Figure 4.8: Comparison of raw and segmented slices.

has been observed at all depths in the samples. If rhizomes or stems are present in the sample, the 3D images show as well that no major fractures were created during their cutting.

Although sample extraction is a potential source of error in result interpretation, the method used here limits stresses applied (no hammering, little twisting) and therefore deformations. However, uncertainties associated to sampling still need to be quantified. X-ray tomography may actually be used to compare the results of different extraction procedures and give insight of their impact on the sample structure. This possible application of X-ray tomography may be the subject of future research.

4.3.2 Segmentation method

Even if good contrast may be seen by mere sight, the noise level of the images was high. Figure 4.6 shows clear overlay between peaks mostly for void and FM phases. Despite of this, the segmentation algorithm based on Hashemi's algorithm shows very satisfactory results for the attribution of uncertain voxels to one phase. Figure 4.8 shows a comparison between a raw image and its segmented version.

A small default of the segmentation method is that gravel grains very close to each other may

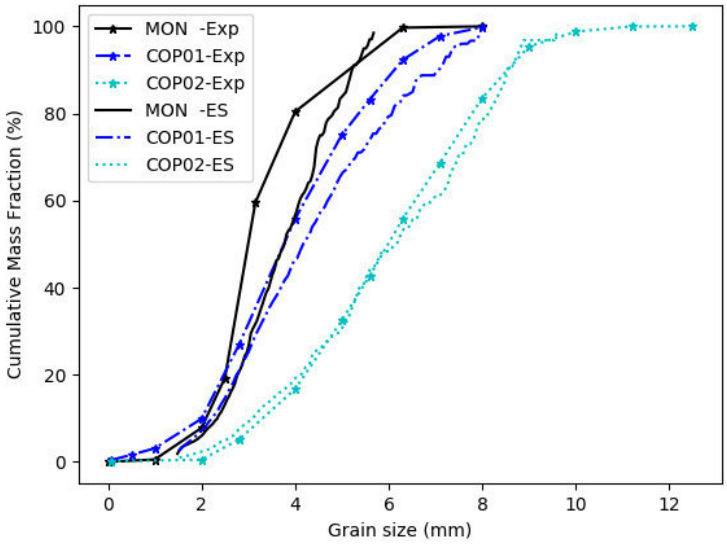

Figure 4.9: Mass and digital gravel grain size distributions for sites MON, COP01 and COP02. (Exp): Experimental (mass) gravel size distribution. (ES): digital gravel size distribution - Equivalent Sphere.

easily fuse. This may impact negatively the computation of a digital gravel size distribution but it can be targeted as well, during segmentation by setting a larger partial threshold for the gravel phase, or by implementing splitting algorithms after segmentation.

4.3.3 Digital gravel size distributions

Because of gravel higher atomic density, it is distinguished very easily in the samples. Thus, the analysis of their size distribution and its consistency with the experimental gravel size distribution is a first way to assess the accuracy of the methodology. Figure 4.9 compares digital and experimental gravel size distributions. There is a satisfactory level of data reconciliation for all types of gravel. However, it is probably limited due to the approximation of equivalent spheres. In a classical sieving operation, the diameter is the smallest dimension of the gravel and therefore may differ from the one of an equivalent sphere. This limitation may potentially be overcome by computing digital gravel size distribution based on the shortest dimension of the smallest 3D surrounding box.

On the one hand, the comparison between experimental and digital gravel size distributions supports the assumption that the sample size is large enough to be representative of the gravel phase. On the other hand, the representativity of void and FM phase would require to perform a Representative Elementary Volume (REV) analysis as described in [126].

4.3.4 Vertical phase distribution - 1D

Deep bed filtration impacts the compactness of the gravel filter. The volume fraction profiles for void, FM and gravel are presented in Figure 4.10. At the exception of sample COP-02, they are suitable to define 3 regions: first, the deposit cake region at the top composed of FM and voids only, second, a transition zone composed of a mixture of gravel, FM and voids, and finally, at the bottom of the sample, the gravel layer that reaches a constant volume fraction value corresponding to the dense packing of gravels. Profiles for COP-01 show a very clear limit of the dense gravel layer below 5 cm depth. This is less clear for COP02 and MON-humid and MON-dried samples and can be associated to the presence of reeds as seen in Figure 4.7.

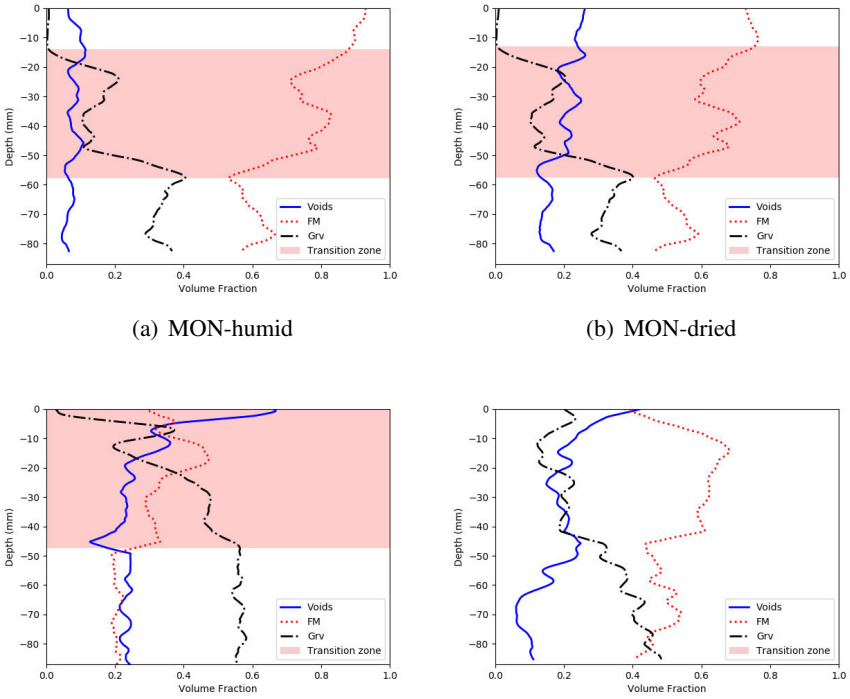

(a) MON-humid (b) MON-dried

(c) COP-01 (d) COP-02

Figure 4.10: Volume fraction profiles.

4.3.5 Vertical phase distribution in 2D and 3D

The compaction of gravel in COP01 is significantly higher than in MON-dried even if COP-01 gravels are coarser than MON ones (Figure 4.11). For MON-dried, FM occupies most of the void space over the entire depth of the sample while, for COP-01, accumulation of FM is more heterogeneously distributed: at the top it occupies a large fraction of the void space and at the bottom it coats gravel leaving most of the inter-grain space empty (Figure 4.12). So far, it is not possible to determine whether the observed differences in gravel compaction and FM distribution are due to the gravel shape, size or to the age of the TW (the accumulated SS load). Wanko et al. [124] pointed out differences in terms of SS removal efficiency between round and crushed sand without being able to identify the mechanism at work. CT scan appears to be a well-suited method to investigate this issue, which is of critical importance in France where alluvial pea gravel is becoming rare.

Consequently, further studies may be carried out to analyze the impact of heterogeneity in gravel size and shape in the accumulation of FM.

4.3.6 Drying

Drying of MON-sample was done to evaluate the enhancement in gray contrast on the images. The humid sample showed a high contrast level just like the dry sample (Figure 4.7). Drying did not reduce the overlays between peaks on the gray-level histogram (Figure 4.6). On the other hand, the volume of voids was strongly affected. Total volume of voids increases highly (Figure 4.10) from a global average of 8% to 19% of the volume of the sample. More interestingly, the Void-FM specific surface also increases (Figure 4.13).

Due to the great influence of the specific surface on drying processes, such information is of major interest in the perspective of studying the rest period of TW. However, it is important to

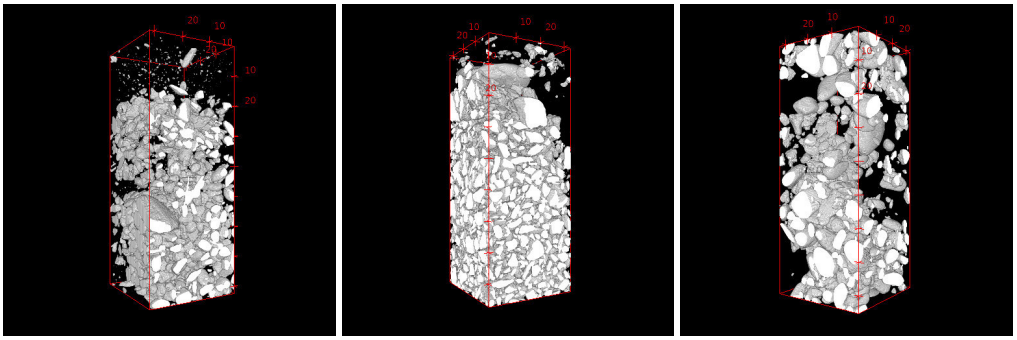

(a) MON (dried and humid). (b) COP-01. (c) COP-02.

Figure 4.11: 3D rendering of gravel spatial distribution.
Scale in mm.

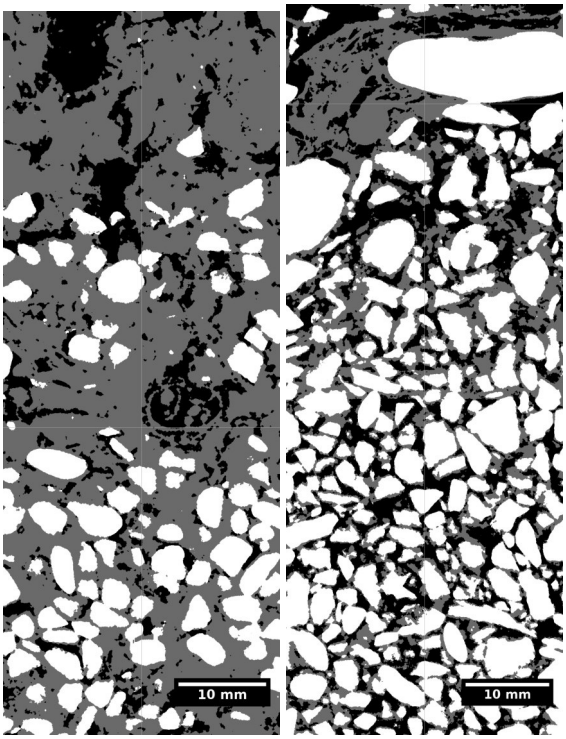

(a) MON-Dried (b) COP

Figure 4.12: Orthogonal views of segmented images.
White: gravel, gray: OM, black: voids.

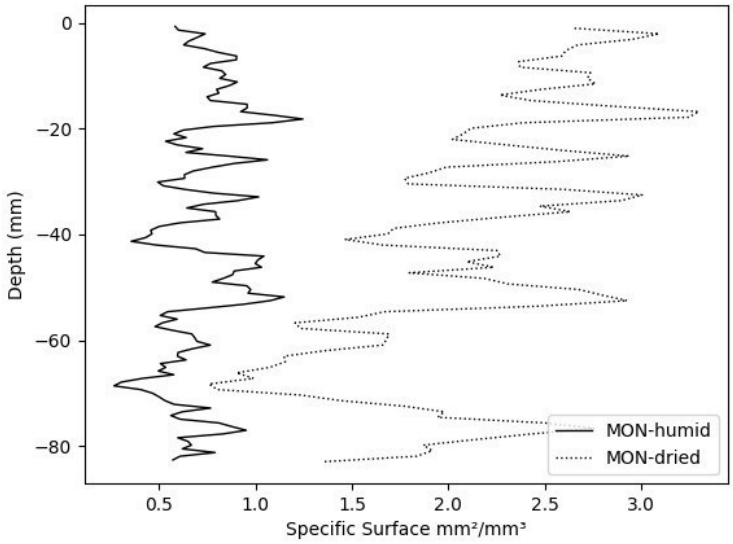

Figure 4.13: Specific Void-OM surface area profiles

keep in mind that the water and FM phases could not be separated with the current methodology. The observed increase in specific surface and void volume is then probably overestimated since some interfaces between FM and water filled pores were probably invisible in the MON-humid sample. Further developments are then required to improve these first results.

The increase in specific surface mostly corresponds to the opening of cracks and voids during the drying process. It is convenient to compute percolating pathways based on the skeleton methodology to get a better geometrical description concerning this phenomenon. A notorious increase of the size and number of connected percolation pathways is clearly evidenced in Figure 4.14. This increase of pathways in the dried sample is most probably due to a combination of water drainage and shrinkage of the FM phase. This phenomenon is probably associated to an increase of the infiltration capacity of TW after a rest period. Further work on the description of these networks should be the subject of future research on this type of media.

This comparison of X-ray CT scans performed on the same sample before and after drying demonstrates that drying does not provide a significant improvement of the scan quality. This result motivates a study of humid samples by X-ray CT to be done and opens an interesting research perspective concerning the analysis void phase changes due to drying and humidification during feeding and rest periods.

4.4 Conclusion

Computed tomography is a promising technique to characterize treatment wetland porous media. The technique was successfully applied to produce 3D images of filtering media sampled in 2 different VFTW full-scale plants. Samples should be manually extracted with care to avoid compaction although a proper quantification of this phenomenon still needs to be carried out.

The samples can be scanned without any pretreatment, such as drying, resulting in satisfactory contrast level between three main phases: void, fouling material and gravel. However, the level of contrast does not allow the differentiation of elements in the fouling material phase to be done, i.e. solids from waste water, plant tissues (roots, rhizomes, leaves...), and water.

The application of specific image processing algorithms is mandatory to exploit the 3D-

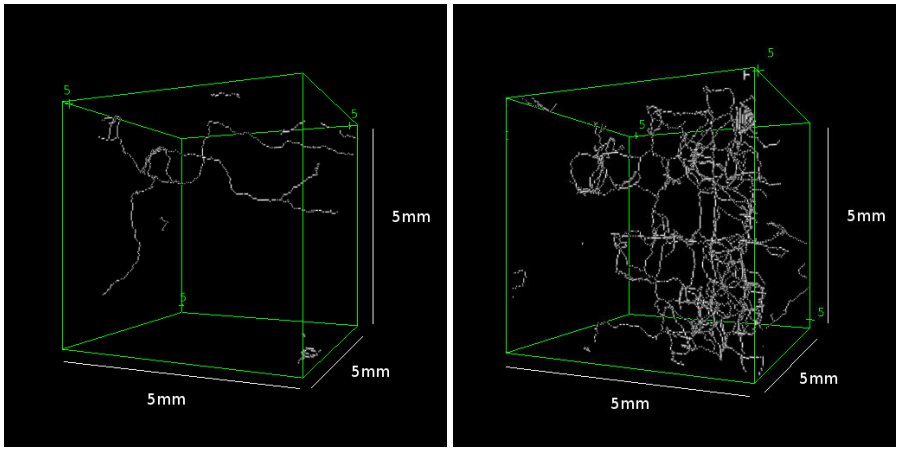

(a) MON-humid. (b) MON-dried.

Figure 4.14: Connected percolation pathways for voids larger than 0.035 mm

images at best. Phase segmentation is the first stage of image processing to obtain quantitative description. Once performed, many tools can be applied ranging from topological description to flow modeling. In this article the focus is restricted to topological description. These descriptions are limited to elements larger than the resolution of the images. The resolution depends on the sample size and the features of the X-ray scanning facility. The next step in the assessment of this methodology is to analyze the representativity of the topological descriptions regarding the sample and the VFTW sizes.

The results, obtained from 4 different scans show significant differences in terms of fouling material content and morphology of the void space. The aim of this study was to evaluate the applicability of X-ray CT to TW filtering media and to develop tools to post-process the results. Results are very encouraging and many tools and methods used in geology to study porous media can be directly applied to TW media. This encourages further application of X-ray CT to study the evolution of the filtering media in TW, and to model particle transport at the pore scale. Such methodology can be very useful to study clogging and changes of porosity structure according to season, loads and operational parameters for instance.

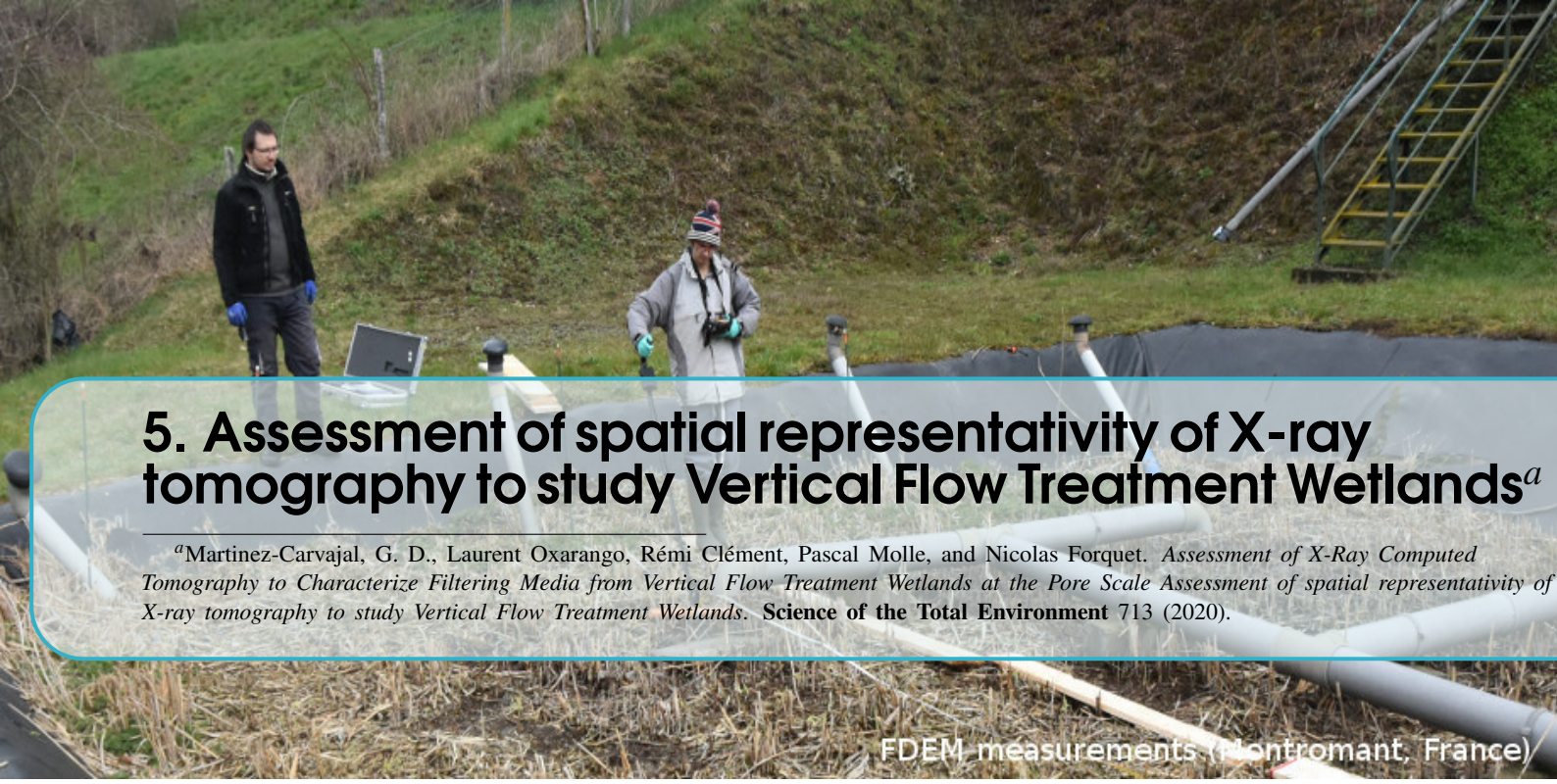

5. Assessment of spatial representativity of X-ray tomography to study Vertical Flow Treatment Wetlands[a]

[a]Martinez-Carvajal, G. D., Laurent Oxarango, Rémi Clément, Pascal Molle, and Nicolas Forquet. *Assessment of X-Ray Computed Tomography to Characterize Filtering Media from Vertical Flow Treatment Wetlands at the Pore Scale Assessment of spatial representativity of X-ray tomography to study Vertical Flow Treatment Wetlands*. **Science of the Total Environment** 713 (2020).

5.1 Introduction

TREATMENT wetlands are a nature-based technology that present an alternative to conventional wastewater treatment technologies [113]. Among the different possible configurations, French Vertical Flow (VF) treatment wetlands have largely been adopted for treatment domestic wastewater for communities under 5,000 people equivalent in France[82]. They are often composed of three parallel first-stage filters followed by two parallel second-stage filters filled with granular materials and planted with *Phragmites Australis*.

The first stage typically contains a 30 cm deep layer of coarse gravel (2 – 6 mm). The three first-stage cells are fed raw with wastewater in an alternating manner; 3.5 days of feeding followed by 7 days of rest. The rules of design and implementation of French VF treatment wetlands can be found in [79]. As the first-stage filters are fed with raw wastewater, solid particles are retained at the surface by cake filtration and in the filter media by deep bed filtration. In first-stage French VF wetlands, deep bed filtration is the predominant solid retention mechanism in newly commissioned filters, whereas cake filtration is the predominant mechanism once a deposit layer is formed. The deposit layer is the result of the accumulation of solids at the filter surface.

The entrapped solids are herein referred to as the biosolids[1], which are present in the deposit layer as well as the gravel filtration layer. Biosolids are characterized by their high organic matter content which ranges from 50% to nearly 90% [47] and form a porous medium whose structure and consistency evolve with time due to water content changes, organic matter mineralization and internal erosion. Kania et al. [47] characterized the surface deposit of 14 French VF treatment wetlands and conclude that the deposit layer on mature wetlands (> 3 years of operation) has lower OM content, lower biodegradability, and higher humification than newly commissioned wetlands ($\leq\sum$ 3 years of operation). Structure of biosolids impacts water and oxygen transfer as well as biological activity [78]. The biosolids in the deposit and gravel layers are home to the microorganisms and micro-fauna responsible for degradation of pollutants. They retain part of the percolating water, and when the wetland is functioning properly, the structure of biosolids maintains a good re-oxygenation capability during rest periods, which is essential to promote mineralization of organic matter [78].

[1]For style purposes, the term “biosolids” is used in this article instead of “fouling material”. The meaning of this term remains exactly the same as in previous chapters of this thesis.

Understanding the structural evolution of biosolids in the deposit and gravel layers is crucial since it constrains maintenance frequency and the lifespan of the treatment wetland. The deposit layer has to be removed every 10 - 20 years to maintain infiltration capacity, and the fouling material accumulation within the granular material inevitably leads to its clogging and therefore defines the lifespan of the system [85].

Investigations on solid retention in treatment wetlands generally focus on Horizontal Flow (HF) treatment wetlands, which are more prone to clogging than VF wetlands due to the fact that HF wetlands generally have a much smaller cross-sectional surface area accepting wastewater, thus they experience a higher areal organic loading rate [51, 22]. They aim at evaluating the degree of clogging and proper functioning of a treatment wetland, and provide little information regarding the underpinning mechanisms because those depend on pore scale properties. In order to gain insight into the pore scale structure, a recent study assessed the application of X-ray Computed Tomography (Xray-CT) to obtain high resolution 3D images of the porous media structure [67]. Promising results were achieved but the study raised the question of the spatial representativity of the samples used for Xray-CT.

Assessing the spatial representativity of Xray-CT images from French VF treatment wetlands is critical to ensure the reliability of pore scale properties that may be derived from these images. French VF treatment wetlands present heterogeneities at both the filter and the pore scales.

At the filter scale, two main types of macro-scale heterogeneities [21] could be considered: uneven distribution of biosolids and uneven reed density. These heterogeneities are most likely controlled by the general design of the filter including its shape and the location of feeding points. Forquet et al.[31] computed the relative water content changes in the deposit layer over a vertical cross sectional area of a mature French VF treatment wetland (20 cm thick deposit layer) during a feeding period using time-lapse Electrical Resistivity Tomography (ERT). Water content in the deposit layer increased by 14% in a region of 50 cm around feeding points and by less than 4% for the rest of the analyzed vertical cross-section. Heterogeneities in the deposit layer are likely to evolve in French VF treatment wetlands due to the reed growth and colonization, the progressive accumulation of biosolids in the pore space of the gravel layer, and the mineralization of biosolids in both the deposit layer and gravel layer. The older a French VF treatment wetland is, the smoother these heterogeneities become. This is especially the case for plants because it may take several years before the plant cover is fully established. Factors affecting the speed of plant establishment include plant species, age, availability of adequate micronutrients, and adaptation to the environmental conditions found in in treatment wetlands [64, 16].

At the pore scale, the French VF treatment wetlands are comprised of gravel, biosolids, water and void space. The representativity of samples at this scale depends on the distribution of these phases in terms of volumetric contents and characteristic sizes. Many studies rely on the computation of the Representative Elementary Volume (REV) to assess the spatial representativity of samples [21, 1, 60]. The 'p'-REV is the minimal volume of a sample from which the volume-weighted average value of the property 'p' is no longer dependent on the volume of the sample and then becomes representative. Several methods have been proposed to assess the REV size. They are all based on iterative processes where the volume integral of the property 'p' is computed over volumes increasing in size but they differ on the origin of this sampling volume: a single point taken in the middle of the sample [21, 1] or multiple points randomly distributed over the sample [126, 98]. In porous media, the most common property analyzed is the void volume fraction (e.g., porosity), but REV of other properties, such as specific surface area (SSA), moisture saturation, coordination number, or local void ratios are also studied [1]. A subject of great interest is to assess whether or not achieving the porosity-REV implies that REV for other properties is achieved too. Some authors have investigated this question and their conclusions vary. Al-Raoush and Papadopoulos [1] found that the porosity-REV is

smaller than the REV for particle size distribution, local void ratio and coordination number for sand samples with different uniformity/gradation degrees. Robinson et al. [21] found larger porosity-REVs than REVs for interfacial area A_i and moisture saturation S_w in wet samples of glass beads and silica sands. However, these authors stated that REV deterministic computation is difficult because of the lack of a robust criteria to determine whether the averaged value of the property 'p' is constant or not.

This work demonstrates the spatial representativity of samples extracted from a first-stage French VF treatment weltand by examining the heterogeneities present at both the pore scale and the filter scale. This is achieved by (i) determining whether the size of the samples is large enough to ensure spatial representativity at the pore scale, and (ii) quantifying the similarity of pore scale structure of samples from the same filter extracted at different locations.

5.2 Materials and methods

5.2.1 FDEM and choice of sampling points

The study was carried out on a full scale French VF treatment wetland in Montromant (Rhône, France). It was designed according to French standards defined in [79] for 200 people equivalent. It has two treatment stages: a first stage consisting of four parallel filters, and a second stage containing two parallel filters. Each filter in the first stage is approximately 64 m^2. Since its commission in 1994, three of the four filters in the first stage were in operation. In 2009, the deposit layer of these filters was removed and the fourth filter in the first stage was put into operation. The duration of the feeding period remained 3.5 days and the rest period was increased from 7 days to 10.5 days. The filtration layer is 30 cm thick and is made of 1 to 6 mm gravels (d_{10} = 2 mm and uniformity coefficient = 1.5). Based on regulatory monitoring measurements performed in 2013, the suspended solids (SS) and the Chemical Oxygen Demand (COD) loads applied to the first stage filter in operation were 158 $g \cdot m^{-2} d^{-1}$ and 262 $g \cdot m^{-2} d^{-1}$, respectively. More details on the site description can be found in [67]. All measurements were conducted on a single first stage wetland cell.

The study was carried out at the VFTW in Montromant (Rhône, France). It has been designed according to French standards defined in [79] to treat effluent from 200 people equivalent. It has two treatment stages, consisting of four filters in parallel for the first stage and two filters in parallel for the second stage. Since its commission in 1994, three of the four filters in the first stage were in operation. In 2009, the deposit layer of these filters was dredged out and the fourth filter in the first stage was put into operation. The duration of the feeding period remained 3.5 days and the rest period was augmented to 10.5 days. More details on the site description can be found in [67]. All measurements were done on a single filter of the first treatment stage. The experiment consisted in successively (i) mapping the TW near surface Electrical Conductivity (EC) and (ii) sampling cores for X-ray tomography in areas of homogeneous EC.

5.2.2 Electrical conductivity mapping

Gravel is a geomaterial having low Electrical Conductivity (EC). On the other hand, the water and organic matter constituting the biosolids present a high EC. Geophysical methods, such as Frequency Domain Electromagnetic Method (FDEM) and Electrical Resistivity Tomography (ERT), thus present interesting capabilities to estimate the spatial distribution of biosolids in the top layer of a French VF treatment wetland. In particular, FDEM presents a suitable sensitivity for highly conductive media [73]. Its application on French VF treatment wetlands is promising considering that EC (the inverse of electrical resistivity) measurements using ERT have shown values between 2.5 and 50.0 $mS \cdot m^{-1}$ in French VF treatment wetlands [81]. FDEM has been widely used by soil scientists to study the spatial variability of soil properties in the field

[24, 52]. It provides a 2D map of the EC. Soil EC measured by FDEM does not allow a direct characterization of soil characteristics like water content or hydraulic conductivity, but their correlation is used to compute estimates of these properties using petro-geophysical models (e.g. Archie's Law).

The FDEM sensors generate a primary oscillating electromagnetic (EM) field, which propagates through the soil. It induces alternating currents that in turn produce a secondary EM field measured by the sensor. Under conditions known as 'low induction number', a linear relationship exists between the quadrature component of the secondary EM field and the electrical conductivity of the soil penetrated by the EM field [13, 14]. This relationship allows the measurement of EC.

In this study, a CMD-TINY electromagnetic induction tool (GF Instruments) was used. It simultaneously collects both in-phase and quadrature component data. The device is a frequency electromagnetic induction sensor with a frequency of 9 KHz composed of two coils, an emitter and a receiver, with an inter-coil spacing of 0.45 m. The depth of the magnetic field penetration was estimated to about 35 cm for the vertical dipole mode. To obtain measurements, the device was swept over the investigated area of the filter. Therefore measurements were carried out at the end of winter 2018, when *Phragmites* were cut off. The pipes that dispose wastewater at the treatment wetland surface are made of plastic and thus do not interfere with the measurements. Data were collected on a regular grid ($\Delta x = 0.5$ m, $\Delta y = 0.5$ m). The map of the EC was computed using a linear interpolation between the points of the grid.

EC data were filtered to eliminate defective points by applying two thresholds:

- Electrical conductivity values below 0.1 $mS \cdot m^{-1}$, the limit of detection of CMD-Tiny, were not taken into account
- Phase changes exceeding 2.5 ppm were eliminated. Measurement of the in-phase component of the signal indicates magnetic disturbance in the ground. If the phase change is above this threshold, the linear relationship between the electrical conductivity and the quadrature component is not verified and the McNeil relationship is thus not applicable [73].

5.2.3 Sampling

FDEM measurements were also used to drive the sampling procedure for Xray-CT. Based on the map of electrical conductivity, three regions, approximately 1 m in diameter, were selected. At the beginning of a rest period, two samples per region, named A and B, were extracted. The samples consisted of cylinders of 5 cm in diameter and 16 cm in height. The extraction method is described in detail in [67]. Samples were identified with a number corresponding to the sampling region and a letter (A or B). Cores A and B were sampled as close as possible to each other. The height of the samples was large enough to contain all the deposit layer and at least 5 cm of the gravel layer. The cross-sectional area of samples was approximately 19 cm^2. After the extraction, all the samples were sealed with a plastic film and stored at 5 °C to avoid water evaporation. They were scanned by X-ray tomography within the following 72 hours.

5.2.4 X-ray tomography and segmentation

Tomographies were performed with a tomograph EasyTom XL (RX Solutions) at University Grenoble Alpes. The scanner was equipped with a 150 kV tungsten X-ray tube. It was operated with an accelerating voltage of 140 kV and a current of 200 μA. A 0.5 mm copper foil filter was put in front of the X-ray source to reduce beam-hardening artifacts. 4480 projections distributed among 360° were recorded. The sensor area was 250 × 200 mm with 2084 × 2084 pixels. Scans were obtained using a helicoid acquisition. The data were reconstructed using a cone-beam algorithm (X-Act 2.0, RX Solutions). 3D images consist of approximately 1500 × 1500 × 4600

voxels ($l \times w \times h$) with a voxel size of 35 μm. No contrast enhancing was performed during the reconstruction. The reconstructed data were then processed and visualized with the public domain ImageJ/Fiji [109] and Python [120] sharewares. A three-phase segmentation of the scans was performed based on a region growing algorithm developed by Hashemi et al. [35]and adapted in a previous study [67]. Segmentation consists in the attribution of the voxels of a digital image to a single phase based on their gray values and those of their neighbors. This algorithm allows to successfully segment three phases: voids, biosolids, and gravels.

In images containing multiple phases, the ranges of gray values corresponding to each phase overlap due to small differences in absorption coefficients, thus generating noise. Segmentation is often preceded by pretreatment routines to facilitate the voxels attribution such as smoothing filters to reduce noise. In this work, the median filter used in [67] has been replaced by an anisotropic filter [7, 90, 119]. A simple diffusion filter reduces noise by smoothing values proportionally to the gradient of gray value. However, it tends to blur the edges between different phases (i.e. interfaces between gravel, voids and biosolids). In anisotropic diffusion, noise is reduced by applying smoothing in the edge tangential direction but not in the normal direction which preserves the location of interfaces better.

The application of the anisotropic filter leads to a better recognition of voxels presenting a Partial Volume Effect (PVE). PVE appears when two phases are taken into account into a single voxel, thus making it more difficult to assign the voxel to a single phase. These voxels are preferentially located at edges of phases, where the gray level gradient is maximum. PVE voxels were defined by thresholding the image of the gradient of gray values using the FIJI's routine 'Find Edges' [67].

5.2.5 Post-treatment

5.2.5.1 Morphological properties

Three pore scale measurements were obtained by image post-processing (after segmentation): volume fraction profiles for each phase (voids, gravel, and biosolids), SSA profiles for the interface between voids and biosolids and pore size distributions of the void phase.

Volume fraction profiles were obtained by computing the ratio between the number of voxels belonging to each phase and the total number of voxels (the sum of the three phases) for each horizontal slice. Profiles were smoothed using a moving average window of 57 voxels in depth with a displacement of one voxel at a time. 57 voxels (2 mm) corresponds to the d_{10} value of the gravel size distribution.

The SSA is obtained by dividing the surface of the interface between voids and biosolids by the bulk volume. The surface of the interface between voids and biosolids was computed using the Cauchy-Crofton cutting line method [54, 55, 107]. This method allows to numerically estimate the interface areas with a better accuracy than the direct counting of interface voxels, which presents a "staircase effect". In addition, it has a much lower computational cost than methods based on surface meshes. For each voxel belonging to the void phase located at the interface with the biosolid phase, the algorithm consists in counting the number of neighboring voxels in the biosolid phase with respect to three families of connection: 1-connected (face-connection), $\sqrt{2}$-connected (2D diagonal/edge connection) or $\sqrt{3}$-connected (3D diagonal/corner connection). The number of connections of each type is then multiplied by a characteristic coefficient obtained from the Voronoi's tesselation of the unit sphere. The sum of these contributions results in the value of the surface. The specific surface area profile was obtained by computing the specific surface areas of subsamples 57 voxels in height without overlay.

The pore size distribution was obtained by computing the local thickness map of the void phase of the segmented images. The local thickness map of a 3D object is another 3D image where each voxel stores the diameter of the largest sphere that fits inside the object and contains

the voxel (without being necessary centered at the voxel). The computation of the map was conducted using the FIJI plugin called Local Thickness Map [37, 105]. This method has previously been used to compute pore size distributions in sandstone [15].

5.2.5.2 Representative Elementary Volume (REV)

The REV for the volume fraction of voids, biosolids and gravels were computed for one of the samples (MON1A) at several 2D slices (1-voxel thick) corresponding to four different depths in the sample. They are herein referred to as void-REV, biosolid-REV and gravel-REV. The average volume fraction of each of the three phases is computed for concentric circular windows of increasing radius ranging from 1 voxel to the sample radius. The volume fractions of each phase are then plotted as a function of the radius of the circular windows. The analysis of several 2D sections using concentric circular elements was preferred to a 3D analysis (using concentric cylinders) because (i) the influence of *Phragmites* on the sample structure is easier to analyze and (ii) French VF treatment wetlands present a natural vertical gradient of phase distribution in the direction of the water flow due to cake and bed filtration of solid particles [67]. Therefore, 3D REV would integrate vertical variations of phase volume fractions that are already analyzed in volume fraction profiles and introduce a bias regarding the minimum representative sample diameter.

5.3 Results and discussion

5.3.1 FDEM and choice of sampling points

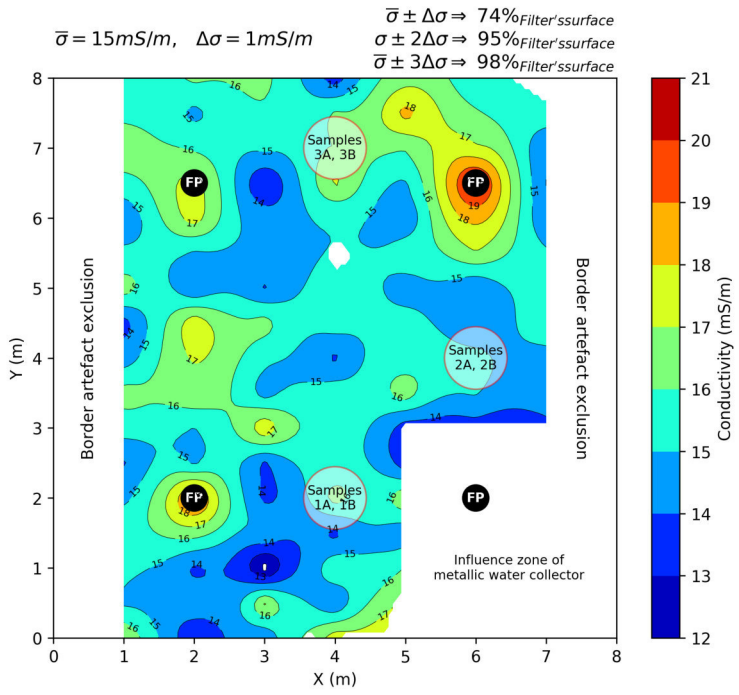

Figure 5.1: Electrical conductivity map of the filter.
FP stands for feeding points. Samples regions are indicated on the map. $\bar{\sigma}$ is the electrical conductivity mean value and $\Delta\sigma$ is the chosen threshold value for the measurement sensitivity.

A map of the electrical conductivity of the topmost layer of the filter is drawn according to the methodology presented in section 5.2.1 (Figure 5.1). This method captures the spatial variation of biosolid content over the entire filter surface. In highly conductive materials, Clément et al.

[19] and McNeil [73] advised to only consider variation ($\Delta\sigma$) larger than 6% of the mean value of EC ($\Delta\sigma$ = 1 $mS \cdot m^{-1}$, in our case) as significant compared to the manufacturer specification, which considers variations larger than $\Delta\sigma$ = 0.1 $mS \cdot m^{-1}$ as significant. EC values within the ranges ($\pm\Delta\sigma$) and ($\pm 2\Delta\sigma$) correspond to 75% and 95% of the filter surface, respectively. The high values of EC (13 - 17 $mS \cdot m^{-1}$) observed for almost the entire surface of the filter indicate a homogeneous distribution of organic matter and water embedded in the biosolids because biosolids present a high moisture content due to capillarity effects and the presence of biomass.

The remaining surface corresponds to circular areas of less than 1 m in diameter located around the feeding points. A significant increase of the EC in these regions is observed, which is most likely a result of the higher organic matter content and water content in the biosolids and/or a larger content of biosolids in depth. These results are complementary to those presented in [31] where electrical resistivity measurements showed that, during a feeding period, the water content in a first stage French VF treatment wetland increased by approximately 7% - 14% at distances less than 0.5 m from the feeding points and by less than 4% for the rest of the filter. When water exits the feeding pipes, it infiltrates predominantly in the vicinity of a feeding point, leading to a preferential accumulation of biosolids and water retained by capillarity. Except for these localized effects, variations of EC in Figure 5.1 do not depend on the distance to the feeding points. This homogeneity may be explained by the age of the French VF treatment wetland (25 years) as it is observed that the homogeneity of the biosolid distribution depends on the age of the facility and the applied load [78].

Values in the white regions on Figure 5.1 are not plotted as they correspond to parts of the filter with specific features that induce artifacts [19]: (i) the freeboard produces an artifact that extends over 1 m from the filter edges. (ii) at the bottom-right part, a metal lid covers the water collector at the outlet of the the French VF treatment wetland which also induces an artifact.

Xray-CT complements the data acquired by electromagnetic mapping. Xray-CT gives insight on the vertical structure and phase distribution of the filter as its resolution (about 100 times better than FDEM data) gives more detail. FDEM can drive the choice of the Xray-CT sample location by identifying areas with homogeneous water and biosolid content. Consequently, Xray-CT sample location may be chosen wisely to achieve good spatial representativity with a limited number of samples. As the surface of the filter is considered to be homogeneous away from the immediate surrounding of the feeding points and in order to compare samples to each other, the sampling points were chosen randomly over this area. The 3 sampling regions are shown in Figure 5.1.

5.3.2 Comparison of pore scale properties between the samples

5.3.2.1 Phase volume fraction profiles

In figure5.2, the volume fraction profiles of each phase (voids, biosolids, and gravels) are drawn for each sample and presented along with an example of 2D vertical slice. Similar trends, observed in all the samples, can be highlighted:

- The void volume fraction is the highest near the surface (50% - 85%) and decreases with depth to levels lower than the two other phases.
- In the first centimeters, the biosolid and the void volume fraction are always predominant.
- At greater depths, the biosolid and gravel volume fractions are the predominant phases.

These observations match the current understanding of filtration mechanisms in French VF treatment wetlands. The deposit layer is built up by cake filtration. This leads to a higher content of biosolids in the deposit layer than in the gravel layer. The high resolution of Xray-CT provides interesting details on the structure of the deposit and biosolids within the filter. Figures 5.2(a) to 5.2(f) illustrate that there is no clear delimitation of the end of the deposit layer and the beginning of the gravel layer at the micro-scale. In particular, the end of the deposit layer cannot be defined

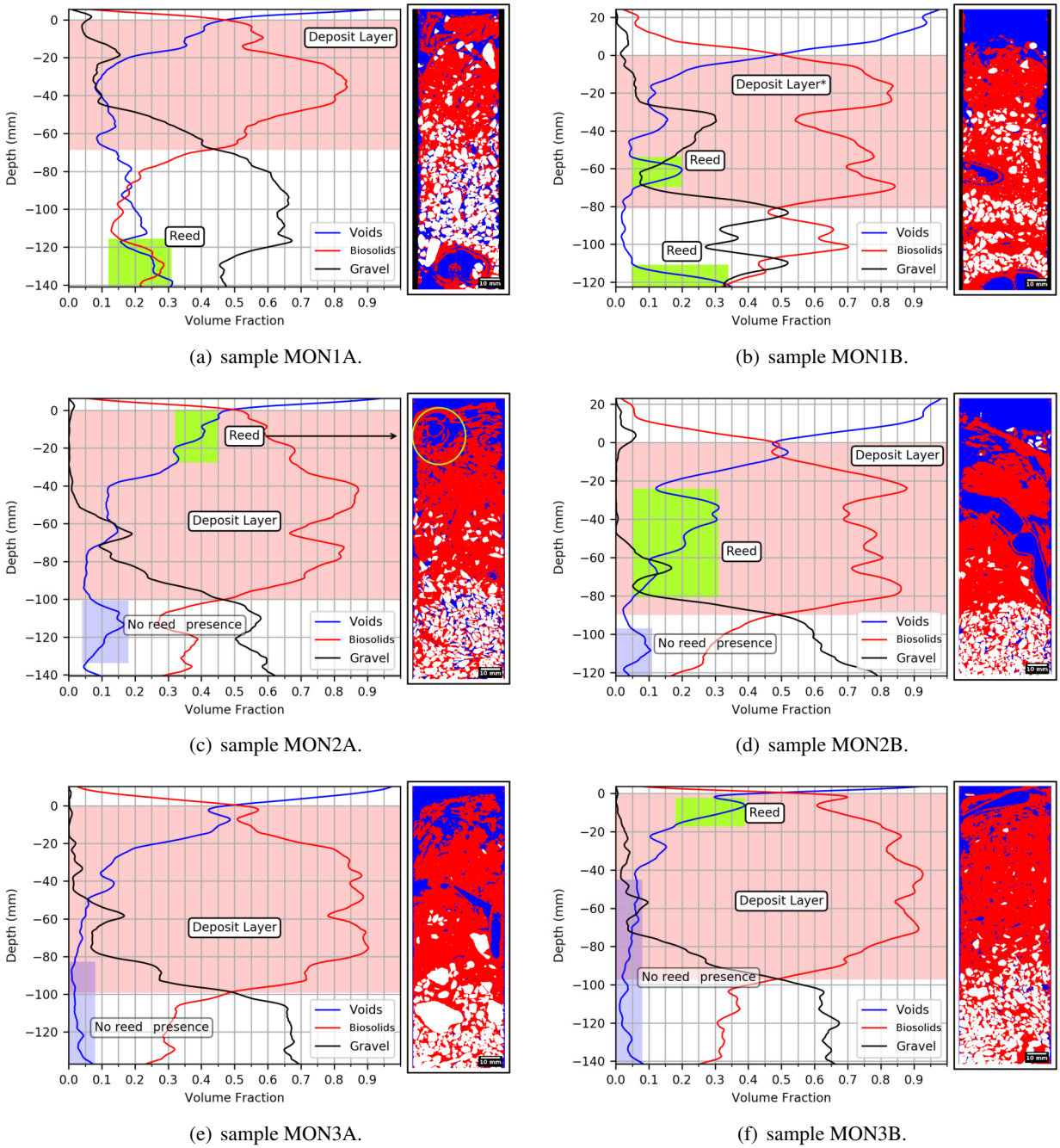

(a) sample MON1A.

(b) sample MON1B.

(c) sample MON2A.

(d) sample MON2B.

(e) sample MON3A.

(f) sample MON3B.

Figure 5.2: Volume fraction versus depth of each phase.
Voids, biosolids, and gravels on the left, 2D vertical slice of the segmented image on the right.

Table 5.1: Thickness and average volume fractions of the constitutive phases for the different layers

	Sample	Volume fraction (-)			Thickness (mm)
		Voids	Biosolids	Gravel	
Deposit layer	MON1A	0.18	0.65	0.16	69
	MON1B	0.13	0.71	0.16	81
	MON2A	0.19	0.71	0.10	100
	MON2B	0.21	0.72	0.06	89
	MON3A	0.14	0.77	0.09	99
	MON3B	0.11	0.80	0.09	97
Gravel layer	MON1A	0.21	0.21	0.58	73
	MON1B	0.08	0.53	0.40	42
	MON2A	0.10	0.34	0.56	41
	MON2B	0.06	0.31	0.63	33
	MON3A	0.03	0.32	0.65	38
	MON3B	0.03	0.34	0.63	44
Deposit + Gravel layers	MON1A	0.21	0.42	0.36	142
	MON1B	0.23	0.57	0.20	123
	MON2A	0.19	0.59	0.22	141
	MON2B	0.28	0.54	0.18	122
	MON3A	0.16	0.61	0.23	137
	MON3B	0.10	0.65	0.25	141

as the depth at which the first gravel appears, as some gravel can be observed near the surface at depths where the biosolid fraction is predominant. This may be explained by segregation mechanism [102]: fine particles of the biosolids move beneath some pieces of gravel forcing them to migrate upwards. However, a systematic transition is observed between the deposit layer (where the void and biosolid phases are predominant) and the gravel layer (where the biosolid and gravel phases are predominant). The inversion of phase predominance is readily identified at the intersection of the biosolid and gravel curves which occurs around 40% - 50% of volume fraction. This systematical behavior is used to define the lower limit of the deposit layer. Similarly, the upper limit of the deposit layer is defined at the intersection of the void and biosolid curves at the top of the samples. The thickness of the deposit layer is represented by the red-shadowed regions in Figures 5.2(a) to 5.2(f). Furthermore, by setting this criterion, it is possible to compare specific features of the deposit layer and gravel layer 5.1.

Deposit layer

Most of the volume in the samples corresponds to the deposit layer. The total thickness of the deposit layer ranges between 7 and 10 cm. Samples MON2A, MON3A and MON3B have a deposit layer thickness of approximately 10 cm. Samples MON1A, MON1B and MON2B have a slightly thinner deposit layer: 7 cm, 8 cm and 9 cm, respectively. Samples from sampling region 1 show the lowest biosolid volume fraction (0.65 - 0.70) followed by sampling region 2 (0.71) and 3 (0.77 - 0.80). Xray-CT can capture small variations of the biosolid volume fraction and of the layer thickness. Nevertheless, the differences obtained among the samples (from 0.1 to 3.0 cm in the deposit layer, and from 1% to 15% in the biosolid volume fraction) may be explained by local compaction associated to maintenance operations (i.e. person walking on the filter) or local accumulation of stems and leaves. It creates a micro-topography that differs from the heterogeneities usually induced by uneven effluent distribution. This micro-topography is

not captured by spatial averaging technique like FDEM but is readily observable by Xray-CT.

To better estimate how the void volume fraction evolves in depth, the contribution of *Phragmites* has to be removed. For over half of the sample, the void volume fraction reaches values ranging from 0% to 15%. High values near the surface may visually be explained by the presence of a large number of macropores which is probably the sign of an ongoing consolidation of fresh biosolids or caused by movement of *Phragmites* stems. Finally, it must be pointed out that despite the low void volume fraction observed at the bottom of the deposit layer, water infiltrates normally on the surface of the filter.

Gravel layer

The phase distribution in the gravel layer (the region below the deposit layer in Figures 5.2(a) to 5.2(f)) tends to be more homogeneous than in the deposit layer with the exception of samples MON1B and MON2B. In other samples, where *Phragmites* are not present, gravel volume fraction ranges from 0.55 to 0.65 which is agreement with the value of 0.65 reported by Kim and Forquet [50]. Depending on the sample, the average value of biosolid volume fraction ranges from 0.21 to 0.53 with a decreasing gradient with increasing depth. The average void volume fraction are less than 0.1 with the exception of sample MON1A. Similar to what has be mentioned earlier for the deposit layer, the high biosolid content and the low porosity appears to not be detrimental to filter operation. It seems that the volume of void space is still large enough to provide gravity-driven infiltration. The void phase identified by tomography corresponds to pores larger than the tomography's resolution (35 $\mu m \cdot voxel^{-1}$). These large pores are often referred-to as the 'open porosity'. To access the micro-porosity inside the biosolid phase it would be necessary to enhance the resolution, which would require smaller sample size. The choice of sample size is discussed in 5.3.3.

In a gravel area with no biosolids, the gravel fraction goes up to 80%, whereas samples show that its fraction could be 5% to 10% lower (sample MON2B and MON2A, respectively) where fouling material is present. This result contradicts the usual understanding of clogging that considers a constant gravel volume fraction. Such a decrease in gravel density is likely due to the mechanical action of the biosolids during its invasion of the gravel pore space as mentioned in previous section.

Singularities

The more accurate the measurement is, the more likely heterogeneities are likely to be seen. These singularities may be explained for most of the cases by specific local features like the presence of reeds.

The presence of *Phragmites* alters considerably the void distribution and biosolid accumulation in the samples. This is particularly the case for sample MON1B (Figure 5.2(b)), where the criterion to define the limits of the deposit layer proposed in this work fails to describe accurately the sample. The green regions in Figures 5.2(a) to 5.2(f) show clearly how the major fluctuations in phase distribution are caused by *Phragmites*. A more homogeneous description could be obtained if *Phragmites* and their *Aerenchyma* were segmented separately. To assess this hypothesis, the image treatment methodology should evolve to a 4-phase segmentation procedure. This is particularly challenging since the contrast between the plant tissues and the biosolids in the gray-scale image is weak. A methodology based on shape recognition might enable such a segmentation.

There are also some fluctuations in the profiles that are not caused by the presence of a *Phragmites* (blue-shadowed regions in Figures 5.2(c) to 5.2(f)). For instance, in samples MON2A and MON2B, the gravel layer contains a zone of relatively low biosolid volume fraction. A simulation of solids transport at the pore scale may help to understand why there is no biosolids in some part of the gravel.

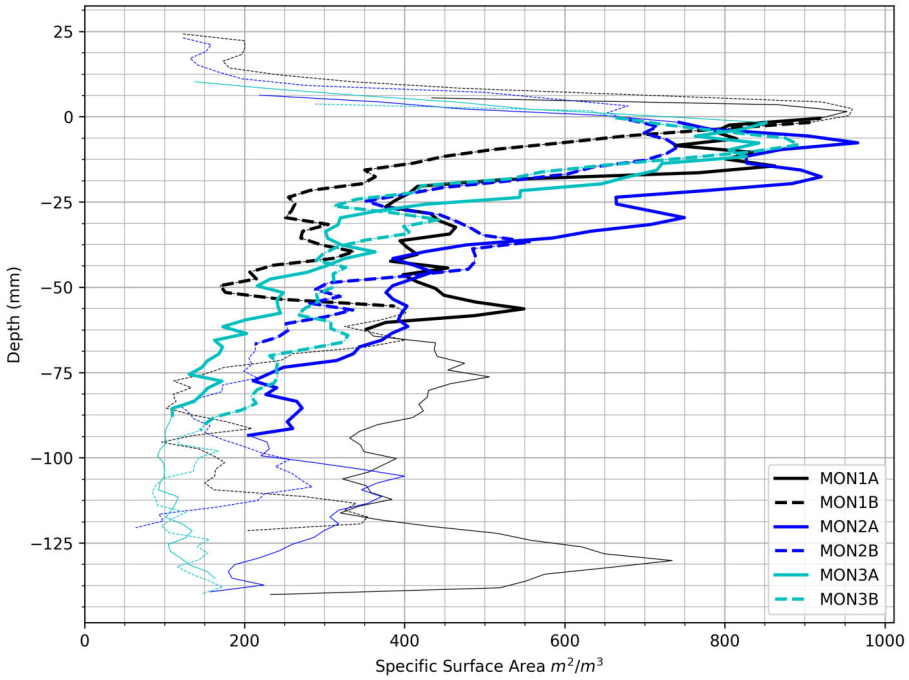

Figure 5.3: Specific Surface Area (SSA) versus depth.
Wider lines correspond to the deposit layer.

Table 5.2: Mean Specific Surface Area (SSA) of the sample constitutive layers.

	Specific Surface Area (SSA) (m^2m^{-3})					
	MON1A	MON1B	MON2A	MON2B	MON3A	MON3B
Deposit layer	539	362	507	468	367	384
Gravel layer	437	222	275	184	112	126

5.3.2.2 Specific surface area profiles

The Specific Surface Area (SSA) is an important parameter for biochemical reactions and for multiphase solute transport modeling. In French VF treatment wetlands, the SSA of the interface between voids and biosolids is of particular interest. Oxygen transport is a limiting factor for nitrification and mineralization [25]. Oxygen diffuses quickly in the air-filled porosity and most of the biological degradation occurs within biosolids [78], therefore the oxygen transfer from the air-filled porosity to the biosolids depends on the SSA of the interface between biosolids and voids.

he SSA profiles of the interface between biosolids and voids in Figure 5.3 show similar trends independently of the sample location. The sections where lines are wider correspond to the limits of the deposit layer following the criterion defined in Section 5.2. The fluctuations in the SSA profiles are due to local variations of void volume fraction and pore size, but the global trends are similar : (i) the highest values are located in the deposit layer ranging from 200 to1000 $m^2 \cdot m^{-3}$ for all the samples, while (ii) in the gravel layer, the range is lower and narrower (100 to 400 $m^2 \cdot m^{-3}$), except for sample MON1A. This may be explained in part by the larger volume of voids in the deposit layer compared to the gravel layer (see Table 5.1). The mean SSA for each layer is presented in table 5.2. The measurement of the SSA following the methodology detailed in Section 5.2.5.1 depends strongly on the resolution of the tomography (35 μm in this study). Increasing the resolution would allow the visualization of smaller pores, which if filled with air, would increase the SSA of the interface between biosolids and voids.

Table 5.3 compares results of this work with predicted and measured values of SSA for different treatment wetland media reported in the literature. Values vary mainly depending on the experimental methodology, and on the 'type' of surface. The comparison must be conducted carefully as each measurement is representative of different characteristics of the media (gravel surface, root surface, biofilm surface, micro-porosity surface) that are relevant at different space scales.

Results agree with theoretical approximations of SSA in other subsurface flow wetland designs [44, 49, 4]. In these approaches, the SSA is computed or measured considering macroscopic features of the media, such as the surface of granular media or the surface of the biofilm developing around the granular material and plant roots. The predicted values in [91] and [49] are considerably lower than the values obtained in this study as they computed the 'effective specific surface area' based on bio-kinetic models. The effective SSA is the active surface where biological reactions can take place. In fact, bacteria would only develop in a small fraction of all the available surface and thus the effective SSA should be lower than the value estimated by this method.

Measurements relying on adsorption/desorption methods yield values 10000 times larger than those of this study. These are molecular scale measurements, which depend on the molecule that is being adsorbed/desorbed (typically $H_2O(g)$ or $N_2(g)$). In the work of [47], the studied samples were taken from the deposit layer of French VF treatment wetlands. Values with a similar order of magnitude of SS were found by [92] and [114] when measuring the specific surface of peat using N_2 adsorption, mercury porosimetry and solution isotherms. However the measurements vary depending on the chemical and physical interactions between the adsorbate and the absorbent. Most of these surfaces are not accessible to Xray-CT methodology due to their location within the biosolids and because characteristic pore sizes are smaller than the scan resolution.

The use of SSA values for the interface between voids and biosolids as parameters in models for transport and reaction in French VF treatment wetlands must be carried out carefully. The measurements from this work are relevant for macroscopic transport of solutes within the open porosity, such as oxygen transport from the atmosphere to the biosolids, and are not relevant for microscopic transport phenomena inside the biosolids, such as adsorption and desorption or biochemical kinetic models.

Compared to other methods, the advantages of using X-ray tomography images to measure the SSA are: (i) a high spatial resolution compared to experimental methods that usually provide a global estimate only, (ii) measurements rely on the actual geometry extracted from the segmented images and there is no assumption of specific pore shape, or particle shape (iii) there is no bias induced by chemical or physical interactions between the adsorbate and the adsorbent. However, the computed values do not represent SSA of pores smaller than the resolution of the tomography, and thus, this approach does not take into account the small capillary pores within the biosolid phase. Nonetheless, small pores are often saturated with water thus limiting oxygen transfer during the feeding period and a part of the rest period.

5.3.2.3 Pore Size Distribution (PSD)

The description of the pore structure of TW is critical for the understanding of pore scale phenomena like fluids flow or solute and suspended solid transport. In Figure 5.4, the PSD of all the samples is plotted for the deposit and gravel layers separately. There is a remarkable similarity among samples regarding the mode, and the dispersion of pore sizes around the median values (Figure 5.5).

Omitting small peaks at the largest sizes, ($>$ 3 mm) which correspond to reed cavities, the distributions in Figures 5.4(a) and 5.4(b) can be described as unimodal. The mode ranges from 0.40 to 0.75 mm, ($\sim$ 10 to 20 voxels) independently of the layer (deposit or gravel) and the

Table 5.3: Comparison of different studies on TW Specific Surface Areas (SSA).

Mass SSA (m^2g)	Volumetric SSA (m^2m^{-3})	Type of media	Type of surface	Method	Pre-treatments	Comments	Source
-	10000	FWS TW[a]	gravels/voids + root surface/voids	Theoretical approximation	-	-	[91]
-	4.4	FWS TW	gravels/voids + root surface/voids	Predicted value	-	-	[91]
-	2.94 - 4.20	FWS TW	biofilm/voids	Predicted from kinetic model for COD degradation	-	Slab geometry assumption	[49]
-	360 - 24000	SSF TW[b]	gravels/voids + root surface/voids	Theoretical approximation	-	-	[44, 49]
-	3.6 - 47.37	SSF TW	biofilm surface surroundoing root/voids	Predicted from kinetic model for COD degradation	-	Cylindrical geometry assumption. Values depend on the biofilm thickness and the root diameter	[49]
8.9×10^{-4}	810	SSF TW	granules/voids	Water gravimetrical	None	surface estimated from water film thickness ($10\mu m$-$60\mu m$), spherical granules	[4]
13.5 - 218	1.35×10^7 - 21.8×10^{7}[c]	Deposit VFTW	deposit/voids	Dynamic vapor sorption	Drying (1 day at 35°C) + sieving (1 mm)	Mixed samples	[47]
-	100-1000	deposit + gravel VFTW	FM/voids[d]	Tomography	None	Depends on the depth of the sample	This work

[a]Free Water Surface (FWS) Treatment Wetland, [b]SubSurface FLow (SSF) Treatment Wetland, [c]Assuming a bulk density of 1000 $kg \cdot m^{-3}$, [d] FM = Fouling Material.

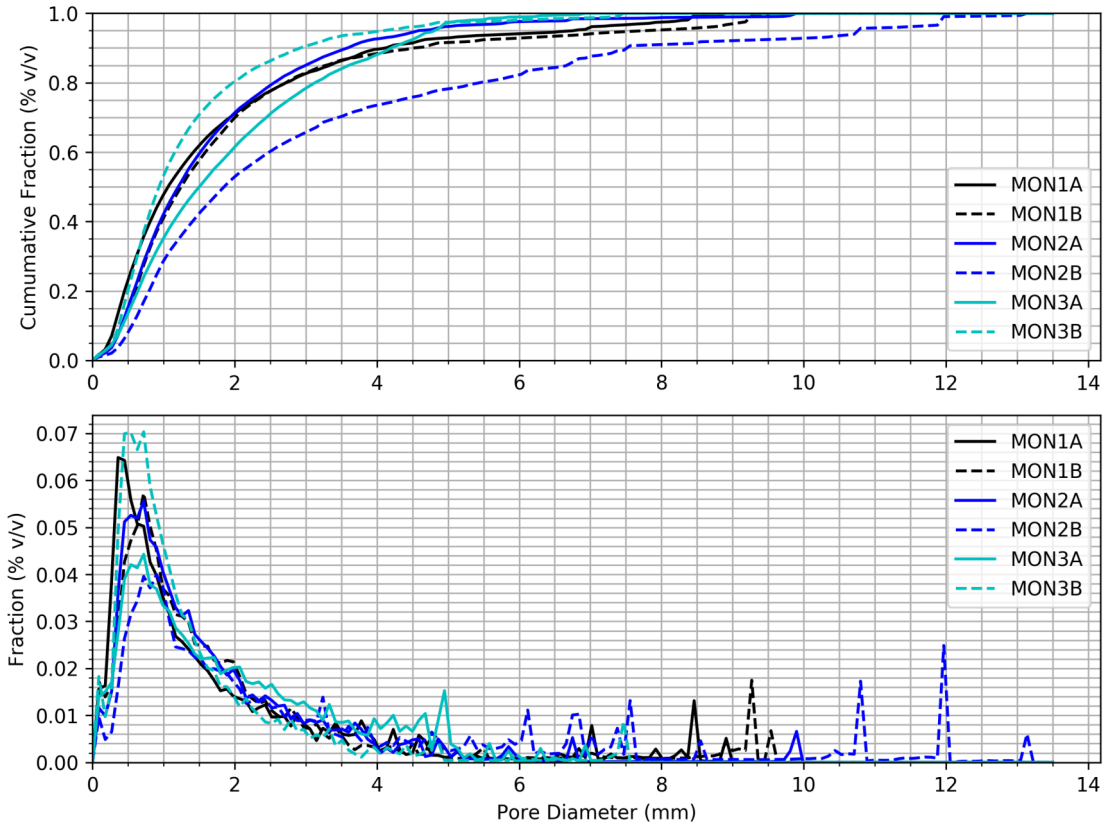

(a) Deposit layer.

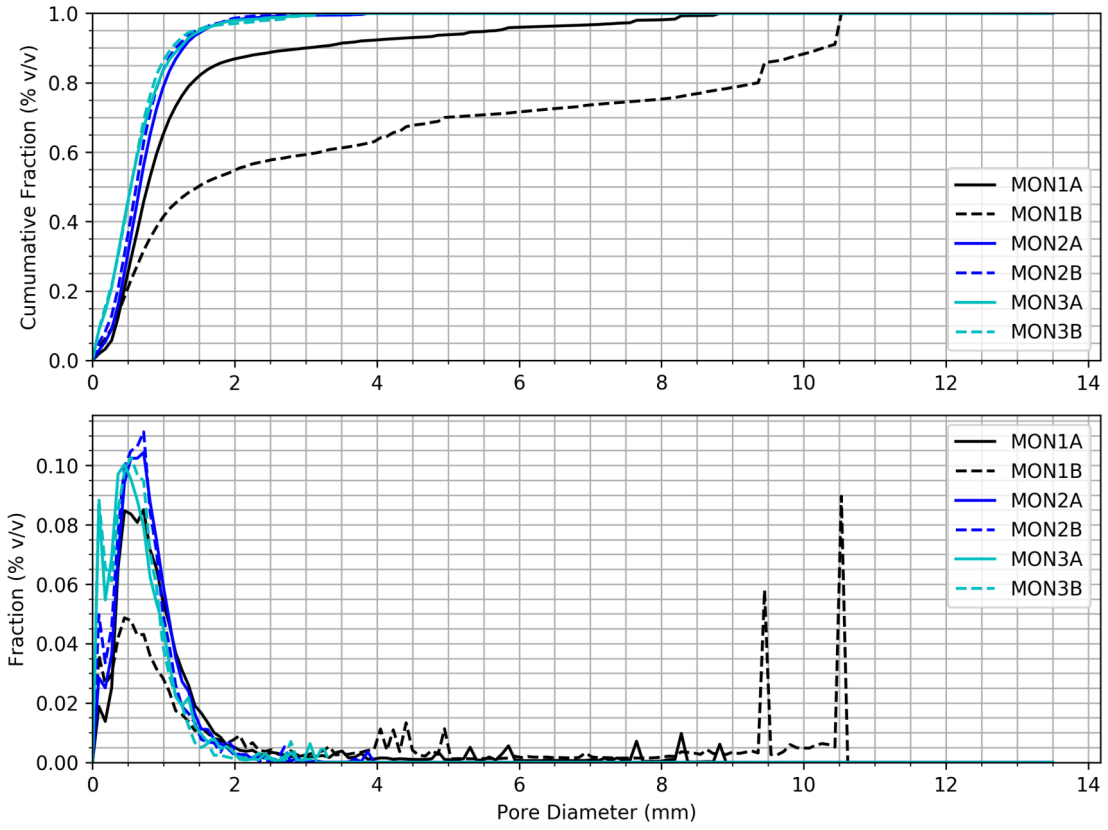

(b) Gravel layer.

Figure 5.4: Cumulative and frequency PSD for the deposit and the gravel layers.

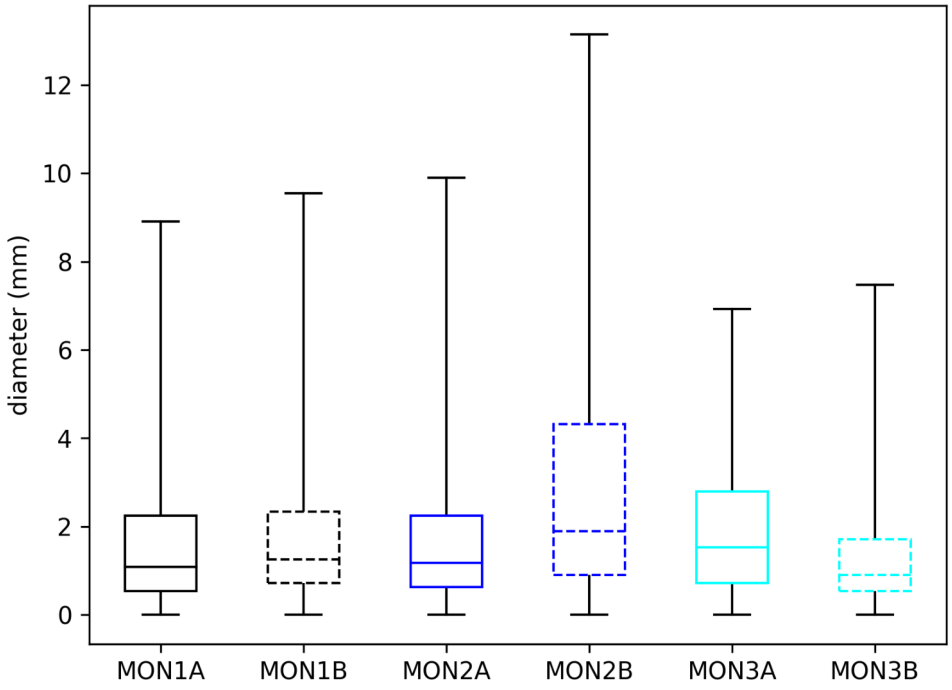

(a) Deposit layer

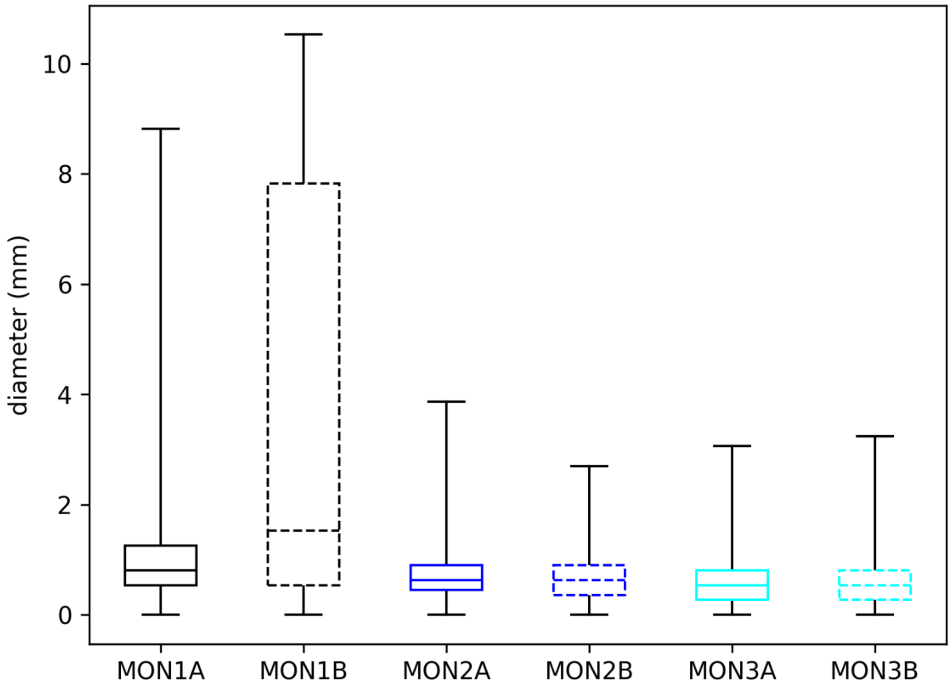

(b) Gravel layer

Figure 5.5: Pore Size Distribution (PSD) boxplots for the deposit and the gravel layers.
Dash lines corresponds to samples where reeds are present.

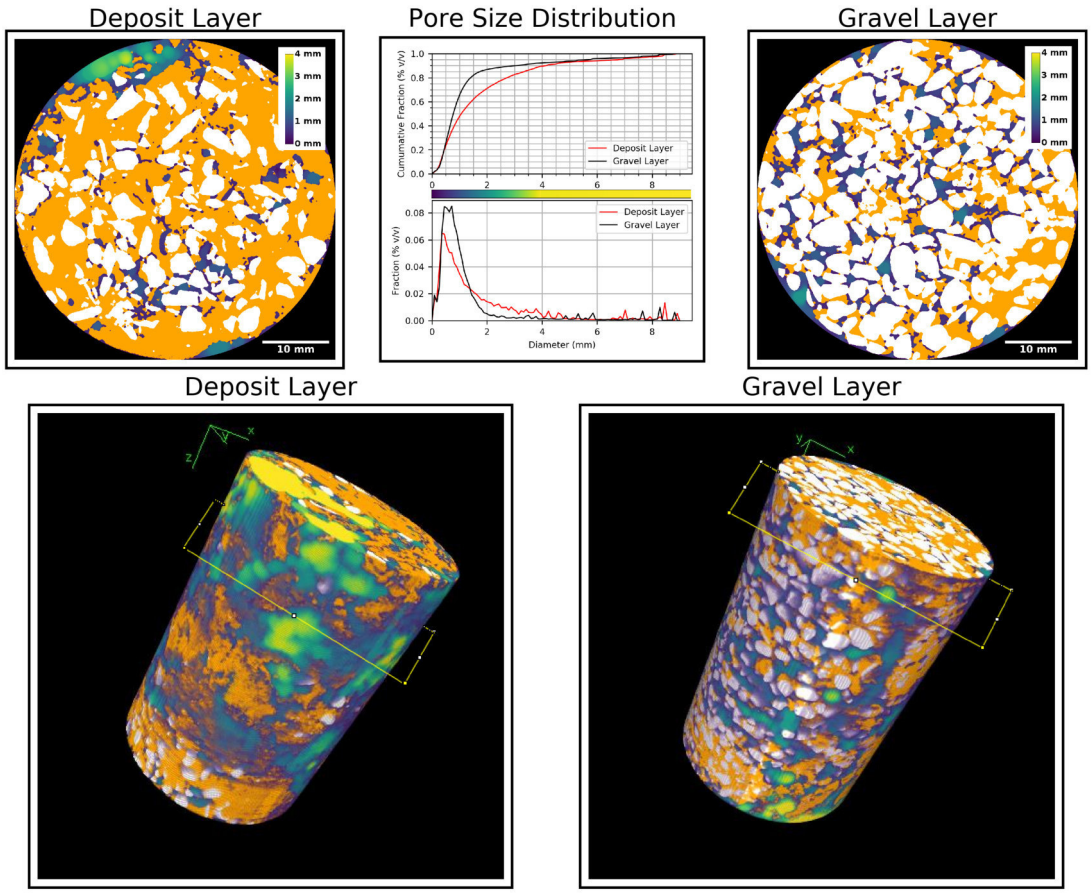

Figure 5.6: 3D rendering of pore local thickness map in the deposit and the gravel layers.

sample location.

In the deposit layer (Figure 5.4), pores smaller than 4 mm represent more than 90% of the void volume for all samples, except for sample MON2B which presents a *Phragmites* occupying a large volume within the deposit layer. In the gravel layer (5.4), the range of pore size is narrower. Pores smaller than 3 mm correspond to more than 95% of the void volume, except for samples MON1A and MON1B which have a *Phragmites* at the bottom of the sample. Some pores in the deposit layer may have been enlarged by movement of *Phragmites* as it can be seen in sample MON2A (Figure 5.2(c)), but this behavior has been observed clearly only once. In contrast, samples MON1B and MON2B contain large *Phragmites* deeper into the sample and no pore enlargement is observed around them. The only relevant difference among the samples is the diameter of the largest pores, which correspond to *Phragmites* (Figure 5.5).

Kim and Forquet [50]describe a bi-modal distribution of pore size. The mode of larger pores they observed matches the one obtained in this study (0.5 mm). The mode of the smaller pores in their work (near 50 μm) is almost at the same order of magnitude than the resolution of the scans in this study, explaining why those pores cannot be observed. This comparison must be interpreted very carefully as (i) the method used in [50] to compute the PSD relies on a different algorithm [26], (ii) the pore-size distribution was calculated on 2D thin section images and (iii) the procedure to produce the thin sections may affect pore shape.

Compared to the thin section method, X-ray tomography provides three main advantages: (i) it provides 3D informations with an acceptable resolution for larger volumes, (four times the

thickness of samples used for thin sections), (ii) 3D tortuosity and 3D pore connectivity can be studied [99], which gives a better description of the sample's morphology, and (iii) no sample pretreatment is needed.

The representativity of tomography has been discussed by comparing pore properties of different samples extracted at different locations in the filter. The heterogeneity within the sample and the smallest representative sample diameter are discussed in the next section.

5.3.3 Representative Elementary Volume (REV)

The void-REV, biosolid-REV and gravel-REV are deduced by analyzing the convergence of the volume fractions to a constant value in Figure 5.7. When convergence is reached, at a certain diameter of circular window, the volume fractions reach a plateau (i.e. plateau of region II in the work of Robinson et al. [21] with a value close to the global volume fraction of the slice. This implies that the sample diameter is large enough to be spatially representative of the heterogeneities of phases distribution that can be observed at the pore scale. Results of this study indicate that a 2D-REV is reached in the deposit and gravel layers, as long as no reed is present in the 2D-slice and the slice is not located near the surface. It seems that for phases with more than 50% of volume fraction, REV is reached when variations are less than $\pm$ 5%. For phases with less than 50% of volume fraction, REV is reached when variations are less than $\pm$ 2.5\%. To our knowledge, this is the first time an analysis of the REV in Xray-CT on first-stage French VF wetlands has been conducted. These results could be complemented by the analysis of the REV for other pore scale properties different than phase volume fraction [1].

Usually, REV assessments in pore scale studies focus on the porosity-REV (i.e. voids-REV). In this study, a particular attention is given to biosolids because most of the microbial activity and the treatment of water-soluble pollutants takes place in this phase [78]. The gravel phase is studied as well as it has been observed that the compaction of the gravel layer decreases as biosolids are retained within the filter.

Figures 5.7(a) to 5.7(e) correspond to four different horizontal (perpendicular to the main water flow direction) 2D-slices taken in sample MON1A: two slices from the deposit layer (one at the top of the deposit and other at a location of maximal biosolid accumulation) and two slices from the gravel layer (with and without *Phragmites* identified inside the slice).

In Figures5.7(b) and 5.7(c), no *Phragmites* is present. The volume fractions for all the phases converge to a global value when the sub-sampling diameter reaches 30\% of the total diameter of the sample (1.5 cm). There are no large oscillations of the volume fractions beyond this point. The reader must be aware that this assessment remains mainly qualitative.

At the top of the deposit layer, the void and biosolid distributions are very heterogeneous. This reflects the fact that the surface of the deposit layer is naturally very irregular. As a consequence the curves for biosolid and void phases in Figure 5.7(a) show no satisfactory convergence.

When a *Phragmites* is present, the biosolid and void distributions exhibit a high degree of heterogeneity, and thus no convergence is reached (Figure 5.7(d). For this slice, a manual segmentation of the reed was performed and is shown in green. Then the REV is deduced for the volume fraction of four phases (void, biosolid, gravel and *Phragmites*) in Figure 5.7(e). The convergence of the void and biosolid volume fractions occurs for smaller radius and a representative volume is reached at 70% of the total diameter of the sample. This does not affect the convergence for the gravel phase. This figure shows that *Phragmites* have an effect on the distribution of biosolids and gravels in its surroundings. It is then relevant to optimize the methodology presented here to obtain four phase segmentations of the samples in order to describe better the morphology of the samples.

For the study of pore scale phenomena using Xray-CT, results demonstrate that the represen-

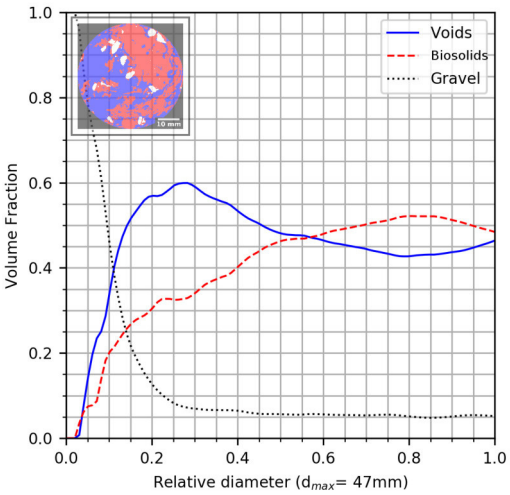

(a) Depth = 0 mm.

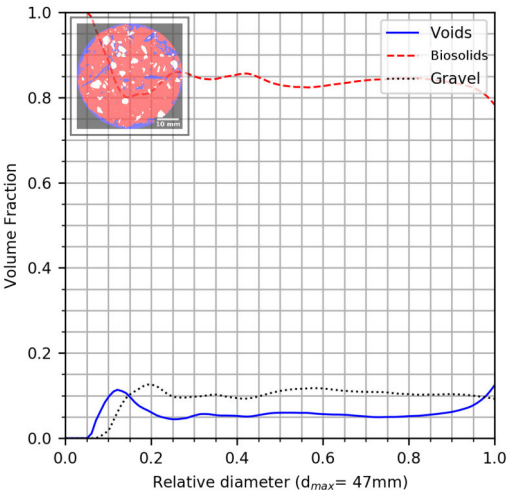

(b) Depth = -45 mm.

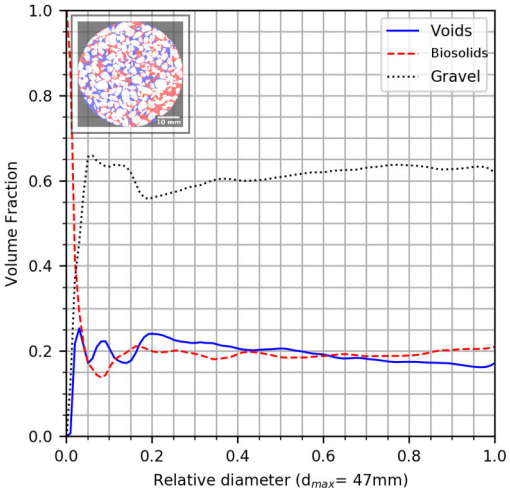

(c) Depth = -85 mm.

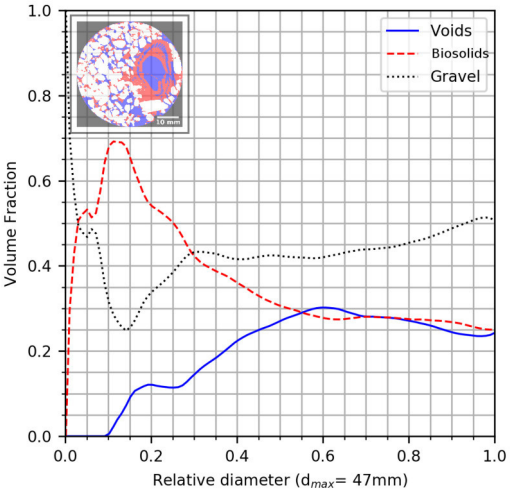

(d) Depth = -124 mm.

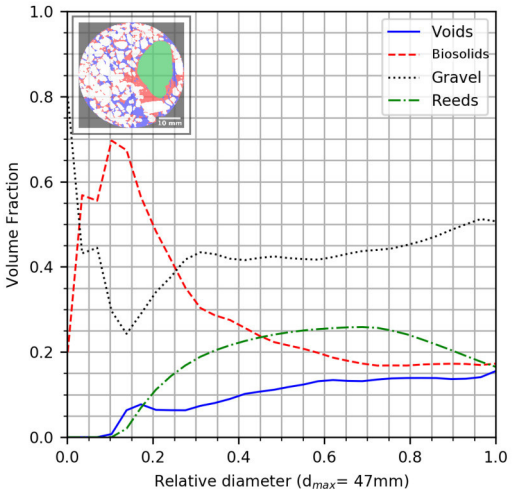

(e) Depth = -124 mm, four phase segmentation

Figure 5.7: Phase volume fraction versus relative diameter at four different depths

tativity of the sample regarding phase volume fractions is achieved at sample diameters larger than 1.5 cm (7.5 times the size of d_{10} of the gravels in this study). However, considering the sensibility of the samples to mechanical deformations during sampling, it is still recommended to extract samples of minimum 5 cm in diameter, which will give a security factor of more than three times the REV size observed in this study.

Conclusions

This study assesses the spatial representativity of pore-scale measurements obtained by Xray-CT of the filtering media in first-stage French VF treatment wetlands. Both the heterogeneity of phase distribution inside a single sample and the differences of pore scale properties between several samples of a treatment wetland have been considered. The results suggest that a sample diameter of 5 cm is large enough to (i) be representative of the heterogeneous phase distribution (voids, fouling material and gravel) at the pore scale, independently of the location of the sample and (ii) preserve the structure of the sample during the sampling by limiting shear stress impact at the core of the sample.

Prior to Xray-CT, the distribution of biosolids in a mature French VF treatment wetland was assessed based on electromagnetic measurements to select sampling points representative of its heterogeneity. FDEM allows a 2D-estimation of the biosolid distribution as electrical conductivity is highly correlated to the thickness of the deposit layer due to its high organic matter and water contents. The electrical conductivity measurements were found to be homogeneous over nearly 95% of the treatment wetland surface. This is explained probably by the age of the wetland and its good maintenance. The remaining 5% of the surface showed high values of electrical conductivity in regions of 1 m in diameter around the feeding points which are explained by preferential water retention and biosolid accumulation at those locations. This information leads to the conclusion that large scale heterogeneities in biosolid distribution cannot be considered as a cause of non-representative Xray-CT for the treatment wetland in this study.

After scanning and segmenting the tomographies, the volume fraction and specific surface area vertical profiles are computed for all the samples. They show several similarities independently of the sampling point. All samples show a vertical stratification of these properties which results from the vertical filtration of wastewater in the treatment wetland. A special focus is put on the transition from the deposit layer to the gravel layer. In order to make better comparisons of pore scale properties, a criterion to delimit the deposit layer is introduced. The upper and lower limits of the deposit layer are located at the intersection of the of the void and biosolid volume fraction profiles and at the intersection of the biosolid and gravel volume fraction profiles, respectively. Though Xray-CT capture very well variation of these properties, samples are not found to be significantly different from each other in the context of first stage French VF treatment wetlands.

The global biosolid volume fraction for the deposit layer and the gravel layer, and the thickness of the deposit layer measured by Xray-CT show an interesting correlation with small variations of EC ($> 1 \mu S \cdot m^{-1}$) measured by FDEM. This could be further exploited to characterize biosolid distribution in French VF treatment wetland being aware that the contributions to the EC measurement of organic matter, moisture, biosolid and gravel volume fractions and the thickness of the deposit layer cannot be distinguished solely by FDEM.

Pore size distributions are similar for all samples; the mode and the range of pores size distribution depend only on the vertical location in the sample (deposit layer or gravel layer). The presence of *Phragmites* is the main cause of non-systematic differences between pore-scale properties of the samples.

A study of the 2D-REV at several depths was conducted for one of the samples. It consists in the analysis of the dependency of the average value of phase volume fractions (voids, biosolids

and gravels) on the size of a sub-sampling circular window. Based on a qualitative assessment of this relationship, REV is estimated to be achieved at one third of the sample diameter (1.6 cm) when the analyzed depth does not include *Phragmites* or strongly heterogeneous features as observed near the top of the sample.

This study sets a solid base for the spatial representativity of further investigations on mechanisms that govern pore-scale filtration and biological treatment in French VF treatment wetlands, including water flow, as well as transport of particulate matter and dissolved oxygen. This is valid for mechanisms depending predominantly on macropore structure, such as gravity driven flow, and advective/diffusive oxygen transport from the atmosphere to the biosolids during the feeding and rest period of the first-stage filters.

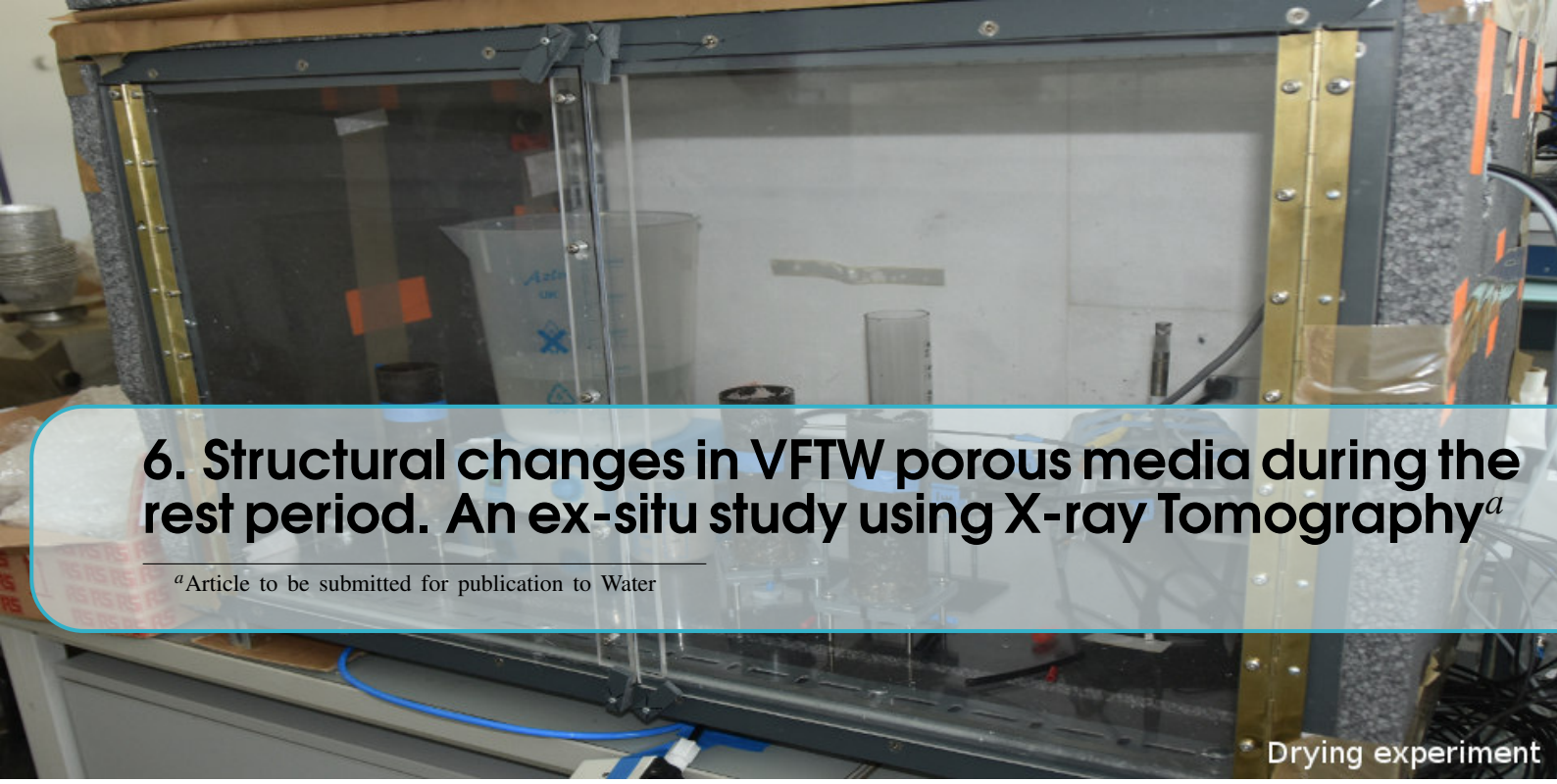

6. Structural changes in VFTW porous media during the rest period. An ex-situ study using X-ray Tomography[a]

[a] Article to be submitted for publication to Water

6.1 Introduction

VERTICAL Flow Treatment Wetlands (VFTW) have become a popular technology to treat domestic wastewater for communities under 5,000 people equivalent (p.e.) in France [82]. French VFTW consist of an arrangement of filters in two successive stages planted with *Phragmites Australis*. First stage filters receive raw wastewater by intermittent batches during 3.5 days and rest for 7 days; three filters are fed intermittently to assure continuous wastewater treatment. They are filled with a coarse granular material (gravel) that allows to retain Suspended Solids (SS). Being fed by raw wastewater, they develop a surface deposit layer [78] after few years of operation. SS are retained mainly by deep bed filtration [36] in newly commissioned filters, and by cake filtration after the development of the deposit layer.

The deposit layer helps to establish a homogeneous distribution of the influent over the TW surface during a batch. Moreover, it is thought to be the siege of most of biological processes that reduce the concentration of pollutants, including degradation of Organic Matter (OM) and nitrification as long as good oxygenation is ensured [78]. Once it reaches 20 cm in thickness, it is recommended to dredge it out to renew the infiltration capacity of the filters and prevent overflow. By the time of dredging, solids from the deposit layer show a good level of mineralization and stability, which makes it suitable for agricultural purposes [79].

Clogging and fouling are major concerns regarding TW operation and performances. Both phenomena consist in the accumulation of solids in the filters, which necessarily leads to a reduction of their water infiltration rate. However, few works in the literature provide a practical definition of clogging, the degree of clogging [95], and its difference with fouling in VFTW. Here, the definition of clogging presented in [95] is considered. In a clogged filter the volume of water received during a batch does not infiltrate completely before the subsequent batch. The degree of clogging could be defined as a function of the percentage of filter surface permanently ponded during two consecutive batches [95]. Such state promotes anaerobic conditions which are unwanted for optimum treatment. In contrast, a fouled VFTW has retained a certain amount of solids within the filtering gravel layer and in the deposit layer without compromising the treatment efficiency. This solid accumulation is herein referred to as biosolids.[1]. The biosolids in the gravel and deposit layers have a important role in wastewater treatment as a home of

[1] For style purposes, the term "biosolids" is used in this article instead of "fouling material". The meaning of this term remains exactly the same as in previous chapters of this thesis.

microorganisms and fauna responsible of Organic Matter (OM) degradation. Biosolids are characterized by their high organic matter content, which ranges from 50% to nearly 90% [47] and form a porous medium whose structure and consistency evolve with time due to water content changes, organic matter mineralization and internal erosion.

The rest period avoids over accumulation of biosolids, which may lead the wetland to a clogged state. During this period, the water content and volume of biosolids decreases by drainage, evapotranspiration and mineralization. Evapotranspiration (ET) is a phenomenon influenced by several physical, meteorological and plant physiological variables. It is the most important process in biosolids dewatering of sludge treating VFTW [122]. Dewatering of biosolids leads to straining, which to its turn facilitates oxygen diffusion into the filters and aerobic mineralization.

In mechanics, straining is a phenomenon observed on a wide class of materials including metals, concrete and geological materials, and is a characteristic feature of inelastic deformations [94]. As the biosolids dry, they are subject to forces tending to contract them generating cracks (strains) through which oxygen penetrates easier. Oxygenation controls the rate of OM degradation and mineralization, therefore understanding the deformation of biosolids in TW would provide insight into phenomena controlling fouling and clogging.

Understanding the underpinnings of solid transport and mineralization is necessary in order to optimize the design and operation rules of French VFTW, especially in scenarii aiming at reducing the footprint of the technology. Although the duration of the feeding and rest periods in [79] has been statistically proven to ensure good treatment performances in French VFTW [82], these rules remain mainly empirical [61]. A mechanistic description of the physical and biological processes in French VFTW is important to understand the dynamics of clogging, especially for cases where clogging has occurred prematurely in French VFTW. It would improve the capability of models to optimize operating conditions (e.g. decreasing the duration of the rest period or increasing the hydraulic loads), and suggest new design and operation rules in order to increase the reliability of the French VFTW technology.

Clogging is strongly linked to physical, chemical, and biological processes and hydraulics in VFTW. In consequence, different methodologies to assess clogging in VFTW are cited in the literature based on the measurement and monitoring of several variables or properties related to these processes, such as: (free)-porosity, solid densities, resistance to erosion, Specific Surface Areas (SSA), chemical composition of biosolids, water infiltration rate, *in/ex-situ* hydraulic conductivity, water content, water residence time, oxygen consumption rate, enzymatic activity, red-ox potential, or even DNA sequencing [85]. However, fouling and clogging are phenomena that consist basically in the filling of void volume by biosolids, where both the amount and the geometrical distribution of them are important.

Only three different methodologies that assess clogging/fouling in VFTW following geometrical descriptions are reported in the literature: geo-endoscopy [11], thin sections [50], and X-ray Tomography [67]. Geo-endoscopy provides (2D) images 6 mm in height and 5 mm in width with resolution of 10 $\mu m \cdot pixel^{-1}$ that capture the vertical profile of solids and porosity occupation in a filter along a borehole. Thin sections are wider (5 cm $\times$ 7 cm), their resolution can reach values of 1 $\mu m \cdot pixel^{-1}$, which makes possible to observe the biosolids microporosity, but their production requires the use of organic solvents to promote drying of the samples, which may alter the structure of biosolids, especially in the deposit layer [66]. X-ray Computed Tomography (X-ray CT) can be used to obtain 3D-morphological descriptions of larger volumes of TW samples without any pretreatment. The resolution is a compromise between the sample size and the size and number of active cells in the X-ray sensor. High-level image processing algorithms are needed to process images from X-ray CT.

In a previous study [67], 3D-images of VFTW samples (5 cm in diameter and 8 cm in height)

were obtained using X-ray CT with a resolution of 35 $\mu m \cdot pixel^{-1}$. It was possible possible to distinguish three main phases: voids, Fouling Material (FM), here also referred to as biosolids, and gravel. The biosolids are an homogeneous phase containing organic and mineral solids, water, and plant tissues. The spatial delimitation of these phases was done by a segmentation method which uses state-of-the-art image processing algorithms to attribute, one-by-one, each voxel (a 3D pixel) to one of the phases. The post-treatment of images consisted in analyzing the volumetric distribution and the morphology of the phases by measuring for instance: volume fractions, SSA, and pore sizes [67]. Phase connectivity is also another pore property studied in pore media consisting mainly of OM [99].

Methodologies like X-ray CT are used to estimate properties of filtering media (e.g. porosity, effective transfer coefficients and hydraulic conductivity) based on a realistic description of its pore structure [99, 2]. Such an upscaling approach constitute an alternative to global approaches, which are generally based on parameter calibration. In contrast, the main concern when studying porous media at the pore scale is to assure the spatial representativity of the measurements. This is still an openly discussed subject in the scientific community. Different approaches and methodologies are proposed to assess the Representative Elementary Volume (REV), which is the volume at which the averaged value of a property is no longer dependent on the size of the sample [1, 21, 126]. A recent study on the assessment of spatial representativity of X-ray CT for the study of VFTW showed that samples 5 cm in diameter are large enough to be representative of the heterogeneous volumetric distribution of all the phases (voids, biosolids and gravel) as long as no reed is present [68].

The recent works on the application of X-ray CT to study VFTW have proven the feasibility and spatial representativity of this methodology [67, 68], which set a solid basis for its use to study dynamic phenomena such as drying occurring during the rest period. X-ray CT seems to be a suitable methodology to study the structural changes of the VFTW during the rest period as (1) it is by far the most applied methodology to obtain good morphological descriptions of pore media [125], (2) it produces realistic (3D) morphological description, (3) it is a non destructive technique, which needs no pretreatment procedure to obtain images of samples from VFTW, and (4) it has been already used to study the dynamics of drying of other type of porous media [58, 57, 71, 59].

In this work, an ex-situ drying experiment simulating the rest period of a French VFTW is carried out. Three samples from a full scale TW were dried in a closed chamber under controlled conditions of temperature and relative humidity. X-ray CT scans were performed at three different times during a period of 10 days. The scans were used to observe the structural changes of the void and biosolid phases. The evolution of (1) volumetric distribution of the biosolid and void phases, (2) the Pore Size Distribution (PSD) of the void phase, (3) the specific biosolid/void SSA and (4) the connectivity of the void phase are studied. Gravimetric measurements of water, volatile suspended solids and ashes in the samples were also performed. The gravimetric and volumetric measurements are combined to estimate changes in the microporosity porosity (defined here as the porosity below the scan resolution) of biosolids. It provides an insight to the evolution of the inner structure of the biosolid phase during the rest period, which is crucial to understand the mineralization of biosolids and thus clogging of VFTW.

6.2 Materials and methods

6.2.1 Study site

The VFTW in Montromant (Rhône, France) was chosen to carry out this study. It has been designed according to French standards presented in [79] to treat effluent from 200 p.e.. It has two treatment stages, consisting of four filters in parallel for the first stage and two filters in

parallel for the second stage. Since its commission in 1994, three of the four filters in the first stage were in operation. In 2009, the deposit layer of these filters was dredged out and the fourth filter in the first stage was put into operation. The duration of the feeding period remained 3.5 days and the rest period was then increased to 10.5 days. A recent assessment of the distribution of biosolids at the surface of the wetland was performed in one of the oldest filters of the first stage in operation using Frequency Domain Electromagnetic Method (FDEM) [68]. The results of this study suggest that the distribution of biosolids in this wetland is homogeneous for about 95 % of the surface. No significant differences in the global content of biosolids in the samples extracted from this region are expected.

6.2.2 Sampling

Three samples were extracted from three different locations inside an homogeneous region delimited by FDEM [68] at the end of a feeding period in November 2018. They were named MON1, MON2, and MON3. Each sample consisted of a plastic cylinder of 5 cm in diameter and 16 cm in height. Samples were tall enough to contain all the deposit layer and an a part of the dense gravel layer beneath. To extract the samples, an area was cleared of reed stems at the sampling points. Then the cylinder was manually inserted. As the it was buried into the filter, gravels surrounding the cylinder were progressively dug out and any rhizome found was cut to avoid compaction and changes in sample structure [67]. After the extraction, all the samples were sealed with a plastic film and stored at 5°C to avoid water evaporation before the beginning of the ex-situ drying experiment.

6.2.3 Ex-situ drying experiment

Drying of biosolids during the rest period of a French VFTW is mainly driven by evapotranspiration (ET). An ex-situ (laboratory) study of the rest period using X-ray CT seems to have practical advantages: (1) variables influencing drying can be easily controlled (2) the experiment is not impacted by stochastic events like rain, which would affect results if several samples were to be extracted at different times during an *in-situ* rest period (3) the comparison of structural changes is easier to perform if the same samples are scanned during the experiment. In such an experiment the drying conditions, especially the temperature and relative humidity of the atmosphere, must be carefully chosen to counter balance the fact that there will be no contribution of mature reeds to evapotranspiration.

An *ad-hoc* plexiglass drying chamber was built to maintain samples at constant conditions of Temperature (T) and Relative Humidity (RH) (Figure 6.1) during the experiment. The chamber measured $90\times50\times40$ cm^3 (l×w×h) and was isolated with a 3 cm thick layer of polystyrene foam to provide thermal insulation. Samples were placed inside and dried for 10 days, (i.e. the duration of the rest period at Montromant's VFTW). Only the top part of the sample was in direct contact with the atmosphere of the chamber. An electrical resistance heater of 80 W regulated by a thermocouple was used to maintain the chamber T around a set value of 25°C. The average T outside the chamber was 21°C. 3 liters of a saturated solution of $Mg(NO_3)_2$ with an extra amount of 200 g of salt was used to maintain the RH in the chamber close to the equilibrium value of 50%. The solution was continuously stirred. A rotating fan with blades of 85 mm in diameter and producing an air current of 3.33 m/s (measured by a portable anemometer GEOS n°11, Skywatch) was used to homogenize T, and RH by rapidly mixing the humid air at the top of the samples with the atmosphere of the chamber. T and RH were continuously monitored and the sample masses were measured once a day during the experiment. Evaporation rates were computed by dividing the mass loss over the sample surface (19.63 cm^2).

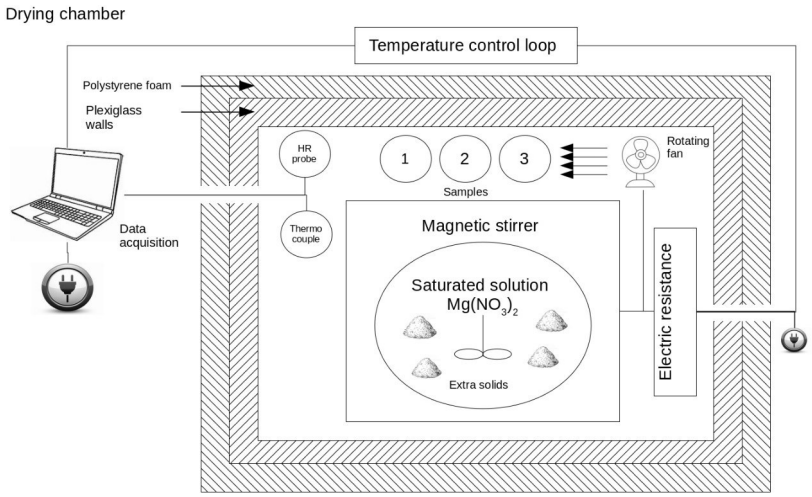

Figure 6.1: A sketch of the drying chamber.

6.2.4 Gravimetric measurements

At the end of the drying period the total water content, Volatile Suspended Solids (VSS), ashes and gravel mass for each sample were estimated by a gravimetric analysis. The total water content was obtained by computing the difference between the initial mass of the samples and the mass after 24 h of drying at 105°C. VSS were computed as the mass loss after calcination of the samples at 550°C. The remaining solids after the calcination, consisting in the mixture of gravel and ash aggregates from the biosolids were separated using a 0.63 mm sieve. To facilitate sieving, ash aggregates were manually broken.

6.2.5 X-ray tomography, image pretreatment and segmentation

A tomography of each sample was performed at days 0, 3 and 10 of the ex-situ drying experiment. The samples were taken out of the drying chamber with a plastic film on the top to avoid water loss by evaporation during the 2 h of scanning. After scanning, the samples were replaced inside the drying chamber. The scans were performed at the Mateis laboratory (Insa Lyon, France) in a scanner equipped with a 160 kV Tungsten X-ray tube. The scanner was operated with an accelerating voltage of 140 kV and a current of 100 μA with an exposure time of 333 ms. A 0.1 mm copper foil filter was put in front of the X-ray source to reduce beam hardening artifacts. 900 projections distributed among 360° were recorded. The sensor area was 250×200 mm^2 and the 3D images consisted of about 1500×1500×1350 voxels (l×w×h) with a voxel size of 35 μm (5.2 cm × 5.2 cm × 4.7 cm). Since the total height of the samples is about 16 cm, each scan was performed in four parts: these parts had a small overlay region of about 200 voxels to help the concatenation during image processing. The data were reconstructed by a filtered back projection Feldkamp-algorithm [28]. The reconstructed data were processed and visualized with the public domain ImageJ/Fiji shareware [109]. The images were then pretreated and segmented for quantitative analysis.

Some noise is present in the images due to overlaps between gray value ranges of each phase in the sample (voids, biosolids, gravel). To reduce noise, the segmentation is classically preceded by pretreatment routines, such as smoothing filters, in order to facilitate voxels attribution. In this work, the median filter used in [67] has been replaced by an anisotropic filter [7, 90, 119]. It reduces the noise by applying a smoothing in edges tangential directions based on a gradient computation but not in the normal direction which preserves better the location of interfaces.

The application of the anisotropic filter, instead of a median filter led to a better denoising of images and recognition of voxels presenting a Partial Volume Effect (PVE). PVE appears when two phases are taken into account into a single voxel, thus making harder its attribution to a single phase. These voxels are preferentially located at the edges of the phases, where the gray level gradient is maximum. PVE voxels were determined by thresholding the image of gray level gradients, which was obtained using the FIJI's routine 'Find Edges' [67]. Voxels with values higher than 75-th percentile of this image were defined as PVE voxels.

Segmentation consists in the attribution of each voxel of a digital image to a single phase based on its gray value and that of its neighbors. In this study three phases were considered: void, biosolids and gravel. They were segmented based on a region growing algorithm developed by Hashemi et al. [35]and adapted in a previous study [67]. This algorithm uses a seed built by thresholding partially the pretreated image. The thresholds define a seed for each phase and are computed based on a Gaussian fitting of the histogram gray values. PVE voxels are excluded from the seed. Remaining voxels are attributed by consecutive dilations of the seeds of each phase until phases reach an interface.

6.2.6 Image post-processing

6.2.6.1 Morphological properties

Five pore scale measurements were obtained by image post-processing (i.e. after segmentation): volume fraction for each phase (void, gravel, biosolids), Specific Surface Area (SSA) profiles for the void/biosolids interface, Pore Size Distributions (PSD) of the void phase, and void connectivity.

Volume fraction profiles

Volume fractions (VF) were obtained by computing the ratio between the number of voxels belonging to each phase and the total number of voxels (the sum of the three phases). Vertical VF Profiles (VFP) were obtained by computing VF per horizontal slice and smoothed using a moving average window of 57 voxels in depth with a displacement of 1 voxel at a time. 57 voxels (2 mm) is a value close to the d_{10} value of the gravel size distribution.

Thickness of the deposit and gravel layers

VF profiles were used to estimate the limits of the deposit and the gravel layers using a criterion introduced in [68]: the beginning of the deposit layer is determined by the first intersection of the curves for the VF of voids and biosolids, and the beginning of the gravel layer (i.e. the end of the deposit layer) is determined by the first intersection of the VF profiles of gravel and biosolids VF. Average values of VF and SSA were computed for the total image and for the deposit and gravel layer separately. PSD computation is also focused on the deposit and gravel layers separately.

Specific Surface Area (SSA)

The SSA is obtained by dividing the void-biosolid surface area by the bulk volume. The void-biosolid surface area was computed using the Cauchy-Crofton cutting line method [55, 54, 107]. This method allows a numerically efficient estimate of interface areas with a better accuracy than the direct counting of interface voxels, which presents a "staircase effect". In addition, it has a much lower computational cost than methods based on surface meshes. For each voxel belonging to the void phase and located at the interface with the biosolid phase, the method consists in counting the number of neighboring voxels in the biosolid phase with respect to 3 families of connection: 1-connected (face-connection), $\sqrt{2}$-connected (2D diagonal/edge connection) or $\sqrt{3}$-connected (3D diagonal/corner connection). The number of connections of each type is then multiplied by a characteristic coefficient obtained from the Voronoi tessellation of the unit sphere. The sum of these contributions results in the value of the surface. SSA profiles were

obtained by computing the SSA of subsections of 57 voxels in height without overlay.

Pore Size Distribution (PSD)

The pore size distribution was obtained by computing the local thickness map of the void phase of the segmented images. The local thickness map of a 3D object is another 3D image where each voxel stores the diameter of the largest sphere that fits inside the object and contains the voxel (without being necessarily centered at the voxel). The computation of the thickness map was done using the FIJI plugin - Local Thickness Map [26, 37, 105]. This method has already been used to compute PSD in sandstones [15].

Connectivity of the void phase

The global connectivity of the void phase (C) was computed as the ratio of the void volume connected to a reference height in the sample V_c divided by the total void volume V_t. Two references are considered in this work: the top of the sample and the top of the gravel layer.

$C = V_c/V_t$

To identify the connected void space, the "connected regions" FIJI's plug-in was used. A connected void is a set of voxels of the void phase where all voxels share at least one face or edge.

A profile of the connectivity is, by analogy, the profile of the ratio of voxels of the void phase connected to the top of the sample divided by the total number of voxels of the void phase at a given height.

Changes in (C) are a function of the relative change of the connected void volume ($\frac{\Delta V_c}{V_c}$) and the total void volume ($\frac{\Delta V_t}{V_t}$), Eq. 6.1. During a drying period, the quantities ΔV_c andΔV_t are always positive. Therefore, an increase of (C) ($\Delta C > 0$) may only be seen if the relative increase of the connected void volume is greater than the relative increase of the total void volume. A decrease in (C) is also possible if the opposite conditions occur.

$$\frac{\Delta C}{C} = \frac{\Delta V_c}{V_c} - \frac{\Delta V_t}{V_t} \tag{6.1}$$

6.2.6.2 Estimation of air-filled microporosity inside the biosolids

Between 2 scans, the volume of wet biosolids tends to decrease less than the corresponding volume of evaporated water obtained by gravimetric measurements (considering the water density of 1 g/cm³). This observation corresponds to a partial water desaturation of pores smaller than the scan resolution inside the biosolids (here referred to as micro-porosity) [103]. At a given stage of drying -*i*- (day 0, 3 or 10), the biosolids could be considered as a three-phase material composed of water, air and solids (mineral or organic):

$$V^i_{biosolids} = V^i_{water} + V^i_{air-microporosity} + V^i_{solids}$$

Assuming that the volume loss of solids by mineralization is negligible when compared to the volume loss of water, the change of volume of biosolids can be computed as follows:

$$\Delta V^i_{biosolids} = \Delta V^i_{water} + \Delta V^i_{air-microporosity}$$

where $\Delta V^i_x = V^i_x - V^{i-1}_x$. Based on the water volume loss and the decrease in biosolid volume computed from the segmentations, and considering the initial volume of biosolids $V^0_{biosolids}$ as reference, the increase of microporosity volume fraction could be estimated as:

$$\Delta\theta^i_{air-microporosity} = \frac{\Delta V^i_{air-microporosty}}{V^0_{biosolids}} = \frac{\left(\Delta V^i_{FM} - \Delta V^i_{water}\right)}{V^0_{biosolids}}$$

Table 6.1: Mean and percentiles of the temperature (T) and relative humidity (RH) in the drying chamber during drying.

Temperature (°C)			Relative Humidity (%)		
5-th percentile	median	85-th percentile	15-th percentile	median	85-th percentile
27.0	27.4	27.6	33.2	48.1	54.8

Table 6.2: Sample composition.

Variable	Unit	Sample 1	Sample 2	Sample 3
Total water (at day 0)	g	138.77	166.72	142.74
Mass of volatile solids (VSS)	g	20.97	22.61	19.95
Mass of ashes	g	17.26	19.71	15.93
Mass of gravel	g	203.77	154.41	187.73
Total water mass fraction (at day 0)	g/g	36.4%	45.9%	39.0%
Volatile solid mass mass fraction (VSS)	g/g	5.5%	6.2%	5.4%
Ash mass fraction	g/g	4.5%	5.4%	4.3%
Gravel mass fraction	g/g	53.5%	42.5%	51.2%

6.3 Results and discussion

6.3.1 Drying conditions and sample composition

Table 6.1 summarizes average conditions of the atmosphere of the drying chamber during the experiment. The median value of the T and RH were 27°C and 48%, respectively. These values are close to the set value for the T control loop and the equilibrium value of a saturated solution of $Mg(NO_3)_2$. For 70% of the duration of the experiment, the HR ranged between 33 % and 54%. This is explained by fluctuations of HR and T due entry of air when the chamber had to be opened to weight the samples and take them to the X-ray scanner.

VSS, ash and gravel masses for each sample are presented in Table 6.2. The mass composition of all samples is very similar differing only by the mass of gravel, which is clearly shown in Table 6.3; the water, ashes and VSS gravimetric contents in the biosolids are similar showing variations of less than 2% in weight. This result is in accordance with FDEM results that indicated an homogeneous distribution of the biosolids at Montromant's VFTW [68]. The reader's attention is drawn on the fact that values presented in Tables 6.2 and 6.3 do not differentiate the composition of biosolids in the deposit layer and gravel layer. All samples lost about 51% of their water during the drying experiment (Figure 6.2 top right). The evaporation rate is slightly higher at the beginning of the experiment for the 3 samples and the observed average evaporation rate is about 2 $mm \cdot d^{-1}$ (Figure 6.2 bottom right). This behavior is classical for drying in a porous media submitted to a constant external flow at its surface [70]. This average value is in the lowest range of ET values that have been observed in different types of TWs. A review of ET in TW [122] reports values ranging from 0.5 to 40 $mm \cdot d^{-1}$ depending on the geographic location, climate, and size of the wetland. Experiments to assess the use of VFTW for activated sludge dewatering

Table 6.3: Composition of biosolids.
At day 0.

Variable	Unit	Sample 1	Sample 2	Sample 3
Water	g/g	78.4%	79.8%	79.9%
Volatile solid mass (VSS)	g/g	11.8%	10.8%	11.2%
Ashes mass	g/g	9.8%	9.4%	8.9%

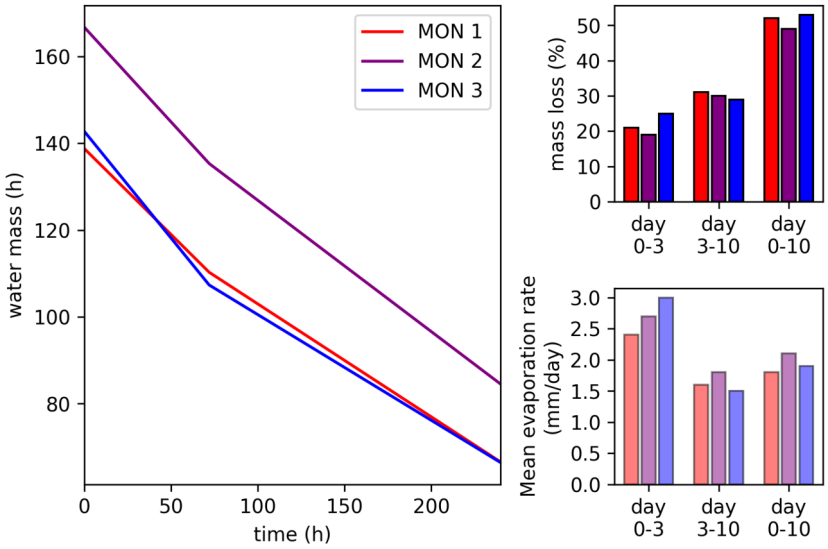

Figure 6.2: Mass changes versus time (left), cumulative mass losses (top right) and evaporation rates (bottom right) during the experiment.

yielded ET rates of the same magnitude [122].

6.3.2 Structural changes

The changes in sample structure during the drying experiment were followed using X-ray CT. Biosolid and void VF changed as well as the PSD, the void/biosolid SSA and the void connectivity to the atmosphere. This information gives insight into the importance of the rest period on preventing clogging in VFTW.

6.3.2.1 Phase volume changes

Entire sample

The computation of the volume of each phase in the whole samples is reported in Table 6.4. First, the stability of the gravel phase should be noticed. Since the gravel should not be affected by the experimental conditions, it is possible to estimate the segmentation methodology accuracy by comparing the gravel volume obtained for each scan. An average error of 1 cm^3 in the segmentation of the gravel phase is obtained. It represents a maximum of 1.7% of the gravel volume (for sample MON2). This observation highlights the reliability of the method to access the phase distribution in VFTW samples. The void and biosolid phases appear strongly coupled because the decrease of volume of biosolids during the drying is compensated by an increase of the void volume. This behavior is due to a combination of two main processes: (1) the evaporation of water, which reveals internal pores in the biosolids that are then segmented as voids, and (2) drying promoting a structural change, or volumetric strain, of the biosolids.

This volumetric strain corresponds mainly to the radial and vertical shrinkage of the biosolids in the deposit layer as it is revealed in Figures 6.3 and Figures 6.4 respectively. The radial shrinkage promoted noticeable displacements of the gravels embedded inside the biosolids of the deposit layer (Figures 6.3(a) to 6.3(c)). It reduces the occupation of solid phases of the sample (biosolids+ gravel) down to an average value of 60% of the initial diameter at the end of the experiment (day 10). Such edge/border effects are common in laboratory column experiments. Compared to field conditions, this phenomenon is clearly an experimental artifact. Considering the high level of shrinkage (both in the radial and vertical direction) and the relatively low evaporative stress applied during the experiment, the biosolids most probably experiment larger

Table 6.4: Volumes of the different phases over the entire sample.

		Volume (cm^3)		
Phase	Sample	Day 0	Day 3	Day 10
Gravel	1	81	79	80
	2	61	60	59
	3	72	71	71
Biosolids	1	148	123	81
	2	178	153	112
	3	150	122	85
Void	1	45	72	113
	2	34	60	101
	3	52	82	119

cracks in full scale wetlands than in the *ex-situ* experiment. In the gravel layer (Figures 6.3(d) to 6.3(f)), gravels constitute a fixed bed with no noticeable displacements or side effects.

Taking into account that the radial shrinkage in the deposit layer would lead to inaccurate estimates of structural properties such as volume fraction, specific surfaces or pore size distributions. In order to limit the sensitivity of such measurements to border effects, a centered circular region of interest (ROI) of 60% of the total diameter of the sample is chosen to perform computations (the region materialized in Figure 6.3(c) by a yellow circle). The value of 60% is chosen because volume fraction profiles were found to be independent of the ROI diameter below this threshold as long as no reed is present. Moreover, this ROI diameter is larger than the REV size of 1.5 cm estimated on similar samples in [68].

The effect of drying on the phase distribution is clearly put forward by the evolution of volume fraction vertical profiles computed on this ROI (Figures 6.4and 6.5).

Gravel layer

The proposed criteria in Section 6.2.6.1 conveniently delineates the gravel and deposit layers which exhibited very distinct behaviors.

Concerning the gravel layer, the distribution of phases in the sample MON1 is the most homogeneous. A dense layer of gravels is observed between 20 mm and 70 mm height with a volume fraction close to 0.6. A layer mainly composed of biosolids is observed at the bottom of the sample (between 0 mm and 20 mm). In samples MON2 and MON3, the presence of reeds in the gravel layer promotes more disturbed profiles (Figure 6.4).

In all cases, gravel layer volumetric contents exhibited small changes during the experiment. The most noticeable change could be seen on MON3 sample at height around 20 mm but it corresponds to a crack during the sample extraction. The average volume fractions in the gravel layer (Table 6.5) exhibit a progressive replacement of the biosolid phase by the void phase. At day 10, this increase of void volume fraction was 0.05, 0.03 and 0.07 for sample MON1, MON2 and MON3 respectively.

Deposit layer

The deposit layer is strongly affected by the drying process (Figure 6.4). Sample MON2 has the thickest deposit layer (10 cm), followed by sample MON1 (7.5 cm) and MON3 (6.5 cm). A very dry layer appears at the uppermost part of each sample, with a thickness ranging from 1 cm to 3 cm for MON1 and MON3 samples respectively. In this layer, the void phase becomes progressively predominant compared to small biosolid clusters supporting some gravels. This observation suggests probably a combination of high initial water content and very low level of compaction of the biosolids in the deposit layer. The deposit layer is likely very sensitive to

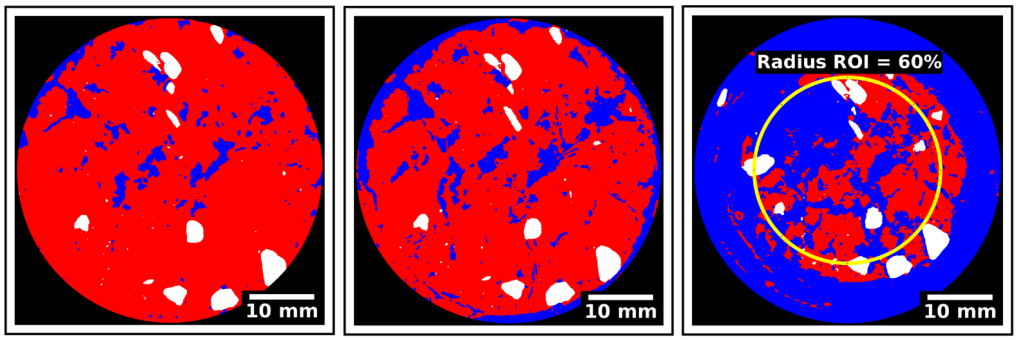

(a) MON1, deposit layer (day 0, height = 116 mm) (b) MON1, deposit layer (day 3, height = 115 mm) (c) MON1, deposit layer (day 10, height = 112 mm)

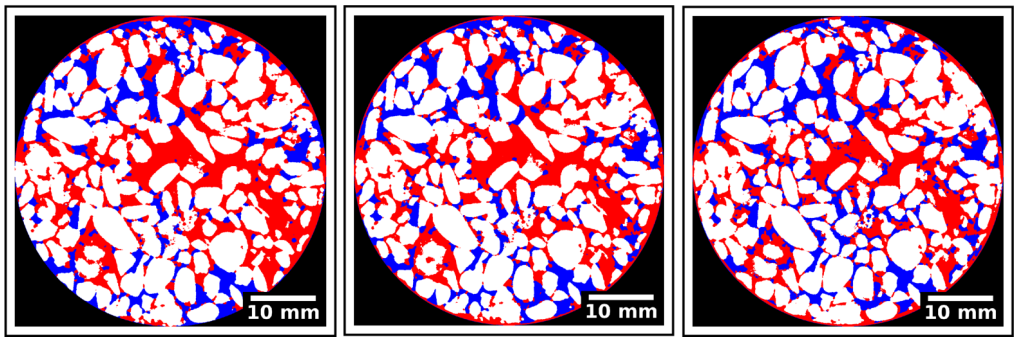

(d) MON1, gravel layer (day 0, height = 33 mm) (e) MON1, gravel layer (day 3, height = 33 mm) (f) MON1, gravel layer (day 10, height = 33 mm)

Figure 6.3: Horizontal slices in the *deposit* layer (a., b. and c.) and in the gravel layer (d., e. and f.) for MON1 sample.

Table 6.5: Average volume fractions of void and biosolids and gravel in the deposit layer and the gravel layer.

Computations were performed for a ROI of 60%.

			Volume fraction				Volume fraction				Volume fraction		
Sample	Layer	Phase	Day 0	Day 3	Day 10	Phase	Day 0	Day 3	Day 10	Phase	Day 0	Day 3	Day 10
MON1	Deposit	Void	0.05	0.08	0.19	Biosolids	0.81	0.76	0.61	Gravel	0.14	0.16	0.20
MON1	Gravel	Void	0.09	0.11	0.14	Biosolids	0.38	0.37	0.34	Gravel	0.53	0.52	0.52
MON2	Deposit	Void	0.09	0.11	0.13	Biosolids	0.79	0.77	0.71	Gravel	0.12	0.12	0.16
MON2	Gravel	Void	0.22	0.24	0.25	Biosolids	0.37	0.35	0.35	Gravel	0.41	0.41	0.40
MON3	Deposit	Void	0.13	0.17	0.19	Biosolids	0.70	0.63	0.48	Gravel	0.17	0.20	0.33
MON3	Gravel	Void	0.15	0.19	0.22	Biosolids	0.46	0.44	0.41	Gravel	0.39	0.37	0.37

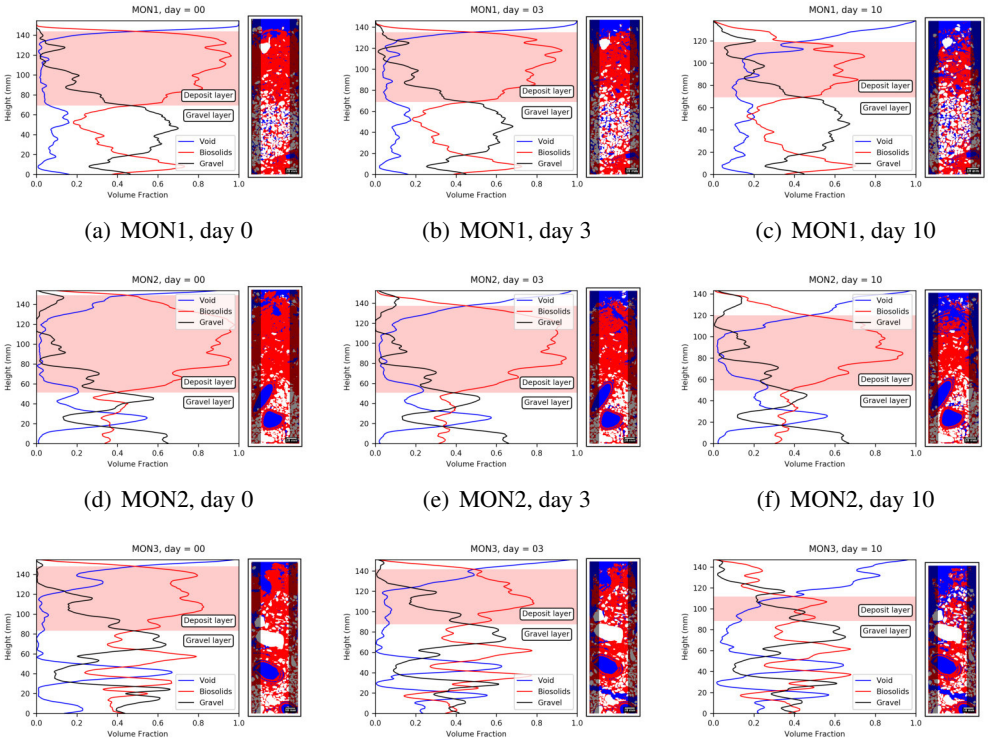

(a) MON1, day 0 (b) MON1, day 3 (c) MON1, day 10

(d) MON2, day 0 (e) MON2, day 3 (f) MON2, day 10

(g) MON3, day 0 (h) MON3, day 3 (i) MON3, day 10

Figure 6.4: Evolution of vertical phase volume fraction profiles and snapshot on a vertical slice of the 3D scan.

Computations were performed for a ROI of 60%.

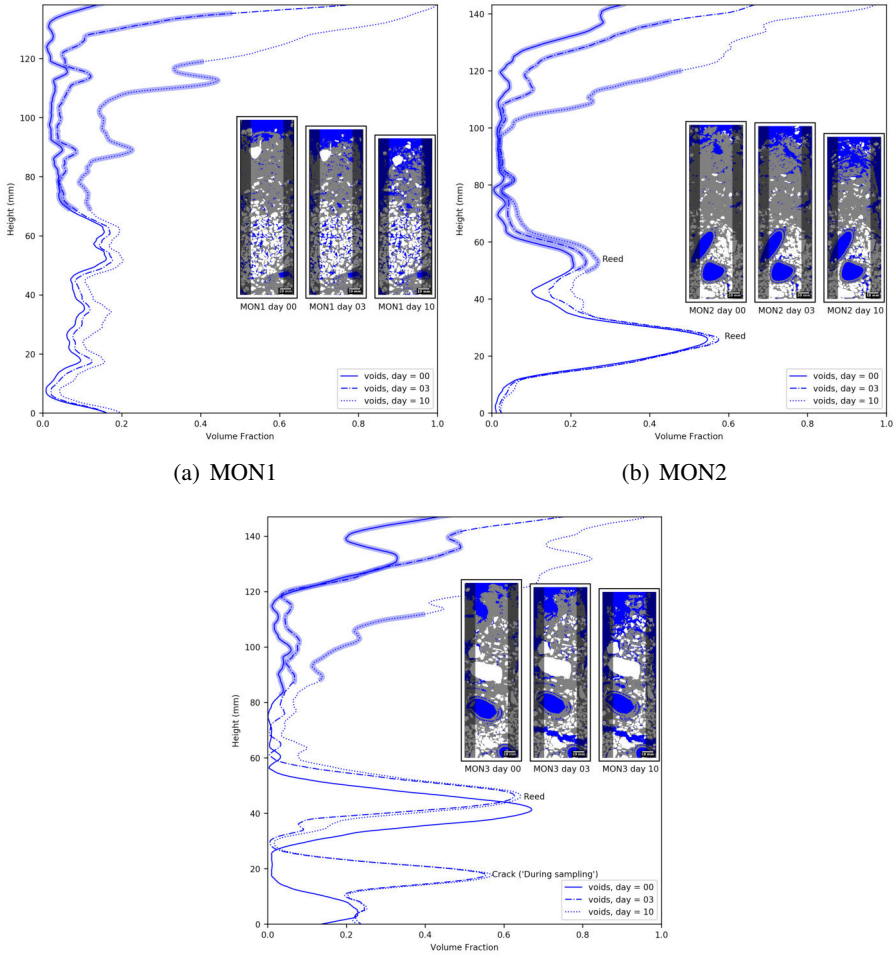

(a) MON1 (b) MON2

(c) MON3

Figure 6.5: Focus on the evolution of the void phase volume fraction profiles.
The deposit layer is represented by a wider trace in the curves.
Computations were performed for a ROI of 60%.

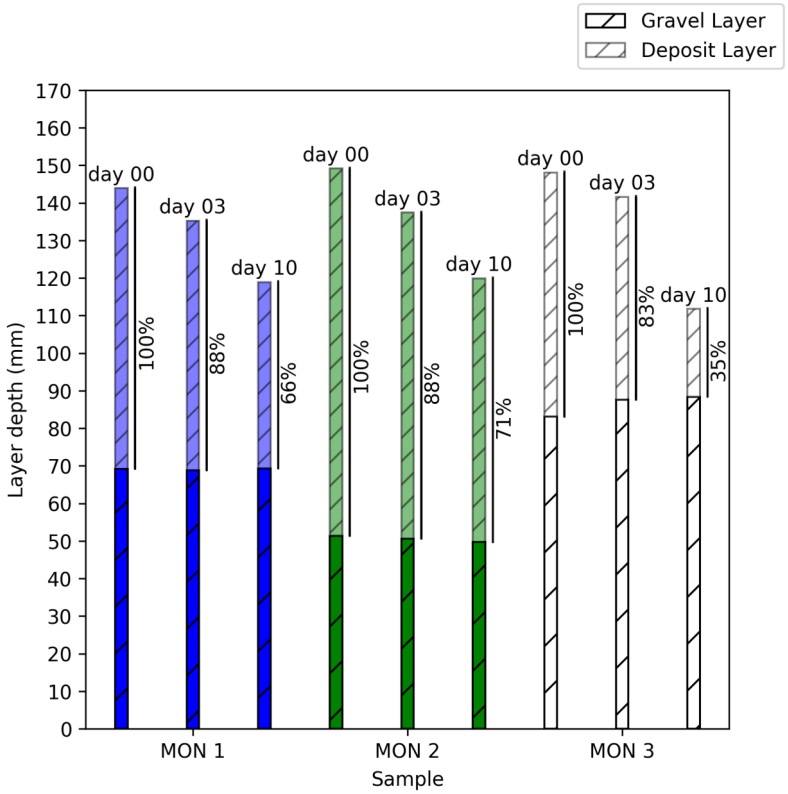

Figure 6.6: Evolution of deposit and gravel layer thicknesses during the drying experiment.
Computations were performed for a ROI of 60%.

wind and plant mechanical effects in the VFTW at the end of the rest period. The deposit layer (delimited by the red shadowed region in Figure 6.3) exhibits a progressive increase of the void volume fraction (Figure 6.5). Similarly to what occurs in the gravel layer, this increase could be partially explained by water evaporation which empties the porous structure in the biosolids. However, the biosolids in the deposit layer experienced a severe structural change during the drying experiment. As mentioned above, it results in a vertical shrinkage of the deposit layer. This settlement of the deposit is summed up in Figure 6.6. The behavior observed for sample MON1 and MON2 are very similar with a reduction of the deposit layer thickness of 12% after day 03 and respectively 34% and 29% after day 10. The deposit layer thickness for sample MON3 must be interpreted carefully as it contains a big gravel at a height that could be still considered part of the deposit layer (Figure 6.5).

The loss of volume of biosolids is higher in the deposit layer than in the gravel layer (Figure 6.5 and Table 6.5). During the experiment, the volume fraction of biosolids reduces in average from 0.77 to 0.60 in the deposit layer and from 0.40 to 0.38 in the gravel layer (Table 6.5). A higher water content combined with a less dense initial state of the biosolids, as well as a shorter distance to the atmosphere in the deposit layer should be the major causes generating these results. Furthermore, due to radial shrinkage, the deposit layer is more influenced by drying than the gravel layer.

The reduction of the thickness of a layer tends to decrease the resistance to water flow. Nevertheless this reduction depends also on the internal structure of the layer, which is discussed in the next sections.

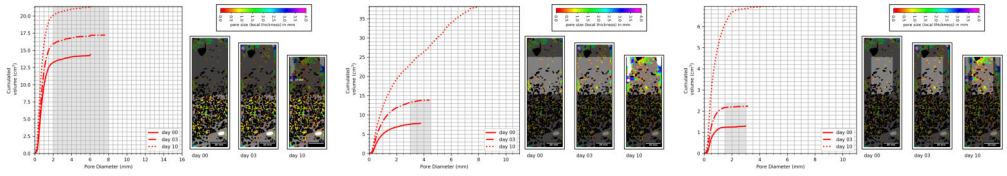

(a) MON1, gravel layer (b) MON1, deposit layer ROI = 100% (c) MON1, deposit layer ROI = 60%

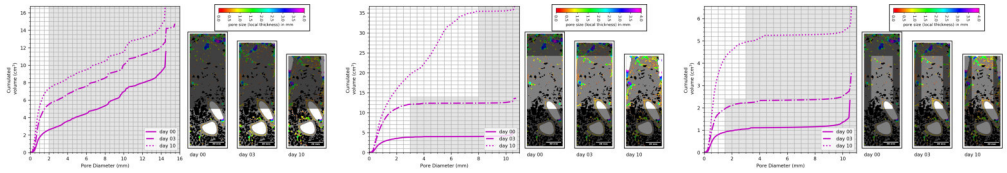

(d) MON2, gravel layer (e) MON2, deposit layer ROI = 100% (f) MON 2, deposit layer ROI = 60%

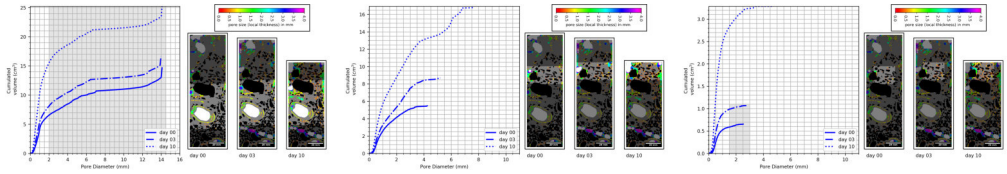

(g) MON3, gravel layer (h) MON3, deposit layer ROI = 100% (i) MON3, deposit layer ROI = 60%

Figure 6.7: Cummulative PSD associated to snapshots highlighting the ROI on which computation are performed (on the right).
The gray regions highlight the diameter ranges where curves are parallel. For these diameter ranges, there was no net increase of the cumulated volume of voids during the drying experiment.

6.3.2.2 Changes in Pore Size Distribution (PSD)

The reduction of volume of biosolids induces changes in the pore structure of the samples. Figures 6.7(a) to 6.7(i) present pores size cumulative distributions based on the computation of the local thickness of the void phase. In these figures, the increase of the volume of a certain pore size class from one day to another is identified by a change of the slope between the PSD at equal pore diameter, i.e. if the curves are parallel in a specific pore size range (gray regions in the cumulative PSD in Figures 6.7(a) to 6.7(i)), there is no net increase of the volume of pores belonging to that range during the drying experiment. Voids corresponding to the hollow part of reed stems are taken into account in the PSD of Figures 6.7(a) to 6.7(i). The analysis should focus only on voids in the biosolid matrix, but a specific segmentation procedure has to be developed. To enhance the visual perception of voids in the biosolid matrix, voxels of the void phase with size larger than 4 mm were set to white as they are likely to correspond to rhizomes.

On the one hand, in the gravel layer (Figures 6.7(a), 6.7(d) and 6.7(g)), pores ranging from 0 to 2 mm show the highest increase in volume. The volume of this size class is at least multiplied by two during the drying. Sample MON1 has a less compact gravel layer than samples MON2, MON3. This is evidenced by its larger volume of pores smaller than 2 mm. It must be highlighted that the gravel layer of sample MON1 is the only one lacking of *Phragmites*. The influence of the presence of Phragmites on biosolids accumulation in the gravel layer should be further studied.

On the other hand, in the deposit layer, the shrinkage of the biosolids provokes large cracks at the edges in the center of the samples (pores larger than 4 mm). Shrinkage located near the border of the samples is responsible of the major part of the void volume increase (Figures 6.7(b), 6.7(e) and 6.7(h)). Computing the PSD ignoring the radial shrinkage if biosolids (ROI 60%,

Figures 6.7(c), 6.7(f) and 6.7(i)) allows focusing on the intrinsic behavior of the biosolid phase. In this case, most of the void volume increase corresponds to pores ranging from 0 to 1.5 mm for the first 3 days of drying and from 0 to 3 mm for the entire experiment.

If the shrinkage cracks in the deposit layer are important to understand water flow in VFTW, the changes in PSD in the gravel layer are essential as well. No void preferential distribution around rhizomes is observed in the gravel layer of these scans.

All samples show an increase of the volume and size of voids during the drying experiments. As mentioned before, these voids may result from evaporation or straining of the biosolids. Unlike evaporation, which replaces water by air in existing pores, straining creates new pores by the alteration of the solids structure. A net increase of porosity and size of voids will decrease the resistance to water flow resulting in an increase of the global hydraulic conductivity.

6.3.2.3 Specific Surface Area (SSA)

The specific surface area is an important parameter that influences oxygen transfer to the biosolids. During a rest period, the specific surface may increase or decrease depending on different structural changes:

- Pores initially filled with water and later filled with air will increase the biosolid/void SSA because in X-ray CT water cannot be distinguished from the biosolids. This desaturation effect could also occur in pores smaller than the image resolution. In the later case, the corresponding increase of void phase volume cannot be captured nor quantified by X-ray CT. Nevertheless, its contribution to the SSA could be very high due to the increase of surface to volume ratio with decreasing pore size.
- If the shrinkage of biosolids is accompanied by cracks formation, an increase of SSA is observed. On the contrary, if the shrinkage is due to a compression of the biosolids it decreases SSA.
- Connection between pores due to cracks will reduce the SSA.

The occurrence of small pores filled with air and not visible (smaller then the CT resolution, 35 μm) increases over time with the siccity, therefore the underestimation of SSA inherent to this methodology increases over time.

According to Figures 6.8(a) to 6.8(c), it is shown that the phenomena in the list above inducing an increase in SSA are predominant over those inducing a decrease of SSA during a rest period.

Except for sample MON1 at day 0, the average SSA is greater in the deposit layer than in the gravel layer (Table 6.6). Although this general trend exists, the SSA profiles (Figure 6.8) show local variations explaining this result. SSA is not the only factor that influences oxygen transport and the degree of mineralization of the biosolids. The age of the biosolids and the size of biosolid aggregates have an important role on mineralization. Thus a greater SSA in the deposit layer does not mean necessarily that their degree of mineralization is higher.

To compare the samples, the ratio SSA/SSA at day 0 for each sample is computed (Table 6.6). For the gravel layer the ratios of increase of all samples are similar. For the deposit layer the ratios reveal a more heterogeneous result. In sample MON2 the increase of SSA is sensibly lower in the deposit layer. This behavior could be in part explained by less pores smaller than 2 mm in the deposit layer in sample MON2 compared to the other samples. These pores correspond to red-to-green colors in the snapshots in Figure 6.8.

SSA measured by X-ray CT is strongly dependent on the resolution of the tomographies. It accounts for surfaces at an intermediate space-scale between microporosity of the biosolids and gravel and root surface. In other words these measurements are more accurate than gravel and root surface estimation but less accurate than adsorption based measurements.

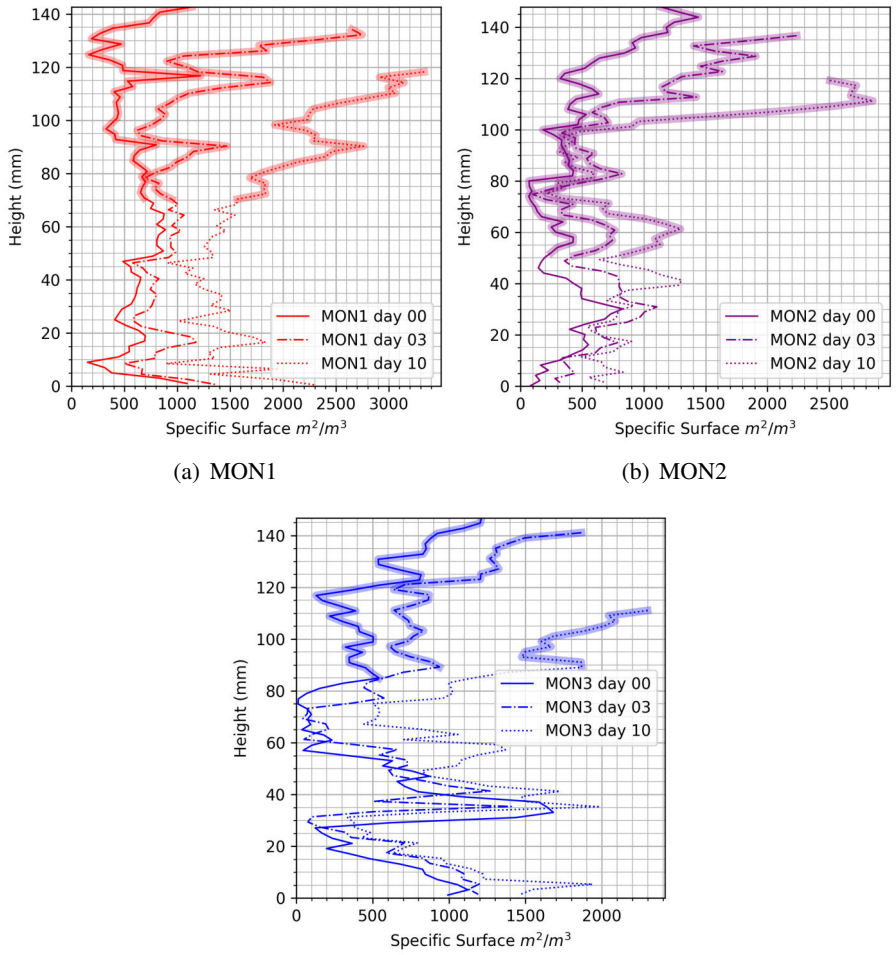

(a) MON1 (b) MON2

(c) MON3

Figure 6.8: Specific Surface Areas profiles.
The deposit layer is represented by a wider trace in the curves.
Computations were performed for a ROI of 60%.

Table 6.6: Average SSA for the deposit and gravel layers and increase over time.
Computations were performed for a ROI of 60%.

		Average SSA in m^{-1}		(SSA day i)/(SSA day 0)	
Sample	Day i	Deposit layer	Gravel layer	Deposit layer	Gravel layer
1	0	552	637	1	1
	3	1202	844	2.2	1.3
	10	2340	1375	4.2	2.2
2	0	501	410	1	1
	3	833	660	1.7	1.6
	10	1081	799	2.2	1.9
3	0	573	549	1	1
	3	981	597	1.7	1.1
	10	1832	994	3.2	1.8

6.3.2.4 Connectivity

Oxygen transport in treatment wetlands depends on the connectivity of the void phase to the atmosphere. A well-connected pore network will ensure oxygenation at all heights within the filter. Connectivity is altered by changes in the distribution of biosolids and of their water content during the feeding and drying period.

Figure 6.9 shows the vertical profiles of the connectivity of the samples during the drying experiment. The computations were done for a ROI of 60%. This consideration is mandatory as results are strongly influenced by border effects. By definition, the connectivity is 100% at the top of the sample and decreases to lower values if the void volume connected to the top of the sample is lower than the total void volume at a certain height.

Changes in value of connectivity depend on two factors: the increase of the connected volume and the increase of the total void volume. If the first is larger than the second, th. The increment of connectivity was higher in sample MON1 followed by sample MON3 and MON2. At the end of the experiment, the connectivity of sample MON1 was fully recovered for almost its entire height (connectivity values rise to more than 90%). Nevertheless, the connectivity of sample MON2 and MON3 was recovered only 5 cm and 2 cm in height respectively (from heights 130 to 80 cm in sample MON2, and from heights 130 to 110 cm in sample MON3).

Samples with higher content of water, thicker deposit layers, and a compacter biosolid phase (with less presence of voids among biosolid aggregates) will require more time to recover their connectivity. This explanation and the characteristics of the samples matches with results in Figure 6.9: (1) sample MON2 has the largest amount of water followed by sample MON3 and MON1 (6.2), (2) at day 0, the deposit layer of sample MON2 was 2.5 and 3.5 cm thicker than that of sample MON1 and MON3 respectively. Samples MON2 and MON3 have also the most compact deposit layer, which is evidenced by the small amount of voids present among biosolid aggregates in figures 6.5(b) and 6.5(c). Although sample MON1 has a thicker deposit layer than sample MON3, water evaporation may have been hindered in sample MON3 by the presence of the big gravel. Also, in sample MON3, the profile for day 0 shows higher values of connectivity than that of day 3 because the bottom of the sample moved downwards when part of the gravel layer fell inside the sampling tube.

Table 6.7 presents the results of average values of connectivity for the whole samples and their gravel layer.

The average connectivity of the gravel layer of sample MON1 was already high from day 0 and increased until almost 90% at the end of the experiment. Figure 6.5(a) shows a good distribution of voids in the gravel layer of this sample since day 0. The average connectivity in the gravel layer of the other samples is very low most certainly because presence of a non connected *Phragmites* in sample MON2 and the development of a big crack not connected to the top of the gravel layer in sample MON3.

The average connectivity of the whole sample increased considerably in sample MON1 and decreased in samples MON2 and MON3. In sample MON1, once the void phase in the deposit layer connected to the void phase at the top of the gravel layer between day 3 and 10, the connectivity augmented considerably. Following the mathematical reasoning presented in section 6.2.6.1, it is concluded that the relative increase of the connected void volume was less than the relative increase of the total void volume in samples MON2 and MON3.

Results of connectivity show an important degree of heterogeneity and therefore raises the question of the the representativity of the observations carried out on a small sample. Despite the porosity-REV was found to be 1.5 cm [68], it might not be applicable to all measurements and especially connectivity which in turn may require larger samples to be precisely determined.

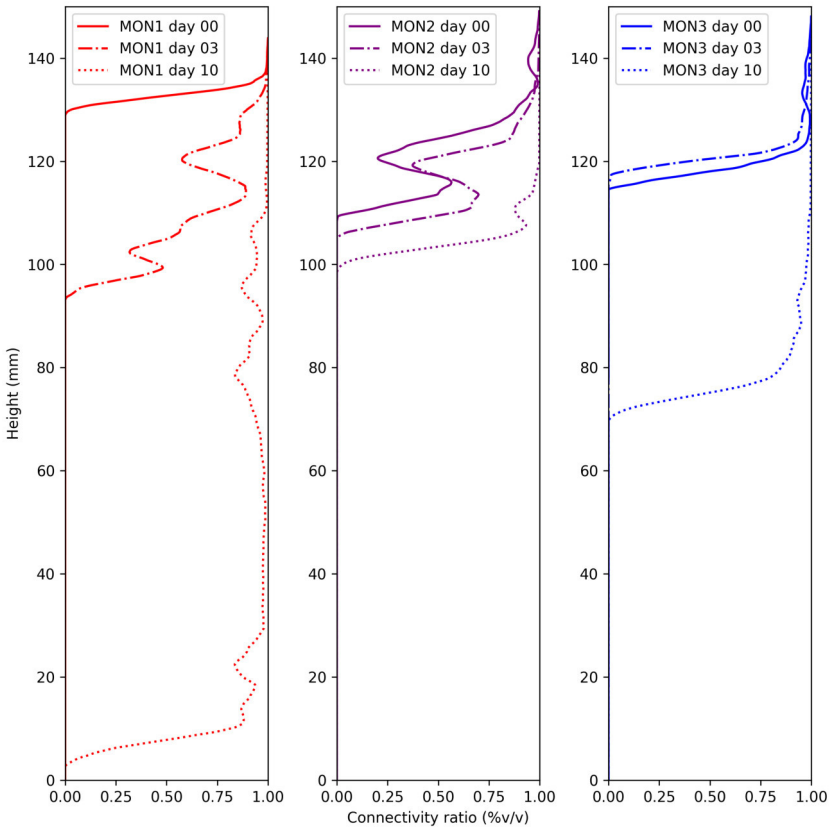

Figure 6.9: Void phase connectivity profiles.
Computations were performed for a ROI of 60%.

Table 6.7: Average values of void connectivity

Sample	Day	Void connectivity	
		gravel layer	whole sample
MON1	0	0.76	0.19
	3	0.76	0.26
	10	0.88	0.91
MON2	0	0.08	0.29
	3	0.09	0.21
	10	0.15	0.20
MON3	0	0.00	0.34
	3	0.00	0.26
	10	0.01	0.22

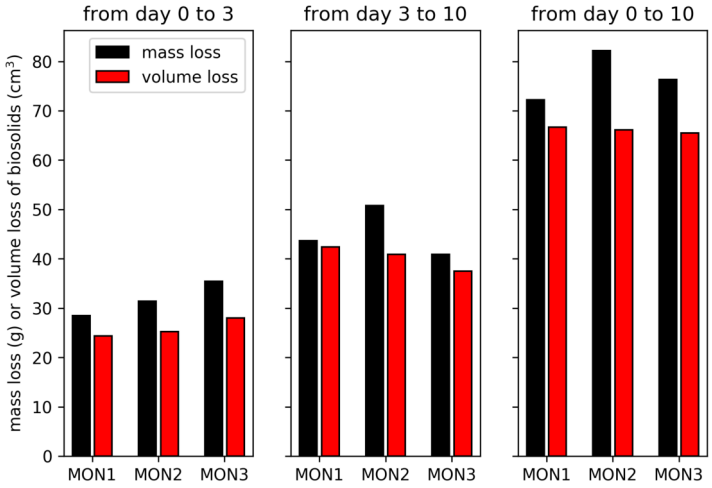

Figure 6.10: Comparison of mass and volume losses.

Table 6.8: Increase of air-filled microporosity volume fraction ($\Delta\theta_{microporosity}$)

	MON1	MON2	MON3
Day 3	0.03	0.04	0.06
Day 10	0.07	0.14	0.13

6.3.2.5 Coupling of imagery and gravimetric methods

Images from X-ray CT can be further exploited when combined with other measurements. In this work the gravimetric measurements and geometrical information are used to describe phenomena that happen under the resolution of the X-ray CT scans.

Despite the volume of air-filled pores smaller than 35 μm (micropores) is impossible to measure, estimations of the increase of volume of this pore size class is possible following the procedure detailed in Section 6.2.6.2. Firstly the mass loss of biosolids is greater than the mass loss corresponding to the volume loss of evaporated water (assuming a density of 1 $g \cdot cm^3$) which is shown in 6.10. Using this values it is then possible to compute the increase ($\Delta\theta_{air-microporosity}$) of the air-filled micro-porosity of the biosolids. Values are presented in 6.8. At the end of the experiment, the air-filled void volume fraction within the biosolids has increased by 0.07 to 0.13. These estimates are averaged on all of the volume of biosolids since only global water content was measured in this experiment, nevertheless, porosity smaller than 35 µm may present a strong heterogeneity in the sample due to: (i) a more intense drying in the deposit layer compared to the gravel layer, (ii) a difference of internal structure between these layers due to the higher mineralization (numerous drying cycles) of the biosolids in the gravel layer. These results are only estimations that rely on the assumption that that solids and water in biosolids are immiscible [103], and that the mass loss of solids by mineralization is negligible. This assumptions must be confirmed.

Such a phenomenon is crucial to understand mineralization and clogging in VFTW. When the micro-porosity is filled with air instead of water, oxygen transport within the biosolids will be controlled by molecular diffusion of oxygen in gas phase which is more than 10,000 higher than in liquid phase ($D_{O_2-H_2O} = 1.97 \times 10^{-5}\, cm^2 \cdot s^{-1}$, T = 20°C, $D_{O_2-N_2} = 2.19 \times 10^{-1}\, cm^2 \cdot s^{-1}$, T = 20 °C).

By coupling gravimetric with tomography the potential of X-ray CT to study physical

processes such as drying of biosolids in VFTW, is expanded beyond the limits of the resolution of the scans. Results presented in this work are encouraging and indicate that the usage X-ray CT or other imagery techniques is suitable to study clogging as well as other physical, chemical and biological processes which are influenced by the structure and spatial distribution of phases present in VFTW.

6.4 Conclusion

This study demonstrates the applicability of X-ray CT to study the structural changes of VFTW at the pore scale during the rest period. An ex-situ experiment was performed in a drying chamber to simulate a rest period of samples containing the deposit layer and gravel layer of French VFTW. An average evaporation rate of 2 $mm \cdot day^{-1}$ was measured which is representative of the lowest values that can be observed in full scale TW. Under this conditions, drying induced major changes in the volumetric distribution and morphology of phases in the samples, which were measured by X-ray CT. At the end of the drying period, the volume of biosolids had reduced to 58% of its initial value in average. Most of the reduction of volume of biosolids is observed in the deposit layer.

This work confirms the applicability of X-ray CT to understand the dynamics of structural changes of biosolids and voids of samples from VFTW during a ex-situ drying experiment. Clogging is essentially a geometrical phenomenon influenced by physical and biological processes in VFTW, thus changes in structure and distribution of biosolids are key elements that should be understood.

The reduction of biosolid volume fraction is 6 times higher in the deposit layer than in the gravel layer and the thickness of the deposit layer is reduced to 68% of its initial value. PSD evolves differently during the rest period depending on the layer. The deposit layer shows an increase of void volume with sizes greater than 4 mm, as a result of radial shrinkage and cracks development. When excluding the border effect an increase of void volume with sizes between 0 to 3 mm results from the drying at the center of the sample. In the gravel layer, the increase of void volume is mainly due to an increase of pores ranging from 0 to 2 mm. The void/biosolid SSA increased at variable ratios from 1.1 to 4.2. The SSA and its increase over time is also greater in the deposit layer. The connectivity of the void phase to the atmosphere was increased from 19% at the beginning to 91% for only one of the samples at the end of the experiment.

The impact of the rest period on water flow in VFTWs has already been discussed qualitatively and quantitatively, but only from a global approach with measurements such as infiltration rates and hydraulic conductivities. Nevertheless, the quantification of phenomena at the origin of changes in IR and K in the rest period, at the pore scale, were missing in the domain of TW, which is a innovative contribution of X-ray CT. Through these measurements, it is confirmed that almost all the changes in the structure of biosolids contribute to an increase of the hydraulic conductivity for the next feeding period, to know: (1) reduction of the thickness of the deposit layer, and increase of the (2) void volume, (3) pore size and (4) connectivity.

By coupling gravimetric measurements with volumetric measurements, the structure of the biosolid phase can be described beyond the limits of X-ray CT resolution. The air filled microporosity is also a key physical variable to understand the dynamics of mineralization and clogging as, it controls the rate of oxygen transfer within the biosolids and their biological degradation. Based on hypothesis on the behavior of water/organic matter mixtures, it was possible to estimate an averaged increase of 0.11 of the air-filled microporosity porosity within the biosolid phase during the drying experiment.

7. Conclusions et perspectives

7.1 Conclusions

7.1.1 Potential, breakthroughs and limitations

THIS study has proven the suitability of X-ray CT to study the porous structure of French VFTW. This methodology produces 3D images with high resolution, in a short amount of time and with enough contrast to identify 3 phases: voids, Fouling Material (FM), and gravel. In tomographies from French VFTW, the FM is an homogeneous phase representing a mixture of organic matter, small mineral particles, water and plant tissues.

A robust segmentation algorithm based on region growing [35] and various other state-of-the-art image processing methods has been written in python and adjusted to the specific needs of samples extracted from French VFTW. The first scans and segmentations demonstrated that small voids surrounded by wet FM can be clearly identified without particular sample preparation (no previous drying). This feature has been exploited to study the drying of French VFTW porous media during an ex-situ drying period.

In this study, cylindrical samples from the first stage of a full-scale French VFTW were analyzed. The sampling required a careful manual methodology to avoid sample alteration, specially when numerous rhizomes were present. The resolution of the scans depends on the size of the sensor in the X-ray scanner, the diameter of the sample and the distance between the X-rays source and sensor. The diameter has been chosen to be 5 cm. It was found to be large enough to limit core alteration during sampling (by shear stress at the edges of the cylinder) to a low level. For this diameter, the optimum resolution of the images was 35 $\mu m \cdot voxel^{-1}$. The spatial representativity of the samples has been studied using a REV analysis in 2D for the volume fraction of each phase (voids, FM, and gravel). The chosen diameter has been found to be large enough to capture well the heterogeneity of this property. Mean stable values of averaged volume fractions are reached at diameters larger than 1.5 cm as long when no rhizome is present. The maximum height of the samples was 16 cm. It contains the whole deposit layer and part of the gravel layer. Longer samples can also be scanned preserving the resolution of the images. This is possible by using a helical scanner or performing several horizontal scans over the total height and concatenating them digitally afterwards. The main limitation in height is defined by the maximal vertical displacement of the platform supporting the sample.

The segmented images can be used to measure several relevant pore scale properties using state-of-the-art image post-processing methods. Some of them were also adapted to the partic-

ularities of the samples and include: phase Volume Fraction (VF) profiles, specific surfaces, voids and gravel characteristic sizes and voids connectivity. The morphological description of the porous media is limited to sizes greater than the resolution of the images. Nevertheless it was proven that estimations of FM micro-porosity (lower than the resolution) can be obtained if X-ray CT and gravimetric measurements are combined during a drying process.

Several breakthroughs have been made in the comprehension of processes occurring in French VFTW thanks to pore scale measurements:

- It has been found that the voids VF reaches low values below 10% or even 5% in the gravel layer of mature French VFTW compared to 30 to 40% in a clean gravel layer. More astonishingly, samples were extracted from TW that have not reached a clogged state. This finding must be considered when choosing the type of model used to simulate water flow in VFTW. In particular, it supports the suitability of dual porosity models, which consider both 'open porosity' and 'FM micro-porosity' to model water flow [83].
- X-ray CT images clearly depict the migration of some gravel grains up into the deposit layer, which were pushed up by the accumulation of small solid particles in the gravel layer, phenomenon also known as the Brazil nut effect [102]. The resulting decompaction of the gravel layer is currently neglected when modeling fouling and clogging in TW [97, 106].
- A criterion has been proposed to define the upper and lower limits of the deposit and gravel layer. It was used to observe with high precision the variation in the thickness of the deposit layer in a mature French VFTW. Differences up to 3 cm in thickness were found between samples extracted at different points from a homogeneous region based on electrical conductivity measurements. These differences can be explained by the impact of maintenance operations, irregularities of the filter surface, and the random accumulation of dead leaves and shunts, which create micro-topography, and are different from heterogeneities usually induced by uneven effluent distribution. These differences in thickness did not appeared to significantly influence the efficiency of the loading on a mature system when observing a batch event at the filter scale: the entire surface was flooded. At a local scale, they cannot be considered negligible as they may represent 30 to 60 % of the ponding height (5 to 10 cm) during a batch and therefore may influence locally processes: formation of a preferential infiltration paths, enhancement or delay of re-oxygenation, development of anaerobic hotspots...
- The pore-scale structure of samples was found to be very similar independently of their location in a mature French VFTW and the thickness of the deposit layer. Pore sizes, specific surfaces and phase volume fractions show alike values which only vary depending on the depth (deposit layer or gravel layer). These findings, together with the 2D-REV analysis, set a first solid basis in terms of spatial representativity of X-ray CT for its application in the study of other processes.
- During drying, porous media from French VFTW show significant changes in their structure. In the ex-situ drying experiment, a FM volume reduction to almost 60% of the initial value was observed. This volume loss corresponded to an increase of void sizes ranging from 0 to 3 mm in the gravel layer and at the center of the deposit layer, and to the formation of bigger shrinkage cracks of more than 4 mm at the topmost part of samples. These experiments demonstrated the importance of the rest period for the renewal of the connectivity of voids to the atmosphere. In 10 days of rest, the void phase connectivity is reestablished, which promotes a rapid renewal of oxygen in the pore media of the TW. It was also observed that shrinkage cracks did not penetrate the whole thickness of the deposit layer. Consequently, if the same phenomenon occurs in-situ; water that preferentially infiltrates through these cracks may only affect the first 0 to 3 cm of the

surface and may not by-pass a large volume of the deposit layer as it was believed so far. These results were obtained in a drying chamber that yield a mean rate of evaporation of 2 $mm \cdot d^{-1}$. If the methodology proved to be suitable to record structural changes, they are expected to be greater in full-scale French VFTW, specially in summer season, where the ET rate is at its maximum.

- An increase of the volume of water free micro-porosity in the FM of 0.07 to 0.14 (v/v) was estimated by measuring the water loss during drying and comparing water volume loss to the volume retraction of the FM phase. The degree of saturation of the FM has important repercussions on transport of oxygen within the FM and, thus, on the degradation and mineralization processes occurring within it.

The volumetric measurements are limited to a 3 phase segmentation: voids within the FM and within reeds are not differentiated neither the different components of the FM. SSA results are limited to the resolution of the scans, and their interpretation must be carefully done. The underestimation of SSA increases inversely to the degree of saturation because more micro-pores in the FM become unsaturated. The treatment and post-treatment of these images require significant computational resources, which vary depending on the specific algorithms that are executed. In order to obtain results in a reasonable amount of time, servers with 128GB in RAM and 12 CPUs were used to treat input images of 8 to 16 GB. Less powerful servers may be used to but they could only process smaller regions of interest (ROI).

7.1.2 X-ray CT, a versatile tool

X-ray CT is a methodology which could be used for different purposes including scientific and routine tool to assess clogging. If somebody wishes to use it as a routine tool, he will be able to download and use scripts and macros from a shared repository. Nevertheless, the most important contribution of X-ray CT is its suitability to study the influence of pore scale structure in transport phenomena. This approach has been proven possible in other domains like: geology, oil production and medicine, where it is sometimes used for engineering purposes (i.e. the estimation of the permeabilities of oil and water in a reservoir), but it is very innovative in the domain of TW. The choice of this method has been driven by the need of more reliable methods to study the clogging in order to predict it. In this work, only the dynamics of structural changes of FM during an ex-situ rest period was studied. Nevertheless many other processes can be studied at the pore scale level and should lead to other breakthroughs that will complete and/or change the comprehension of TW, which still have the reputation of being black boxes. A list of perspectives of the use of imagery techniques, experiments and models to study TW is presented further.

7.1.3 X-ray CT a “spatially representative tool”

A well founded basis for the use of X-ray CT have been set in this study by establishing a robust segmentation methodology (Chapter 4) and analyzing the spatial representativity of samples (Chapter 5). Nevertheless representativity is still an open subject of discussion, as it depends on the phenomenon on which a study focuses.

We still encourage to perform laboratory-scale studies with columns of diameters not less than 5 cm, and to use fouled gravel with no rhizomes or clean gravel. Nevertheless, representativity must be always studied for variables like voids connectivity specially in oxygen transfer or water flow through. Analyzing the connectivity-‘REV’ is important and far from being an easy task in media that fouls progressively.

7.1.4 X-ray CT, a compact tool

Compared to other methodologies or techniques to study TW, X-ray CT is a compact tool. Many pore scale but also large scale measurements can be done by processing a single image. The measurements of void volume, FM volume, connected voids, SSA, pore sizes distribution, gravel sizes have been demonstrated. Moreover, these measurements do not rely on any simplification or assumption of geometrical structure.

Other pore scale properties like tortuosity, hydraulic conductivities, dispersion coefficients, or global mass/heat transfer coefficients can be estimated performing simulations at the pore scales followed by upscaling procedures. These topics are discussed further below in the perspectives section.

Once estimation of these parameters/properties are validated experimentally, X-ray CT may find a privileged position among all the methodologies to study pore properties in TW as it may reduce drastically the time and resources necessary to perform separate laboratory measurements. A comparison of the incertitude by different techniques still needs to be done.

7.2 Perspectives

Altough the original purpose of this doctorate was to study solid transport in French VFTW at the pore scale to understand fouling and clogging better, this thesis could only set the basic elements to endeavor such an ambitious project. X-ray CT can be used as a tool to (1) characterize fouled/clogged porous media and (2) define the geometry for simulations of transport phenomena. Further results following both approaches will help to understand the processes occurring in TW at the pore scale, and expected to be used to optimize their operation and design. This is succinctly resumed by the French motto: “Bien comprendre pour agir” (understand better to take more effective action)

Several perspectives are presented focusing on 3 investigation topics: oxygen transport, drying and re-hydration of FM, water flow and solid transport.

7.2.1 Oxygen transport

The importance of oxygen transport in mineralization of FM and thus in fouling and clogging of TW has been reminded several times in this thesis. Phenomena related to oxygen transport include diffusion or advection trough macro-porosity and micro-porosity, interaction with the FM phase (e.g. absorption or adsorption) and reaction.

An experiment to monitor oxygen transport was already performed during this PhD simultaneously to the ex-situ drying experiment presented in chapter 6. Five oxygen probes (Presens) of about 4 mm in diameter were inserted 0.5 cm into the samples and placed every 2.5 cm from the top. Figure 7.1 shows the the location of the probes. A sixth probe recorded oxygen air concentration. All the probes were calibrated into a 0 - 100% scale in gas phase. A N_2(g) flow of approximately 1 $m \cdot s^{-1}$ (D = 5 mm) was fed through the bottom of the sample for at least ten minutes until all probes measured 0% (Figure7.2). After the N_2(g) flow was stopped the samples were naturally re-oxygenated by the air present inside the chamber and the oxygen concentration profile was recorded for one day. This procedure was executed twice, once at the beginning and once at the end of the rest period.

Figure 7.3 presents the evolution of local oxygen measurements. At the beginning of the rest period, there was no systematic correlation between the distance of the oxygen probe to the top of the sample, from where oxygen was re-entering the sample, and the time at which the oxygen concentration starts to raise again. While at the end of the rest period, it was systematically observed that the closer a probe is from the top, the faster the concentration raises. This difference is probably explained by the increase in void connectivity.

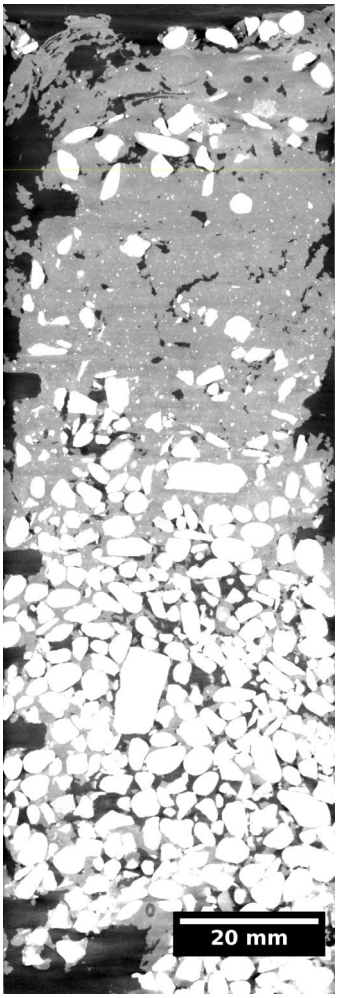

Figure 7.1: Vertical snapshot of an X-ray scan.
Holes left by oxygen probes are noticeable on the left.

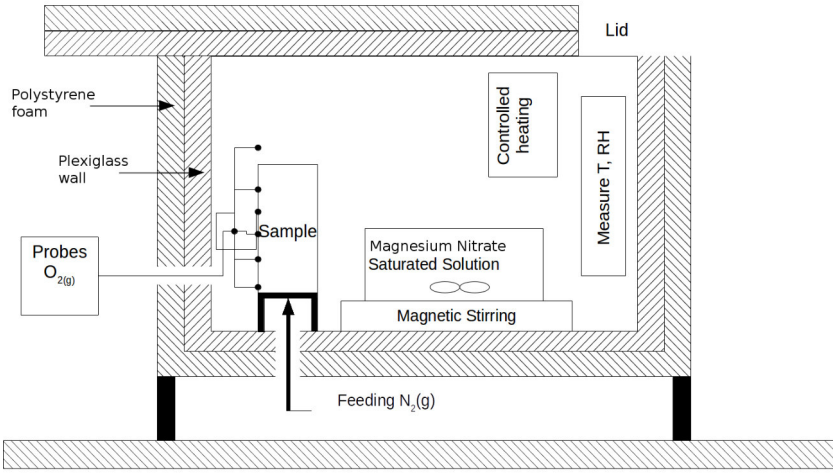

Figure 7.2: Experimental setup for oxygen depletion and re-oxygenation

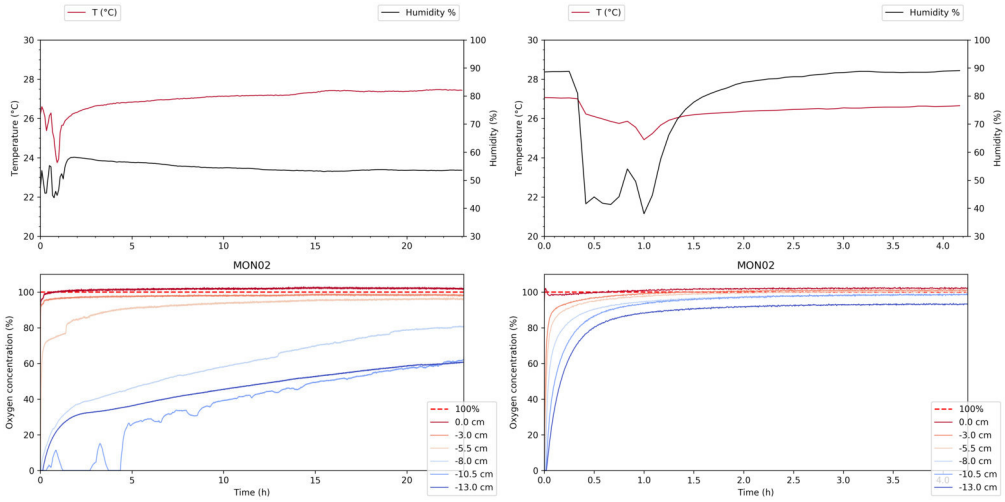

(a) after 1 day of rest (b) after 10 days of rest

Figure 7.3: Oxygen, T and relative humidity measurements.
Results correspond to sample MON2 in the drying study from chapter 6.

To explore this assumption, we aim at modeling oxygen transport using the pore structure description provided by X-ray CT. Currently, there exist two ways of modeling transport phenomena at the pore scale: direct modeling and Pore Network Modeling (PNM) [8].

In direct modeling, the equations modeling transport phenomena are solved in a discretization of the voids phase which represents closely its real morphology. In PNM, the voids phase is transformed into an 'equivalent' pore network (like a resistor network) represented by an arrange of spheres (pores, defined by a radius and the position of their center) interconnected by cylinders (throats, defined by their radius and length, and their position). The equations modeling transport phenomena are solved in this simplified geometry.

Preliminary results of direct modeling of oxygen transport were already obtained during this PhD. As a first step, oxygen diffusion was modeled using Fick's law in the void phase of a small portion of porous medium. The mass transfer equations were implemented in a C program using the finite volumes numerical method and solved using MUMPS. The code is based on the work of Ortega Ramirez to model flow and transport properties in granular soils at the pore scale [98]. Figure 7.4 shows a 3D profile of oxygen concentration in stationary state. The FM and gravel phases were set as walls and thus no phase transfer is modeled between the voids and FM.

Altough the use of direct simulation to study oxygen transport showed already satisfactory results, its computational cost is huge when solving equations in the whole samples, specially when keeping the same mesh proportioned by X-ray CT. Therefore, efforts will have to focus on domain meshing, the alternative being to use PNM.

If pore-scale numerical models are able to explain why oxygen concentration raises faster at some location than other, they could be used to improve parameter estimation of larger scale model (Darcy's scale) either by using a upscaling procedure like described in [8], or by identifying a metric of interest like the tortuosity.

Evaluating the tortuosity of real porous media is a challenging task. Tortuosity is defined as constant global ratio ($\frac{L}{L_0}$), where L is the total length of a tortuous pathway and L_0 is the total displacement in the main flow direction (Figure 7.5). This is a strong simplification of the morphology of real porous media, where connected and also not connected pathways (in fouled porous media) are multiple. However, it is one of the parameters that allows to take into account geometric complexity in transport phenomena at the macroscale. There exists algorithms

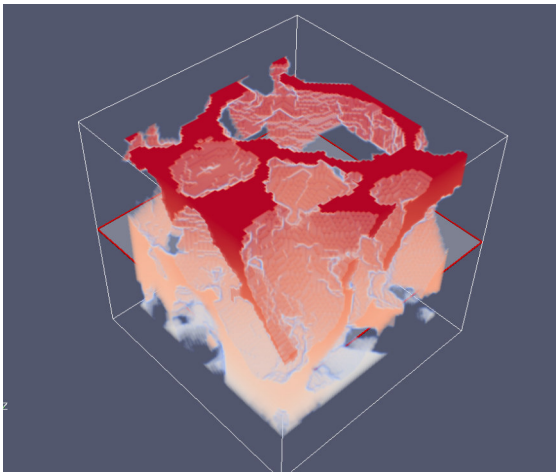

Figure 7.4: 3D simulated profile of oxygen concentration in the void phase in a $(3mm)^3$ domain.
Red to white shades correspond to 100%-0% of oxygen concentration. Main flux direction is vertical downwards. The transparent regions correspond to the fusion of gravels and FM.

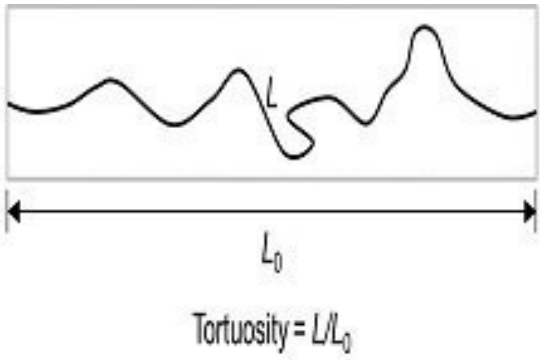

Figure 7.5: Concept of Tortuosity

available in FIJI and python libraries which estimate the shortest and longest distances between two points in images representing tortuous media. A next step in the study is to assess these tools to measure tortuosity based on the morphology of real porous media. Such an approach is different from an estimation of tortuosity by fitting models at the continuous scale to experimental data. When model parameters are measured instead of being fitted, their validity to describe a phenomenon can be assessed better. This practice helps developing mechanistic models. In this approach, parameter fitting is reduced and thus, the model validity is not limited to the size and variety of the dataset that was used to calibrate it.

For the study of tortuosity the segmentation algorithm has to be improved and the skeletonization of the voids phase may need to be adapted to reduce artifacts like those presented in Figure 7.6. These artifacts are caused by segmentation errors and corresponds to aggregates of FM and gravels completely surrounded by voids with no contact point with the rest of the solid matrix.

Finally, the reoxygenation experiment is not the one of a passive porous media. It is likely that the oxygen consumption in the FM is high. Therefore it will be first necessary to make assumption to exploit the data. In order to study separately oxygen transport and reaction we propose to generate a 3D printing of fouled porous media using the segmentations of X-ray scans. The non reactive solid phase (plastic made) will be the fusion of the gravel and FM

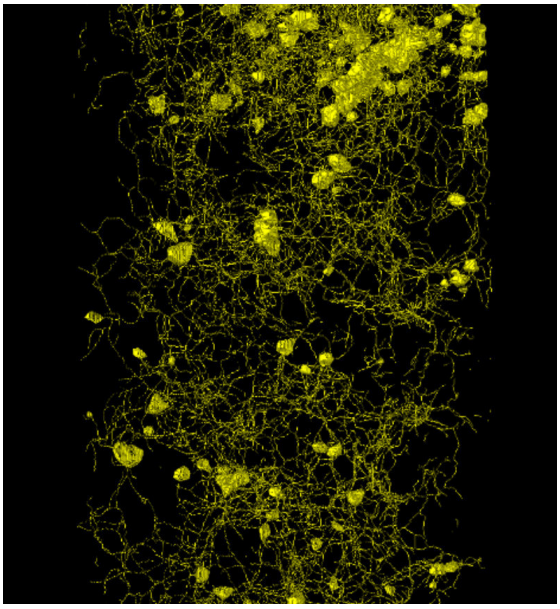

Figure 7.6: Example of a skeleton of the void phase.

phases. Then, the oxygenation (or deoxygenation) dynamics can be measured locally following the experimental protocol presented above.

In order to include oxygen consumption into models, two approaches could be proposed: reactions (i) in a 'liquid'/gas phase reactor or (ii) in a solid/gas catalytic reactor. They do not take into account the different reaction pathways followed by oxygen in biological reactions which would be a complicated approach. However they may describe an average behavior of oxygen consumption.

The first approach considers FM as an homogeneous phase resembling to a liquid in contact with a gas phase (macropores). This approach is perhaps more suitable when the FM in French VFTW is saturated in water. In this approach oxygen is assumed to be absorbed into the 'liquid' phase and then react. The rapidity of these process is influenced by the absorption equilibrium, the rate of diffusion of oxygen in the liquid phase and the rate of reaction of oxygen.

In the second approach FM is considered as a catalytic reactor with two different phases (a) organic solid phase (with low humidity) and (b) micro-porosity. This approach is perhaps more suitable when the FM has a very low degree of water saturation. In this approach oxygen is assumed to be adsorbed into the solid phase and then react. The rapidity of these processes is influenced by the adsorption equilibrium, diffusion in the micro-porosity, and the rate of reaction of oxygen.

7.2.2 Drying and re-hydration of FM

Drying of the FM is important as it decreases its volume, increases its porosity thus enhancing oxygen penetration. If during the rest period dewatering, shrinkage and mineralization of the FM are important subjects to be studied, during the feeding period, humidification, swelling of the FM, SS filtration and biofilm growth within the porous media are important as well. Two major perspectives can be discussed: (1) studying the effect of ET in structural changes of FM at the pore scale and (2) studying the structural changes of the micro-porosity of the FM.

7.2.2.1 Evapotranspiration effects

The study of the effect of ET could be done ex-situ using young reed sprouts or in-situ. It would require some methodological development like the identification of the reed roots and rhizomes

as it was already suggested in Chapters 4, 5 and 6. On the one hand, the segmentation of hollow cavities, characteristic of rhizomes, could be achieved with a specific development of the image processing algorithms based on shape recognition. On the other hand, the segmentation of plant tissues may require a specific pretreatment of the sample. The difficulty arises from the fact that the gray level corresponding to plant tissues in the raw image is within the range of gray values associated to the FM.

In botanics, staining techniques are used to identify specific plant tissues, e.g. roots that have been mycorhized can be visualized by microscopy after a pretreatment that includes staining using trypan blue [121]. Similarly, contrast chemical that enhance contrast for targeted tissues in X-ray CT could be used. Root and rhizome can also be identified by Magnetic Resonance Imagery (MRI). Metzner et al. [75] performed X-ray CT and MRI scans on root systems in soil. MRI data could be fused with X-ray CT scans as the former are usually of poorer resolution.

7.2.2.2 Structural changes within the FM

The study of the structural changes of FM micro-porosity could be carried out using X-ray CT at better resolutions (imaging with a voxel size of 6 μm has been performed at MATEIS laboratory, INSA) but would require to work with smaller samples.

The study of the development of micro-porosity could be complemented by the study of plastic properties [122], hydrotextural properties [123] and drying kinetics [117] of the FM from French VFTW. Monitoring changes in the bulk density of the FM during drying requires estimation of the incertitude in volume measurements by X-ray CT.

A better description of the FM and its changes over time may help answer major scientific questions in the field of TW:

- Oxygen diffusion within the FM is of critical importance because most the biochemical reactions that permits pollutant removal occurs within it. The combination of modeling and pore-scale imaging could describe how FM thickness impacts oxygen transport and whether or not can be neglected as it is done in state-of-the-art modeling approach for TW (CWM1).
- Biofilm is generated by bacterial growth in optimal conditions but also by synthesis of exopolymers when they suffer particular stresses such as low humidity and low oxygen concentration [72]. This biofilm is particularly more viscous and resistant to evaporation. A 3D map of oxygen and water content in the FM based on simulations of oxygen and drying of the FM at the pore scale could be used to predict the preferential locations for biofilm development.
- Heterogeneous distribution of water content, distance from the wetlands surface and plant roots and, by extension, gradients of oxygen concentration are conditions that create gradients of red-ox potential. Different bacterial metabolic pathways are predominant at specific red-ox potential [25]. Simulating a map of red-ox potential may help to predict preferential locations of different metabolic types of bacteria in TW, identifying spots where different reactions may occur (e.g. nitrification, denitrification, sulphates reduction, and methanization).

7.2.3 Water flow and solid transport

Understanding the mechanisms governing water flow in TW is essential to improve the understanding of their performance in pollutant removal, and the adjustment of the hydraulic loads. A study of water flow at the pore scale among others help choosing or developing adequate models for water flow.

The use of X-ray CT to observe dynamic phenomena like fluid flow is possible using equipments capable of capturing images in a very short time lapse. For the moment their use has been privileged in studies for medicine, oil extraction and radioactive waste disposal

[115]. Nevertheless a study of stationary water flow could be endeavored with "less" powerful equipments if during the scanning a stationary water content profile is reached. The success of the experiment relies also on the possibility of segmenting four phases: gravel, voids, and FM and water separately.

In X-ray CT scans of pore media containing two fluids (e.g. carbonate rocks with oil and water) it is a common practice to add high molecular weight soluble salts to water like NaI or CsCl, usually named contrast agent or dopant, in order to enhance the contrast. In the case of VFTW, if the contrast agent is not adsorbed by the organic matter in FM, this may allow differentiating water-filled porosity from organic solids inside the FM. An alternative to contrast chemical usage is the Neutron Imaging (NI).

NI has the potential of quantifying the water content in soil samples. NI images similar to X-ray CT images but are produced following a different principle. While in X-ray a material absorbs more or less photons depending on the density of its atom nuclei, in NI the material absorbs neutrons depending on the ability different elements to absorb them. Hydrogen has the particularity of being able to absorb neutrons more than many other atomic elements in wastewater or granular media including (N, O, Na, Mg, Si, P, S, K, Ca, Fe). It only absorbs less neutrons than Al and Cl.

Usually, NI requires longer exposure times than X-ray CT, but has proven to capture successfully the structure of the rhizosphere in germinating seeds of chickpeas [80]. Two type of images were produced in this study with resolutions of 50 and 200 μm/vox from cylindrical samples of 2.7 cm in diameter and 10 cm in height. Similarly to MRI, it would be beneficial to fuse data obtain by NI with those obtained by X-ray CT-scan.

X-ray CT may be used to follow the accumulation of solids in an experiment where a sample with porous media (filled either with clean or partially fouled gravel) is fed with a suspension of solids in water. Some considerations could be taken into account:

- Adjusting the load of SS, and the duration of the feeding and rest periods to accelerate the fouling process,
- Using a synthetic solids suspension whose particles are made of molecules with larger molecular and thus tracked as a different phase by X-ray CT.
- Study the migration of fragmented FM particles from the deposit layer into the gravel layer FM induced by water flow.
- Studying biofilm growth only with an influent with organic soluble load but not SS load in a clean gravel layer
- Studying the influence of gravel shape and gravel size distribution on solid accumulation

For the study of solid transport, direct modeling seems to be a-priori the best approach as PNM cannot reproduce all the filtration mechanisms influenced by pore geometry. There must be a coherence between the model used to simulate water flow and that used to simulate solid transport. Solid particles move firstly following current lines and are then intercepted by mechanisms influencing them to cut the current lines: Brownian motion, interception, sedimentation and inertia.

If this task seems difficult, recent work has proven to successfully model solid transport at the pore scale using direct modeling [76]. In this work fluid flow is modeled in the void phase using the Navier-Stokes equations and solid transport is simulated using 'granular flow modeling'. It consists in simulating the movement of spherical particles in suspension and their retention in pore media by summing up all the forces acting on each particle: gravitational/buoyant forces, contact forces (particle-particle and particle-surface), and hydrodynamic drag force. In their study the Van der Waals, electric double layer and Brownian forces were neglected, as the particles exceeded 30 μm. Such a methodology could be adapted to the specificities of TW, where the particle size range is larger.

If this approach could be an initial step for modeling fouling and clogging, it takes into account only physical mechanisms that foul the granular media. The biofilm growth should also be modeled. The speed of fouling by biofilm growth has been studied experimentally and modeled for simple geometries in the work of [29, 86].

Some challenging tasks will be to model (1) the change of structure of the FM during the rest period (shrinkage), (2) the detachment of particles during the rest period (3) their remobilization to deeper zones in the granular media as they are dragged by the flow of water during the subsequent feeding period (4) the expansion of the gravel layer due to the accumulation of solids.

Similarly to oxygen diffusion, flow and transport model at the pore scale may help to better estimate parameters used in models at the Darcy's scale and therefore to perform better predictions. This procedure is called upscaling.

Upscaling consists in any procedure allowing to obtained an averaged behavior of the phenomena occurring in porous media at a lower scale. Upscaling leads to the estimation of parameters used in models working at a larger scale (like the hydraulic conductivity in Darcy's Law). In the larger scale, the media is considered as a continuum where the presence of multiple phases is modeled by volumetric fractions, like porosity or saturation. This continuum assumption is regularly called the Darcy's scale.

When averaging a phenomena simulated at the pore scale, the complexity of the geometry in porous media is implicitly considered in the resulting averaged parameter. This approach accomplishes the same objective than fitting the same parameter using an experimental measurement. The advantage of upscaling compared to empirical fitting would be the possibility of finding a relationship between pore scale properties and the averaged parameter rather than fitting a parameter with a new experiment every time the structure of the sample changes.

For flow and transport, upscaling would lead to two important advances:

- By averaging fluid flow modeled by Navier-Stokes equations at the pore scale, the hydraulic conductivity can be estimated.
- In the case of solid transport, averaging granular flow at the pore scale may lead to the estimation of parameters like the filtration coefficient of the Deep Filtration Model (DFM) [76].

PNM can also be used to generate parameters of models at the Darcy's scale. [8] presents how it is possible to estimate relative permeability and dispersion coefficients using PNM.

The advantage working with models at the Darcy's scale is that they may be used to simulate a process in the entire spatial domain and to simulate long-time cases, like the evolution of fouling in several years of operation of a TW, without the high computational cost of pore scale models.

Fouling and clogging in TW are processes that involve a lot of other processes: fluids flow, biological activity, solid transport, drying. To simulate fouling in a long time scenario one of the possibilities that could be finally considered is the development of a surrogate model. A simple definition of a surrogate model could be a model of models. They are fast to compute and built using machine learning methods based on the results of models applied to a representative range of test cases. The choice of these cases is critical to assure the representativity of the simulations of the surrogate model.

Surrogate models could then be finally used to predict clogging in TW. They could be used to optimize TW operation in order to delay interventions to alleviate clogging as much as possible or even to redefine the design guidelines for construction of TW.

8. Bibliography

[1] Riyadh Al-Raoush and Apostolos Papadopoulos. Representative elementary volume analysis of porous media using X-ray computed tomography. *Powder Technology*, 200(1):69–77, June 2010.

[2] Morteza Aminnaji, Arash Rabbani, Vahid J. Niasar, and Masoud Babaei. Effects of Pore-Scale Heterogeneity on Macroscopic NAPL Dissolution Efficiency: A Two-Scale Numerical Simulation Study. *Water Resources Research*, n/a(n/a).

[3] Anonymous. Arrêté du 21 juillet 2015 relatif aux systèmes d'assainissement collectif et aux installations d'assainissement non collectif, Ã l'exception des installations d'assainissement non collectif recevant une charge brute de pollution organique inférieure ou égale à 1,2 kg/j de DBO5, 2015.

[4] D. Austin, D. Maciolek, B. Davis, and S. Wallace. Damköhler number design method to avoid clogging of subsurface flow constructed wetlands by heterotrophic biofilms. *Water Science and Technology*, 56(3):7–14, 2007.

[5] Jähne Bernd. *Digital Image Processing*. Springer-Verlag Berlin Heidelberg, 6th editio edition, 2005.

[6] Bernd, J. *Digital Image Processing*. Springer-Verlag Telos, Berlin ; New York, November 1991.

[7] P. Bhattad, C. S. Willson, and K. E. Thompson. Segmentation of Low-contrast Three-phase X-ray Computed Tomography Images of Porous Media. In *Advances in Computed Tomography for Geomaterials*, pages 254–261. John Wiley & Sons, Ltd, 2013.

[8] Martin J. Blunt, Branko Bijeljic, Hu Dong, Oussama Gharbi, Stefan Iglauer, Peyman Mostaghimi, Adriana Paluszny, and Christopher Pentland. Pore-scale imaging and modelling. *Advances in Water Resources*, 51:197–216, 2013.

[9] S. Bolte and F. P. Cordelières. A guided tour into subcellular colocalization analysis in light microscopy. *Journal of Microscopy*, 224(3):213–232, 2006.

[10] Gunilla Borgefors. On Digital Distance Transforms in Three Dimensions. *Computer Vision and Image Understanding*, 64(3):368–376, November 1996.

[11] Breul, P. and Gourves, R. In Field Soil Characterization: Approach Based on Texture Image Analysis. *Journal of Geotechnical and Geoenvironmental Engineering*, 132(1):102–107, January 2006.

[12] J. Brisson and F. Chazarenc. Maximizing pollutant removal in constructed wetlands: Should we pay more attention to macrophyte species selection? *Science of The Total Environment*, 407(13):3923–3930, June 2009.

[13] G. Calamita, A. Perrone, L. Brocca, B. Onorati, and S. Manfreda. Field test of a multi-frequency electromagnetic induction sensor for soil moisture monitoring in southern Italy test sites. *Journal of Hydrology*, 529:316–329, October 2015.

[14] James B. Callegary, James M. Leenhouts, Nicholas V. Paretti, and Christopher A. Jones. Rapid estimation of recharge potential in ephemeral-stream channels using electromagnetic methods, and measurements of channel and vegetation characteristics. *Journal of Hydrology*, 344(1):17–31, September 2007.

[15] Chun Chang, Quanlin Zhou, Timothy J. Kneafsey, Mart Oostrom, Thomas W. Wietsma, and Qingchun Yu. Pore-scale supercritical CO2 dissolution and mass transfer under imbibition conditions. *Advances in Water Resources*, 92:142–158, June 2016.

[16] F. Chazarenc, V. Gagnon, Y. Comeau, and J. Brisson. Effect of plant and artificial aeration on solids accumulation and biological activities in constructed wetlands. *Ecological Engineering*, 35(6):1005–1010, June 2009.

[17] F Chazarenc and G Merlin. Influence of surface layer on hydrology and biology of gravel bed vertical flow constructed wetlands. *Water Science & Technology*, 51(9):91–97, 2005.

[18] Bernard Chocat, editor. *Ingénierie écologique appliquée aux milieux aquatiques. Pourquoi ? Comment ?* ASTEE, 2013.

[19] Remi Clement, Marine Audebert, Simon Loisel, and Sylvain Moreau. Straightforward assessment of horizontal leachate injection system using frequency domain electromagnetic induction method. *Environmental Research and Technology*, 1(2):13–17, April 2018.

[20] Cordelières, F.P. 3d object counter [ImageJ Documentation Wiki], 2009.

[21] Molly S Costanza-Robinson, Benjamin D Estabrook, and David F Fouhey. Representative elementary volume estimation for porosity , moisture saturation , and air-water interfacial areas in unsaturated porous media : Data quality implications. 47:1–12, 2011.

[22] Mateus Pimentel de Matos, Marcos von Sperling, and Antonio Teixeira de Matos. Clogging in horizontal subsurface flow constructed wetlands: influencing factors, research methods and remediation techniques. *Rev Environ Sci Biotechnol*, 17(1):87–107, March 2018.

[23] Hu Dong. *Micro-CT imaging and pore network extraction*. PhD thesis, Imperial College London, 2007.

[24] James A. Doolittle and Eric C. Brevik. The use of electromagnetic induction techniques in soils studies. *Geoderma*, 223-225:33–45, July 2014.

[25] Gabriela Dotro, Günter Langergraber, Pascal Molle, Jaime Nivala, Jaume Puigagut, Otto Stein, and Marcos von Sperling. *Treatment wetlands*. Number Volume 7 in Biological wastewater treatment series. IWA Publishing, London, 2017. OCLC: ocn984563578.

[26] Bob Dougherty, Johannes Schindelin, Michael Doube, Richard Domander, Mark Hiner, Curtis Rueden, David Coeurjolly, and Karl-Heinz Kunzelmann. *Local Thickness*. 2017.

[27] G. F. Hua, W. Zhu, J. Q. Shen, Y. H. Zhang, and Y. T. Zeng. The Role of Biofilm in Clogging Process in Vertical Flow Constructed WeTland. *Applied Engineering in Agriculture*, 29(1):61–66, 2013.

[28] L. A. Feldkamp, L. C. Davis, and J. W. Kress. Practical cone-beam algorithm. *J. Opt. Soc. Am. A, JOSAA*, 1(6):612–619, June 1984.

[29] F. Felício, J. Pisoeiro, R. Cardoso, and A. Galvao. A methodology for evaluation of the bioclogging effect in porous media. In *IWA Specialist Conference on Wetland Systems for Water Pollution Control*, number October, pages 207–210, 2018.

[30] Nat Fonder and Tom Headley. The taxonomy of treatment wetlands: A proposed classification and nomenclature system. *Ecological Engineering*, 51:203–211, February 2013.

[31] N. Forquet, A. Morvannou, P. Molle, and M. Vanclooster. Imaging of vertical flow constructed wetland using electrical resistivity tomography and time domain reflectometry. In *WETPOL conference, 03/07/2011-08/07/2011, Prague, CZE*, page 1, 2011.

[32] Nicolas Forquet. *Two-Phase Flow Modelling of Vertical Flow Filters for Wastewater Treatment*. PhD thesis, Universite Louis Pasteur Strasbourg, 2009.

[33] Nicolas Forquet, Catherine Boutin, and Pierre Breul. Contrôle des installations d'assainissement non collectif : l'apport déterminant des outils de diagnostic non destructifs. *Sciences Eaux Territoires*, Numéro 9(4):98–101, 2012.

[34] Jean-Michel Gobat, Michel Aragno, Willy Mathey, Collectif, and René Bally. *Le sol vivant: Base de pédologie-biologie des sols*. Lausanne, 3 edition edition, 2010.

[35] Mir Amid Hashemi, Ghonwa Khaddour, Bertrand FranÃ§ois, Thierry J. Massart, and Simon Salager. A tomographic imagery segmentation methodology for three-phase geomaterials based on simultaneous region growing. *Acta Geotech.*, 9(5):831–846, October 2014.

[36] J. P. Herzig, D. M. Leclerc, and P. Le. Goff. Flow of suspensions through porous media - application to deep filtration. *Ind. Eng. Chem.*, 62(5):8–35, May 1970.

[37] T. Hildebrand and P. Rüegsegger. A new method for the model-independent assessment of thickness in three-dimensional images. *Journal of Microscopy*, 185(1):67–75, 1997.

[38] Ulrike Homberg, Daniel Baum, Steffen Prohaska, Ute Kalbe, and Karl Josef Witt. Automatic Extraction and Analysis of Realistic Pore Structures from μ CT Data for Pore Space Characterization of Graded Soil. *International Conference on Scour and Erosion, Paris*, pages 345–352, 2012.

[39] A. N. Houston, W. Otten, R. Falconer, O. Monga, P. C. Baveye, and S. M. Hapca. Quantification of the pore size distribution of soils: Assessment of existing software using tomographic and synthetic 3D images. *Geoderma*, 299:73–82, 2017.

[40] G. F. Hua, L. Li, Y. Q. Zhao, W. Zhu, and J. Q. Shen. An integrated model of substrate clogging in vertical flow constructed wetlands. *Journal of Environmental Management*, 119:67–75, April 2013.

[41] G. F. Hua, W. Zhu, L. F. Zhao, and J. Y. Huang. Clogging pattern in vertical-flow constructed wetlands: Insight from a laboratory study. *Journal of Hazardous Materials*, 180(1):668–674, August 2010.

[42] C. R. Ison and K. J. Ives. Removal mechanisms in deep bed filtration. *Chemical Engineering Science*, 24(4):717–729, April 1969.

[43] S. Judd and C. Judd. *The MBR book*. The MBR Book. 2006.

[44] R.H. Kadlec and R.L Knight. *Treatment Wetlands*. Boca Raton, Florida, 1996.

[45] Robert H. Kadlec, Scott Wallace, and Scott Wallace. *Treatment Wetlands*. CRC Press, July 2008.

[46] M. Kania, M. Gautier, A. Imig, P. Michel, and R. Gourdon. Comparative characterization of surface sludge deposits from fourteen French Vertical Flow Constructed Wetlands sewage treatment plants using biological, chemical and thermal indices. *Science of The Total Environment*, 647:464–473, January 2019.

[47] M. Kania, M. Gautier, P. Michel, and R. Gourdon. Study of aggregation in surface sludge deposits from 14 full-scale French constructed wetlands using particle size distribution and dynamic vapor sorption analyses. *Water Science and Technology*, 77(1):79–90, 2018.

[48] M. Kania, M. Gautier, Z. Ni, E. Bonjour, R. Guégan, P. Michel, P. Jame, J. Liu, and R. Gourdon. Analytical indicators to characterize Particulate Organic Matter (POM) and its evolution in French Vertical Flow Constructed Wetlands (VFCWs). *Science of The Total Environment*, 622-623:801–813, May 2018.

[49] N. R. Khatiwada and C. Polprasert. Assessment of effective specific surface area for free water surface constructed wetlands. *Water Science and Technology*, 40(3):83–89, 1999.

[50] Boram Kim and Nicolas Forquet. Pore-scale observation of deposit within the gravel matrix of a vertical flow constructed wetland. *Environmental Technology*, 37(24):3146–3150, December 2016.

[51] Paul Knowles, Gabriela Dotro, Jaime Nivala, and Joan García. Clogging in subsurface-flow treatment wetlands: Occurrence and contributing factors. *Ecological Engineering*, 37(2):99–112, February 2011.

[52] Egidio Lardo, Aissa Arous, Assunta Maria Palese, Vitale Nuzzo, and Giuseppe Celano. Electromagnetic induction: A support tool for the evaluation of soil CO2 emissions and soil organic carbon content in olive orchards under semi-arid conditions. *Geoderma*, 264:188–194, February 2016.

[53] T. C. Lee, R. L. Kashyap, and C. N. Chu. Building Skeleton Models via 3-D Medial Surface Axis Thinning Algorithms. *CVGIP: Graphical Models and Image Processing*, 56(6):462–478, November 1994.

[54] David Legland, KiÃªn KiÃªu, and Marie-FranÃ§oise Devaux. Computation of Minkowski Measures on 2d and 3d Binary Images. *Image Analysis & Stereology*, 26(2):83, 2011.

[55] Gaëtan Lehmann and David Legland. Efficient N-Dimensional surface estimation using Crofton formula and run-length encoding. *The Insight Journal*, page 852, February 2012. Revision: 2.

[56] Johannes Lehmann and Markus Kleber. The contentious nature of soil organic matter. *Nature*, 528(7580):60–68, December 2015.

[57] A. Leonard, S. Blacher, P. Marchot, and M. Crine. Use of X-Ray Microtomography to Follow the Convective Heat Drying of Wastewater Sludges. *Drying Technology*, 20(4-5):1053–1069, June 2002.

[58] A. Leonard, S. Blacher, P. Marchot, J. P. Pirard, and M. Crine. Image analysis of X-ray microtomograms of soft materials during convective drying. *Journal of Microscopy*, 212(2):197–204, 2003.

[59] Angélique Léonard, Silvia Blacher, Pierre Marchot, Jean-Paul Pirard, and Michel Crine. Moisture Profiles Determination During Convective Drying Using X-Ray Microtomography. *The Canadian Journal of Chemical Engineering*, 83(1):127–131, 2005.

[60] J. H. Li, L. M. Zhang, Y. Wang, and D. G. Fredlund. Permeability tensor and representative elementary volume of saturated cracked soil. *Can. Geotech. J.*, 46(8):928–942, August 2009.

[61] Liénard, A. Vertical flow constructed wetlands fed with raw sewage: Historical review and recent developments in France. In *12th International Conference on Wetland Systems for Water Pollution Control, 04/10/2010-08/10/2010, Venise, ITA*, 2010.

[62] W. Brent Lindquist, Arun Venkatarangan, John Dunsmuir, and Teng-fong Wong. Pore and throat size distributions measured from synchrotron X-ray tomographic images of Fontainebleau sandstones. *Journal of Geophysical Research: Solid Earth*, 105(B9):21509–21527, 2000.

[63] W.B. Lindquist, S.-M. Lee, D.A. Coker, K.W. Jones, and P. Spanne. Medial axis analysis of void structure in three-dimensional tomographic images of porous media. *Journal of Geophysical Research B: Solid Earth*, 101(4):8297–8310, 1996.

[64] R. Lombard-Latune, L. Pelus, N. Fina, F. L'Etang, B. Le Guennec, and P. Molle. Resilience and reliability of compact vertical-flow treatment wetlands designed for tropical climates. *Science of The Total Environment*, 642:208–215, November 2018.

[65] José luis Arias López. *Vertical-flow constructed wetlands for the treatment of wastewater and stormwater from combined sewer systems*. PhD thesis, 2013.

[66] MacLeod, G., Adderley, P., Simpson, I., and Wilson, C. Thin Section & Micromorphology, 2018.

[67] G. D. Martinez-Carvajal, Laurent Oxarango, Jérôme Adrien, Pascal Molle, and Nicolas Forquet. Assessment of X-ray Computed Tomography to characterize filtering media from Vertical Flow Treatment Wetlands at the pore scale. *Science of the Total Environment*, 658:178–188, 2019.

[68] German Dario Martinez-Carvajal, Laurent Oxarango, Rémi Clément, Pascal Molle, and Nicolas Forquet. Assessment of spatial representativity of X-ray tomography to study Vertical Flow Treatment wetlands. *Science of the Total Environment*, 713:136510, 2020.

[69] F. Masi, A. Rizzo, and M. Regelsberger. The role of constructed wetlands in a new circular economy, resource oriented, and ecosystem services paradigm. *Journal of Environmental Management*, 216:275–284, June 2018.

[70] W. Masmoudi and M. Prat. Heat and mass transfer between a porous medium and a parallel external flow. Application to drying of capillary porous materials. *International Journal of Heat and Mass Transfer*, 34(8):1975–1989, 1991.

[71] Jonathan P. Mathews, J. Denis N. Pone, Gareth D. Mitchell, and Phillip Halleck. High-resolution X-ray computed tomography observations of the thermal drying of lump-sized subbituminous coal. *Fuel Processing Technology*, 92(1):58–64, January 2011.

[72] James W. McKinley and Robert L. Siegrist. Soil Clogging Genesis in Soil Treatment Units Used for Onsite Wastewater Reclamation: A Review. *Crit. Rev. Environ. Sci. Technol.*, 41(24):2186–2209, dec 2011.

[73] D.J. McNeill. Electromagnetic terrain conductivity measurements at low induction numbers. Technical Report Technical Note TN-6, GEONICS, 1980.

[74] L. Mercoiret, P. Molle, and N. Forquet. Domestic wastewater characteristics in French rural areas: concentrations and ratios for treatment plant under 2000 population equivalent (120kg of bod 5 a day). In *3rd International Congress Smallwat11. Wastewater in Small Communities. Towards the Millennium Development Goals (MDG) and the Water Framework Directive (WFD), 25/04/2011-28/04/2011, Seville, ESP*, page 5, 2011.

[75] Ralf Metzner, Anja Eggert, Dagmar van Dusschoten, Daniel Pflugfelder, Stefan Gerth, Ulrich Schurr, Norman Uhlmann, and Siegfried Jahnke. Direct comparison of MRI and X-ray CT technologies for 3d imaging of root systems in soil: potential and challenges for root trait quantification. *Plant Methods*, 11(1):17, March 2015.

[76] Maryam Mirabolghasemi, Maša Prodanović, David DiCarlo, and Hongyu Ji. Prediction of empirical properties using direct pore-scale simulation of straining through 3D microtomography images of porous media. *Journal of Hydrology*, 529(P3):768–778, 2015.

[77] P. Molle, A. Liénard, A. Grasmick, and A. Iwema. Effect of reeds and feeding operations on hydraulic behaviour of vertical flow constructed wetlands under hydraulic overloads. *Water Research*, 40(3):606–612, February 2006.

[78] Pascal Molle. French vertical flow constructed wetlands: a need of a better understanding of the role of the deposit layer. *Water Sci Technol*, 69(1):106–112, January 2014.

[79] Pascal Molle, A. LiÃ©nard, C. Boutin, G. Merlin, and A. Iwema. How to treat raw sewage with constructed wetlands: An overview of the French systems. *Water Science and Technology*, 51(9):11–21, 2005.

[80] Ahmad B. Moradi, Andrea Carminati, Doris Vetterlein, Peter Vontobel, Eberhard Lehmann, Ulrich Weller, Jan W. Hopmans, Hans Jörg Vogel, and Sascha E. Oswald. Three-dimensional visualization and quantification of water content in the rhizosphere. *New Phytologist*, 192(3):653–663, 2011.

[81] A. Morvannou. *Dynamic modelling of nitrification in vertical flow constructed wetlands*. PhD Thesis, UniversitÃ© Catholique de Louvain, 2011.

[82] A. Morvannou, N. Forquet, S. Michel, S. Troesch, and P. Molle. Treatment performances of French constructed wetlands: results from a database collected over the last 30 years. *Water Sci Technol*, 71(9):1333–1339, May 2015.

[83] A. Morvannou, N. Forquet, M. Vanclooster, and P. Molle. Which Hydraulic Model To Use In Vertical Flow Constructed Wetlands? In *13th International Conference on Wetland Systems for Water Pollution Control, 25/11/2012-29/11/2012, Perth, AUS*, page 9, 2012.

[84] Ania Morvannou, Jean-Marc Choubert, Marnik Vanclooster, and Pascal Molle. Modeling nitrogen removal in a vertical flow constructed wetland treating directly domestic wastewater. *Ecological Engineering*, 70:379–386, September 2014.

[85] Jaime Nivala, Paul Knowles, Gabriela Dotro, Joan GarcÃa, and Scott Wallace. Clogging in subsurface-flow treatment wetlands: Measurement, modeling and management. *Water Research*, 46(6):1625–1640, 2012.

[86] Laurent Orgogozo, Fabrice Golfier, Michel Buès, and Michel Quintard. Upscaling of transport processes in porous media with biofilms in non-equilibrium conditions. *Advances in Water Resources*, 33(5):585–600, 2010.

[87] Jean-Marie PÃ©tÃ©managnan Ouattara, Lacina Coulibaly, Seydou Tiho, and Germain Gourène. Comparison of macrofauna communities in sediments of the beds of vertical flow constructed wetlands planted with Panicum maximum (Jacq.) treating domestic wastewater. *Ecological Engineering*, 35(8):1237–1242, August 2009.

[88] Laurent Oxarango. *Transferts de Chaleur et de Masse dans des structures poreuses multi-échelles*. PhD thesis, 2004.

[89] Tamás Gábor Pálfy. DESIGN OPTIMIZATION OF CSO CWS KEY PROCESSES AND DEVELOPMENT OF A MODELLING TOOLKIT. 2016.

[90] Vladimir Pilny and Jiri Janacek. *Anisotropic Diffusion 2D*. 2006.

[91] Chongrak Polprasert and Nawa Raj Khatiwada. An integrated kinetic model for water hyacinth ponds used for wastewater treatment. *Water Research*, 32(1):179–185, 1998.

[92] V. J. P. Poots and G. McKay. The specific surfaces of peat and wood. *Journal of Applied Polymer Science*, 23(4):1117–1129, 1979.

[93] William K Pratt. Digital Image Processing. In *Digital Image Processing*, pages i–xix. John Wiley & Sons, Inc., 2006.

[94] Jean H. Prevost and Benjamin Loret. Dynamic strain localization in elasto-(visco-)plastic solids, part 2. plane strain examples. *Computer Methods in Applied Mechanics and Engineering*, 83(3):275–294, November 1990.

[95] Bernhard Pucher and Guenter Langergraber. The state of the art of clogging in vertical flow Wetlands. *Water (Switzerland)*, 11(11), 2019.

[96] Arash Rabbani, Saeid Jamshidi, and Saeed Salehi. An automated simple algorithm for realistic pore network extraction from micro-tomography images. *Journal of Petroleum Science and Engineering*, 123:164–171, 2014.

[97] Amin Reza Rajabzadeh, Raymond L. Legge, and Kela P. Weber. Multiphysics modelling of flow dynamics, biofilm development and wastewater treatment in a subsurface vertical flow constructed wetland mesocosm. *Ecological Engineering*, 74:107–116, January 2015.

[98] Miriam Patricia Ortega Ramírez, Laurent Oxarango, and Alfonso Gastelum Strozzi. Effect of X-ray CT resolution on the quality of permeability computation for granular soils: definition of a criterion based on morphological properties. *Soil Res.*, 57(6):589–600, September 2019.

[99] F Rezanezhad, W L Quinton, J S Price, D Elrick, T R Elliot, and R J Heck. Examining the effect of pore size distribution and shape on flow through unsaturated peat using 3-D computed tomography. *Hydrology and Earth System Sciences Discussions*, 6(3):3835–3862, 2009.

[100] Eva Risch, Oriol Gutierrez, Philippe Roux, Catherine Boutin, and Lluís Corominas. Life cycle assessment of urban wastewater systems: Quantifying the relative contribution of sewer systems. *Water Research*, 77:35–48, June 2015.

[101] Laurence Rolland. *ANALYSES COMPARATIVES DE SYSTÈMES D'INFILTRATION-PERCOLATION : COLMATAGE ET OUTILS DE DIAGNOSTICS*. PhD thesis, UNIVERSITE MONTPELLIER II, 2009.

[102] Anthony Rosato, Katherine J. Strandburg, Friedrich Prinz, and Robert H. Swendsen. Why the Brazil nuts are on top: Size segregation of particulate matter by shaking. *Phys. Rev. Lett.*, 58(10):1038–1040, March 1987.

[103] Thierry Ruiz and Christelle Wisniewski. Correlation between dewatering and hydro-textural characteristics of sewage sludge during drying. *Separation and Purification Technology*, 61(2):204–210, July 2008.

[104] Rebeca N. Sacramento, Yulong Yang, Zhenjiang You, Alex Waldmann, André L. Martins, Alexandre S. L. Vaz, Pacelli L. J. Zitha, and Pavel Bedrikovetsky. Deep bed and cake filtration of two-size particle suspension in porous media. *Journal of Petroleum Science and Engineering*, 126:201–210, February 2015.

[105] Toyofumi Saito and Jun-Ichiro Toriwaki. New algorithms for euclidean distance transformation of an n-dimensional digitized picture with applications. *Pattern Recognition*, 27(11):1551–1565, November 1994.

[106] Roger Samsó, Joan García, Pascal Molle, and Nicolas Forquet. Modelling bioclogging in variably saturated porous media and the interactions between surface/subsurface flows: Application to Constructed Wetlands. *Journal of Environmental Management*, 165:271–279, January 2016.

[107] Luis A Santaló. *Integral Geometry and Geometric Probability*. Cambridge University Press, Cambridge, 2 edition, 2004.

[108] Joelle Sasse, Enrico Martinoia, and Trent Northen. Feed Your Friends: Do Plant Exudates Shape the Root Microbiome? *Trends in Plant Science*, 23(1):25–41, January 2018.

[109] Johannes Schindelin, Ignacio Arganda-Carreras, Erwin Frise, Verena Kaynig, Mark Longair, Tobias Pietzsch, Stephan Preibisch, Curtis Rueden, Stephan Saalfeld, Benjamin Schmid, Jean-Yves Tinevez, Daniel James White, Volker Hartenstein, Kevin Eliceiri, Pavel Tomancak, and Albert Cardona. Fiji: an open-source platform for biological-image analysis. *Nat Methods*, 9(7):676–682, July 2012.

[110] Steffen Schlüter, Adrian Sheppard, Kendra Brown, and Dorthe Wildenschild. Image processing of multiphase images obtained via X-ray microtomography: A review. *Water Resources Research*, 50(4):3615–3639, 2014.

[111] Pierre Soille. *Morphological Image Analysis: Principles and Applications*. Springer-Verlag New York, Inc., Secaucus, NJ, USA, 2 edition, 2003.

[112] K. Stamatakis and Chi Tien. Cake formation and growth in cake filtration. *Chemical Engineering Science*, 46(8):1917–1933, January 1991.

[113] M Sundaravadivel and S Vigneswaran. Constructed Wetlands for Wastewater Treatment. *Critical Reviews in Environmental Science and Technology*, 31(4):351–409, 2001.

[114] Anna Szafranek-Nakonieczna and Riccardo Paolo Bennicelli. Ability of peat soil to oxidize methane and affect temperature and layer deposition. *Polish Journal of Environmental Studies*, 19(4):805–810, 2010.

[115] Thiery, C. Tomographie à rayons X. *Techniques de l'ingénieur CND : méthodes globales et volumiques*, base documentaire : TIB585DUO(ref. article : p950), December 2013.

[116] Antonina Torrens, Pascal Molle, Catherine Boutin, and Miquel Salgot. Removal of bacterial and viral indicator in vertical flow constructed wetlands and intermittent sand filters. *Desalination*, 246(1-3):169–178, 2009.

[117] Robert Treybal. *Mass Transfer Operations*. McGraw-Hill, 3rd editio edition, 1981.

[118] S. Troesch, A. Liénard, P. Molle, G. Merlin, and D. Esser. Sludge drying reed beds: Full- and pilot-scale study for activated sludge treatment. *Water Science and Technology*, 60(5):1145–1154, 2009.

[119] D. Tschumperlé and R. Deriche. Vector-valued Image Regularization with PDE's: A Common Framework for Different Applications. In *Proceedings of the 2003 IEEE Computer Society Conference on Computer Vision and Pattern Recognition*, CVPR'03, pages 651–656, Washington, DC, USA, 2003. IEEE Computer Society. event-place: Madison, Wisconsin.

[120] Guido Van Rossum and Fred L Drake Jr. *Python tutorial*. Centrum voor Wiskunde en Informatica Amsterdam, The Netherlands, 1995.

[121] Horst Vierheilig, Andrew P. Coughlan, Urs Wyss, and Yves Piché. Ink and Vinegar, a Simple Staining Technique for Arbuscular-Mycorrhizal Fungi. *Appl. Environ. Microbiol.*, 64(12):5004–5007, December 1998.

[122] Julie Vincent. *Les lits de séchage de boue plantés de roseaux pour le traitement des boues activées et les matières de vidange : adapter la stratégie de gestion pour optimiser les performances*. thesis, Montpellier 2, December 2011.

[123] Julie Vincent, Nicolas Forquet, Pascal Molle, and Christelle Wisniewski. Mechanical and hydraulic properties of sludge deposit on sludge drying reed beds (SDRBs): Influence of sludge characteristics and loading rates. *Bioresource Technology*, 116:161–169, July 2012.

[124] A. Wanko, R. Mose, and A. Liénard. CapacitÃ©s de traitement d'un effluent de synthÃšse en infiltration percolation. *Revue des Sciences de l'Eau*, 18/2(CQELY.18852 ; 05/0177):165–175, 2005.

[125] Dorthe Wildenschild and Adrian P. Sheppard. X-ray imaging and analysis techniques for quantifying pore-scale structure and processes in subsurface porous medium systems. *Advances in Water Resources*, 51:217–246, January 2013.

[126] Dongxiao Zhang, Raoyang Zhang, Shiyi Chen, and Wendy E. Soll. Pore scale study of flow in porous media: Scale dependency, REV, and statistical REV. *Geophysical Research Letters*, 27(8):1195–1198, 2000.